Optical properties of lamellar systems under high magnetic fields

Alex Delhomme

THÈSE

Pour obtenir le grade de

DOCTEUR DE L'UNIVERSITÉ GRENOBLE ALPES

Spécialité : NANOPHYSIQUE

Arrêté ministériel : 25 mai 2016

Présentée par

Alex DELHOMME

Thèse dirigée par **Clément FAUGERAS** ,Chargé de recherche, Université Grenoble Alpes
et co-encadrée par **Benjamin PIOT**,Chargé de recherche, Université Grenoble Alpes

préparée au sein du **Laboratoire LNCMI - Laboratoire National des Champs Magnétiques Intenses**
dans **l'École Doctorale Physique**

Propriétés optiques de systèmes lamellaires sous champ magnétique intense

Optical properties of lamellar systems under high magnetic fields

Thèse soutenue publiquement le **21 janvier 2022**,
devant le jury composé de :

Monsieur ADAM BABINSKI
Professeur, Uniwersytet Warszawski, Rapporteur
Monsieur FAUSTO SIROTTI
Directeur de recherche, CNRS DELEGATION ILE-DE-FRANCE SUD, Rapporteur
Monsieur JOHANN CORAUX
Directeur de recherche, CNRS DELEGATION ALPES, Président
Monsieur JULIEN PERNOT
Professeur des Universités, UNIVERSITE GRENOBLE ALPES, Examinateur
Madame ANGELA VASANELLI
Professeur des Universités, UNIVERSITE PARIS 7 - DENIS DIDEROT, Examinatrice

Remerciements

Je souhaite, tout d'abord, remercier Clément Faugeras, mon directeur de thèse. Il m'a donné l'opportunité de poursuivre en doctorat, m'a accordé sa confiance et m'a accompagné, durant ces trois années et demie. Mon passage au Laboratoire national des champs magnétiques intenses du CNRS aura été une expérience enrichissante, m'offrant la possibilité de m'engager dans des travaux passionnants. Je garderai de très bons souvenirs des nuits blanches passées dans les expériences en champ magnétique intense, avec à la clé, de bonnes ou moins bonnes surprises, lors de ces mesures nocturnes. Cette période a parfois été aussi pour moi une épreuve d'endurance. Je remercie Clément de m'avoir soutenu et guidé vers la réussite. Je lui témoigne toute ma gratitude.

Je souhaite ensuite, remercier mon co-directeur, Benjamin Piot, pour nos collaborations périodiques. Je lui suis reconnaissant d'avoir organisé ma soutenance de thèse de la meilleure des manières, au vu des conditions sanitaires particulières.

Je remercie Ivan Breslavetz, Milan Orlita et Marek Potemski pour leurs conseils éclairés. J'inclus également toutes les personnes du LNCMI qui m'ont aidé de bien des manières. Parmi eux, je salue mes camarades doctorants Piotr Kapuscinski, Diana Vaclavkova et Jan Wyzula. Nous avons commencé cette aventure grenobloise ensemble et je les remercie de leur présence et de leur aide.

Je remercie mes amis Clément Girot et Michaël Nale, compagnons de la première heure sur la route du doctorat. Je leur dois des moments inoubliables passés en leur compagnie … de ceux qui scellent une amitié sincère, dans la joie comme dans les moments difficiles. Cette aventure n'aurait pas été la même sans eux.

Enfin, je remercie mes parents Luc et Nadine, mon frère et ma belle-sœur Sacha et Calliope, ainsi que ma sœur Léna pour leur soutien indéfectible, lorsque la route était longue.

Résumé en français

Les dichalchogenures de métaux de transition semi-conducteurs (TMD) constituent un groupe de matériaux faisant preuve de propriétés optiques singulières, qui en font de bons candidats pour des applications dans le domaine de l'optoélectronique à l'échelle nanométrique. Bien qu'elles aient été étudiées depuis maintenant plus d'un demi-siècle, elles ont suscité un regain d'intérêt lors de l'intense activité scientifique impulsée par la découverte du Graphène en 2004. Comme pour le graphite, les cristaux *massifs* de s-TMD sont constitués de l'empilement de plans monocristallins liés les uns aux autres par la force de van der Waals. Le caractère direct ou indirect du gap électronique des TMD dépend de l'épaisseur du cristal : le gap indirect observé pour les TMD massifs évolue progressivement vers un gap direct dans le cas de la monocouche. En 2010, il a été démontré que les monocouches de MoS_2 étaient bien des semi-conducteurs de gap directs faisant preuve d'un fort couplage rayonnement matière, résultant en l'observation d'excitons avec une très forte énergie de liaison. Le fort couplage spin orbite dans ces matériaux, combiné à la physique de vallées, héritée d'une Zone de Brillouin très similaire à celle du graphène, a popularisé l'étude des monocouches et multicouches de TMD. La facilité avec laquelle deux monocouches peuvent être interfacées a élargi le champ d'étude aux hétérobicouches de TMD. Ces hétérostructures de type II, dont le caractère direct ou indirect du gap électronique est conditionné par l'angle θ entre les deux monocouches, sont le siège de recombinaisons excitoniques dont le trou et l'électron sont chacun localisés dans une couche différente. Comme dans le cas des excitons confinés dans des doubles puits quantiques couplés, le faible recouvrement entre les fonctions d'onde des deux particules résulte en l'accroissement de l'énergie de liaison, ainsi qu'en un plus long temps de vie de l'exciton. De plus, l'angle θ (ainsi que l'écart de paramètre de maille entre les deux matériaux de l'hétérobicouche) induit la formation d'un moiré atomique à l'interface de l'hétérostructure ce qui a stimulé la recherche théorique et expérimentale visant à étudier ces excitons intercouche piégés dans le potentiel moiré. A cet égard, la magnéto-spectroscopie est une technique de choix pour caractériser les propriétés optiques et électroniques de ces systèmes. En effet, la brisure de symétrie imposée par le champ magnétique résulte en la levée de dégénérescence entre les énergies des deux composantes émises par les vallées +K et –K. La différence d'énergie entre ces deux composantes, proportionnelle au champ magnétique appliqué, définit le facteur-g dont signe et la valeur absolue donne des informations cruciales pour l'identification des bandes impliquées dans les processus de recombinaison optique.

Dans ce manuscrit seront présentés les résultats d'expériences de spectroscopie et de magnéto-spectroscopie visant à étudier les propriétés optiques et électroniques de systèmes lamellaires sous l'influence d'un fort champ magnétique.

Abstract in english

Semiconductor transition metal dichalcogenides (TMDs) are a group of materials showing unique optical properties making them good candidates for opto-electronic applications at the nanoscale. While these compounds have been studied for more than half a century already, they have gained interest during the intense stimulation of scientific research on atomically thin crystals initiated by the first isolation of graphene in 2004. Just like graphite, bulk TMD crystals consist of a stack of atomically thin planes held together by van der Waals forces. The momentum alignment of TMDs 'electronic gap strongly depends on the thickness of the crystal and transition from a momentum-indirect gap in the bulk and in few-layers systems, to a direct momentum gap in monolayers. In 2010, MoS_2 monolayers have been shown to be momentum-direct gapped semiconductors showing a very strong coupling to light resulting in the creation of excitons with a high binding energy. The strong spin-orbit interaction observed in these materials, coupled to the valley physics inherited from their graphene-like Brillouin zone, has popularized the study of monolayers and few-layers TMDs. The ability to easily stack together TMD monolayers of different materials has resulted in the fabrication of TMD heterobilayers showing a staggered band gap, for which the interlayer twist angle θ tunes the momentum alignment between the Brillouin zones of the two layers and enhances the recombination of interlayer excitons at the K valleys of the heterostructure. Just as spatially indirect excitons localized in coupled quantum wells, the weak overlap of the particles' wave functions resulting of their physical separation leads to an increase of the exciton binding energy and an enhancement of its lifetime. Moreover, both θ and the different lattice parameters of the two constituent monolayers introduce a moiré pattern in the 2D heterobilayer crystal which has stimulated the theoretical and experimental study of these moiré trapped interlayer excitons. In this regard, magneto-spectroscopy has become a technique of choice to investigate the optical and electronic properties of these heterostructures, as the breaking of time reversal symmetry imposed by a magnetic field lifts the energy degeneracy between the $\sigma+$ and $\sigma-$ polarized emission from +K and -K valley. The resulting energy difference between the two components is proportional to the magnetic field and defines the exciton g-factor, which sign and magnitude gives crucial information on the spin and valley indices of the electronic sub band involved in the recombination. In this manuscript, we will show the results of optical and magneto-optical experiments designed to study the optical and electronic properties of lamellar systems under high magnetic fields.

Organisation du manuscrit

Dans le Chapitre 1, nous introduirons les différents concepts nécessaires à la compréhension de la physique des excitons dans les monocouches et les hétérobicouches de TMD à travers une revue de l'état-de-l 'art.

Dans le Chapitre 2, nous présenterons l'instrumentation utilisée dans le cadre des expériences décrites dans la suite de cet ouvrage.

Dans le Chapitre 3, nous présenterons les résultats d'expériences visant à caractériser nos échantillons afin de les comparer à la littérature.

Dans le Chapitre 4, nous présenterons les résultats d'expériences originales de spectroscopie et de magnéto-spectroscopie. Nous focaliserons notre discussion sur l'influence qu'a la densité excitonique sur la forme et l'énergie du spectre de recombinaison des excitons intercouches.

Dans le chapitre 5, nous discuterons de la signification du signe et de la valeur du facteur-g et présenterons un modèle simple, basé sur l'observation des facteurs-g des excitons dans les monocouches, pour estimer le facteur-g des excitons intercouches.

Dans le chapitre 6, nous expliquerons le résultat principal de cette thèse, qui est l'observation d'une interaction exciton-phonon résonante en champ magnétique. Nous exploiterons la finesse de cette interaction pour résoudre l'influence locale du potentiel cristallin causé par l'angle θ sur les propriétés de l'exciton intercouche.

Structure of the manuscript

In Chapter 1 we will introduce the different concepts necessary to understand the physics of excitons in TMD monolayers and heterobilayers through a review of the state-of-the-art literature.

In Chapter 2, we will present the experimental setups used to obtain the results shown in the rest of the manuscript.

In Chapter 3, we will show the results of photoluminescence mapping and magneto-spectroscopy experiments designed to characterize our samples

In Chapter 4, we will present the results of photoluminescence excitation experiments, excitation power dependence and magneto-photoluminescence experiments in high magnetic field. We will focus our discussion on the influence of the interlayer exciton density over the interlayer exciton photoluminescence spectrum.

In Chapter 5, we will discuss the significance of the sign and magnitude of the g-factor and present a very simple model, based on observations made in TMD monolayers, to predict the g-factor of interlayer exciton.

In Chapter 6, we will present the main result of this manuscript, which is the observation of a magneto-resonant exciton- chiral phonon interaction. We will then exploit the finesse of this interaction to resolve how the underlying potential landscape caused by the twist angle between the monolayers affects the properties of the interlayer through an energy dependent g-factor.

Contents

Chapter 1: Introduction to TMD heterobilayers.

1.1/ Introduction:

In this chapter, we will introduce the different concepts necessary to understand the physics of interlayer excitons in transition metal chalcogenides through a review of the literature. We will present the crystal properties and electronic band structure of transition metal chalcogenides from the bulk state down to the monolayer. We will discuss the interaction of these materials with light and the resulting optical selection rules. We will catalogue the different excitonic complexes that have been observed in TMD monolayers using optical spectroscopy techniques such as photoluminescence, absorption and reflectance contrast spectroscopy. Finally, we will discuss the influence of an external magnetic field on the optical properties of TMD monolayers.

We will then shift our discussion toward TMD heterobilayers, which are van der Waals heterostructures created by stacking together two monolayers of different materials. This leads to the creation of a semiconductor heterostructure presenting a staggered electronic gap. The twist angle θ between the two constituent TMD tunes the alignment of their respective Brillouin zone, which defines the momentum alignment of the interlayer gap. If the interlayer gap is direct in momentum space, the heterobilayer can then host interlayer excitons, i.e. electron-hole complexes in which the two bound particles are localized in different monolayers, similarly to spatially indirect excitons in coupled quantum wells. Moreover, the differences in the lattice parameters between the two constituent monolayers introduce a moiré pattern in the 2D heterobilayer crystal and thus a moiré pattern on the potential trapping the interlayer excitons. We will review the recent studies about these interlayer excitons trapped in the moiré potential of TMD heterobilayers, which display properties that are very different from the ones of excitons in TMD monolayers, defined in this case as intralayer excitons. Because of the modulation of the potential introduced by the moiré pattern, interlayer excitons in TMD can be seen as a quantum dots like system . We will conclude our review of interlayer excitons by a discussion about the evidences of moiré reconstruction at the interface of TMD heterobilayers. Recently, experimental data have questioned the moiré description that considers constituent monolayers as completely rigid and point toward a local reconstruction into homogeneous domains minimizing the stacking energy of the system.

1.2/ Properties of TMD:

1.2.1/General discussion on TMDs

Transition Metal Dichalcogenides (TMD) are a family of material with chemical formula MX_2, where M is a transition metal atom (such as Ti,V,Mo or W) and X is one of the three chalcogens Se,S or Te. More than 60 different TMDs are currently known and they can exhibit strikingly different properties depending of the metal/chalcogen atom combination [Pulkin 2016]. A common ground however can be found in the mechanical properties of these compounds in the sense that most of the TMDs are layered materials: the bulk compound, just like graphite, consists of a stack of monoatomic planes held together by the van der Walls (vdW) force.

Before going into the specifics of the crystal cell and band structure, it must be noted that TMDs can be stable in several structural phases corresponding to different stacking orders. The two common structural phases are either trigonal prismatic (2H stacking) or octahedral (1T), with an additional but marginal rhombohedral (3R) configuration. In the 2H phases, chalcogen atoms in every other atomic planes are located on top of each other in the ABA configuration while 1T and 3R both correlates to the ABC stacking order. Depending on the particular combination of transition metal and chalcogen, the thermodynamically stable phase can be either 2H of 1T (however the other configuration can still generally be found as a metastable phase). In the case of multilayer and bulk samples, the properties of TMD can further be influenced by possible distortions that lower the periodicity. They can for examples result in the formation of metal−metal bonds or charge density wave phases. This gives rise to a large family of materials with varying properties making them useful for nanoelectronics and nanophotonics applications [Mak 2016]. In this manuscript however, we will restrict ourselves to semiconductor TMDs and use this general term to describe only compounds with a transition metal from the VIth column of the periodic table (ie. Mo of W based) with either S or Se atoms as chalcogen, crystallizing in the 2H/3R phases (cf Fig(1.1)).

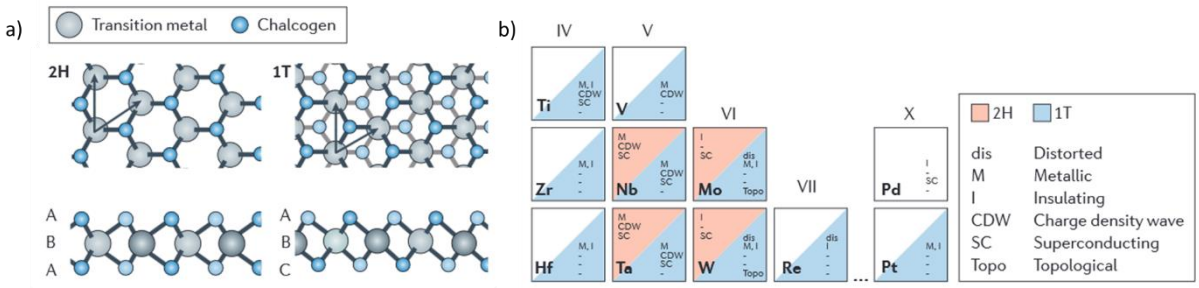

Fig1.1 a) Atomic structure of single layers of transition metal dichalcogenides (TMD) in their trigonal prismatic (2H), and distorted octahedral (1T) phases. Lattice vectors and the stacking of atomic planes are indicated. **b)** 'Periodic table' of known layered TMD, organized based on the transition metal element involved, summarizing their existing structural phases (2H, 1T or other, as in the case of Pd-based TMDCs) and indicating the presence of distorted structural phases and observed electronic phases. Figure adapted from [Pulkin 2016].

1.2.2/ Crystal structure

In the crystal cell of group VI semiconductor TMDs, each metal atom is sandwiched between two planes of three chalcogen atoms. The in-plane repetition of this cell shapes the monolayer into three parallel atomic planes, a transition metal plane between two chalcogen. This forms a nearly 2D (0,6 nanometer thick) hexagonal lattice, with one metal atom occupying the A site, while the B site is occupied by two chalcogen atoms and the C site is unoccupied. This breaks inversion symmetry in the cell (taking the metal atom as an inversion center, any chalcogen atom is sent to an empty C site) and reduces its symmetry group from C_6 to C_3. The monolayer Brillouin zone is also hexagonal (cf Fig(1.2.c)), but because of this reduced symmetry, neighboring K points cannot be considered as equivalent, this gives rise to an alternation of +K and -K valleys at the corners of the hexagon related by time reversal symmetry. This is absolutely capital, as the major optical and electronic properties of TMDs monolayer discussed in this manuscript arise from these K and –K valleys.

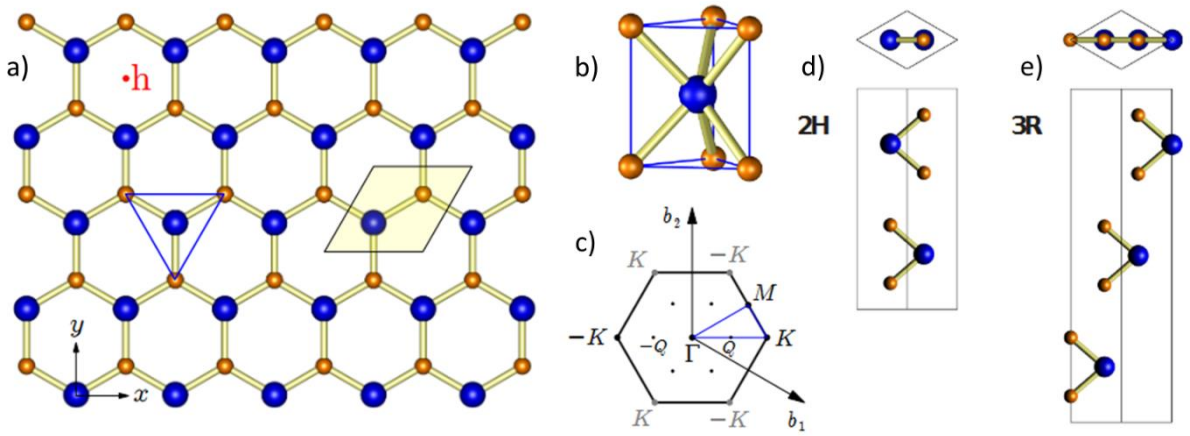

Fig1.2 a) Top view of group-VIB TMD monolayers. The blue and orange spheres represent M and X atoms respectively. The light yellow diamond region is the 2D unit cell with lattice constant a. **b)** Trigonal prismatic coordination geometry, corresponding to the blue triangle in top view. **c)** The first Brillouin zone. *b1* and *b2* are the reciprocal lattice vectors. **d)** Top and side views of the unit cell of bulk or bilayer of 2H stacking. **e)** Unit cell of bulk group-VIB TMDs of 3R/1T stacking. Figure adapted from [Liu 2015]

As specified above, the 2H configuration correlates to the ABA stacking order, which means that in the case of the bulk crystal structure, all neighboring monolayers are flipped by 180° with respect to each other, as such, there is an alternation of A and B sites along the Z axis. The 3R/1T phase however exhibits a rhombohedral symmetry: in the case of a trilayer, the metal atom at the A site of the first layer is located directly below the B site of the second layer, which is in turn below the unoccupied C site of the third layer. The 3R bulk phase, consisting of the repetition of these trilayers, corresponds to the ABC stacking type. It is to be noted that the majority of naturally exfoliated TMD thin films exhibit an ABA stacking corresponding to the 2H configuration. First-principles calculations based on density functional theory shown in [Santosh 2015] compare the relative stability of various phases of TMDs and establish that the 2H configuration minimizes the stacking energy compared to the 3R/1T configurations.

1.2.3/ Band structure

In the rise of the research on graphene [Geim 2007], TMD have become popular materials in the search for quasi 2D gapped systems as their mechanical properties allow for an easy

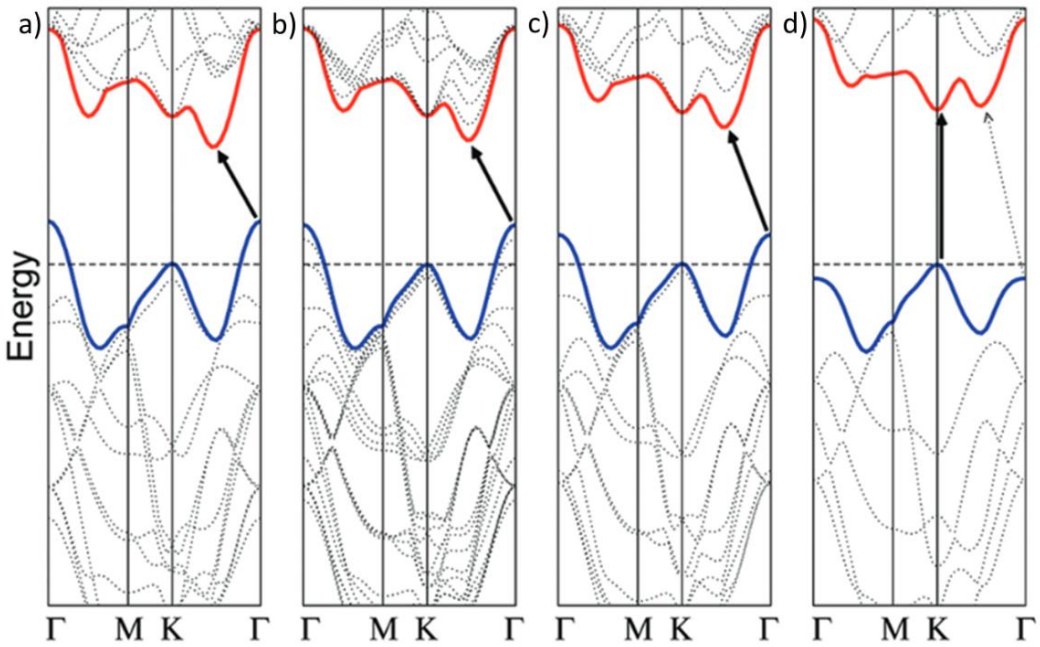

Fig.1.3 Calculated band structures of **a)** bulk MoS_2, **b)** quadrilayer MoS_2, **c)** bilayer MoS_2, and **d)** monolayer MoS_2. The solid arrows indicate the lowest energy transitions. Bulk MoS_2 is characterized by an indirect bandgap. The direct excitonic transitions occur at high energies at K point. With reduced layer thickness, the indirect bandgap becomes larger, while the direct excitonic transition barely changes. For monolayer MoS_2 in d), it becomes a direct bandgap semiconductor. Figure adapted from [Splendiani 2010].

exfoliation down to the monolayer. The transition from the bulk material to the monolayer form alters the electronic band structure of TMDs from indirect gap semiconductor to direct gap semiconductor. Fig(1.3) illustrates this transition by picturing the band structure of MoS_2 as a function of the number of layers. In the case of bulk TMD, three important high symmetry points should be considered : the Γ point at the center of the Brillouin zone, the previously mentioned K (or in that case equivalent -K) points and the Q (-Q) points, situated halfway between Γ and K. In the bulk form, the conduction band minimum is situated at the Q point, while the top of the valence band is at the Γ point, which results in a momentum indirect gap. When decreasing the number of layers, the conduction band around the Q point progressively shifts to the higher energies (which makes the band minimum shift toward K) while the valence band at the Γ point shifts to lower energies. The conduction and valence bands around K point are weakly affected. Finally, and only for the monolayer, both the conduction band minimum and valence band maximum sit at K point, which results in a momentum direct gap. This is a fundamental difference with other semiconductors like GaAs for which the electronic gap is located at the center (Γ point) of the Brillouin zone [Ehrenreich 1960]. As we will see later in this chapter, this is fundamental to the unique optical properties observed in TMD monolayers.

First principle calculations in [Cappelluti 2013] describe this change of the band structure. The authors consider MoS_2 within a tight binding model, in which all electronic bands of the band structure consist of a mix of orbitals arising from the transition metal or chalcogen atoms that can be generalized to the other group VI TMDs. In this case, we consider the 4d orbitals from the metal atom M and 2p orbitals from the chalcogen X. Tab(1.1) shows the orbital mix composing the conduction and valence bands at the K,Q and Γ points of interest of the Brillouin zone. The conduction and valence bands at K point mainly involve respectively M-d_0 (composed of d_{x^2}, d_{y^2} and d_{xy} orbitals) and M-d_2 (d_{z^2}) orbitals with a minor presence of in-plane

State	Majority of orbitals	Minority of orbitals
K_c	M-d_{z^2}	X-p_x,p_y
K_v	M-$d_{x^2-y^2}$,d_{xy}	X-p_x,p_y
Q_c	M-$d_{x^2-y^2}$,d_{xy}	M-d_{z^2}, X-p_x,p_y,p_z
Γ_v	M-d_{z^2}	X-p_z

Tab1.1 Orbital compositions of Bloch states at the conduction band critical points K_c and Q_c, and valence band critical points K_v and G_v in monolayer TMDs. Table adapted from [Liu 2015]

X-$p_{x/y}$ chalcogen orbitals. Since M-d_0 and X-$p_{x/y}$ are in-plane components, there is no expected overlap of these orbitals between neighboring layers. The out-of-plane orbital M-d_2 is also not expected to overlap significantly due to the central position of the metal atom in the TMD monolayer crystal plane. Thus, the orbital mix of the conduction and valence bands at K point are not affected by the presence of neighboring layers, hence this is why the band structure at K point is independent of the crystal thickness. In the case of the Γ point , the orbital mix of the valence band presents a non-negligible proportion of the out of plane X-p_z while the conduction band at Q point is composed of a mix of the out-of-plane X-p_z and in-plane X-$p_{x/y}$ components. Both these orbitals arise from the chalcogen atoms at the edges of the TMD crystal plane, and thus show an overlap with the orbitals from neighboring layers. This is especially the case for X-p_z which is an out-of-plane component and results in the shift of the band structure at Q and Γ points shown in Fig(1.3).

1.3/ Light-matter coupling in TMDs:

1.3.1/ Excitons

In 3D semiconductors, the excitation of an electron by an incident photon promotes it to the conduction band, leaving behind an empty state surrounded by an electronic sea. This empty state can be seen as a quasi-particle, a hole with a positive charge, which interacts with the electron by the Coulomb interaction. The attractive Coulomb interaction is described by the Coulomb potential:

$$V_{eh}(r) = \frac{e^2}{4\pi\varepsilon_{eff} r} \qquad Eq(1.1)$$

With e the electron's charge and ε_{eff} the effective dielectric constant of the material. The electron and the hole can exist as a bound complex inside the gap E_G of the material: the exciton, which recombines in a photon with an energy E_{PL} inferior to E_G. The difference between E_G and E_{PL} defines the binding energy E_B. In TMD ML, the greater spatial confinement imposed by the reduced dimensionality of the system leads to an enhancement of the Coulomb interaction and to the formation of excitons with a high binding energy ($E_B \sim 500$ meV [Chernikov 2014, Wang 2015] compared to $E_B \sim 21$ meV in bulk GaN [Shan 1996]).

In analogy with 2D hydrogenic Rydberg series [Zaslow 1967], the exciton can be described as a fundamental state, the 1s state, and a series of excited states denominated 2s,3s,etc... In this model, the binding energy of the n^{th} excited state is written :

$$E_B{}^{(n)} = \frac{Me^2}{2\hbar^2 \varepsilon_{eff}{}^2} \times \frac{1}{(n-\frac{1}{2})^2} \qquad Eq(1.2)$$

With M the excitonic reduced mass $1/(m_e^{-1} + m_h^{-1})$. The radius of the electron-hole orbit of the nth state is written :

$$r^{(n)} = \frac{\varepsilon_{eff}}{M} n a_B \qquad Eq(1.3)$$

With $a_B$the exciton Bohr radius of the hydrogenic fundamental state.

$E^{(0)}$ is the binding energy of the fundamental state and $E_G - E_B{}^{(0)}$ defines the optical gap i.e. the minimum energy of the photon to excite an electron in the material.

$E^{(n)}$ decreases with n and the excited states can be seen, still in analogy with the hydrogen atom, as an increasing separation between the electron and the hole. When n in infinite, the particles of the excitons are no longer bound since the binding energy is zero and $r^{(n)}$ is infinite. Fig(1.4) shows the adsorption of a material dominated by the excitonic effect.

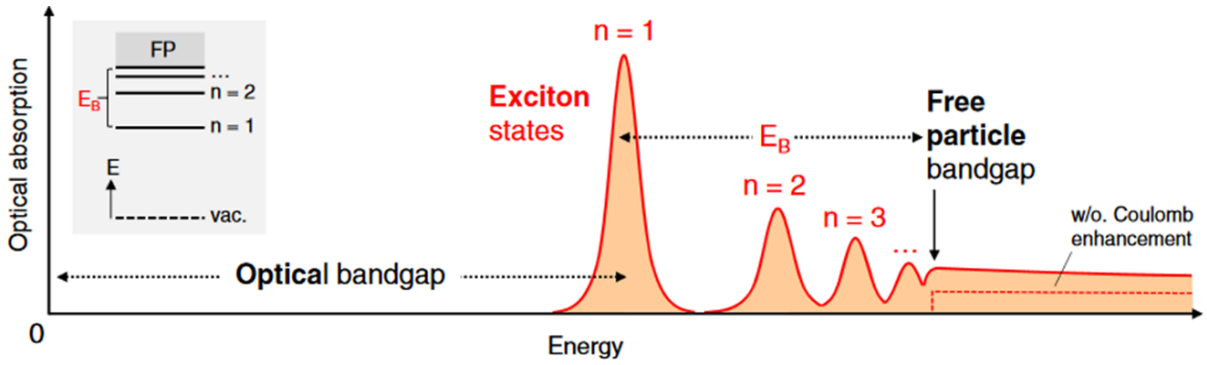

Fig1.4 Schematic illustration of the optical absorption of an ideal 2D semiconductor including the series of bright exciton transitions below the renormalized quasiparticle band gap. In addition, the Coulomb interaction leads to the enhancement of the continuum absorption in the energy range exceeding the exciton binding energy. The inset shows the energy level scheme of the excitonic Rydberg series, the exited states are designated by their principal quantum number n, with the binding energy of the exciton ground state denoted by E_B below the free-particle (FP) band gap. Figure adapted from [Wang 2018]

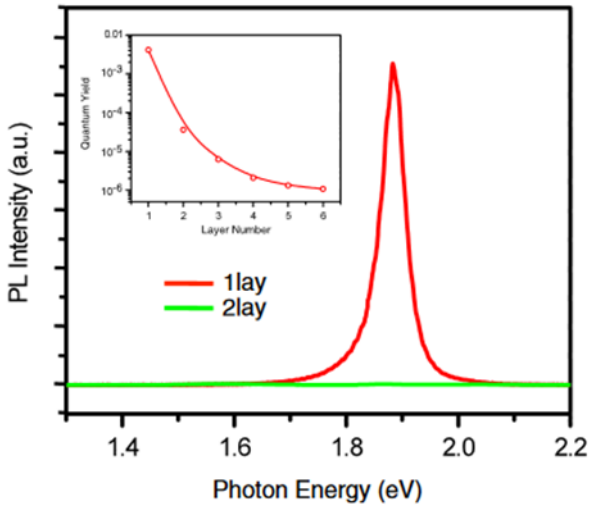

Fig1.5 PL spectra for mono and bilayer MoS_2 samples in the photon energy range from 1.3 to 2.2 eV. Inset: PL quantity yield of thin layers for N =1–6. Figure adapted from [Mak 2010].

Evidences of the exciton recombination in TMD have first been shown in [Mak 2010, Splendiani 2010]. In these papers, the authors present the photoluminescence spectrum of excitons in MoS_2 as a function of the number of monoatomic layers in the crystal. They observe a strong enhancement of the photoluminescence intensity between the bilayer and monolayer samples corresponding to the transition of the electronic band structure to a direct gap configuration (cf Fig(1.5)).

In [Chernikov 2014, He 2014], the authors probe the excitonic Rydberg series in a WS_2 monolayer using reflectance contrast spectroscopy technique. Fig(1.6.a) shows the reflectance spectrum of the fundamental state and the first four excited states. The additional feature at lower energy corresponds to a three-particle complex in which the exciton binds a free carrier: the trion. We will discuss the specificities of the trion later in this chapter.

The authors observe discrepancies between the energies predicted by the 2D hydrogenic Rydberg series and the measured positions of the excitonic excited states 1s and 2s, which are the states with the lowest spatial extent (cf Fig(1.6.b)). They fit the remaining points with the 2D hydrogenic Rydberg series from which they derive the values of the electronic bandgap and more importantly an excitonic binding energy of $E^{(0)} = 0{,}32 \pm 0{,}04$ eV which is much higher than the usual values found in other common semiconductors ($E_B \sim 5$ meV and $E_B \sim 20$ meV in 3D GaAs and 2D AlGaAs/GaAs). This highlights the specificities of TMD excitons in which the strong dielectric screening due to the confinement in the monolayer results in a weak coulomb interaction between the electron and the hole and in an enhancement of the exciton biding energy. Since the binding energy defines the stability of the exciton with respect to temperature (an exciton is thermally stable if $E_B > k_b T$), TMD excitons are stable even at room temperature. Thus, the optical properties of TMD monolayers are dominated by excitonic resonances.

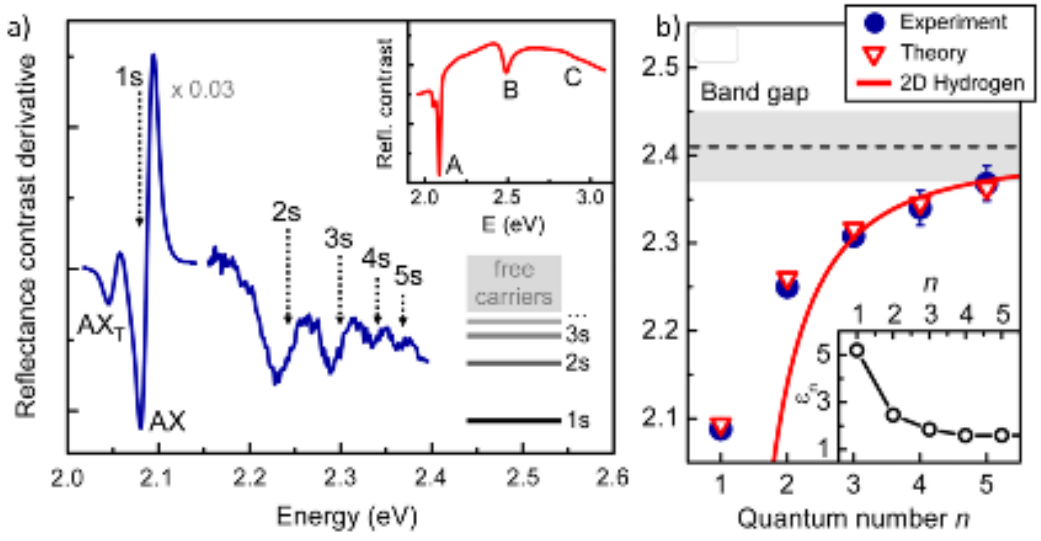

Fig1.6 a) The derivative of the reflectance contrast spectrum of the WS_2 monolayer. The exciton ground state and the higher excited states are labeled by their respective quantum numbers (schematically shown at the bottom right). The spectral region around the 1s transition (AX) and the trion peak (AXT) of the A exciton is scaled by a factor of 0.03 for clarity. The inset shows the as-measured reflectance contrast $\Delta R = R$ for comparison, allowing for the identification of the A, B,and C transitions. **b)** Experimentally and theoretically obtained transition energies for the exciton states as a function of the quantum number n. The fit of the n=3,4,5 data to the 2D hydrogen model is shown for comparison. Gray bands represent uncertainty in the quasiparticle band gap from the fitting procedure. Corresponding effective dielectric constants are shown in the inset. Figures adapted from [Chernikov 2014].

1.3.2/ Dielectric screening in TMD monolayers

The impossibility to fully describe the excitonic Rydberg series using the 2D hydrogenic model [MacDonald 1986] is attributed to the fact that the Coulomb potential $V_{eh}(r)$ fails to take into account the fundamental property of TMD excitons : the electric field of the excitonic dipole passes through the boundaries of the monolayer into the surrounding medium (cf Fig(1.7.a)). This means that the dielectric screening is not only defined by the dielectric constant of the material, but also by the dielectric environment at the top and bottom interfaces of the monolayer.

Thus, a screened potential taking into account the neighboring dielectric environment is necessary: the Rytova-Keldysh potential $V_{RK}(r)$ is better suited to describe the electrostatic interaction of two charges e_1 and e_2 within a thin 2D dielectric continuum encased between two top and bottom layers of dielectric constant ε_t and ε_b.

$$V_{RK}(r) = \frac{e_1 e_2}{r_0}\frac{\pi}{2}\left(H_0\left(\frac{(\varepsilon_t+\varepsilon_b)r}{2r_0}\right) - Y_0\left(\frac{(\varepsilon_t+\varepsilon_b)r}{2r_0}\right)\right) \qquad Eq(1.4)$$

Where H_0 and Y_0 are Struve and Bessel functions.

The Rytova-Keldysh potential [Rytova 1967, Keldish 1979] has been widely used to describe the Coulomb interaction of few-body complexes in monolayer TMDs. However, this potential also introduces a strong environmental dependence of the binding energy of the trion, which has not been experimentally verified. Recent work [Van Tuan Dinh 2018] sought to correct this apparent discrepancy by refining the current vision of the TMD monolayer and considering the dielectric screening of the chalcogen planes at the boundaries of the monolayer from the central atomic plane(cf Fig(1.7.b)). The corrected potential is coherent with the non-hydrogenic Rydberg series of neutral excitons as well as the weak environmental dependency of the trion's binding energy.

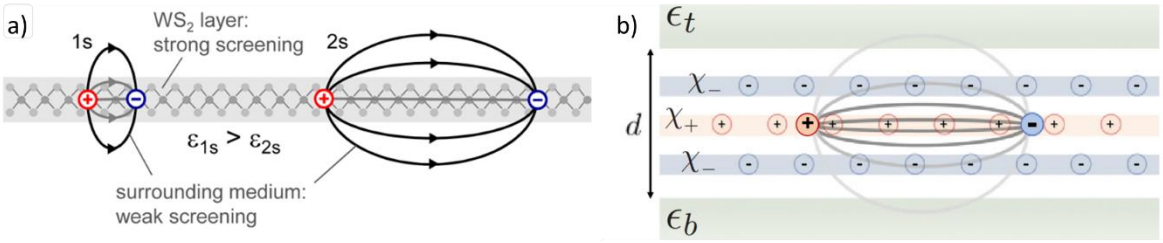

Fig1.7 a) Schematic representation of electron-hole pairs forming 1s and 2s excitonic states in a non uniform dielectric environment. Figure adapted from [Chernikov 2014]. **b)** The ML is modeled as three atomic sheets with polarizabilities χ^+ for the central one (Mo/W) and χ^- for the top and bottom ones. Screening from the chalcogen sheets helps to confine the field lines in the ML, thereby reducing the dependence on the bottom and top materials. Figure adapted from [Van Tuan Dinh 2018].

1.3.3/ h-BN encapsulation

The strong dependence of the excitonic Coulomb interaction on the dielectric environment of the monolayer [Grzeszczyk 2020] has impulsed a series of efforts to engineer the dielectric screening of TMD, notably to decouple the monolayer from its substrate. In this regard, hexagonal Boron Nitride (h-BN) encapsulation has grown to become the most popular

technique for protecting TMD monolayers. Originally considered as a high quality substrate for graphene based applications [Dean 2010], h-BN shows the same mechanical properties as 2D van der Waals crystals. The very high band gap of the material (5,97eV) lies far above the range of visible light an makes it an ideal insulator [Park 2021] for other TMD monolayers. While the lattice mismatch between h-BN ($a = 0{,}25$ nm) and group VI TMD is important ($a = 0{,}32$ nm), the atomically flat hexagonal crystal offers a smooth surface for TMD monolayers. The dielectric constant of h-BN (ε~3-4) results in a different dielectric screening of the exciton [Raja 2017] as compared to the SiO_2 substrate and protects the monolayer of charge transfers from the surrounding environment. The top layer has the added benefits of protecting the sample against external impurities. h-BN encapsulation has rapidly become a standard of sample fabrication and has brought unparalleled progress in the study of TMD excitons by bringing observation and the engineering of the intrinsic properties of these materials in our reach.

In [Cadiz 2017], the authors compare the photoluminescence spectra of non encapsulated and encapsulated monolayers of group-VI semiconductor TMDs (cf Fig(1.8)). The effect ofencapsulation is quite impressive! A drastic reduction of the linewidth of the exciton from a FWHM ΔE~100 meV to mere ΔE~5 meV (cf Tab(1.2)) is observed as well as the emergence of many additional features corresponding to exciton complexes.

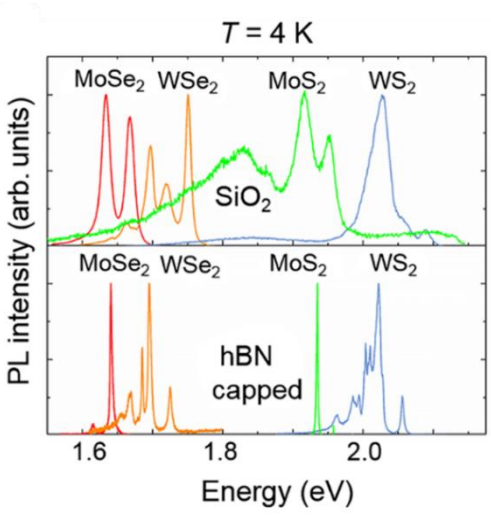

Fig 1.8 Typical PL spectra for different TMDC MLs at T = 4 K when deposited directly onto SiO2 (top) and when capped with h-BN (bottom). Figure adapted from [Cadiz 2017].

	Neutral exciton linewidth (meV)
MoS_2 (Commercial)	2.0–4.5
MoS_2 (*CPT* grown)	3.9–5.0
$MoSe_2$ (VPT grown)	2.4–4.9
WSe_2 (Commercial)	3.9–4.2
WS_2 (Commercial)	4.3–4.8

Tab 1.2 Neutral exciton linewidth at T=4K measured on different TMD monolayers encapsulated with hBN. Table adapted from [Cadiz 2017].

1.4/ Fine band structure of monolayer TMDs:

1.4.1/ Spin orbit coupling

Spin-orbit coupling (SOC) couples the angular momentum L and spin S with $H_{SO} = L.S$ and can be seen as an intrinsic magnetic field splitting the spin-up and spin-down sub-band, shifting them from the previously degenerate energy position by an energy $E_{SOC} \propto k.s$ depending on k the wave vector and s the spin. It is immediately visible that, depending on the valley and on the spin indices, E_{SOC} takes negative or positive values and presents the following symmetry relation:

$$E_{SOC}(K,s) = E_{SOC}(-K,-s) = -E_{SOC}(-K,s) = -E_{SOC}(K,-s) \qquad Eq(1.5)$$

One can see the time reversal symmetry $E_{SOC}(K,s) = E_{SOC}(-K,-s)$ as well as the lack of inversion symmetry $E_{SOC}(K,s) \neq E_{SOC}(-K,s)$. The sub-band splitting in a given valley is written:

$$\Delta_{SOC} = E_{SOC}(K,s) - E_{SOC}(K,-s) = 2E_{SOC}(K,s) \qquad Eq(1.6)$$

The sign of the splitting gives the band ordering (which spin sub-band lies on top of the other) in a given valley, which, as we will see later is critical to the gap and the optical properties of a material. It is to be noted that opposite valleys have the same splitting in absolute value but an opposite band ordering.

The origin of the valence band SOC is well understood : as mentioned above, the valence band states arise from an orbital mix largely dominated by the d_2 transition metal orbital with a quantum orbital number $m_{l(M)} = 2\tau = \pm 2$ depending of the valley index τ with a minor contribution of the chalcogen atom p_x and p_y orbitals with $m_{l(X)} = \pm 1$. Considering a_M and $a_X$the coefficient representing the weight of the metal and the chalcogen orbital in the band state mix and Δ_M/Δ_X the parameters representing the atomic contribution to the SOC , a phenomenological approximation of Δ_{SOC} in the valence band can be established as :

$$\Delta_{SOC} \propto a_M m_{l(M)} \Delta_M + 2a_X m_{l(X)} \Delta_X \qquad Eq(1.7)$$

	$\Delta_M\ (meV)$	$\Delta_X\ (meV)$
MoS_2	87	50
WS_2	274	55
$MoSe_2$	94	188
WSe_2	261	232

Tab 1.3 Parameters of Eq(1.7) obtained by DFT calculations for different TMD monolayers. Table adapted from [Kosmider 2013].

Both contributions have the same sign in both valleys, which explains the single ordering configuration that is observed at K and –K regardless of the ML material. Values for the relevant M and X atoms, extracted from [Kosmider 2013], are presented in Tab(1.3) and Tab(1.4). Because of the dominating proportion of M orbital in the mix, the valence band SO

			MoS_2		WS_2		$MoSe_2$		WSe_2	
	$m_{l(M)}$	$m_{l(xX)}$	a_M	a_X	a_M	a_X	a_M	a_X	a_M	a_X
$C1$	-1	-1	0.63	0.19	0.63	0.19	0.65	0.18	0.65	0.18
C	0	-1	0.86	0.07	0.90	0.05	0.86	0.07	0.89	0.05
V	$+2$	$+1$	0.80	0.10	0.79	0.11	0.82	0.09	0.79	0.10
$V1$	$+1$	0	0.28	0.36	0.25	0.38	0.34	0.33	0.30	0.35

Tab 1.4 Parameters of Eq(1.7) obtained from TB for different TMD monolayers. Values from [Kosmider 2013].

splitting is almost entirely caused by the transition metal contribution, thus explaining the lower splitting values for Mo based materials .

In the case of ML conduction band, the orbital mix does not change in proportion and is still dominated by the contribution of metallic ions. The M orbital from which the band state arise however is no longer $M-d_2$ but $M-d_0$ with $m_{l(M)}=0$ which would simplify Eq(1.7) down to the sole X contribution.

$$\Delta_{SOC} \propto 2a_X m_{l(X)} \Delta_X = -2a_X \tau \Delta_X \qquad Eq(1.8)$$

The splitting magnitude is thus greatly reduced due to the minimal proportion of orbitals from the chalcogen atoms in the orbital mix, roughly by an order of magnitude in fact, if one considers the 85% metal 15% chalcogen coefficient. However, one would then expect a single conduction band ordering configuration for all materials as the chalcogen contribution is always negative (positive) at +K (-K) point.

An interesting way to solve this apparent discrepancy is to consider the interband coupling between the conduction bands C and the higher order conduction C1 and valence V1 bands using second order perturbation theory. Considering the projection of C band Bloch states onto another band B, the energy coupling $\delta E_{C/B}^{TM}$ writes:

$$\delta E_{C/B}^{TM} \propto \frac{\Delta_M \left|\left\langle \Psi_{C(K,s)} \middle| J \middle| \Psi_{B(K,s)} \right\rangle\right|^2}{\varepsilon_C - \varepsilon_B} \qquad Eq(1.9)$$

$$\equiv \delta E_{C/B}^{TM} \propto \frac{\Delta_M \left|\left\langle \Psi_{C(K)} \middle| L^+ \middle| \Psi_{B(K)} \right\rangle \langle s_C | S^- | s_B \rangle\right|^2 + \Delta_M \left|\left\langle \Psi_{C(K)} \middle| L^- \middle| \Psi_{B(K)} \right\rangle \left\langle s_C \middle| S^+ \middle| s_B \right\rangle\right|^2}{\varepsilon_C - \varepsilon_B} \qquad Eq(1.10)$$

Which takes non zero values in two cases only:

$$\underline{\text{Case 1}}\ m_{l(C)} = m_{l(B)} + 1 = +1 \ \text{ and } \begin{cases} s_{C=} \downarrow \\ s_{B=} \uparrow \end{cases}$$

$$\underline{\text{Case 2}}\ m_{l(C)} = m_{l(B)} - 1 = -1 \ \text{ and } \begin{cases} s_{C=} \uparrow \\ s_{B=} \downarrow \end{cases}$$

Considering the values of m_l indexed in Tab(1.4), case 1 corresponds to the coupling between the spin-down conduction sub-band and the spin-up sub-band for which $m_{l(B)} = -1$ i.e. the C1 spin-up sub-band, resulting in a negative energy shift $\delta E^{TM}_{C/C1(\downarrow)}$:

$$\delta E^{TM}_{C/V1(\downarrow)} \approx \frac{\Delta_M \tau a_M}{\varepsilon_C - \varepsilon_{C1}} < 0 \qquad Eq(1.11)$$

Similarly, case 2 couples the spin-up conduction sub-band and the spin-down V1 sub-band resulting this time in a positive energy shift $\delta E^{TM}_{C/V1(\uparrow)}$:

$$\delta E^{TM}_{C/V1(\uparrow)} \approx \frac{\Delta_M \tau a_M}{\varepsilon_C - \varepsilon_{V1}} > 0 \qquad Eq(1.12)$$

$$\Delta_{SOC} = \delta E^{TM}_{C(\uparrow)} - \delta E^{TM}_{C(\downarrow)} - a_X \tau \Delta_X = \tau(a_M \Delta'_M - a_X \Delta_X) \text{ with } \Delta'_M = \frac{\Delta_M}{\varepsilon_C - \varepsilon_{V1}} - \frac{\Delta_M}{\varepsilon_C - \varepsilon_{C1}} \qquad Eq(1.13)$$

This formulation, simplified compared to [Kosmider 2013], has the merit of exposing the two opposite contributions competing in the conduction band splitting. Thus, since the valence band ordering is always the same, two band orderings are possible depending on the material. Tab(1.5) shows experimental values of Δ^{cond}_{SOC} taken from the literature.

	MoS_2	WS_2	$MoSe_2$	WSe_2
$\Delta^{cond}_{SOC}\ (meV)$	+14	+40	−1.4	+55

Tab 1.5 Experimental values of Δ^{cond}_{SOC}. The values for $MoSe_2$ and MoS_2 are taken from [Robert 2020] and the one for WSe_2 and WS_2 are taken from [Wang 2017].

The SO splitting value at K point thus classifies TMDs into two categories, depending of the spin index of the bottom conduction sub-band and top valence sub-bands. If the SOC is negative, the bottom conduction sub-band and top valence sub-bands have the same spin index (i.e., spin up/down at +K/-K), the material is classified as “bright”, if the spin index is different (positive SOC), it if classified as “dark”. Both configurations are represented on Fig(1.9).

Considering once again the α_m (mainly $d_2, d_0\ and\ p_0$) orbitals involved in the mix of Bloch band states, the wave functions a K points are invariant under the C_3 rotation, thus the Bloch state is eigenstate of the C_3 operator with eigenvalue:

$$C_3 \alpha_m = e^{-i\frac{2m\pi}{3}} \alpha_m \qquad Eq(1.14)$$

It is to be noted that since valleys of opposite indices are related by time reversal symmetry, the eigenvalue at -K point is the complex conjugate of the +K point value. From here one can very naturally establish the coupling selection rules by determining the matrix element for the interband optical transition between two states Ψ_i and Ψ_j.

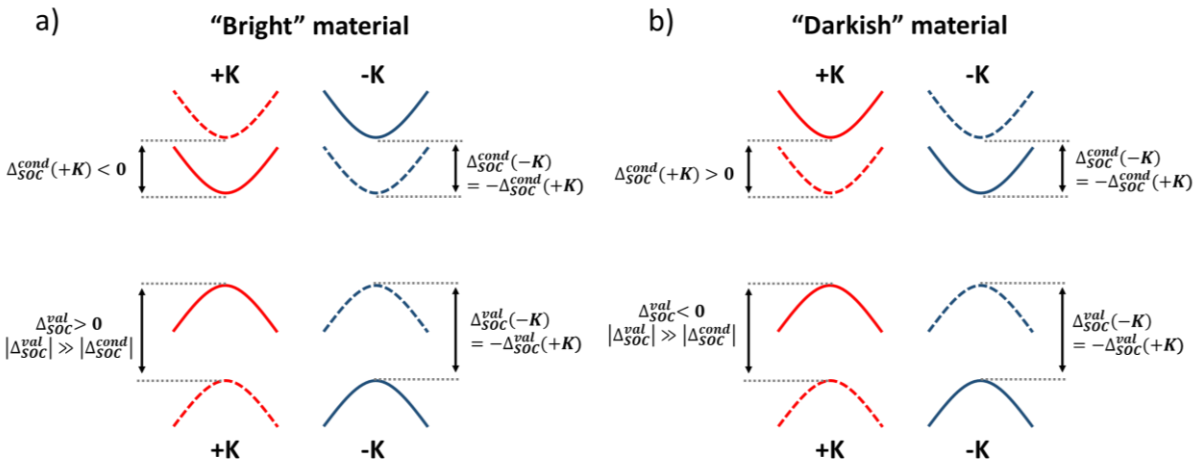

Fig.1.9 : **a)** Band ordering at the +K and –K valleys of a "bright" monolayer. **b)** Band ordering at the +K and –K valleys of a "darkish" monolayer. The spin down/up sub-bands are represented as dashed/straight lines.

$$\langle \Psi_i | P_\pm | \Psi_j \rangle = \langle \Psi_i | C_3^{-1} C_3 P_\pm C_3^{-1} C_3 | \Psi_j \rangle$$
$$= \langle C_3 \Psi_i | C_3 P_\pm C_3^{-1} | C_3 \Psi_j \rangle = \langle C_3 \Psi_i | P_\pm | C_3 \Psi_j \rangle$$
$$= e^{-i\frac{2\pi}{3}(m_j - m_i \pm 1)} \langle \Psi_i | P_\pm | \Psi_j \rangle \qquad Eq(1.15)$$

Since the oscillator strength $|\langle \Psi_i | P_\pm | \Psi_j \rangle|^2$ characterizes the transition coupling strenght to $\sigma \pm$ polarized light, Eq(1.15) is only correct with nonzero $\langle \Psi_i | P_\pm | \Psi_j \rangle$ if $m_j - m_i \pm 1 = 0$ modulo 3. The two possible values correspond to coupling with $\sigma_\pm$polarized light at the $\pm$K valley which means that excitons in the +K/-K valleys recombine into photons with the σ+/ σ- helicity. This is the valley polarization effect, which is characteristics of TMDs and has been extensively studied [Mak 2012, Jones 2013]. From an experimental point of view, it implies that the emission of the sample will be a mix of σ_+ and σ_-polarized components ($I(\sigma_+)$ and $I(\sigma_-)$ respectively), and its polarization is quantified by the helicity coefficient ρ :

$$\rho = \frac{I(\sigma_+) - I(\sigma_-)}{I(\sigma_+) + I(\sigma_-)} \qquad Eq(1.16)$$

In the case of unpolarized or linearly polarized excitation, both valleys are excited simultaneously and the part of $I(\sigma_+)$ and $I(\sigma_-)$ in the PL signal is rigorously 50/50. Results from photoluminescence measurements presented in [Mak 2012] show that the excitonic emission in a given valley can be quenched by exciting the TMD with light of opposite helicity. This is showcased in Fig(1.10) where a MoS_2 monolayer is excited purely with σ_- polarized light and the PL signal is almost entirely σ_- polarized, showing a near unity helicity coefficient.

It is interesting to note that these selection rules are another marker of inversion symmetry breaking, as inversion symmetry transforms effectively +K into -K but leaves the polarization unchanged, they are however in line with time reversal symmetry since it switches both the

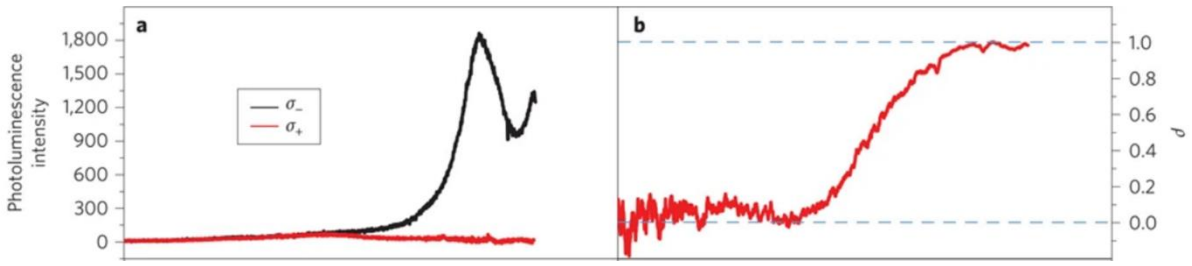

Fig1.10 **a)** σ_- (black) and σ_+- (red) resolved photoluminescence spectra for monolayer MoS_2 on h-BN (collection is polarized σ_-) **b)** Corresponding photoluminescence helicity ρ. Figure adapted from [Mak 2012].

valley index and the polarization. Therefore, it is expected that valley polarization is conserved in odd layer-numbered multilayers but disappear in even layer-numbered multilayers based on these symmetry considerations.

1.4.2/ Selection rules of optical transitions

Let us go back to the "bright" and "dark" material denominations, Fig(1.11) shows an updated version of Fig(1.9) where the sub-bands have been indexed with their respective angular momentum J_z calculated using the center of the hexagon as the center of rotation. Because of time reversal symmetry, angular momentum in +K and -K takes opposite values but have the same magnitude. The excitonic selection rules are then applied to any transition from a conduction to a valence sub-band, regardless of the spin by calculating the change of angular momentum ΔJ_z :

$$\Delta J_z = J_z^{conduction} - J_z^{valence} \qquad Eq(1.17)$$

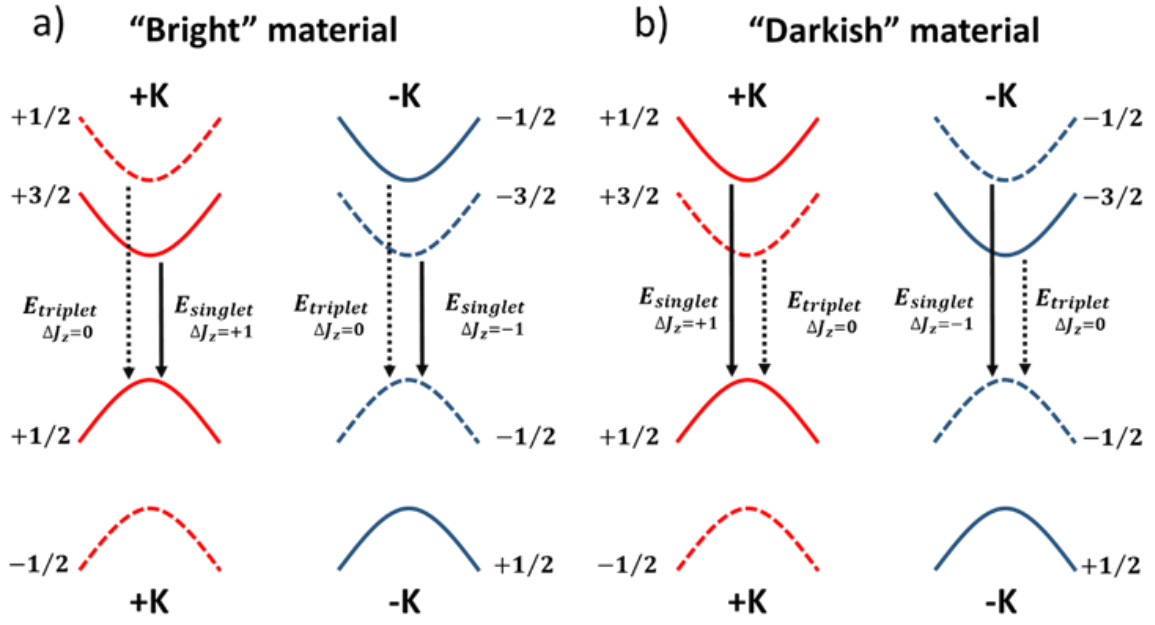

Fig1.11 **a)** Band ordering at the +K and –K valleys of a "bright" monolayer. **b)** Band ordering at the +K and –K valleys of a "darkish" monolayer. The "bright" optical transitions are represented by plain arrows ("dark" transitions by dashed arrows). Each sub-band is indexed by its momentum J_z.

Looking at transitions involving sub-bands with the same spin index, such as the lowest energy intergap transition of "bright" materials: $\Delta J_z = +1$ at K point and $\Delta J_z = -1$ at -K point, this is coherent with the respective valley coupling with σ_+ and σ_-polarised light. Excitons recombining from this singlet spin state are denominated as "bright" excitons, arising from "bright" transitions.

Now let us take a look at the lowest energy interband transition in "dark" materials which is a "spin dark" triplet state transition. In this case, the change of angular momentum is $\Delta J_z = 0$ in both valleys. This means that excitons recombining from these spin triplet state transitions do not carry angular momentum along the z axis and are thus denominated "dark excitons". Note that W based compounds are not called "dark" materials because they do not couple to light, but because their ground state, the lowest energy transition, is a spin triplet state. As such, features usually observed on the PL spectra of "darkish" materials (such as in Fig(1.8)) do not arise from the ground state, but from the singlet state transition at higher energy. Dark excitons are optically active, as evidenced in [Wang 2017] , the emission from this "forbidden" state can be observed by collecting light in the in-plane direction, as opposite to the out-of-plane direction for "bright" excitons. Several experiments have sought to "brighten" these transitions by external means, such as coupling to polaritons [Zhou 2017] or by using magnetic fields [Molas 2017] to force the emission in the direction perpendicular to the monolayer plane, the latter will be discussed in this chapter as part of the effect of magnetic field on TMD excitons.

To conclude on the different band orderings of the conduction sub-bands in different materials, the value of conduction band splittings can either be positive and negative and divides the TMD family into "bright" and "dark" materials. This SOC value stems from the orbital mix involved in the band Bloch state which is most heavily impacted by the d-orbital of the Metal atoms. Therefore it would seem logical to divide TMD between bright Mo based and dark W based materials as deduced from theoretical calculation from [Kosmider 2013]. Optical measurements on $MoSe_2$, WSe_2 and WS_2 also support this claim, but the case of MoS_2 came under scrutiny because of the small predicted value of its conduction band splitting. In fact, results from several experiments clearly showed that the spin singlet state was lying at a lower energy compared to the triplet [Molas 2017, Robert 2020]. Recent ab initio calculation [Bieniek 2020], bring theoretical input to these claims and explain the peculiar case of MoS_2 by a determinant effect of effective mass on the band ordering. The main proposition of this paper can be seen in Fig(1.12). While the majority of the spin-up sub-band lies above its spin-down counterpart, the higher sub-band curvature (i.e. the higher electron effective mass) results in a higher binding energy for the triplet spin state. Therefore, although the bottom of the spin-down conduction sub-band is below the bottom of the spin-up conduction sub-band, the differences of binding energy result in the opposite ordering for the excitonic state. To illustrate this effect, we present the brightening of the spin

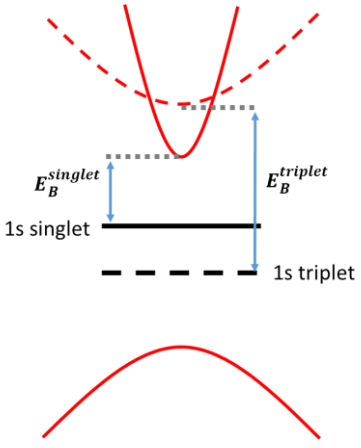

Fig1.12 Band ordering between the spin-up (straight lines) and spin-down (dashed lines) sub-band in ML MoS_2. Because of the difference of effective mass, $E_B^{triplet} > E_B^{singlet}$, and the spin triplet state appears below the energy of the spin singlet state. Figure inspired from [Bieniek 2020].

triplet state i.e. the "dark" exciton in a MoS_2 ML by the effect of a magnetic field applied in the plane of the ML [Robert 2020]. This result, presented in Fig(1.13), shows that the spin triplet state appears at a lower energy than the spin singlet state, similarly to what is observed in W based materials [Molas 2017, Zhou 2017, Zhang 2017].

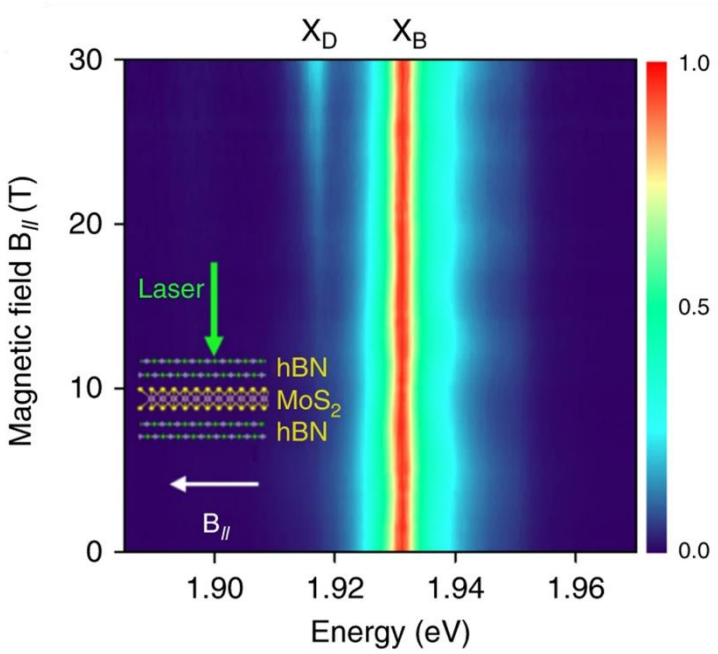

Fig1.13 Color map of the variation of the PL intensity in MoS_2 as a function of B//. The dark exciton X_D is brightened by the magnetic field and appears below the energy position of the bright exciton X_B (the PL intensity of the bright exciton has been normalized at each field). Figure adapted from [Robert 2020].

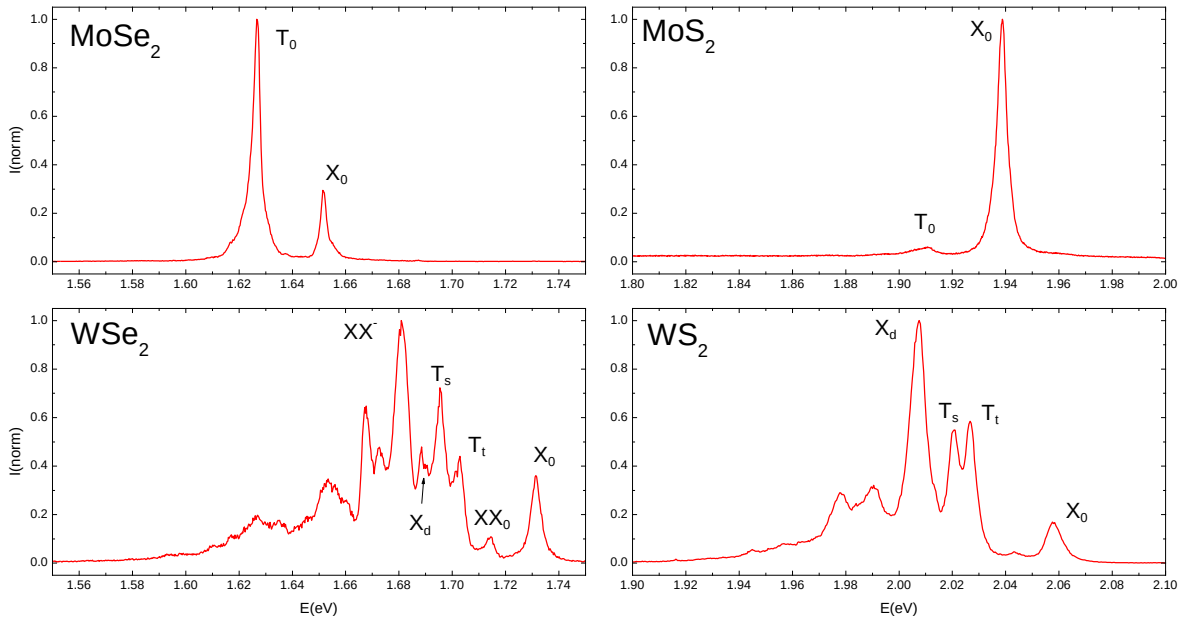

Fig 1.14 Typical PL spectra for different TMDC MLs at T = 4 K when encapsulated with h-BN. The samples were measured with an excitation energy of $E = 2{,}41$ eV and an excitation power of $P = 50$ µW. We have indexed the PL spectra with X_0 the "bright" exciton, T_0 the trion, T_t/ Ts the triplet/singlet trions, X_d the "dark" exciton and XX^- the charged biexcitons based on value found in the literature (see Tab(1.6)).

1.5/ Photoluminescence and magneto-photoluminescence of TMD excitons:

1.5.1/ General discussion

Let us go back to the zoology of excitonic complexes in TMD monolayers. We will start by describing the "bright" photoluminescence spectrum of group-VI TMD monolayers such as the one shown in Fig(1.8). In Fig(1.14) we have plotted PL spectra measured on our own TMD monolayers samples and assigned the observed PL peaks to optical transitions based on their relative energy position to the bright exciton (cf Tab(1.6)). We will now discuss the origin of the PL peaks corresponding to Mo based monolayers. In a second time, we will do the same for the PL spectrum of W based monolayers.

	$X_0(eV)$	$XX_0(meV)$	$T_0/T_t(meV)$	$T_s(meV)$	$X_d(meV)$	$XX^-(meV))$
$MoSe_2$	1.651	–	$-25^{[1]}$	–	–	–
MoS_2	1.939	–	$-28^{[1]}$	–	–	–
WSe_2	1.731	$-17^{[2]}$	$-29^{[2]}$	$-35^{[2]}$	$-43^{[2]}$	$-50^{[2]}$
WS_2	2.058	–	$-31^{[3]}$	$-38^{[3]}$	$-50^{[4]}$	–

Tab 1.6 Absolute (for the bright exciton) and relative (for the other transitions) **e**nergy position of the Pl peaks observed on Fig(1.14). The transitions have been assigned by comparing the relative energy positions from [**1**] [Robert 2020] [**2**] [Barbone 2018] [**3**] [Vaclavkova 2018] [**4**] [Wang 2017].

1.5.2/ Photoluminescence spectra of TMD monolayers

In the case of Mo based TMD, the photoluminescence spectrum consists of two peaks. The high energy peak (1,65 eV and 1,95 eV for $MoSe_2$ and MoS_2) corresponds to the spin bright exciton we mentioned previously. The lower energy peak (1,62 eV and 1,93 eV for $MoSe_2$ and MoS_2) corresponds to a trion : athree particle bound state in which an exciton couples to a free carrier. The carrier can either be an electron (negative trion X-) or a hole (positive trion X+). A trion recombines by emitting a photon and the final state is a free carrier in the valence band or the conduction band and the energy difference between the two peaks corresponds to the binding energy of the trion. This binding energy is one order of magnitude lower than the binding energy of the exciton (a few tens of meV) and is it is still high enough for the trion to remain stable at room temperature but can only be separated from the neutral exciton at low temperature. Because it involves a free carrier, the trion is sensitive to the doping of the sample. In [Ross 2013], photoluminescence experiment on a gated $MoSe_2$

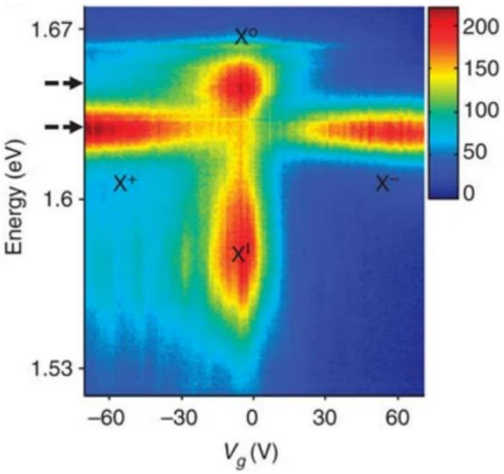

Fig1.15 $MoSe_2$ PL (color scale in counts) plotted as a function of back-gate voltage. Near zero doping, we observe mostly neutral and impurity-trapped excitons. With large electron (hole) doping, negatively (positively) charged excitons dominate the spectrum. Figure adapted from [Ross 2013].

monolayer shows that tuning the samples doping between the n doped and p doped regime effectively switches the trion emission between the X- and X+ states (cf Fig(1.15))

In comparison the photoluminescence spectrum of the W based TMDs shows more peaks. Unlike $MoSe_2$ in which the highest energy sub-band is depleted a $T = 4$ K, both conduction sub-bands can be populated (the sub-band with the highest energy is the optically bright state) which results in two possible configurations for the trions (cf [Vaclavkova 2018]). Fig(1.16) shows these two configurations : the spin singlet trion binds two electrons with different spin states, while the spin triplet trion (intervalley trion) binds two electrons with different spin states (and different valleys due to the exclusion principle). Due to the momentum separation between the +K and –K valleys, the recombination of the triplet spin trion is an intravalley process [Kapuscinski 2020] and has the same selection rules as the exciton. The photoluminescence spectra also exhibit multi excitonic complexes : the biexcitons XX and the charged biexciton XX- peaks resulting from the recombination of four-particles complexes.

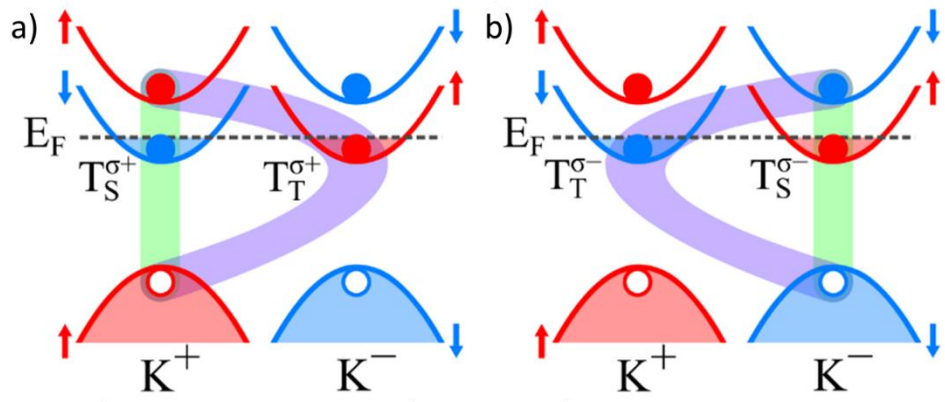

Fig1.16 Schematic illustration of the circularly-polarized **a)** σ+ and **b)** σ−singlet (TS) and triplet (TT) trions formed at K+ and K−points of the Brillouin. The red (blue) curves indicate the spin-up (spin-down) sub-bands. The electrons (holes) in the conduction (valence) band are represented by closed (open) circles. Saturation of green and violet colors is related to the probability of trions formation. Figure adapted from [Kapuscinski 2020]

1.5.3/ Photoluminescence of momentum forbidden or spin forbidden excitons

Before discussing the case of spin dark excitons, we will present the case of a momentum dark transition (or intervalley transition). Transitions between the conduction band and the valence band of valleys are normally forbidden because of the large momentum separation. However in [He 2020], the authors observe the brightening of a normally momentum dark intervalley transition by phonon emission. This is different from phonon replica seen in [Li 2019] which does not result in an intervalley recombination. The phonons mediating this recombination are chiral phonons [Zhang 2015'] at the high symmetry points of the Brillouin zone, carrying a pseudo angular momentum $PAM = \pm 1$. They have been reported to couple to trions in WS_2 ML [Zinkiewicz 2021], to quantum dots in WSe_2 monolayers [Chen 2019] as well as mediating the intervalley transfer of holes in the same material [Zhu 2018]. The brightening process of the intervalley transition is shown in Fig(1.17) : instead of relaxing non radiatively to the bottom of the conduction band of the +K valley, the electron relaxes to the bottom of the conduction band in the –K valley by the emission of a phonon with a large momentum k .

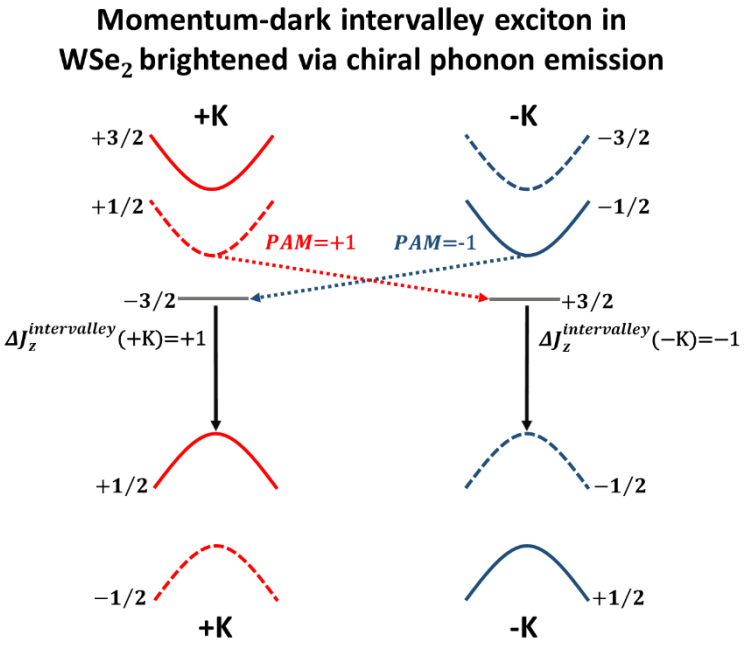

Fig1.17 Band structure of monolayer WSe_2 at +K and –K valleys. Spin-up sub-bands at +K/-K point are shown as red/blue plain lines (spin-down sub -ands at +K/-K point as red/blue dashed lines). Each sub-band is indexed by its angular momentum J_z, defined modulo 3. Black arrows represent the recombination path of the intervalley spin singlet state exciton. The red and blue dotted lines represent the intervalley transfer of the electron and they are indexed by the PAM of the chiral phonon. Figure inspired by [He 2020].

As we have explained earlier, the spin dark exciton recombination emits in the in-plane direction (cf Fig(1.18)) of the monolayer and is typically absent in the PL spectra measured with an out-of-plane collection. However, using a collection lens or an objective with a sufficiently high numerical aperture, it is possible to collect the photoluminescence of the dark exciton from the edges of its emission cone (cf the WSe_2 and WS_2 PL spectra shown in Fig(1.14), measured with lenses with NA=0,56 and an objective with NA=0,62 ,respectively). The

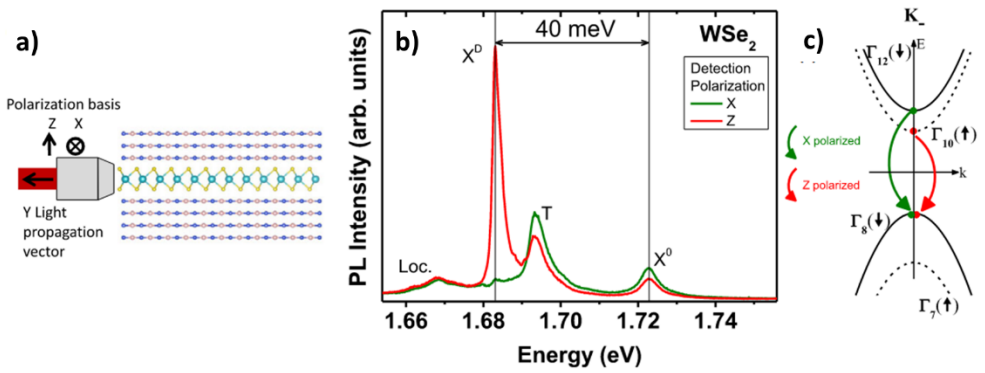

Fig1.18 a) Schematics of the excitation or detection geometry of the PL for light light propagating parallel to the ML plane, detection of the PL from the edge of the sample **b)** Detection of the PL from the edge of the sample. The polarization of the detected light is in the ML plane (x direction), green line, or perpendicular to it (z direction), red line. **c)** the green and red arrows show the transitions optically active for x-polarized and z-polarized light, respectively (light propagating parallel to the ML plane). Figure adapted from [Wang 2017].

signature of dark excitons is a supplementary peak in the PL spectrum, centered 43 meV and 50 meV below the bright exciton in WSe_2 and WS_2 [Molas 2017, Wang 2017]. This emission can be observed directly in monolayers of darkish materials, as the conduction band of the spin triplet state is always populated. In monolayers of "bright" materials, the lowest energy state is the spin singlet state and the spin orbit splitting, which is higher than the thermal fluctuation at low temperature, quenches the dark emission. We will show how an external magnetic field applied in the plane of the monolayer both brightens the emission of the "dark" exciton and forces its emission in the direction perpendicular to the ML plane regardless of the material.

1.6/ Optical properties of TMDs under a magnetic field:

1.6.1/ General discussion.

In this section, we will describe the influence of a magnetic field on the optical properties of TMD monolayers through the results of different experiments. We will start by presenting the Zeeman valley splitting of TMD excitons and will then explain the diamagnetic shift of the excited states excitonic Rydberg series. We will then focus our discussion on the brightening process of the "dark" exciton as well as the diamagnetic shift of the "dark" excitonic Rydberg series.

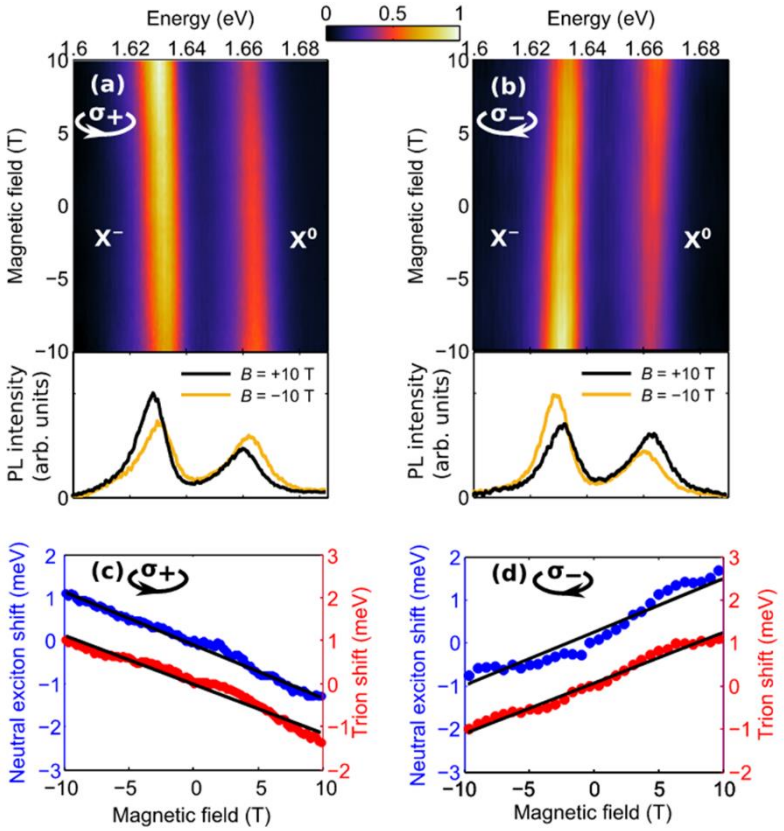

Fig1.19 a) and **b)** False color representation of the σ and σ− polarized PL spectra of monolayer $MoSe_2$ in the low doping regime as a function of the strength of the applied perpendicular magnetic field. The spectra for fields of $B = \pm 10$ T are presented below the color map. The spectra are normalized to yield the same integrated intensity for the neutral and charged excitons, with a smooth background subtracted. **c)** and **d)** Extracted Zeeman shift of the neutral and trion energies for σ±. Figure adapted from [Li 2015].

1.6.2/ Valley Zeeman effect

In [Li 2015], the authors investigate the effect of an out-of-plane magnetic field on the photoluminescence spectrum of a $MoSe_2$ monolayer. The results of their polarization resolved measurements, reproduced in Fig(1.19), show that the energy position of the two oppositely polarized components of the photoluminescence spectrum shift toward opposite energies. More precisely, the energy position of the σ+ polarized components of the WSe_2 bright exciton, resulting from the recombination in the +K valleys, linearly shifts toward lower energies with a rate of $0{,}12\ \mathrm{meVT^{-1}}$. Symmetrically, the σ- polarized components resulting from the recombination in the –K valley linearly shift toward higher energies at the same rate.

This is the valley Zeeman effect [Srivastava 2015, MacNeill 2015], which reflects the energy shift of the sub-bands involved in the recombination process according to their magnetic momentum (cf Fig(1.20)). The correction to the energy of an optical transition is :

$$E(B) = E_0 - (\mu_{c\perp} - \mu_{v\perp})\mu_B B \qquad Eq(1.18)$$

Where μ_B is the Bohr magneton $\mu_B = 5{,}788\ \mathrm{eV.T^{-1}}$ and $\mu_{c/v\perp}$ the out-of-plane magnetic momentum of the conduction/valence sub-band involved in the recombination process.

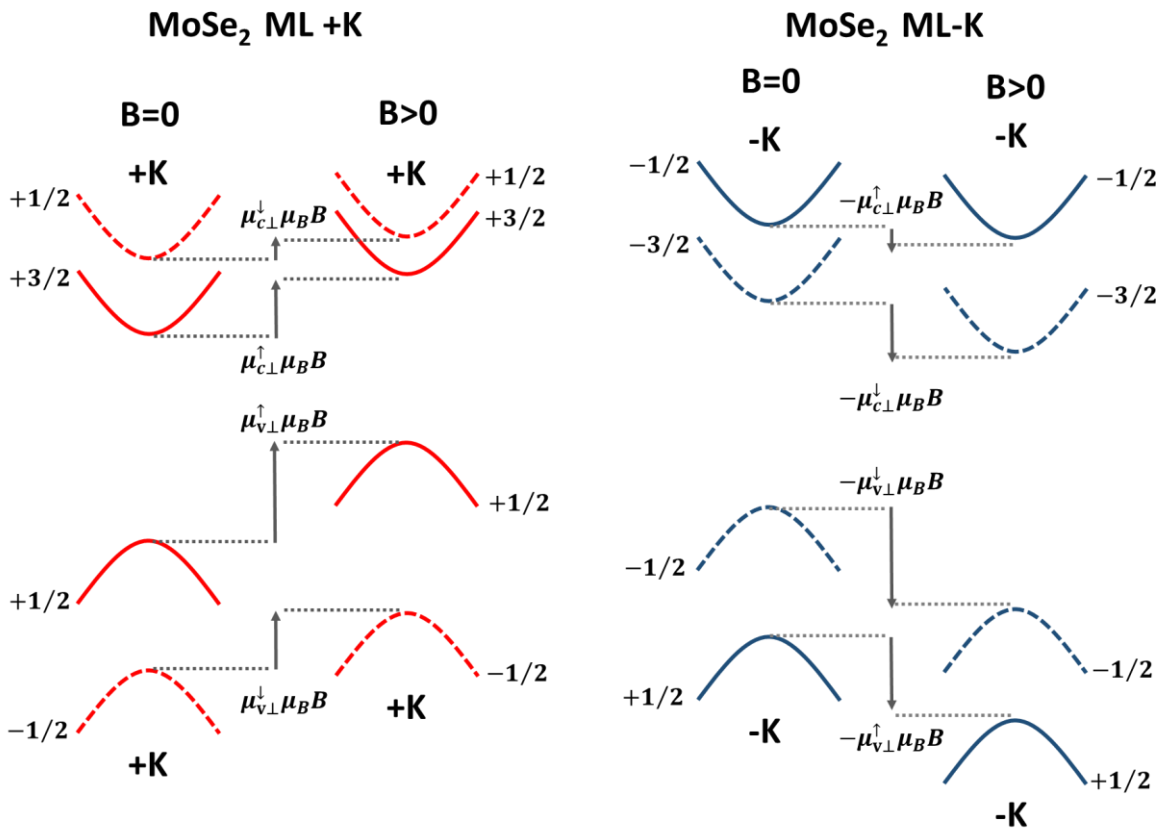

Fig1.20 Shift of the band structure of $MoSe_2$ with the magnetic field B in the valley +K and -K Spin-down sub-bands in the +K valley are shown as red dashed lines (spin-up sub-bands as red straight lines). Spin-down sub-bands in the -K valley are shown as blue dashed lines (spin-up sub-bands as blue straight lines) Each sub-band is indexed by its angular momentum J_z and its shift with the magnetic field in eV as a function of $\boldsymbol{\mu}_{c/v\perp}^{\downarrow/\uparrow}$ the out-of-plane magnetic moment of the spin down/up conduction/valence sub-band .

It is already apparent that the magnitude of the Zeeman shift of an optical transition can be used to obtain experimental estimations of the magnetic momentum of the bands involved in the recombination processes. Practically, the Zeeman shift of the components of an optical transition in a monolayer TMD is expressed as a function of μ_B and characterized by the Landé g-factor :

$$g = \frac{E(\sigma+) - E(\sigma-)}{\mu_B B} \qquad Eq(1.19)$$

Where $E(\sigma \pm)$ is the energy of the σ± polarized component. It is to be noted that the sign of the g-factor is defined according to the selection rules of the transition. As an example : In Fig(1.19), the $\sigma +$ polarized emission redshift and the $\sigma -$polarized emission blueshifts which means that the g factors of the bright exciton and of the trion in $MoSe_2$ are negative. We have compiled the g-factors from the literature of the bright excitonic and trionic transitions in Tab(1.7).

	X_0	T_0/T_t	T_s	X_d	X_r
$MoSe_2$	$-4.2^{[1]} - 4.0^{[2]}$	$-3.7^{[1]}$	–	$-8.63^{[2]}$	–
MoS_2	$-1.8^{[2]} - 1.8^{[5]}$ $-4.6^{[7]}$ $-1.7^{[8]} - 4.0^{[8]}$	$-3.1^{[5]}$	–	$-6.5^{[2]}$	–
WSe_2	$-4.3^{[1]} - 3.7^{[3]}$	$-4.4^{[3]}$	$-4.5^{[3]}$	$-9.4^{[3]}$	$12^{[6]}$
WS_2	$-4.0^{[1]}$	$-4.1(PL)^{[4]}$ $-3.0(RC)^{[4]}$	$-4.1(PL)^{[4]}$ $-4.7(RC)^{[4]}$	$-9.4^{[1]}$	–

Tab1.7 Typical values of the g- factor found in the literature for different optical transitions. The values have been extracted from [**1**] [Koperski 2018] [**2**] [Robert 2020] [**3**] [Li 2019] [**4**] [Kapuscinsky 2020] [**5**] [Klein 2021] (values considered near the charge neutrality point) [**6**] [He 2020] [**7**] [Cadiz 2017] [**8**] [Goryca 2019].

Remarkably, these transitions have all a negative g-factor, with the exception of the momentum dark intervalley exciton which means that in the case of zero momentum recombination, the optical gap in the +K valley decreases while the one in the –K valley increases. This highlights the property of the band structure of monolayer TMDs : the magnetic moment of the valence band is greater than the one of the conduction band. Similarly, the higher magnitude of the g-factors measured for the spin dark and momentum dark transitions give us a first evidence of the spin and valleys contributions to the g-factor but we will discuss this at length in Chapter 5.

The wide range of reported values for the g-factor of the "bright" exciton X_0 in MoS_2 ML evidences the g-factor is not only a property of the bands involved in the optical process and that other parameters affect its value. To illustrate this, we present in Fig(1.21) the results of optical experiments PL on a gated MoS_2 ML aiming at investigating the effect of the free carrier concentration in the ML on the experimentally measured exciton g-factor [Klein 2021]. In this

figure, we can clearly see that the measured exciton g-factor (black points in Fig(1.21)) changes when the free carrier density is tuned away from zero.

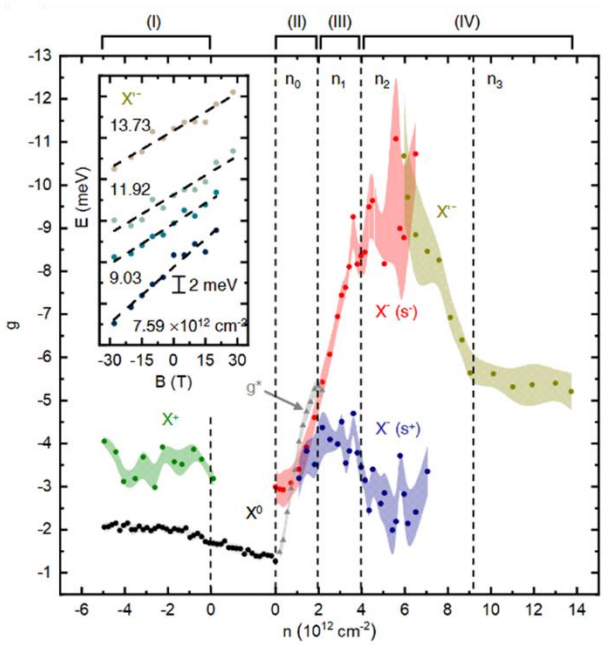

Fig1.21 Carrier density dependent g-factors of X_0 (black and gray data), the negatively (red and blue data) and positively(green data) charged excitons X^- and X^+. Figure adapted from [Klein 2021].

1.6.3/ Effect of the magnetic field on the excitonic excited states.

To illustrate the effect of the magnetic field on the excitonic Rydberg series, we present the results of a magneto-PL experiment on an h-BN encapsulated WSe_2 monolayer. Fig(1.22) shows the energy position of the fundamental state (1s) and the first excited state (2s). We observe that the energy shift of these states show a quadratic component with the magnetic field. In the case of the fundamental state, this quadratic component is small next to the linear Zeeman shift but this is clearly not the case for the first excited state. This quadratic component is the diamagnetic shift μ_2, the second order term of the action of the magnetic field on the exciton. Taking the expression of the diamagnetic coefficient of excitons in quantum wells in [Walck 1998], we write :

$$\mu_2 = \frac{e^2}{8Mc^2}\langle r^2 \rangle \qquad Eq(1.21)$$

Where $\langle r^2 \rangle$ is a square length describing the extent of the excitonic state in the in-plane direction (practically $\sqrt{\langle r^2 \rangle}$ is the electron-hole distance). According to the 2D hydrogenic model, $\sqrt{\langle r^2 \rangle}$ is expected to increase linearly with n (cf

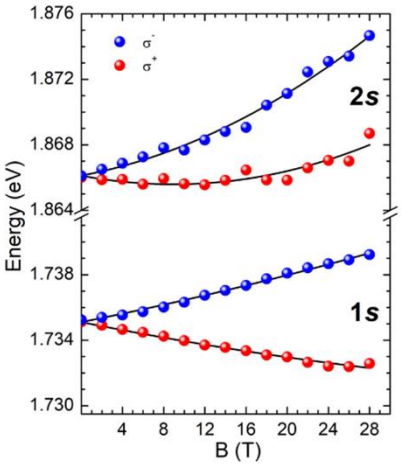

Fig1.22 Central energy position of A exciton 1s and 2s states as a function of the magnetic field for the two polarizations. The solid black lines are the results of fits including both the valley Zeeman effect and the diamagnetic shift. Figure adapted from [Delhomme 2019].

Eq(1.3)), therefore the diamagnetic shift is expected to increase quadratically with n. In [Stier 2016], the authors measure the absorption spectrum of a h-BN encapsulated WSe_2 exfoliated directly over the 3.5 µm core of an optical fiber. They achieve to resolve separately the first four states of the bright excitonic Rydberg series and measure their energy position with a polarized collection under a pulsed magnetic field swept between $+65$ T and -65 T. They observe an increasingly quadratic shift corresponding to the increase of the excitonic radius [Zipfel 2018].

1.6.4/ Brightening of the spin dark excitons.

In [Molas 2017] the authors explain how applying an in-plane magnetic field results in the brightening (the increase of the intensity with the magnetic field) of the spin dark exciton of a WSe_2 monolayer. They consider a WSe_2 monolayer under a magnetic field $B = (B_x, B_y, 0)$. They consider the Zeeman term of the Hamiltonian acting on the conduction band state :

$$H_Z = \frac{1}{2}\mu_{c\parallel}\mu_B(\boldsymbol{\sigma_x}B_x + \boldsymbol{\sigma_y}B_y) \qquad Eq(1.20)$$

They express the Hamiltonian in the basis of the excitonic states $\{|\tau, d\rangle, |\tau, b\rangle\}$ with τ the valley index and $d/\,b$ the dark/bright character of the transition i.e. the spin index in relation with . ($|\tau, d\rangle$ correspond to $|+,\downarrow\rangle$ and $|-,\uparrow\rangle$ and $|+,\uparrow\rangle$ and $|-,\downarrow\rangle$ correspond to $|\tau, b\rangle$). They find the eigenstates which are mixed states written:

$$\begin{cases} |1, mix\rangle = \frac{|\tau,b\rangle}{1+w/2} - \frac{\mu_{c\parallel}\mu_B B_{+\tau}|\tau,d\rangle}{2\Delta_{SOC}^{cond}} \\ |2, mix\rangle = \frac{|\tau,d\rangle}{1+w/2} - \frac{\mu_{c\parallel}\mu_B B_{-\tau}|\tau,b\rangle}{2\Delta_{SOC}^{cond}} \end{cases} \qquad Eq(1.22)$$

With $w = \left(\frac{\mu_{c\parallel}\mu_B B_\parallel}{2\Delta_{SOC}^{cond}}\right)^2 \ll 1$ a parameter describing the mixing between the dark and bright excitonic states, and with $B_{\pm\tau} = B_x \pm iB_y\tau$.

Since w increases quadratically with B, the intensity of the dark state increases due to its crescent admixture with the bright exciton which forces the emission in the direction perpendicular to the monolayer plane. This effect allowed for the observation of the dark excitons in WSe_2 [Molas 2017, Zhang 2017, Molas 2019, Robert 2017] and WS_2, the "darkish" materials, but also in MoS_2 and in $MoSe_2$ [Robert 2020] as we have shown in Fig(1.13).

Very recently, the excitonic Rydberg series of the "dark" exciton have been observed in a WSe_2 ML. In [Kapuscinsky 2021], these "dark" excited states are brightened under a magnetic field in the-plane of the monolayer (cf Fig(1.23)) and the first four states of both the bright and dark excitonic Rydberg series can be resolved. It is observed that while the energy separation between the successive excited states of the "bright" excitonic Rydberg series is not the same as that of the "dark" excitonic Rydberg series, this can be strictly explained [Molas 2019'] by differences of relative mass. The fit of the energy position of both series gives an experimental estimation of the SOC of ML WSe_2 $\Delta_c = 14$ meV.

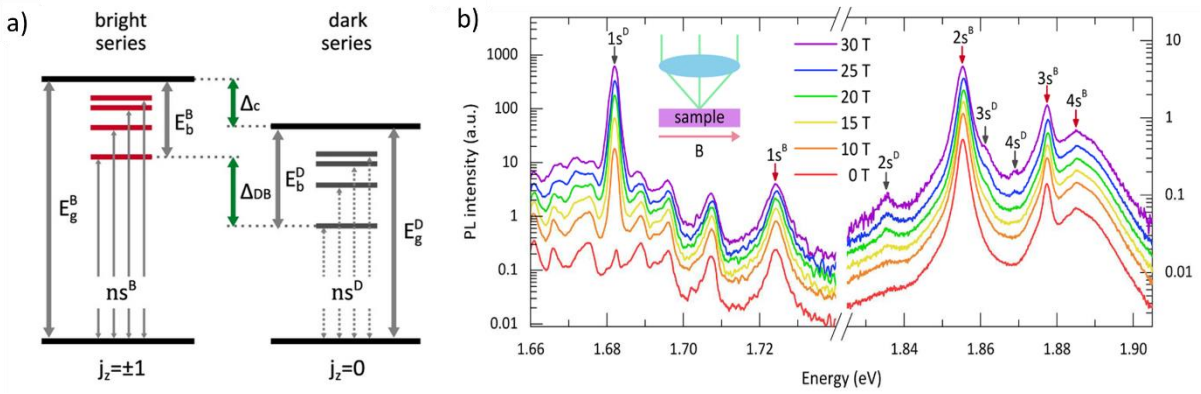

Fig1.23 **a)** The energy diagram of excitonic transitions: Rydberg series of bright (ns^B) and dark (ns^B) resonances. The horizontal red and dark grey lines represent bright and dark excitonic levels, respectively. The light grey arrows represent the band gaps for bright and dark excitons ($E_g^{B/D}$) and the binding energies of the ground states of bright and dark excitons ($E_b^{B/D}$). The energy splitting between ground states of bright and dark excitons (Δ_{DB}) and the conduction band spin-orbit splitting (Δ_C)) are represented by the green arrows. **b)**Low-temperature photoluminescence spectra measured at selected in-plane magnetic fields in the energy region of both ground (left panel) and excited states (right panel). Spectra were shifted for clarity and normalized to the $1s^B$ feature in the lower energy region and to the $2s^B$ feature in the higher energy region. Note that the intensity scales differ for these two regions. The inset schematically shows the "back scattering" geometry used in the experiment, where the excitation and the collected light beams are quasi-perpendicular to the sample surface. Figure adapted from [Kapuscinsky 2021].

1.7/ TMD heterobilayers:

1.7.1/ General discussion.

We will conclude this chapter by a discussion on the main optical properties of TMD heterobilayers which consist in type-II heterostructures fabricated by interfacing together two TMD monolayers of different materials [Geim 2013]. The basis of the optical properties of these samples are largely derived from those of its constituent monolayers but we will see that the crystalline environment at the interface of the two MLs, if engineered correctly, results in the appearance of very original effects. We will first talk about the band gap alignment of the heterobilayer by comparing the energy of the bands of different materials. Then, we will focus on the momentum separation between the CB minimum and the VB maximum, which as we will show is dependent of the twist angle θ between the crystal axis of the monolayer. We will show that the control of this alignment angle can give rise to different type of excitons than the one we have presented until now : the interlayer exciton.

Then, we will shift our discussion on the formation of moiré patterns in the crystalline potential of the heterostructure due to both the alignment angle or/and the lattice mismatch of the two constituent layers, which results in the appearance of a long range order in the HBL on the scale of hundreds of nanometers. This moiré description of the HBL potential has been widely used to explain the optical properties of TMD heterobilayers, but we will see that recent evidences of lattice reconstruction i.e local realignment between the two monolayers question the reality of the coincidence between crystalline moiré pattern and interlayer exciton recombination. We

will then discuss the main optical properties of interlayer excitons : their formation process through the real space interlayer transfer of carriers from the ML bright excitons as well as the influence of the excitation power over the interlayer exciton lineshape. Finally, we will discuss the behavior of these interlayer excitons in an out-of-plane magnetic field by presenting a compilation of the magneto-PL results commonly found in the literature.

It is to be noted that the description of interlayer excitons in TMD heterobilayers has evolved concomitantly to the work presented in this manuscript, and that this evolution has largely inspired the discussions of results presented in the following chapters. Thus, in this literature review, we will present the foundation of the optical properties of TMD interlayer excitons while leaving some elements to be discussed in next chapters .

1.7.2/ The band gap of a TMD heterobilayer.

As we have briefly mentioned above, TMD heterobilayers are fabricated by stacking together two different TMD monolayers. In [Kang 2013], the authors have investigated the band alignment in heterostructures fabricated with group-VI semiconductors TMD. They perform the ab initio calculations of many structural parameters of these materials, including the energy position of the conduction and valence bands. This calculation is represented on Fig(1.24), which evidences that most heterobilayers built with a combination of group-IV TMDs (with S, Se and Te as a chalcogen and W and Mo as a metal) results in a staggered gap i.e. a type II heterostructure.

This configuration of the band structures [Ponomarev 2018] results in the possibility for TMD heterobilayers to host low energy interlayer excitons i.e. excitons for which the two bound particles are physically localized in different monolayers, similarly to spatially indirect excitons in coupled quantum wells. As an example : in the case of a $MoSe_2/WSe_2$ heterobilayer and according to Fig(1.23), the lowest energy optical transition recombination path is between the

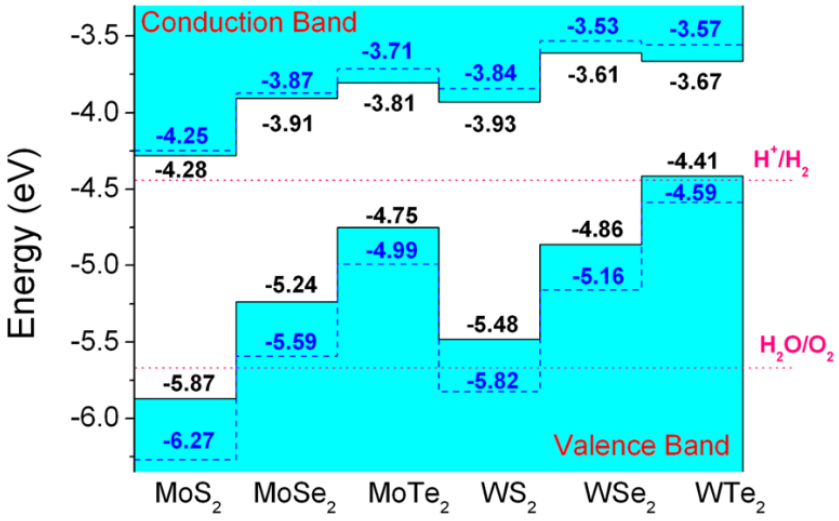

Fig1.24 Calculated band alignment for MX_2 monolayers. The dotted lines indicate the water reduction (H^+/H_2) and oxidation (H_2O/O_2) potentials. The vacuum level is taken as zero reference. Figure adapted from [Kang 2013].

bottom of the conduction band of $MoSe_2$, which would thus host the electron, and the top of the valence band of WSe_2 (which would host the hole). However, this recombination of interlayer emission can only be realistically envisaged if the interlayer gap is momentum direct. This is where a second parameter, the angle θ between the crystalline axes of both materials, comes into play [Grzeszczyk 2021].

One of the greatest assets of TMD is the possibility to engineer the optical and dielectric properties of a sample by playing on many degrees of customization opened by the layered properties of 2D van der Waals crystals (control of the thickness, encapsulation, etc...). One of these degrees of freedom is the angle θ between the crystallographic axis of the two constituent monolayers. Fig(1.24) shows the basis of this interlayer gap valley alignment : in real space, rotating the top monolayer of the heterostructure by an angle θ also tunes the alignment of the Brillouin zones of the two materials. In this representation, we consider a simplified vision of the heterobilayers in which both materials have the same lattice parameters.

Because of the C_3 symmetry characteristic of TMD monolayers, there are two angles that result in the direct momentum alignment between the high symmetry points of the Brillouin zones. These two angles are θ=0° (H type stacking), for which the $\pm K$ valleys of the first monolayer are aligned on the $\pm K$ valleys of the second monolayers, and θ=60° (R type stacking) for which the $\pm K$ valleys of the first monolayer are aligned on the $\mp K$ valleys of the second monolayer. There is also a third angle θ=20° for which the valley alignment of the ML is momentum indirect in the first Brillouin zone but momentum direct in the second Brillouin zone in the $\pm K$ on $\mp$ configuration . It is to be noted that the difference between the θ=0° and θ=60° alignments lies not in the width of the optical gap, but in the spin ordering of the heterobilayer band structure. Fig(1.25) shows the band structure of a $MoSe_2/WSe_2$ heterobilayer for both configurations : for θ=60°, the lowest energy optical transition is a singlet spin state while it is a spin triplet state for the θ=60°. We will discuss the selection rules of these two configurations in Chapter 5.

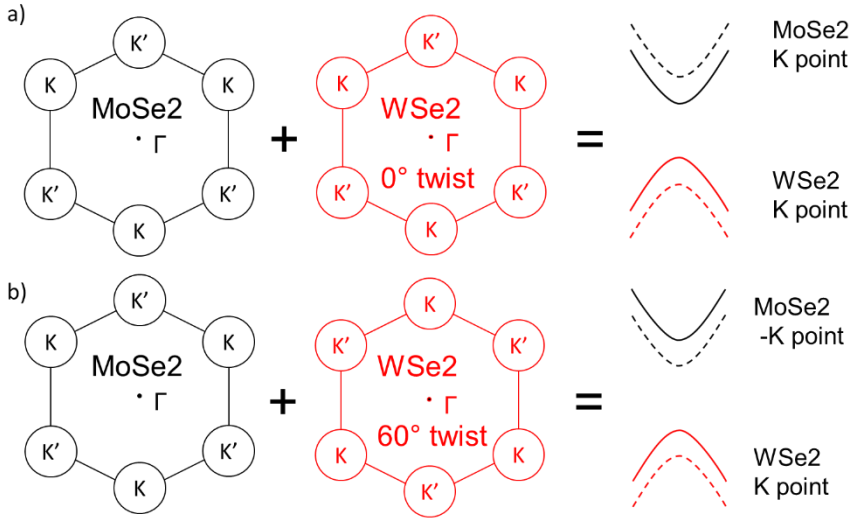

Fig1.25 Heterobilayer valley alignment by the twist angle θ between the two materials. **a)** The θ =0° alignment result in a +K on +K momentum alignment for the heterobilayer gap and the lowest energy optical transition path is a spin singler state state. **b)** The θ =60° alignment result in a +K on -K momentum alignment for the heterobilayer gap and the lowest energy optical transition path is a spin triplet state.

1.7.3/ TMD heterobilayer moiré crystal lattice.

In [Lu 2019], the authors model the crystal lattice of a $MoSe_2/WSe_2$ heterobilayer for twist angles close the H and R types stacking (θ=0+δ° and θ=60+δ°) , as represented in Fig(1.26). This results in the momentum misalignment of the Brillouin zones of both monolayers by an angle δ which increases to 2δ for the second Brillouin 3δ for the third etc... Thus, the K points of both monolayers are momentum misaligned until the point where the cumulative misalignments $n\delta = 60°$. In this case the valley alignment becomes the opposite to that of the original configuration. The original configuration is reestablished for a cumulative misalignment of $n\delta = 120°$. In the real space, this results in the detuning of the crystal cell of the monolayers by a distance d written :

$$d = 4a\sqrt{1 - \cos(\frac{\delta}{2})^2} \qquad Eq(1.23)$$

Where a is the lattice parameter considered identical for both monolayers. This distance d is also cumulative until the local order is restored when $nd = a$.

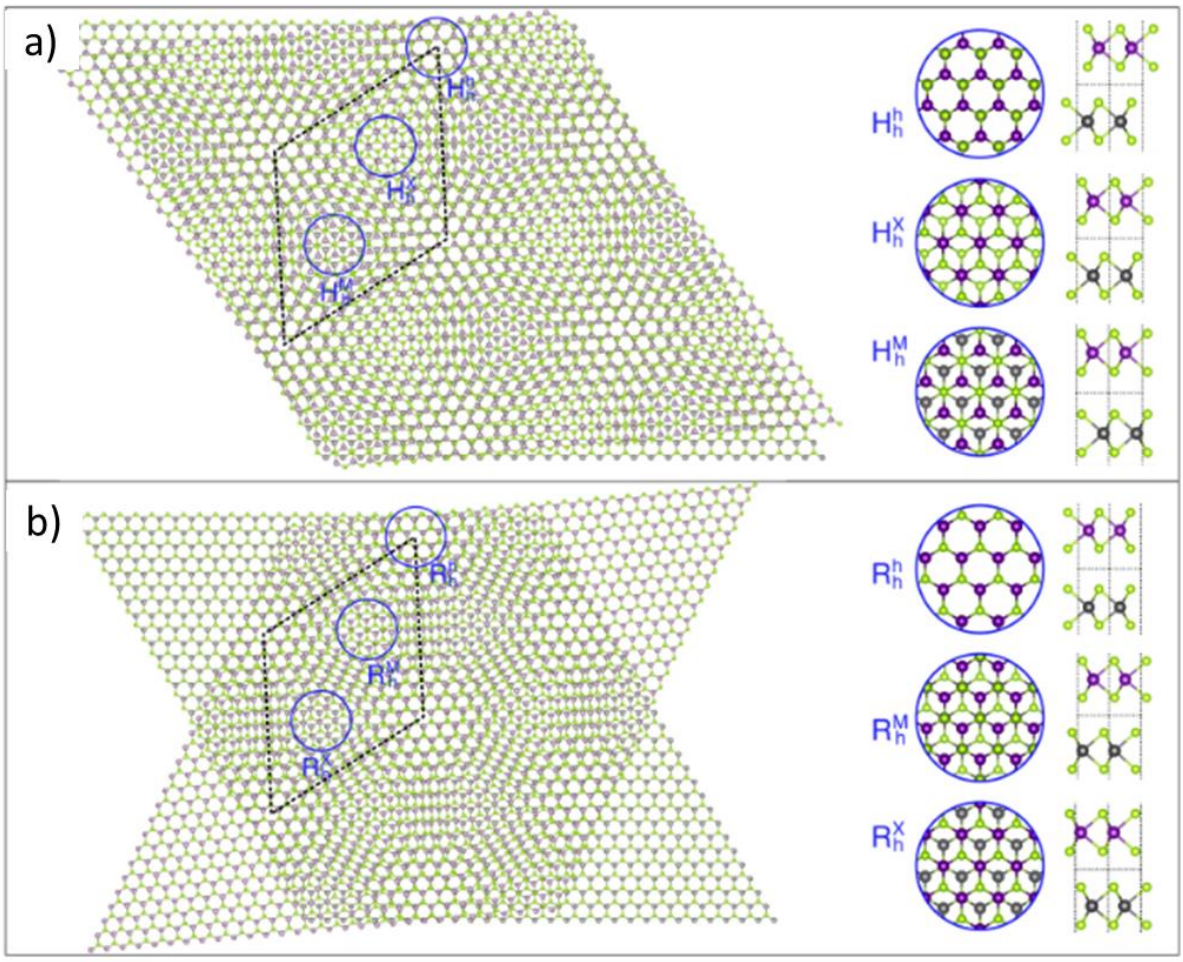

Fig1.26 The schematic plots of two main types of twisting $MoSe_2$ /WSe_2 bilayer heterostructures. **a)** is the H-type twisting structure rotated from the AA′ stacking style, and **b)** is the R-type twisting structure rotated from the AA stacking style. Six local stacking styles (atomic registries) are identified and amplified with top and side views. Figure adapted from [Lu 2019].

This means that the lattice structure of the heterobilayer can only be described on the scale of $\frac{3\pi}{3\delta}$ by the periodicity of a moiré supercell, which is delimited by the dotted lines on Fig(1.25). In reality, even in the case of a perfect alignment (δ=0), the difference of lattice parameters between the monolayer TMDs results in the apparition of a moiré pattern. Inside the supercell, different atomic alignment coexist and a complex optical response can be expected. However, it is considered that the direct neighborhood of the high symmetry points of the supercell, defined in [Yu 2017] as the atomic registries of the supercell are homogeneously stacked. Furthermore, the authors perform GW calculations of the interlayer band gap and the oscillator strength of the interlayer excitons' out-of-plane dipole and remark that there is a dependence of both parameters on the interlayer registries (cf Fig(1.27)). They observe a clear maximum of the oscillator strength on the H_h^h and R_h^h registries corresponding to the case of perfect H (0°) and R (60°) type atomic alignment respectively. This points toward a single atomic registry as the origin of interlayer excitonic recombination in moiré TMD heterobilayers Tran[2019].

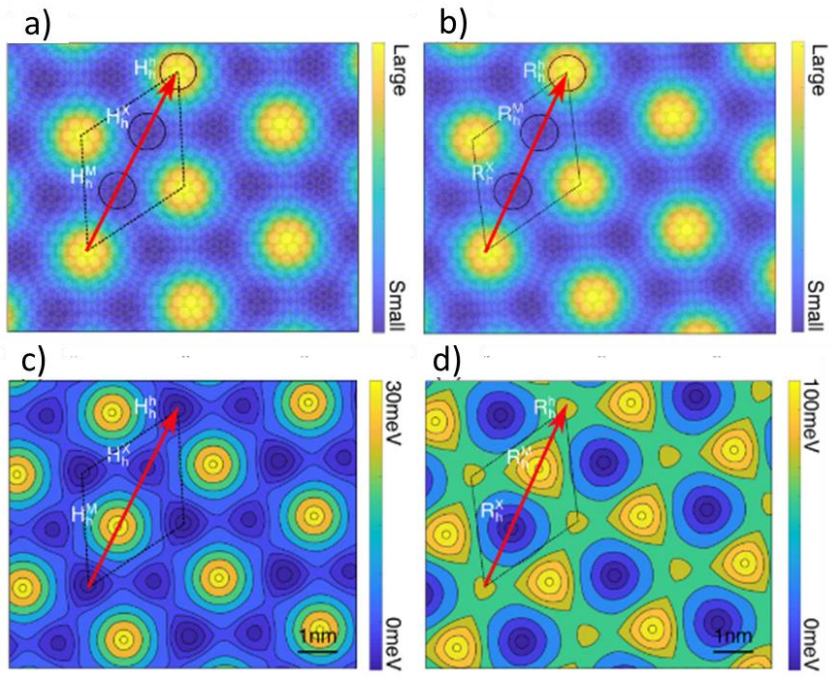

Fig1.27 **a)** and **b)** are the interpolated dipole oscillator strength of the H-type and R-type twisted $MoSe_2$ /WSe_2 bilayers, respectively. **c)** and **d)** are the interpolated interlayer exciton energy of the H-type and R-type twisted bilayers, respectively. The lattice mismatch and SOC are included. Figures adapted from [Lu 2019].

1.7.4/ TMD interlayer excitons photoluminescence and magneto-photoluminescence.

Before discussing the evidences of interface reconstruction in TMD heterobilayers, we will present the observed properties of interlayer excitons through a short review of the literature, as the moiré theory presented previously has been the general vision of interlayer excitons up to until recently. The PL signature of interlayer exciton recombination, which is the apparition of a PL peak at the low energy of the interlayer band gap, has been observed in heterobilayers constituted of many different materials. In Tab(1.8), we have compiled the different reported energy values of the interlayer gap as a function of the heterobilayer constituent materials. Most

of the literature detailing the PL and magneto PL spectra of interlayer excitons have been measured in heterobilayers of $MoSe_2/WSe_2$ however it would seem that the values of the intralayer gap is quite consistently reported to be around $E = 1{,}4$ eV regardless of the material

	$X_I(eV)$	θ	g
$MoSe_2/WSe_2$	$1.40^{[1]}$	60	-15
	$1.273-1.400^{[2]}$	60	–
	$1.35-1.400^{[3]}$	0 to 60	–
	$1.39^{[4]}1.33^{[4]}$	0	$+6.7$
		20	-15.9
		60	-15.9
	$1.36^{[5]}1.33^{[5]}$	–	$+6.06$
			-10.06
	$1.4^{[6]}$	60	10.7
			15.2
	$1.35^{[7]}$	–	–
	$1.39^{[8]}$	–	-15.8
	$1.42^{[9]}$	–	16.2
	$1.40^{[10]}$	56.4	$+12.2$
			-16.0
	$1.37^{[11]}$	0	$+5.2$
	$1.39^{[11]}$	60	-14.4
	$1.37^{[12]}$	–	–
MoS_2/WSe_2	$1.0^{[13]}$	2.2	–
$MoSe_2/MoS_2$	$1.35^{[14]}$	0 to 60	–
WSe_2/WS_2	$1.4^{[15]}$	50	15.4
			11.8
	$1.45-1.55^{[16]}$	0	–
	$1.4^{[17]}$	0	–

Tab1.8 Typical values of the g- factor found in the literature for different optical transitions. The values have been extracted from [**1**] [Nagler 2017] [**2**] [Rivera 2015] [**3**] [Nayak 2017] [**4**] [Seyler 2017] [**5**] [Joe 2019] [**6**] [Wang 2019] [**7**] [Jauregui 2018] [**8**] [Brotons-Gisbert 2020] [**9**] [Baek 2020] [**10**] [Brotons-Gisbert 2021] [**11**] [Holler 2021] [**12**] [Nagler 2017'] [**13**] [Karni 2021] [**14**] [Zhang 2018] [**15**] [Montblanch 2021] [**16**] [Jin 2019] [**17**] [Yuan 2020]. If there is no sign before the value of the g factors, it means that it was not mentioned specifically in the reference.

(with the only exception of WSe_2/MoS_2 [Karni 2021]. In [Nayak 2017], the authors study the PL spectra of interlayer excitons as a function of the twist angle in heterobilayers of $MoSe_2/WSe_2$. They show that the PL peak of interlayer excitons is quenched if the twist angle is not close to either 0° or 60° (cf Fig(1.28)) which is consistent with the idea of an interlayer gap valley alignment by layer twisting. We will not elaborate about the specificities of each magneto-PL report cited in Tab(1.8), as the discussions of the results presented in Chapter 5 and Chapter 6 will already draw from the contemporary literature. Instead, we would like to extract a general consensus from this table to which we can refer later. The general tendency is that regardless of the materials, heterobilayers aligned with θ=0° exhibit a positive g-factor $g = +6$ (cf [Seyler 2017] and [Holler 2021]) which is already higher than what is observed in regular TMD monolayers. The positive sign is also intriguing since the lowest energy transition in a 0° aligned monolayer is a "bright" spin state which always results in a negative g factor in TMD monolayers. In the case of the H (60°) stacked heterobilayers however, the magnitudes

of the g-factor are higher than any other g factor measured in 2D vdW materials with consistent reports of g=-16 for the interlayer exciton. Furthermore, [Brotons-Gisbert 2021] reports on the observation of an interlayer exciton split into two peaks, one which exhibits the large negative g factor g=-16 and the other which exhibits the large positive g-factor g=+12. A similar case is recently reported in [Montblanch 2021] and while the authors do not specify the sign of the g factors, the figures in the paper hints that, the two peaks shift toward opposite energies with the magnetic field. In [Wang 2017], the magneto PL measurement is not polarization resolved but the magnitudes of the two g factors match the one in the two previous references.

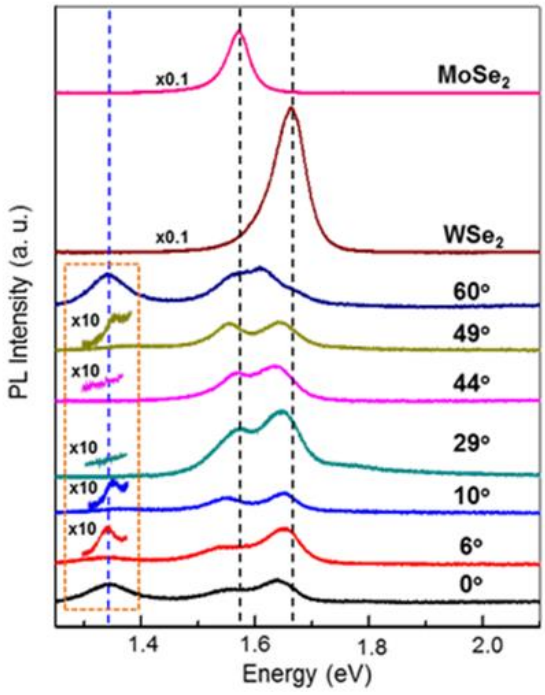

Fig1.28 Room-temperature PL spectra of $MoSe_2$ / WSe_2 , HSs for various twist angles (0 to 60°) under μ50 W laser excitation at 2.54 eV (488 nm laser). The direct excitonic peak positions for $MoSe_2$ (1.57 eV) and WSe_2 (1.66 eV) are marked with vertical black dashed lines. While the interlayer exciton appear at 1.35 eV for twist angles close to 0° and 60°. Figure adapted from [Nayak 2017].

1.7.5/ Interlayer exciton formation process and decay

In [Jin 2019] the authors investigate the photoluminescence of interlayer excitons in a WSe_2/WS_2 heterobilayer. They perform at PLE experiment on the interlayer peak and scan the excitation energy over the energy range of the WSe_2 intralayer exciton. They observe that the integrated intensity of the interlayer exciton PL peak increases drastically when the excitation energy is tuned into resonance with features originating from the intralayer PL (cf Fig(1.29)). Moreover, the intensity of the interlayer exciton completely collapses (by three orders of magnitude) when the excitation energy is lower than the energy range of the intralayer

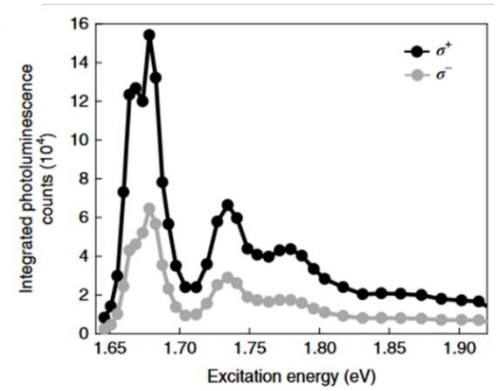

Fig1.29 PLE spectra of a WSe_2/WS_2 heterobilayer measured by monitoring the σ+ and σ− emission intensity of the 1.43 eV emission peak. Figures adapted from [Jin 2019].

spectrum. This means that it is very inefficient to excite directly the interlayer gap, and that interlayer excitons originate from the excitation of intralayer optical transitions.

The interlayer formation process is schematized in Fig(1.30) and was first described in [Hong 2014]. It consists in the ultrafast (t~100 fs) interlayer transfer of particles originating from the intralayer exciton which then form interlayer excitons [Cebalos 2014]. The lifetime of these IX has been studied through numerous time decay measurements and the lowest reported values are of the order of a couple nanoseconds in non-encapsulated samples (cf [Rivera 2015], which is already three orders of magnitudes higher than the reported decay times of intralayer excitons. Reported decay times in encapsulated heterobilayers are of the order of tens of nanoseconds [Nagler 2017 ,Joe 2019, Montblanch 2021] with sometime long lived components of a few hundreds nanoseconds [Holler 2021, Jauregui 2018, Miller 2017]. This high lifetime is attributed to the physical separation between the two particles of the interlayer exciton, which results in a weak overlap of their wavefunctions (cf [Lu 2019]) thus, a weak oscillator strength of the optical dipole and thus, an enhanced lifetime.

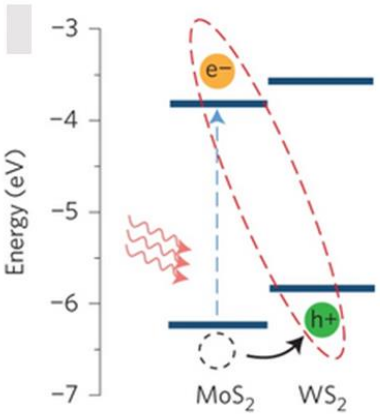

Fig1.30 Schematic of the interlayer formation process in a MoS_2/WS_2 heterostructure, Optical excitation of the MoS2 A-exciton will lead to layer-separated electron (e−) and hole (h+) carriers. Figure adapted from [Hong 2014].

1.7.6/ Influence of the excitation power on the interlayer PL spectrum

A well-known property of the interlayer exciton PL spectrum is the influence of the excitation power over its energy position. [Nagler 2017'] and [Brotons-Gisbert 2020] report a blue shift of the interlayer PL peak with an increasing excitation power. The reported magnitude of these shifts is of 10 meV between $P = 1$ µW and $P = 100$ µW and a shift of 10 meV between $P = 2$ µW and $P = 90$ µW, respectively. This is described as the evidence of a repulsive dipole-dipole interaction between interlayer excitons [Li 2020]. [Nagler 2017'] describes this interaction using a model of spatially indirect excitons in coupled quantum wells shown in [Laikhtman 2009].

Fig(1.31) shows a side view of excitons confined in coupled quantum wells separated by a distance d. In the case of our heterobilayers, d is the interlayer distance which is of the order of a few tenth of an angstrom for the supercell atomic registries according to [Yu 2017]. The spatial separation between the electron and the hole creates an out-of-plane

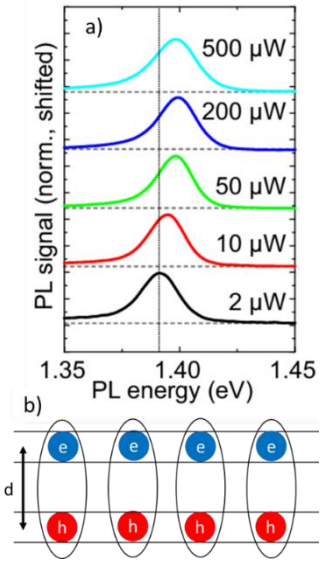

Fig1.31 a) PL spectra of the IX measured at 4.5 K as a function of excitation power. The vertical line serves as guide to the eye. Figure adapted from [Nagler 2017'] **b)** Excitons in coupled quantum wells. d is the separation between the centers of the wells. Figure indpired from [Laikhtman 2009].

electric dipole, which induces a difference of potential $\Delta\Phi$ between the two TMD monolayers:

$$\Delta\Phi = \frac{4\pi n_{IX} e d}{\varepsilon_0 \varepsilon_r} \qquad Eq(1.24)$$

With ε_r the permittivity of the material. The repulsive dipole-dipole interaction is considered as the mean field approximation of the action of the interlayer collective on a single dipole, whose expression is similar to the energy stored in a plate capacitor:

$$\Delta E = \frac{4\pi n_{IX} e^2 d}{\varepsilon_0 \varepsilon_r} \qquad Eq(1.25)$$

This approximation, requires two conditions. First, it requires that the dipole-dipole repulsion be inferior to the electron-hole attractive interaction, which is necessary for the formation of interlayer exciton. This means that the average distance between interlayer excitons must be large before the interlayer distance. This imposes a first condition on the interlayer density n_{IX}:

$$n_{IX} d^2 \ll 1 \qquad Eq(1.26)$$

The second condition to mean field approximation is that correlations between excitons can be neglected i.e that the inter-excitons distance is large with respect to the exciton thermal wavelength $\lambda_{th} = \sqrt{\frac{2\pi\hbar^2}{M k_B T}}$ with $1/M = ({m_e}^{-1} + {m_h}^{-1})$ the reduced mass of the exciton. This second condition on n_{IX} is written:

$$n_{IX} {\lambda_{th}}^2 \ll 1 \qquad Eq(1.27)$$

For a temperature of $T = 4{,}5$ K, the thermal wavelength of the interlayer exciton can be of the order of $\lambda_{th} \approx 10$ nm. In [Nagler 2017'], the authors reverse the formula of Eq(1.25) and use the measured redshift as a parameter to estimate the interlayer exciton concentration in their samples.

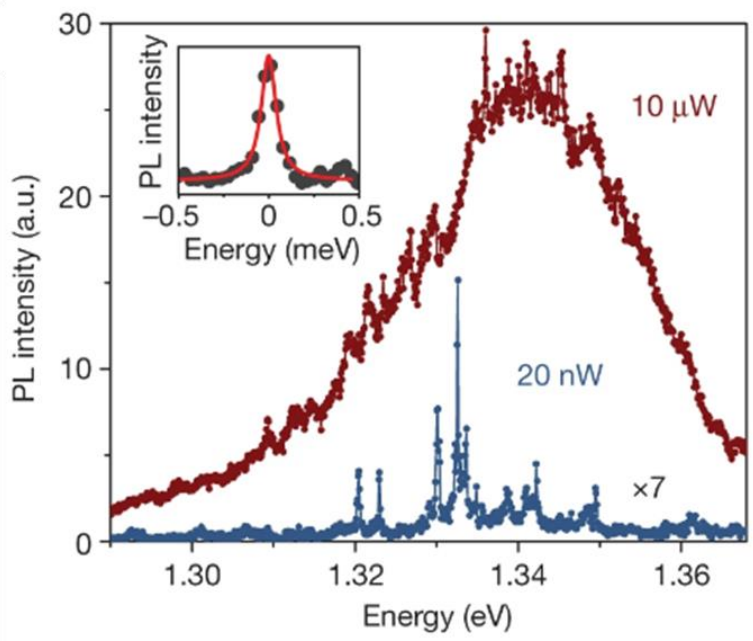

Fig1.32 Comparison of interlayer exciton photoluminescence from a heterobilayer with a 2° twist angle at excitation powers of 10 μW (dark red) and 20 nW (blue). Inset, a Lorentzian fit to a representative photoluminescence peak indicates a linewidth of approximately 100 μeV. Figure adapted from [Seyler 2017].

The second characteristic effect of the excitation power is the change in line shape of the interlayer PL spectrum when the excitation power is reduced below the µW. This effect is notably reported in [Seyler 2017] and shows that the main PL peak of the photoluminescence spectrum becomes a series of sharp ($FWHM \sim 100$ µeV) features (cf Fig(1.32)). Magneto PL experiments show that every sharp peak exhibit the same g factors, and time correlation measurements shown in [Baek 2020] evidences that these peaks emissions correspond to single photon emissions. Thus, an explanation is that the PL spectrum of interlayer excitons at low excitation power originates from individual excitons trapped close to the dominant atomic registry of the moiré supercell in analogy to the PL properties of ensembles of quantum-dots when reducing the number of emitting Qdots [Marzin 94].

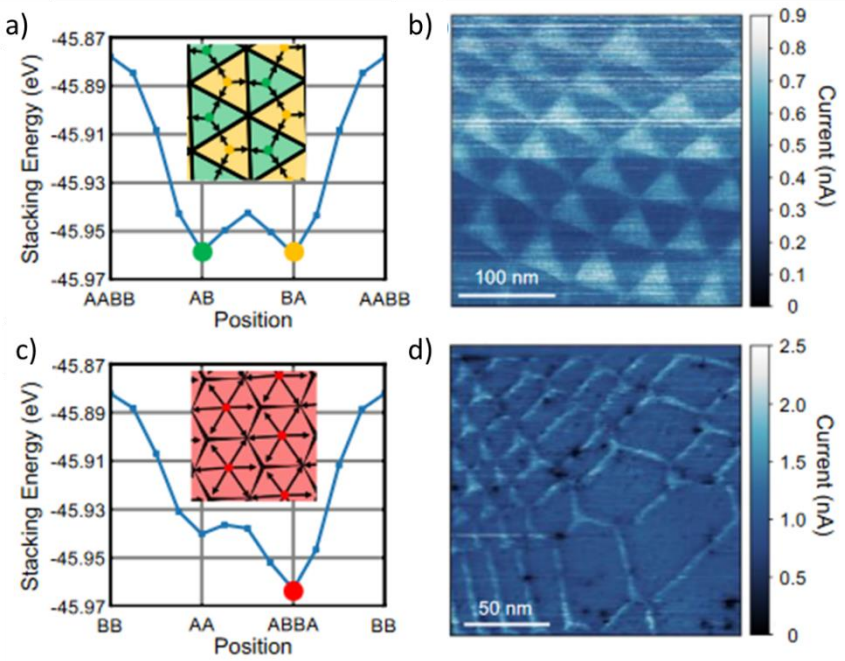

Fig1.33 a) Interlayer stacking energy as a function of stacking orientation along the atomic registry centers of the supercell. AB (H_h^X) and BA (H_h^M) are degenerate global minima, which suggests that AB and BA regions will grow to form larger domains. A diagram indicating the direction of the expected AB and BA domain expansion is shown in the inset. **b)** Conductive AFM (CAFM) image of a 0°+δ heterostructure showing alternating triangular domains of different conductivity. We estimate δ = 0.4° for this structure The existence of two distinct types of domains is consistent with the prediction of atomic reconstruction of the lattice two degenerate low energy stackings shown in b). **c)** Interlayer stacking energy as a function of stacking orientation along the atomic registry centers of the supercell.. ABBA (R_h^h) structure is the global minimum, which suggests that ABBA regions will grow to form larger domains. A diagram indicating the direction of the expected ABBA domain expansion is shown in the inset. **d)** CAFM image of a 60°+δ heterostructure showing hexagonal domains of the same conductivity separated by domain boundaries of different conductivity. We estimate δ = 0.5 - 0.8° for this sample. Figures adapted from [Rosenberger 2020].

1.7.7/ Evidences of moiré domain reconstruction.

This theory of the moiré supercell has been widely used to explain the properties of TMD heterobilayers, but it has recently been questioned by evidences of lattice reconstruction in TMD heterobilayers. In [Rosenberger 2020], the authors calculate the energies of the different

atomic staking configuration predicted in the moiré supercell for both the H and R alignments. The resulting stacking energies are shown in Fig(1.33.a) and Fig(1.33.c). The H stacking configuration (0°) exhibits two degenerate minima corresponding to the H_h^X and H_h^M atomic registries while the R stacked configuration (60°) has a single minimum corresponding to the R_h^h atomic register i.e. the perfect +K on –K stacking. They perform conductive Atomic Force Microscopy and observe that, contrarily to the moiré supercell picture, the two TMD monolayers reconstruct their interface to maximize the area of favorably staked domains. The heterobilayer can thus be considered as homogeneously stacked domains separated by strained borders. Similar STEM measurements shown in [Weston 2021] also describe this interface reconstruction and DFT calculation of the interlayer gap band structure for different stacking types, shown in [Phillips 2021] also point toward the existence of favorable stacking configurations. However, this recombination was only observed for small deviation of the perfect H or R alignment ($\delta \sim 3°$) which did not perfectly match the PL angle dependence shown in [Nayak 2017] (δ up to 10° for a complete exctinction of the interlayer PL). In [Parzefall 2021], the authors present compelling evidences that interlayer exciton recombination are correlated to reconstructed domains. These results are shown in Fig(1.34) : the authors map both the interlayer exciton PL and the low energy Raman Stokes and anti-Stokes spectra of an encapsulated $MoSe_2/WSe_2$ heterobilayer. In the areas affected by domain reconstruction, the Raman peaks corresponding to the breathing modes of both monolayers disappear and a new peak is observed. The mapping of this Raman signature of domain reconstruction reveal that the interlayer PL peak is only observed at reconstructed domains which is a complete change of perspective in the vision that we have of the crystal potential of TMD heterobilayers.

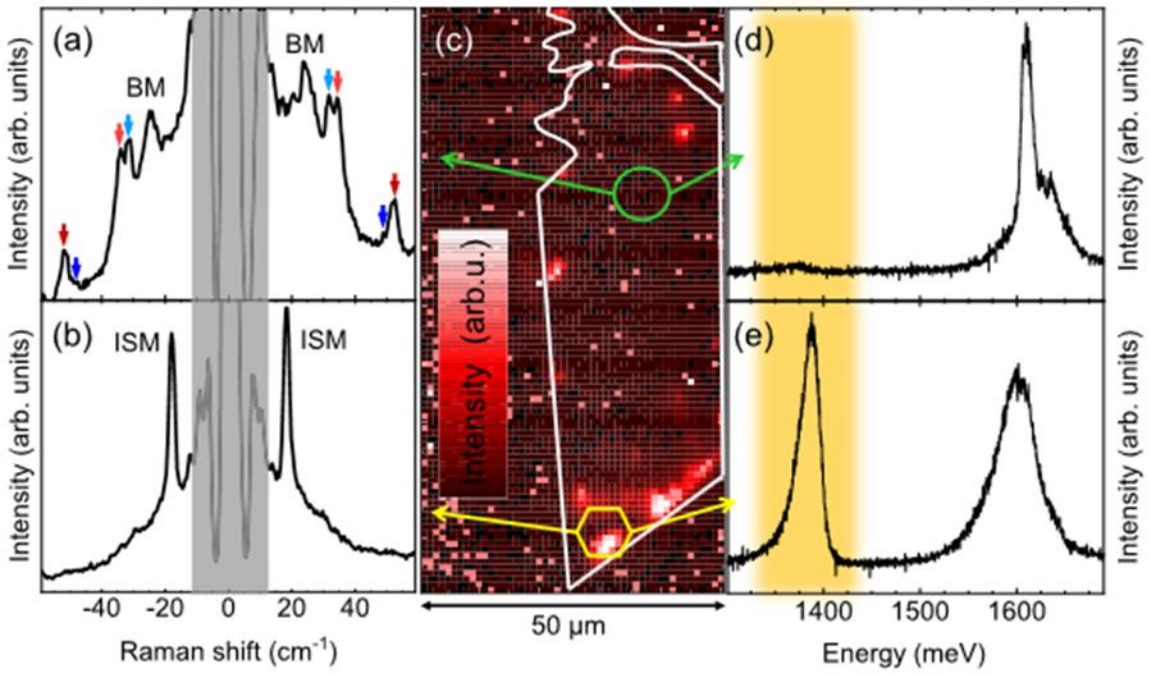

Fig1.34 a) Stokes/antistokes spectra from the region, indicated by a green circle in c). The arrows mark positions of moiré phonons, BM labels the breathing mode of the bilayer. **b)** Stokes/antistokes spectra from the region inside the yellow hexagon in c). An interlayer shear mode ISM can be observed in this region. **c)** Color map of low temperature µ PL intensities in the spectral region of the interlayer exciton, around 1390 meV. **d)** PL spectrum from the region marked with a green circle in (c). **e)** PL spectrum from the region, marked with a yellow hexagon in (c). The yellow-shaded region highlights the interlayer exciton. Figure adapted from [Parzefall 2021]

1.8/ Conclusion:

In this chapter, we have introduced the different concepts necessary to understand the physics of interlayer excitons in transition metal chalcogenides through a review of the literature. We have decribed the crystal structure of TMDs and explained how the electronic gap of these materials switches from momentum indirect in bulk and few layers state to momentum direct in the monolayer. We have discussed the coupling of the +K and – K valleys of the Brillouin zone to light through the recombination of valley polarized excitons. We then have listed the different features observed in the PL spectra of "bright" and "dark" materials and discussed the effect of an external magnetic field on these optical transitions.

Finally, we have focused our discussion on TMD heterobilayers which are van der Waals heterostructures created by stacking together two monolayers of different TMD materials. We have discussed the momentum alignment of the staggered interlayer gap and the emergence of the moiré pattern in the crystal lattice. We have presented an overview of the reported g factors in TMD heterobilayers and quickly discussed the interlayer exciton dynamics. Finally, we have discussed the recent evidences of moiré domain reconstruction in TMD heterobilayers.

Chapter 2: Experimental techniques

2.1/ Introduction:

In this chapter, we will present the different experimental setups and techniques used to obtain the results shown in the following chapters. We will start with the instrumentation : first, will present a room temperature set up which has been used for the characterization of our samples. We will then show the low temperature setup which have been used to perform the spatial mapping of the PL of our samples shown in Chapter 3, as well as the power dependence and the photoluminescence excitation experiment shown in Chapter 4. Finally, we will describe the setups that have been used to perform the magneto-PL and magneto-Raman scattering experiments shown in Chapter 6. For each of these platforms, we will detail the excitation sources used, the spectrometers, the optics and in the case of the magneto-PL setups, we will describe the two types of probes used to position the sample in the center of the magnetic field

Then, we will discuss the experimental techniques used to obtain the results presented in the next chapters. These techniques are principally the photoluminescence techniques (PL, magneto PL, PLE) as well as the Raman spectroscopy technique. For the magneto-photoluminescence technique, we will detail how we have extracted the sign and the magnitude of the interlayer exciton's g-factor presented in later chapters.

2.2/ Zero magnetic field setup at room temperature

This setup, schematized in Fig(2.1), allows for room temperature measurement without the use of a magnetic field. The sample is placed on a microscope platform and is illuminated by a halogen lamp while a camera is used to acquire the image of the sample below the microscope objective. The sample is placed under the focus point of the laser using moving stages, a stack of piezo-electric motors can be used to attain micrometric control of the samples' position as the area of the samples can be as small as a few square micrometers. The sample is excited by a HeNe 633nm laser with a spot diameter of 1µm at its focus point, while several density filters are used to control the excitation laser power. The sample's emission is collected by the objective and the backscattered laser is blocked by a high-pass 633 nm filter. The emission is focused in the slit of a diffraction spectrometer. Inside the spectrometer, a carousel can switch between three different gratings (300, 600 of 1500 g/mm) depending of the needed spectral resolution and spectral window. The emission is finally reflected to a 1340X100 pixels nitrogen cooled CCD camera. The setup is ideal for sample fabrication as it allows to quickly characterize materials exfoliated onto PDMS and decide which can be used to fabricate a vdW heterostructure. More generally, it is adapted for room temperature spatial mapping measurements.

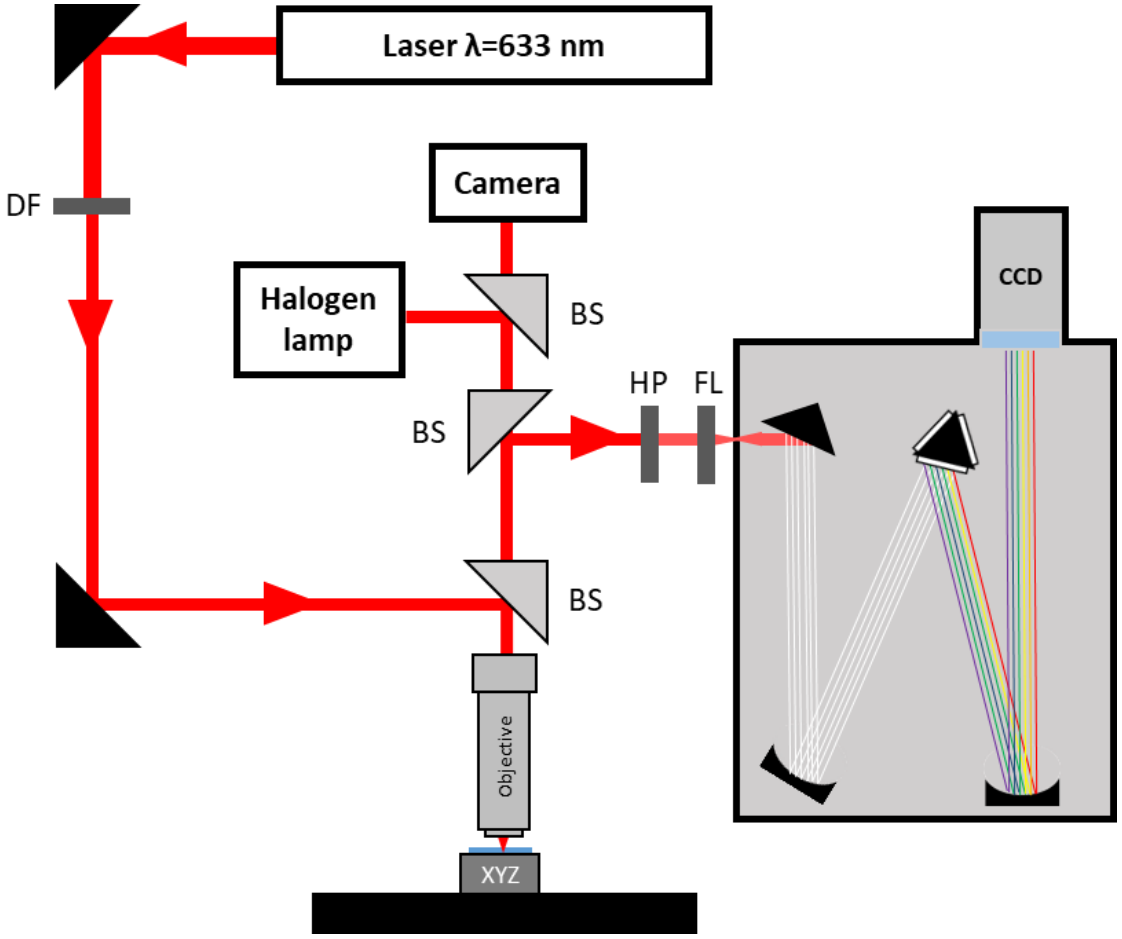

Fig2.1 Experimental setup used for ambient temperature characterization. BS are beam splitters, DF is a density filter and HP is a 633 nm short pass filter, FL is a focalization lens.

2.3/ Modular spectroscopy set up

2.3.1/ General discussion

With the exception of the previous setup, the instrumentation is very modular, excitation sources and spectrometers are fixed on moving tables and can be switched depending of the need of the experiment. This allows the realization of diverse spectroscopy measurements (PL, Raman scattering and reflectivity) in a large range of excitation and collection energy. Additional experimental modules can be added to explore other degree of freedom (temperature control, carrier density, pressure etc...). The excitation sources and spectrometers are used between two platforms : a low temperature/ zero magnetic field setup and the magneto-optical experiment setup i.e. the magnets.

2.3.2/ Excitation sources

When a resonant excitation is not necessary, such as in the characterization experiments shown in the next chapter, we use an Argon-ion continuous wave laser with an excitation energy of $E = 2.41$ eV, well above the optical bandgap of any group IV TMD. For Raman scattering spectroscopy experiment, a series of three volumic Bragg filters are placed in the collection path, before the spectrometer, to reject the backscattered laser, this prevents CCD saturation as well as laser scattering inside the spectrometer. This allows for the visualization of low intensity features $(100\ cm^{-1})$ on the Raman scattering spectrum.

In the cases of experiments with resonant excitation, we have used two sources with tunable excitation. First, a Titanium-sapphire (Ti:sapph) laser tunable between 690nm and 1100nm. This laser is used to tune the excitation to the energy of optical transitions of Se based TMD monolayers (such as the "bright" exactions of $MoSe_2$ and WSe_2 ML). The laser is pumped by a 532 nm semiconductor diode and its emission is cleaned by a prism-based monochromator. If the need arises, we use a quartz-wedge achromatic depolarizer to depolarize the laser emission. The second energy tunable source is a dye laser also pumped with a 532 nm semiconductor diode. We have used this laser with a rhodamine dye and tuned the excitation energy between 560 nm and 625 nm. This allowed us to excite resonantly with the B excitons of Se based TMDs . Similarly to the Ti:sapph , the laser emission is cleaned by a prism based monochromator.

In the case of PLE experiments and resonant Raman scattering experiments, we have used pairs of low-pass/high-pass tunable filters to clean the emission and reflect backscattered laser . Both of these tunable excitation sources can either be used as free beam excitation or injected in optical fibers thought FC/PC or SMA connectors.

2.3.3/ Collection

Two types of spectrometers can be used for collection. The first one is a single grating spectrometer, similar to the one shown in Fig(2.1), which can switch between three gratings of 300,600 and 1800 g/mm. High spectral resolution is privileged for Raman spectroscopy while large acquisition windows are necessary for large spectral feature.

The second type of spectrometer is a triple grating spectrometer consisting of three successive stages. It can be used just like a single grating spectrometer (in this case the polychromatic light

pass only through the third stage) with the possibility to switch between three gratings of 500,1500 and 2000 g/mm. It can also be used in the triple triple configuration (the polychromatic light passes trough the three stages successively). This configuration can be used in two modes : additive and subtractive. In the additive mode, all three stages contribute to the dispersion of the light. In the subtractive mode, which is the mode we used for the resonant Raman scattering experiment shown in Chapter 6 : the polychromatic light is dispersed by the grating of the first stage, then reflected to the second stage while a slit between the first and second stage acts as a band pass filter. The dispersed light is then recombined by the grating of the second stage and reflected into the third stage in which it is dispersed again and projected onto the CCD. This allows for an efficient rejection of the scattered laser.

2.3.4/ Low temperature, zero magnetic field platform

The design of this platform is the same as the one shown in Fig(2.1), with the added possibility to use any of the excitation sources and spectrometers mentioned above, and the addition of a cold finger cryostat, a photograph is shown in Fig(2.2). The sample is fixed on top the cold finger and the chamber is pumped down to $5{,}10^{-6}$ mBar to avoid condensation on the sample's surface. Liquid helium trickles through a parallel circulation system to cool the sample by conduction down to 4,5 K. The cold finger cryostat incorporates a heater, piloted by a controller, that can regulate the temperature of the sample from 4,5 K to 300 K, and wires inside the chamber can be used to control any additional devices (additional in situ temperature measurement or electrical gating for example.. The excitation power is controlled by an optical density wheel and the beam is focused on the sample by an X50 Apochromatic 0.65 NA objective in a 1 µm diameter spot through the glass cap of the cryostat.

Fig2.2 Cold finger cryostat fixed onto movable stages. The chamber is connected by two parallel circuits to a pumping blocs seen in the background and to a He vessel, on the right. The Lakeshore temperature controller can be seen at the bottom left of the picture.

2.3.5/ Magneto-optical experiment setup

LNCMI Grenoble is a service laboratory that focuses on experiments in a high magnetic field, the magneto spectroscopy team disposes of two sources of magnetic field: the usual "low field"

source is a superconductive coil cooled at liquid Helium temperature. This magnet can apply up to $\pm$ 14 T and has a 50 mm bore radius. High magnetic fields up to $\pm$30 T are applied using resistive magnets also used in the 50 mm bore radius configuration. The dimensions of the magnets impose a spatial constrain upon the experimental setups: the field center is located ~450 mm from the top of the magnet, and the instrumentation has to be adapted to the magnet bore radius. This means that the sample is fixed at the bottom of a probe i.e. a sealed, non-magnetic, metallic tube that has been alternatively pumped and flushed with gaseous helium to prevent unwanted gas condensation. The probe is then inserted in a helium bath cryostat extending thought the magnet's cavity to reach the center of the magnetic field. An atmosphere of gaseous helium (of the order of 100 mBar) is left inside the probe prior to the insertion to act as the exchange gas between the helium bath and the sample.

We have used two different type of probes : a fiber optics probe, and a free beam probe. In both cases, the samples are fixed on top of a piezo-electric motor stack with a sub-micrometer spatial resolution and a 5 mm amplitude in the three directions, allowing for a very precise positioning of the sample below the 1 µm diameter excitation spot. Two motors (X and Y axis) are equipped with position encoders which allow a precise mapping of the sample's properties.

As we have seen in Chapter 1, an out-of–plane magnetic field lifts the valley degeneracy and shifts the band structure of the ML according to the spin and valley indices of the sub-band, this is the Zeeman effect. Alternatively, a magnetic field applied in the plane of the monolayer mixes the states of the "dark" exciton with the one of the "bright" exciton, forcing its emission in a direction perpendicular to the monolayer. Fig(2.3) pictures the sample holders used to position the ML in relation to the magnetic field. In the configuration for which the magnetic field if perpendicular to the incidence of the light (Faraday geometry), the sample holder is a simple non magnetic metallic support that can be fixed on top of the piezo stack. In the configuration for which the magnetic field is perpendicular to the incident light (Voigt geometry), the sample is fixed vertically and the light is reflected by a mirror at a 45° angle.

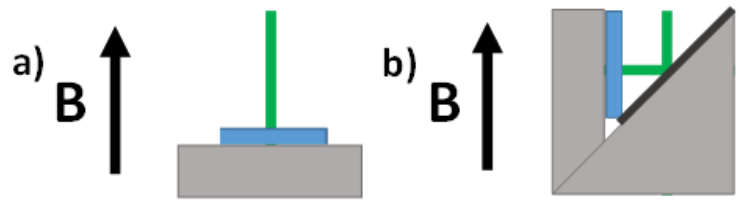

Fig2.3 Sample holders for the **a)** Faraday geometry, the direction of the magnetic field is parallel to the incident light **b)** Voigt geometry, the direction of the magnetic field is perpendicular to the incident light.

The fiber optics based probe (cf Fig(2.4)) relies on optical fibers for both the excitation and the collection. The excitation fiber guides the beam from the excitation source to the bottom of the probe. As such, the free optical path of the path of the excitation beam to the sample is only a few centimeters long. The excitation beam is collimated by a lens, reflected by a mirror onto a dichroic beam splitter and focused on the sample by a second lens. The sample's emission and the backscattered laser are collected and guided out of the probe by the collection fiber.

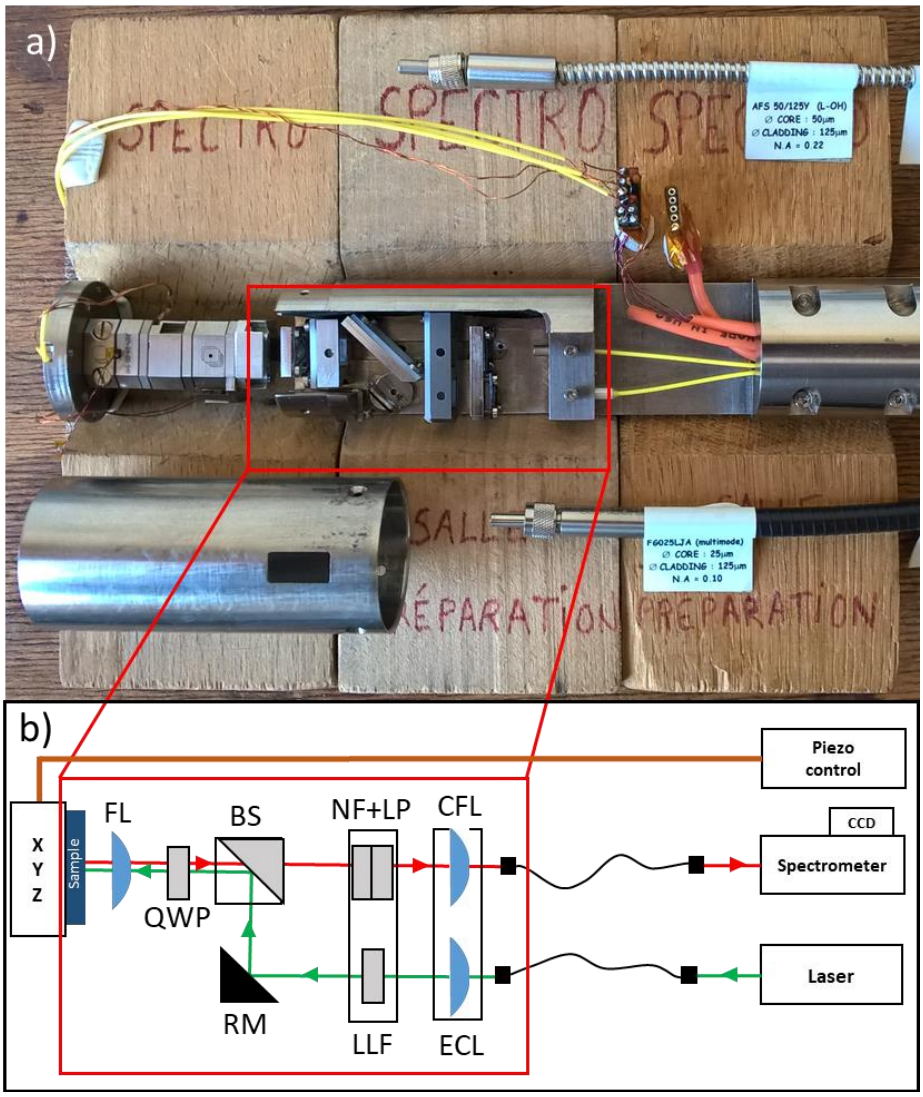

Fig2.4.a) Picture of the bottom of the fiber optics based probe. The excitation/collection fibers are the black/metallic clad fibers. The sample is fixed on top of three piezo electric motors (left side, above piezo protection shell) connected to a piezo-controller by the yellow and copper wires **b)** Schematic of the optics at the bottom of the probe for a typical polarization resolved PL measurement. The excitation beam (green line) is focused by a lens (FCL), cleaned by a laser line filter (LLF), reflected on a tunable mirror (RM) and a 50/50 beam splitter (BS) and focused on the sample by a lens (FL). The emission signal (red line) is collected by a lens and circularly analyzed by the succession of a quarter wave platen (QWP) and a linear polarizer (LP). The reflected laser is blocked by a notch filter (NF). A collection focalization lens (CFL) focuses the emission in the collection fiber.

Relevant optical elements are positioned along the excitation and collection paths in the head of the probe. Fig(2.4.b) pictures the optics installed for a typical polarization resolved measurement.

Since all the optics are located at the bottom of the sealed probe, it is not possible to correct misalignments of the injection and collection paths during the measurement. Such misalignments are likely to happen during the cooling down of the probe, as the metallic holders of the mirror, dichroic beam splitter and the three lenses expand and contract during the cooling process. These misalignments can reduce the collected signal intensity by one to two orders of magnitude. It is also not possible to change the polarization optics without opening the probe.

In the case of the free beam probe, the path of the beam is free between the top of the probe, on which all the optical element are placed, and the spectrometer. Fig(2.5.b) shows a top view schematic of the top of the probe. The excitation beam is guided from the source to the top of the probe by an optical fiber in order to minimize the effect of magnet vibrations on the excitation. These vibrations are important in the case of restive magnets due to large flow of deionized water (up to $1000\ m^3h^{-1}$) involved in the cooling of the installation. The beam passes through a collimating lens and is reflected by a volumic Bragg filter (for laser excitation) or a mirror (in the case of a white light source). Polarization optics or optical filters can be placed

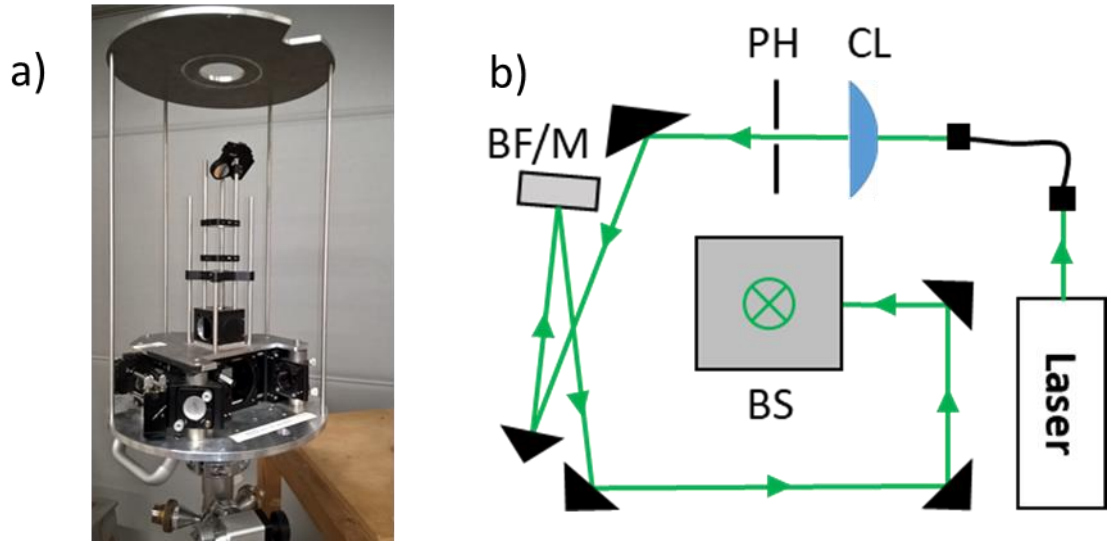

Fig2.5 a) Photograph of the top of the free beam probe. **b)** Top view schematic of the optical path of the excitation beam. The beam passes through a collimating lens (CL) and is reflected by a volumic Bragg filter or a mirror (BF/M). The beam is then reflected onto the central beam splitter BS and is sent at the bottom of the probe.

in the path of the beam, which is reflected by a beam splitter to the bottom of the probe through a glass window, and focused on the sample by an apochromatic objective, which is the only optics inside of the probe. The sample's emission and the backscattered laser are collected and focused to a mirror at the top the probe and reflected to the spectrometer (cf Fig(2.6)). The free path of the collected light represents a distance of several meters. The objective can be changed depending of the wavelength of the emission.

Contrarily to the fibered probe, it is possible to correct misalignments and change the optics at will during measurement. This allows the experimentalist to switch filters, polarization optics and even excitation sources during measurement without having to remove the probe from its cryostat. The only optical element inside the probe is an apochromatic objective, of which the focal distance is stable for a large range of wavelength. Several of these objectives can be interchanged depending of the experimenter's need (high or low NA, optimal wavelength range, etc...).

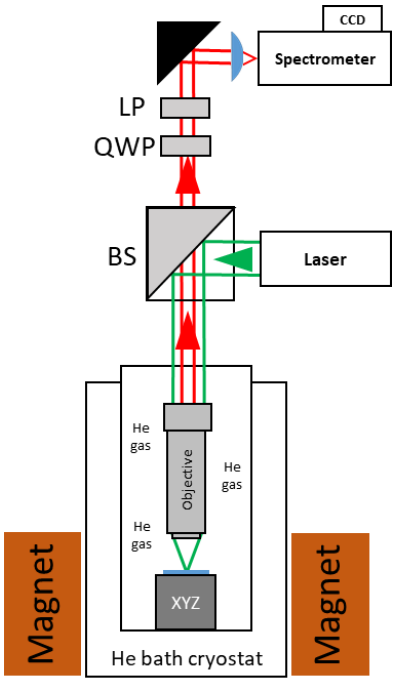

Fig2.6 Side view of the excitation and collection paths for a typical polarization resolved magneto-PL measurement. The optics on top of the probe (i.e. the optics in Fig(2.4)) are not shown.

2.4/ Experimental techniques

2.4.1/ Photoluminescence spectroscopy

In luminescence spectroscopy, we probe the populations of the different excited optical transitions [Shree 2020]. Thus, photoluminescence is a technique of choice to probe interlayer excitons, as they are low energy transitions with a formation process involving the intralayer transfer of particle created by the excitation of the intralayer gap [Hong 2014]. Nevertheless, photoluminescence can still be used to probe the absorption properties of a sample through a photoluminescence excitation experiment (PLE) in which the intensity of a chosen transition is recorded while the excitation energy is tuned across other optical transitions. This probes both the absorption of the recorded state and the relaxation efficiency between the excited and recorded states. The results of such an experiment are shown in Chapter 4.

In the following chapters, we will show magneto-PL spectra of interlayer excitons and we will put a great emphasis on the sign and magnitude of the g-factor. Thus we will now discuss how we have extracted these two parameters. Usually, the Zeeman energy is defined as the energy difference between the energy positions of the σ+ and σ- polarized emissions at the same value of the magnetic field. However, since the Zeeman shift is proportional to the magnetic field, the energy position of the $\sigma+$ polarized component for a magnetic field +B is the same as the energy position of the $\sigma-$ polarized component for a magnetic field –B. In other words : $E(\sigma+,B) = E(\sigma-,-B)$. Thus in polarization resolved magneto-PL, we calculate the Zeeman energy of the exciton from as single component (either polarized $\sigma+$ or $-$) between its energy position at a magnetic field +B and at a magnetic field –B. This is schematized on Fig(2.7).

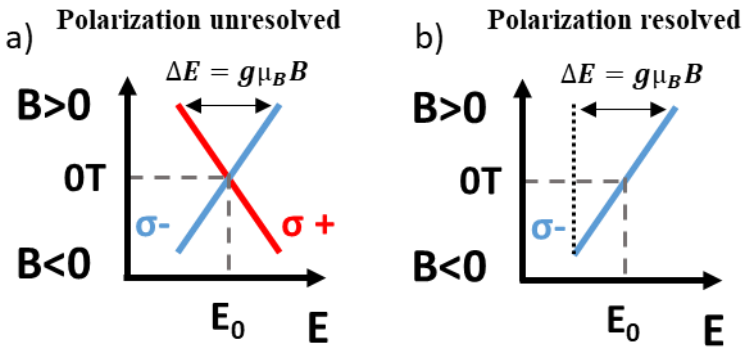

Fig2.7 a) Polarization unresolved magneto-Pl measurement, the Zeeman energy is defined as the energy difference between energy of the σ+ and σ- polarized emissions at the same value of B **b)** polarization resolved measurement, the Zeeman energy of the exciton is calculated from energy positions of a single component by the energy difference between its position + B and -B.

In polarization resolved magneto-PL experiments, it is difficult to know precisely which polarization is selected by the polarization optics. In practice, we do so by considering the shift of the "bright" intralayer excitons, which show a negative g-factor. If the energy position of the exciton blueshift with an increasingly positive magnetic field, the polarization that is selected by the optics is $\sigma -$ (and $\sigma +$ if the intralayer excitons redshift). Thus, for the interlayer excitons, the sign of the g-factor is determined by comparing the Zeeman shift of the interlayer and of the intralayer excitons. If both shift in the same direction, the g-factor of the interlayer excitons is negative (positive for a shift in the opposite direction). This is schematized in Fig(2.8).

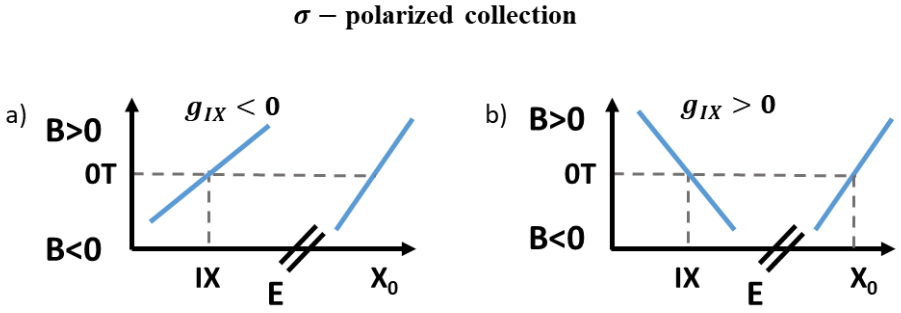

Fig2.8 Polarization resolved measurement, the selected polarization is σ- . **a)** the energy positions of the interlayer and intralayer excitons blueshift with the magnetic field : the g-factor of the interlayer exciton is negative **b)** the energy position of the interlayer exciton redshifts with B while the one of the intralayer excitons blueshifts : the g-factor of the interlayer exciton is positive.

2.4.2/ Raman scattering spectroscopy

Raman scattering spectroscopy is an experimental technique relying on the inelastic scattering of excitation photons with a very well defined energy onto the vibrational energy states of the system. In TMD monolayers, these states are the phonon modes. In the Raman scattering process, an incident photon of the laser can absorb or emit a phonon of the crystal therefore losing (Stokes) or gaining (anti-Stokes) an energy corresponding to the energy of the phonon mode. The photon is scattered and can then be collected and analyzed. This Raman scattering process can either involve one or two phonons. In the case of the one phonon process, the

condition of momentum conservation imposes that the emitted/absorbed phonon originates from the center of the Brillouin zone ($q \approx 0$) [Zhang 2015]. In the two phonon Raman scattering processes, the phonons must have opposite wavectors but can then originate from the edges of the Brillouin zone. The excitation energy is important in the process of Raman scattering, when the excitation energy is tuned in resonance with the energy of an optical transition of the system, the enhancement of the signal leads to the appearance of new peaks in the resonant Raman scattering spectrum. Such spectrum is shown in Chapter 6.

2.5/ Conclusion

In this chapter, we have detailed the experimental set ups used in the study of interlayer excitons in TMD heterobilayers. We have shown the room temperature and low temperature set up that we have used to characterize our samples at zero magnetic field. We have presented the two different probe designs used in magneto-spectroscopy experiments. Then, we have presented the experimental techniques that have been used to obtain the results presented in the next chapters.

Chapter 3: Sample characterization.

3.1/ Introduction:

In this chapter, we will present the h-BN encapsulated $MoSe_2/WSe_2$ heterobilayers that we have studied using the experimental setups presented in Chapter 2. As we have seen in Chapter 1, the long range order introduced by the moiré pattern is inversely proportional to the value of either the misalignment angle δ or the lattice parameter mismatch between the two heterobilayers. Since WSe_2 and $MoSe_2$ have very close lattice parameters (0,328 nm and 0,329 nm respectively), the size of the moiré supercell is predicted to be of the order of a few hundreds nanometers. Furthermore, a small lattice parameter mismatch means that the angles corresponding to a momentum direct gap in the +K on +K and +K on -K stacking configurations are close to $\theta = 0°$ and $\theta = 60°$, respectively. The fabrication of these heterostructures relies on conventional techniques that are commonly employed to manipulate 2D materials. Atomically thin layers of TMDs are obtained by mechanical exfoliation of bulk crystals: this mechanical cleaving technique is a staple of the sample fabrication of atomically thin crystals, including graphene, and is described in [Yi 2015]. The exfoliated crystals have been transferred onto Si/SiO_2 substrates and suitable flakes have been identified by their optical contrast under an optical microscope. The heterostructures have been assembled in the same glove box with a conventional pick-up and release technique [Castellanos-Gomez 2014] based on either PPC/PDMS (Polypropylene carbonate /polydimethylsiloxane) or PC/PDMS (polycarbonate) polymer stacks placed on glass slides. The $MoSe_2$ monolayer has been stacked on top of WSe2 and the constituent monolayers have been aligned so the edges of their respective flakes superimpose which produces a structure with an alignment angle close to either $\theta=0°$ or $\theta=60°$ due to the C3 symmetry of TMD monolayers. Finally, the heterobilayers have been encapsulated between bulk flakes of h-BN. In this chapter, we will show the results of photoluminescence and magneto-photoluminescence spectroscopy experiments that aim at characterizing the optical and magneto-optical properties of four different heterosctructures. This characterization mainly consists in the spatial mapping of the photoluminescence emitted by the intralayer excitons of the constituent $MoSe_2$ and WSe_2 monolayers, as well as the photoluminescence signature of the interlayer exciton. These heterostructures have been fabricated by Nicolas Ubrig of the Department of Quantum Matter Physics of the University of Geneva as part as a collaboration with the group of Prof. Alberto Morpurgo.

3.2/ Optical characterization $MoSe_2/WSe_2$ heterobilayers

3.2.1/ General discussion

The first step of sample characterization consists in mapping the photoluminescence signal of the structures. As we have mentioned in Chapter 1, the line shape of the intralayer excitons are a good indication of the quality of the materials, the efficiency of the encapsulation and the appearance of defects during the fabrication process. Fig(3.1) shows a photograph of the four samples under an optical microscope objective with a X100 magnification, the borders of the $MoSe_2$ and WSe_2 monolayers are traced with red and yellow lines respectively . The bottom and top bulk h-BN layers appear as large multicolored flakes, the different colors correspond to different thicknesses of the bulk. Because the exfoliated flakes of WSe_2 and $MoSe_2$ rarely have the same size, there will generally be three different domains in the structure: one domain consisting of an encapsulated WSe_2 monolayer, a second consisting of an encapsulated $MoSe_2$ monolayer and the third domain of the encapsulated heterobilayer within which both monolayers overlap. Accordingly, the PL spectrum of our samples will present three main features: the photoluminescence spectra of both the $MoSe_2$ and WSe_2 monolayers and a third feature stemming from the interlayer recombination.

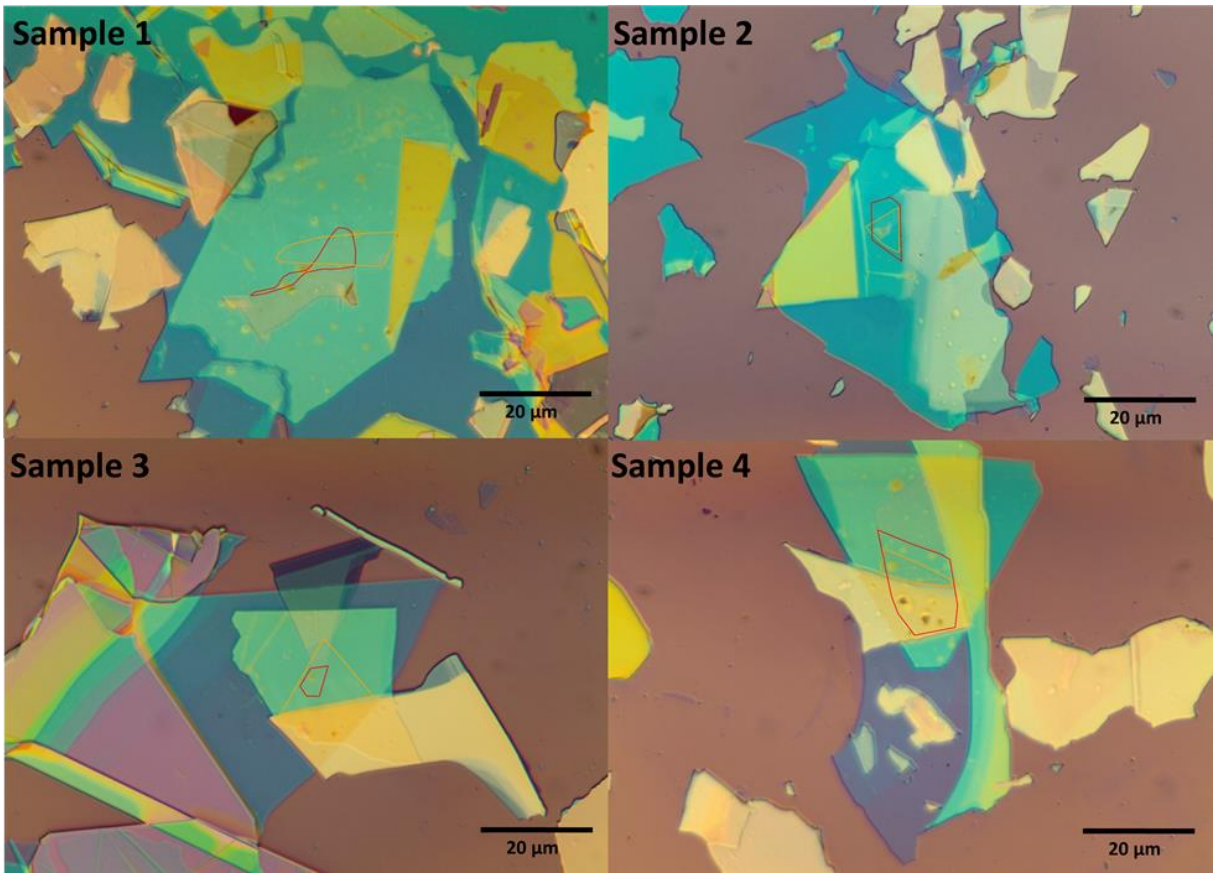

Fig3.1 Photograph of the four h-BN encapsulated $MoSe_2/WSe_2$ heterostructures taken under a microscope (X100 zoom). Yellow and red lines respectively show the borders of the WSe2 and MoSe2 monolayers. The heterostructures are encapsulated between large flakes of h-BN appearing in shades of golden, blue and purples according the local thickness of the bulk.

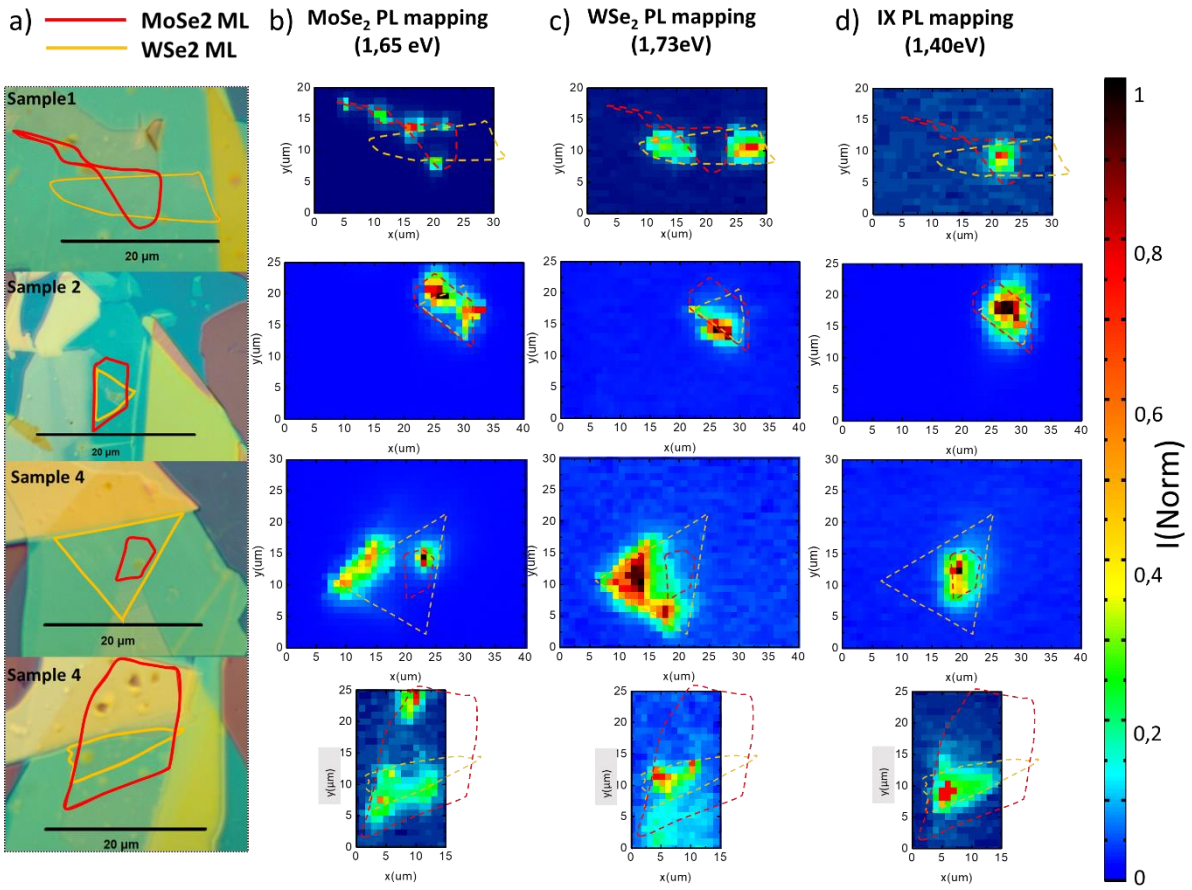

Fig3.2 a) Close up view of the heterobilayers area of Fig(3.1) **b)** Spatial mapping of the photoluminescence of the $MoSe_2$ monolayer **c)** Spatial mapping of the photoluminescence of the WSe_2 monolayer **d)** Spatial mapping of the photoluminescence of interlayer excitons. These maps have a resolution of 1x1µm and have been measured at $T = 4{,}5K$. The samples were excited using a laser with $\lambda = 514\,nm$ and $P = 40\mu W$ with the exception of Sample 4, which was excited by Ti-Saph with $\lambda = 710\,nm$ and $P = 40\,\mu W$.

Both the $MoSe_2$ and WSe_2 monolayer photoluminescence spectra show signal in similar range of energy, between $E = 1{,}61$ eV and $E = 1{,}66$ eV for $MoSe_2$ and between $E = 1{,}62$ eV and $E = 1{,}72$ eV for WSe_2. These two spectra are expected to overlap at the location of the heterobilayer with the concomitant apparition of the interlayer excitons' photoluminescence signal at lower energy ($E = 1{,}4$ eV). We thus spatially map the photoluminescence signal of the four heterostructures, using the low temperature photoluminescence setup described in Chapter 2, in the two energy ranges corresponding to the intralayer and interlayer excitons. Fig(3.2) shows the resulting photoluminescence maps for the four heterostructures, each map has a spatial resolution of $1\,\mu m \times 1\,\mu m$. Fig(3.2.b) shows the spatial maps of the photoluminescence intensity integrated at $E = 1{,}65$ eV and thus maps the recombination of the $MoSe_2$ intralayer exciton while Fig(3.2.c) shows the spatial recombination of the WSe_2 intralayer exciton (the integrated intensity at $E = 1{,}72$ eV). Finally, Fig(3.2.d) shows the spatial maps of the interlayer exciton recombination ($E = 1{,}40$ eV). We have superimposed the boundaries of the TMD monolayers on the photoluminescence map to highlight the spatial correlation between the photoluminescence signal and the monolayer edges. This methodology allows us to locate the different domains of our structure and to address them individually. The intensity of the intralayer PL is expected to be lower on the HBL domain, which seems to be

the case on Sample 1 but we will see that the spatial inhomogeneity of the Pl signal makes it difficult to define a general tendency over the four samples.

3.2.2/ Characterization of the monolayer domains

The shape of the intralayer spectrum varies greatly from sample to sample. Fig(3.3) shows the photoluminescence spectrum measured at different locations of the $MoSe_2$ and WSe_2 monolayer domains of Sample 1. The monolayers photoluminescence spectra are spatially very inhomogeneous: the positions and the widths of the intralayer exciton can change completely when changing the position of the excitation spot on the sample. This indicates rather large spatial fluctuations of the dielectric environment. In the case of WSe_2 (Fig(3.3.a)) : there are a few instances in which the intralayer WSe_2 spectrum exhibits comparable quality to state of the art encapsulated monolayers. These locations are characterized by a very sharp excitonic peak (typically a FWHM of $\Delta E \sim 4$ meV [Cadiz 2017, Manca 2017]) and by a structured spectrum at lower energy from which the trion, the spin "dark" exciton and the neutral and charged biexcitons can be resolved separately, they also show a FWHM of $\Delta E \sim 4$ meV. However, this is not representative of the whole WSe_2 monolayer domain and these high quality locations are quite rare. Over the few square micrometers of the WSe_2 monolayer domain, the energy position of the "bright" exciton PL peak shifts between 1,729 eV and 1,736 eV and can broaden up to a FWHM of $\Delta E \sim 8$ meV. The broadening is accompanied by the loss of the structured low energy spectrum as the Pl peaks of the different optical transitions broaden and merge. There are also some instances of very broad ($\Delta E \sim 20$ meV) excitonic peak showing two separated components which indicates the response of two different dielectric environment below the laser spot. At these locations, only a broad ($\Delta E \sim 10$ meV) trion can be resolved from the low energy continuous spectrum. The photoluminescence spectrum of $MoSe_2$ monolayer domains, shown in Fig(3.3.b) exhibits the same behavior. The width of the excitonic emission line varies between 3 meV and 6 meV, which is broader than the reported values for high quality encapsulated monolayers [Robert 2020], and its position shifts between 1,649 eV and 1,654 eV. There are instances of split excitonic and trionic peaks as well which can result in a broadening of the line shape up to a FWHM ~ 8 meV . This behavior is consistent over the monolayer

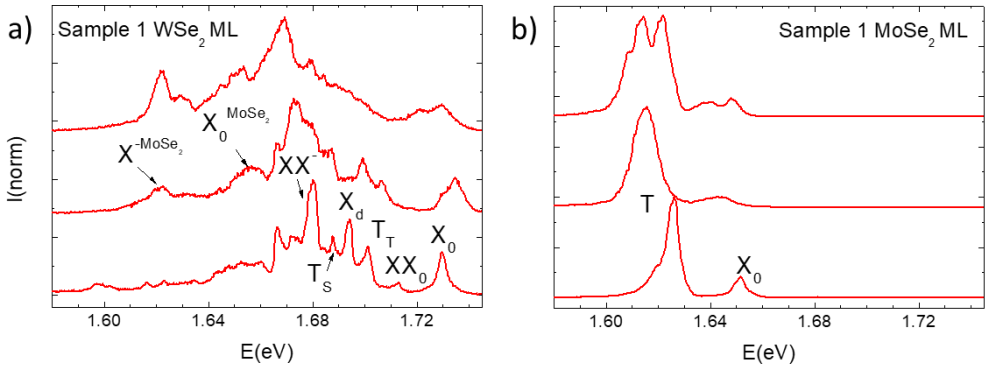

Fig3.3 a) WSe_2 photoluminescence spectrum measured at different locations of the WSe_2 monolayer domain of Sample 1 **b)** $MoSe_2$ photoluminescence spectrum measured at different locations of the $MoSe_2$ monolayer domain of Sample 1. The spectra originate from the PL mapping data shown in Fig(3.2) and the PL peaks have been assigned to optical transitions in the same way than in Fig(1.14). The spectra are ordered from top to bottom by the quality of the optical properties they represent .

domains of the four heterostructures and is most likely the result of the heterobilayer fabrication process. As we have seen in Chapter 1, the optimization of the monolayer's dielectric environment through h-BN encapsulation results in the structuration of the low energy PL spectrum. Conversely, a general broadening of the PL peaks means that the TMD monolayer is locally decoupled from the h-BN capping layers. This spatial fluctuation of the TMD/h-BN interface is the result of local defects [Rhodes 2019] and impurities introduced during the fabrication process, some of which can be seen on the close up visuals shown in Fig(3.2.a) as small stains or bubbles [Stolyarova 2009, Rodriguez 2021] trapped between the components of the heterostructure. While there is no firm consensus on the contents of these bubbles, they are widely believed to be trapped hydrocarbons from air contaminants present in ambient laboratory conditions. Such bubbles both strain and decouple the TMD from the h-BN and are eliminated by global or local [Boddison-Chouinard 2019] thermal annealing.

3.2.3/ Characterization of the heterobilayer domain

As we have mentionned in Chapter 1, the PL spectrum of the heterobilayer domain presents two features corresponding to the intralayer (which is the superposition of the WSe_2 and $MoSe_2$ monolayers) and interlayer PL spectra. Fig(3.4) shows intralayer PL spectra measured at different locations of the heterobilayer domains for the four samples. The spatial inhomogeneity of the PL spectrum is the same as in the monolayer domains and we observe a similar broadening of the intralayer exciton's peak as well as similar shift of its energy position. In the case of Sample 1 and Sample 2, the PL peaks of the $MoSe_2$ exciton and trion dominate the spectrum, while the WSe_2 exciton is barely visible. The intralayer signature of the heterobilayer domain of Sample 1 and Sample 2 looks like the superposition of an encapsulated $MoSe_2$ monolayer and an encapsulated WSe_2 monolayer, which would indicate a good interfacing between the constituent TMDs and the h-BN flakes. The intralayer spectrum of Sample 3 is

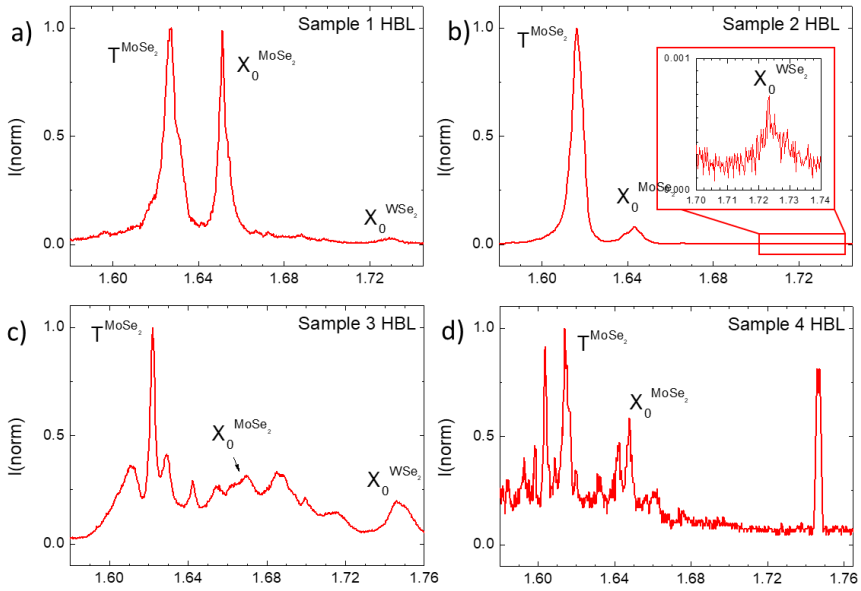

Fig3.4 Intralayer photoluminescence spectra measured on the heterobilayer domain of **a)** Sample 1 **b)** Sample 2 **c)** Sample 3 **d)** Sample 4 (The PL peak at $E = 1{,}75$ eV comes from the excitation laser) The spectra originate from the Pl mapping data shown in Fig(3.2).

quite different: while features from both the WSe_2 and $MoSe_2$ spectra can be observed, their intensity is of comparable magnitude. In the case of Sample 4, the intensity of the intralayer PL spectrum is very weak despite resonant excitation conditions. By contradiction with the observation made on Sample 1 and Sample2, this could be due to a weak interfacing of the two monolayers and/or the top and bottom h-BN. It is however to be noted that because of the important spatial inhomogeneity observed in the TMD monolayer domains of the heterostructure, it is not possible to comment on a possible influence of the heterobilayer stacking on its intralayer PL spectrum. In other words, the spatial inhomogeneity displayed in the heterobilayer domain is in line with the spatial inhomogeneity of the monolayer domains.

The second feature of the HBL photoluminescence spectrum is the low energy PL peak centered at $E = 1{,}4$ eV, characteristic of the interlayer exciton recombination. Fig(3.5) shows interlayer PL spectra measured at different location of the four HBL domains. Similarly to its intralayer counterpart, the interlayer excitonic lineshape is also very sample dependent. Sample 1 exhibits a single peak with a FWHM of the order of $\Delta E \sim 4$ meV centered on $E = 1{,}395$ eV as well as a broader emission between $E = 1{,}33$ eV and $E = 1{,}36$ eV attributed to excitons trapped in the strain field of the heterostructure [Kremser 2020]. Contrarily to the intralayer exciton spectrum, whose lineshape can change completely within a few micrometers, the energy position of the interlayer excitonic peak is quite homogeneous. While we do observe a small variation of the energy position of the main peak of the order of $1meV$ over the whole sample, the shape of the photoluminescence spectrum does not change. The PL spectrum of Sample 2 also shows a single feature centered at $E = 1{,}39$ eV (with fluctuations of the energy position between $E =$

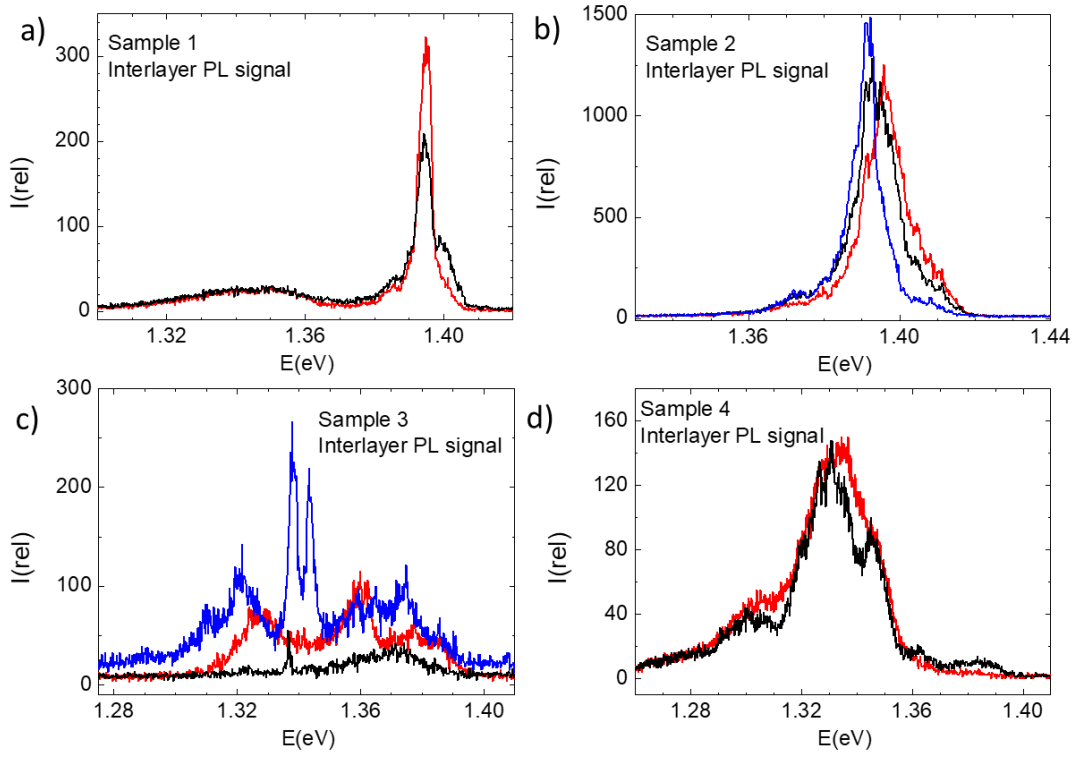

Fig3.5 Interlayer photoluminescence spectra measured on the heterobilayer domain of **a)** Sample 1 **b)** Sample 2 **c)** Sample 3 **d)** Sample 4. The spectra originate from the Pl mapping data shown in Fig(3.2). The intensity of the spectra is normalized by the acquisition time.

1,389 eV and $E = 1{,}396$ eV), but the peak is broader ($\Delta E \sim 15$ meV) , and is more intense. In comparison, the lineshape of the interlayer exciton observed in Sample 3 and Sample 4 are very different. Despite emitting in the same range of energy, the intensity measured on Sample 3 signal is completely dependent on the position. The photoluminescence spectrum can exhibit two, three or even four features depending on the location. The four featured spectrum is also the one showing the peaks with the smallest linewidth : two sharp peaks ($\Delta E \sim 3$ meV) centered on $E = 1{,}338$ eV and $E = 1{,}344$ eV between two broader ($\Delta E \sim 10$ meV) lower intensity bumps centered on $E = 1{,}320$ eV and $E = 1{,}372$ eV. The interlayer excitonic lineshape of Sample 4 is a much broader structure ($\Delta E \sim 100$ meV) centered at $E = 1{,}33$ eV, which lie well below the energy of interlayer excitons in other investigated samples. The energy position is spatially homogeneous and the intensity of the feature is the lowest of the four samples.

Based on the energy position, lineshape and on the intensity, the two samples showing the most similarities are Sample 1 and Sample 2 while it looks difficult to define a common tendency to the four samples. The only characteristic shared by these PL emissions is their extreme spatial localization. Fig(3.6) shows the spatial mapping of the interlayer excitons' integrated intensity. This figure corresponds to the intensity maps shown in Fig(3.2.d) with the addition of a z-axis highlighting the "hot spot" emission pattern of the interlayer emission. While the heterobilayers area span over a few micrometers in both the x-axis and y-axis, the intensity of the interlayer is centered on a much-localized maximum and moving away from this position results in a sharp decrease of the interlayer intensity. In the rest of this manuscript, the location of the excitation spot will systematically be at this maximum of intensity.

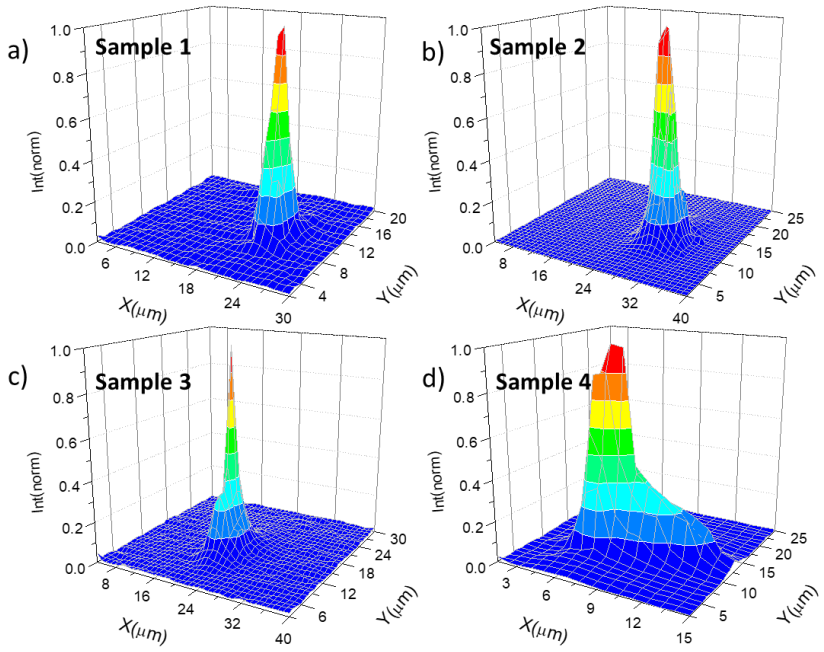

Fig3.6 3D map of the integrated intensity of the interlayer PL peak measured in **a)** Sample 1 **b)** Sample 2 **c)** Sample 3 **d)** Sample 4 The intensity value is a normalization of the intensity integrated over the whole interlayer PL spectrum.

3.3/ Magneto-optical characterization of $MoSe_2/WSe_2$ heterobilayers

The second step of characterization consists in measuring the photoluminescence response of our heterobilayers under the influence of a magnetic field. In this chapter, we will only show the results of magneto-spectroscopy experiments that aim at characterizing the alignment angle of our samples. As we have discussed in Chapter 1, one of the very intriguing characteristics of $MoSe_2/WSe_2$ heterobilayer interlayer excitons is that the Zeeman shift of the interlayer exciton corresponds to values of the g-factor that are impossible to observe in regular TMD monolayers. The two notables values of the g-factors are $g = -15{,}9$ and $g = +6{,}7$ observed in heterobilayers aligned with an angle of $\theta = 60°$ and $\theta = 0°$ respectively [Seyler 2017, Montblanch 2021] with hints of a second transition with a positive g factor in 60° aligned monolayers [Brotons-Gisbert 2021, Wang 2019] . At this point, the alignment angle of our samples is still undetermined and we do not have the means to discriminate between $\theta = 60°$ and $\theta = 0°$ [Psilodimitrakopoulos 2019]. Thus, we will obtain an approximation of θ by measuring the g-factor of the interlayer excitons in our heterobilayers and compare their values to the ones of the literature.

We have performed a magneto-PL photoluminescence experiment using the superconducting coil, presented in Chapter 2 with which we sweep the magnetic field between $B = -14$ T and $B = +14$ T. The temperature of the samples is T=4,5 K and the excitation energy is $\lambda = 514$ nm with an excitation power of $P = 40$ µW. As we have mentionned in Chapter 2 , we

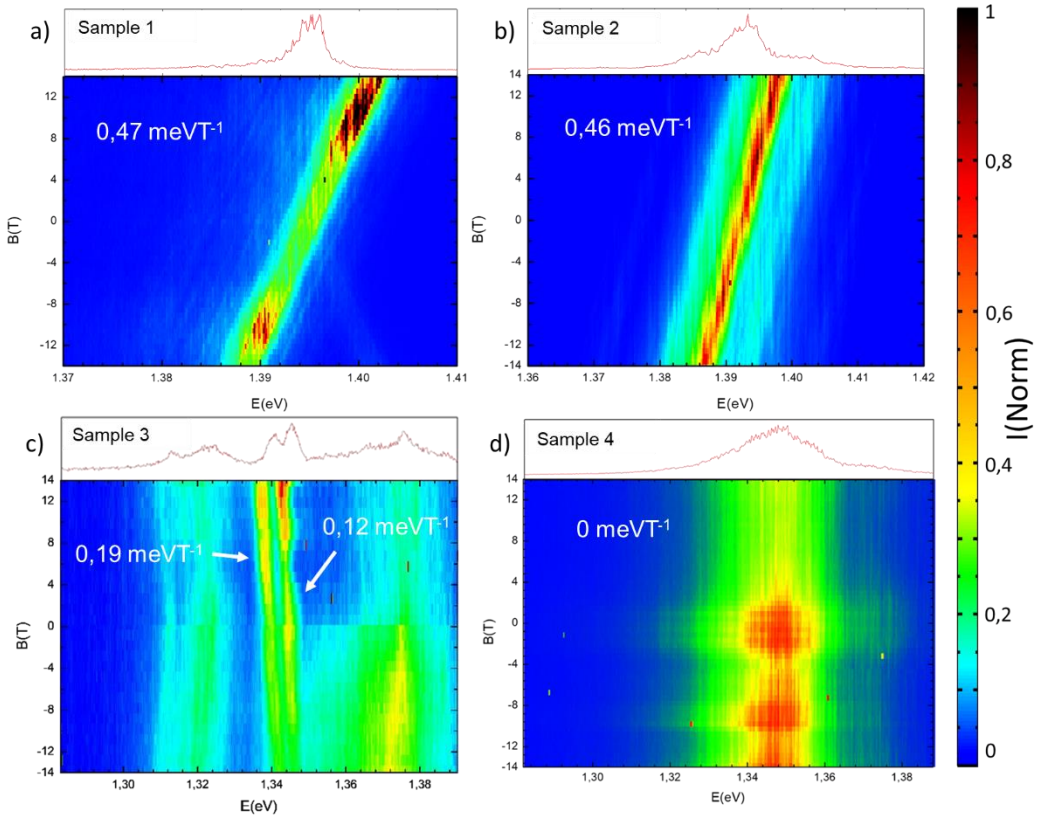

Fig3.7 False color maps of the interlayer magneto-Pl spectra measured in **a)** Sample 1 **b)** Sample 2 **c)** Sample 3 **d)** Sample 4. For each map, a PL spectrum of the interlayer exciton, measured at $B = 0T$, is show on top as a reference. The magnetic field is swept between $B = -14$ T and $B = +14$ T with a 1T step. The temperature of the samples is T=4,5K and the excitation energy is $\lambda = 514$ nm with an excitation power of $P = 40$ µW. The modulations of the emission intensity with the magnetic field, most visible on d), are due to the Faraday effect.

will determine the sign of the g factor by comparing the Zeeman shifts of interlayer and intralayer excitons while the magnitude of the g factor will be calculated from the energy positions of single valley component for opposites magnetic field. The results of this magneto-PL experiment are shown on Fig(3.7). Sample 1 and Sample 2 exhibit a pronounced shift in magnetic field with a rate of $0{,}47\ \mathrm{meVT^{-1}}$ and $0{,}46\ \mathrm{meVT^{-1}}$ which corresponds to a g-factor of $g = -15{,}9$. This is similar to what has been reported for 60° aligned HBL [Seyler 2017] . This shift rate is four times higher than the one usually measured in monolayer $MoSe_2$ and WSe_2. In comparison the two central lines in the PL spectrum of Sample 3 shift at a much slower rate : $0{,}19\ \mathrm{meVT^{-1}}$ and $0{,}12\ \mathrm{meVT^{-1}}$ corresponding to g-factor of $g = +6{,}5$ and $g = +4{,}1$ which is in line what is reported for 0° aligned $MoSe_2/WSe_2$ heterostructures [Seyler 2017]. The interlayer peak measured in Sample 4 is not affected by the magnetic field and does not show any shift up to B=14T.

This lack of interaction with the magnetic field, combined with the broad lineshape and low intensity of the interlayer and intralayer PLsignal make us question the real origin of the PL observed in Sample 4. The non existent Zeeman shift excludes the possibility of any excitonic recombination, intralayer of interlayer. It seems more likely that this emission originates from extrinsic disorder i.e. contaminants deposed on the surface of the heterobilayer during fabrication.

3.4/ Conclusion:

We have characterized the optical properties of our samples and took a glance at their behavior when applying a magnetic field. We have observed the important spatial inhomogeneity of the intralayer excitons PL which makes it difficult to define a common trend between our samples. Nevertheless, we have observed that two of the heterobilayers were showing similar properties, which has been confirmed by the results of a magneto-PL experiment. Thus, we can assume that both Sample 1 and Sample 2 are aligned with an angle of 60°. In the case of Sample 3, we have observed Zemman shifts compatible with the behavior reported in heterobilayers aligned with a twist angle of 0°. However, despite multiple tries, we have never been able to reproduce the results shown in Fig(3.7.c). It is unclear if this is due to bad measurement conditions or alteration of the heterobilayer due to thermal cycling. In the case of Sample 4, we have concluded that the PL emission centered on $E = 1{,}33$ eV dit not originate from interlayer excitonic recombination, but rather from contaminants trapped at the interface of the heterobilayer. Thus, the results presented in the rest of this manuscript are exclusively obtained by the joint study of Sample 1 and Sample 2.

Chapter 4: Presentation of the experimental results

4.1/ Introduction:

In this chapter, we will present the results of an ensemble of experiments carried on Sample 1 and Sample 2. We have probed the magneto-optical properties of these two samples using photoluminescence, absorption and magneto-photoluminescence techniques. Initially, we will discuss the influence of the excitation power on the lineshape of the interlayer photoluminescence spectrum. We have tuned the power of our excitation laser source across three orders of magnitude, between $P = 50$ µW and $P = 10$ nW. While the change of the interlayer photoluminescence spectrum shape at low excitation power is a well-known characteristic of TMD moiré excitons (cf Chapter 1), we want to point out that the continuous transition between the high excitation power and low excitation power regimes is a direct visualization of the decreasing excitonic surface density in the sample. Next, we will present the results of a photoluminescence excitation experiment probing the optical absorption of the interlayer exciton in Sample 1. Finally, we will show the results of magneto-photoluminescence experiments for a magnetic field up to $B = 30$ T, which are the main results presented in this manuscript. We have measured magnetic field resonant anomalies in the intensity of the σ+ and σ- polarized components of the interlayer emission, whose detailed description requires a very high field resolution.

4.2/ Power dependence of the interlayer exciton photoluminescence

4.2.1/ General discussion

As we have seen in Chapter 1 the influence of the excitation power over the photoluminescence spectrum of interlayer excitons is two-fold and defines two different regimes of excitation. At high excitation power, the PL spectrum is affected by the repulsive exciton-exciton interaction [Laikhtman 2009] between the out-of-plane dipoles of the interlayer excitons. This effect is observed as the blueshift of the interlayer PL peak when the excitation power increases, proportional to the interlayer exciton density. The second effect is seen as a change of the PL spectrum's line shape which transforms from a broad feature to a discrete series of sharp peaks. This discrete spectrum is seen as the PL signal of individual excitons trapped in the moiré potential.

We seek to explore these two excitation regimes and to measure a full power dependence of the interlayer PL spectrum in which we tune the excitation power across three order of magnitudes, between $P = 50$ µW and $P = 10$ nW. We carry out this measurement at low temperature ($T = 4{,}5$ K) on the zero field experimental setup described in Chapter 2. The excitation energy is $E = 1{,}72$ eV, in resonance with the energy of "bright" excitons in WSe_2 monolayers. This enhances the formation of interlayer excitons [Seyler 2017] and allows us to access high interlayer densities with minimal laser heating of the sample's surface. Fig(4.1) shows the results of this power dependence for Sample 1 and Samples 2.

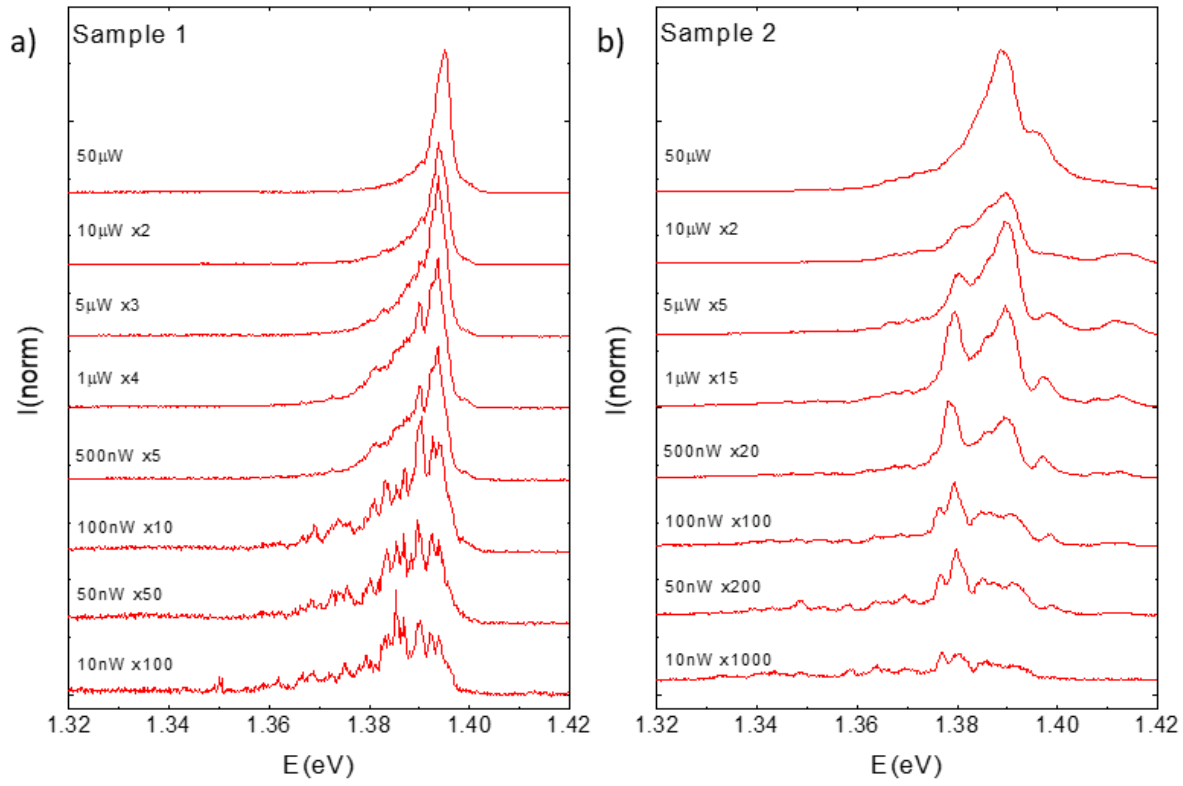

Fig4.1 Interlayer exciton PL spectrum as a function of the excitation power for a) Sample 1 and b) Sample 2. The intensity has been normalized by the acquisition time, then scaled up .

We observe a clear change in the lineshape of the interlayer excitons PL spectrum. As expected, the main interlayer peak progressively transforms into a discrete series of sharp features. The width of the main interlayer peak is 4 meV in Sample 1 and 14 meV in Sample 2 while the sharp lines visible at low excitation power display a FWHM~100 µeV in both samples. Note that these lines appear at an energy that is lower than the position of the main excitonic peak.

We also observe the predicted blueshift of the interlayer PL with increasing excitation power. This effect is easier to observe in Sample 1 because of the sharpness of the peak. Fig(4.1.a) shows the energy position of the main excitonic peak as a function of the excitation power. We observe a blueshift of 1,1 meV between the positions of the main peak at $P = 300$ nW and $P = 50$ µW. The effect is more difficult to observe in Sample 2, as the different features structuring the interlayer excitonic jitter at high excitation power. Nevertheless, it is still possible to follow the blue shift of an auxiliary peak, appearing at a lower excitation power and shown in Fig(4.2.b). The energy position of this line can be followed from $P = 300$ nW to $P = 10$ µW and show a total blue shift of 2,6 meV (cf Fig(4.2.d)). For both samples, the energy positions does not shift linearly with the excitation power and tend toward a stable value. While the rate of the blue shift appears to be one order of magnitude higher in the case of Sample 2, the energy differences between the position at high (tens of µW) and low (tens of nW) excitation power are of the same order of magnitude for both samples and coherent with values observed in [Nagler 2017] and [Brotons-Gisbert 2020].

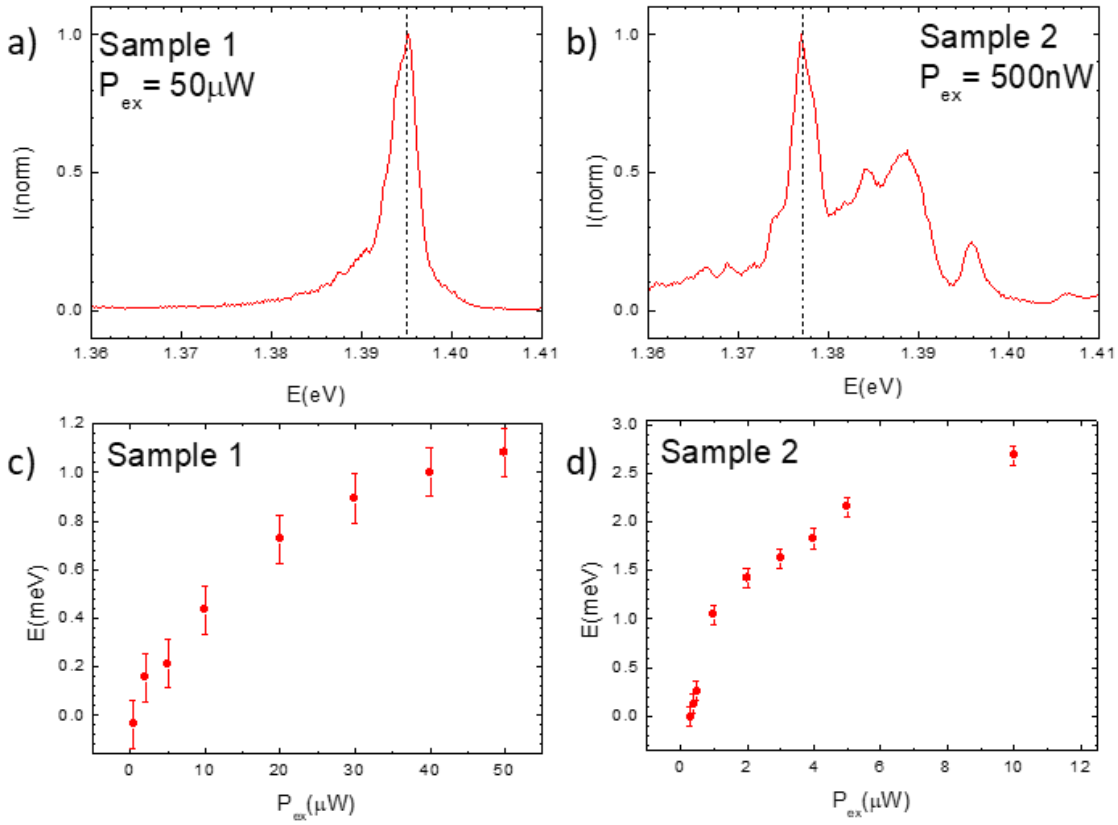

Fig4.2 a) Interlayer exciton spectrum of Sample 1 under an excitation power of P=50 µW. The dashed lines mark the main PL peaks of which the blueshift as a function of the excitation power is plotted in **c). b)** Interlayer exciton spectrum of Sample 2 under an excitation power of P=500 nW. The dashed line marks an auxiliary peak of which the blueshift as a function of the excitation power is plotted in **d)** The error bars in c) and d) correspond to the spectrometer energy resolution.

4.2.2/ Interlayer exciton density estimated from the excitation power.

We will try a crude estimate of the interlayer excitons number created during an experiment. We express Φ the photon flux generated by the excitation source as a function of the excitation power P :

$$\Phi = \frac{P}{h\nu S} = \frac{P}{h\frac{c}{\lambda}\times\pi\times R^2} \qquad Eq(4.1)$$

Where $h\frac{c}{\lambda}$ is the energy of the exciton and S (R) the surface (radius) of the excitation spot. As presented in Chapter 1, the formation of interlayer excitons in TMD heterobilayers is a two-step process. First, intralayer excitons are created in the constituent monolayers, then one particle bound in the intralayer exciton transfers from its original layer to the second monolayer. Thus, $h\nu$ is the energy the laser in resonant excitation condition with the spin "bright" exciton of the $MoSe_2$ or WSe_2 monolayer.

We can thus write Eq(4.1) with numerical factors:

$$\Phi = \frac{P}{6{,}63\times10^{-34}\times\frac{3\times10^{8}}{750\times10^{-9}}\times\pi\times10^{-8}} = P\times 1{,}2\times10^{25}\ \mathrm{cm^{-2}s^{-1}}$$

$$Eq(4.2)$$

We multiply Eq(4.2) by τ the interlayer exciton lifetime to obtain an approximation of the exciton density n_{IX} as a function of the excitation power. The reported measured values in $MoSe2/WSe_2$ encapsulated bilayers [Joe 2019, Nagler 2017] are of the order of a few tens or nanoseconds.

$$n_{IX} = \Phi\times10^{-8} = P\times1{,}2\times10^{17}\mathrm{cm^{-2}} \qquad Eq(4.3)$$

We can thus assume from Eq(4.3) that the exciton density varies between $n_{IX} = 10^{12}\ \mathrm{cm^{-2}}$ at $P = 50\ \mu\mathrm{W}$ and $n_{IX} = 10^{9}\ \mathrm{cm^{-2}}$ at $P = 10\ \mathrm{nW}$. These values are likely to be significant overestimations of n_{IX}, as we have considered that every intralayer exciton forms an interlayer exciton by transfer of its hole in the WSe_2 monolayer which is disproved by the fact that we can observe the photoluminescence spectra of both constituent monolayers on the HBL part of our samples (cf Fig(3.4)). We also have considered that every photon emitted by the excitation source is absorbed by the $MoSe_2$ monolayer which is even more absurd and disproved simply by the fact that we can observe laser backscattered by the sample in the PL spectra. For these reasons, the values of n_{IX} given above should only be seen as conservative upper boundaries of the possible excitation density in our heterostructures while the real values are likely to be a couple of orders of magnitude lower.

We can compare our estimation of n_{IX} to the density of atomic sites available for interlayer recombination n_{site}. We take into account the moiré surface reconstruction evidences presented in [Rosenberger 2020, Weston, Parzefall 2021, Phillips 2021] and consider that the surface of our heterostructures solely consists of homogeneous $+K$ on $-K$ stacked domains while the area covered by the strained borders is negligible. The characteristic length of the reconstructed domains is of a few tens of nanometers The density of atomic sites available for interlayer recombination is thus :

$$n_{site} \sim 10^{12}\ \mathrm{cm}^{-2} \qquad Eq(4.4)$$

The ratio n_{IX}/n_{site} is coherent with the saturation of the PL at high excitation power ($n_{IX}/n_{site} \sim 1$) as well as the lineshape of the PL spectrum at low excitation power ($n_{IX}/n_{site} \ll 1$).

4.2.3/ Interlayer exciton density estimated from the blueshift of the PL spectrum

We will now make a second estimation of n_{IX} from the measured blueshift of the interlayer PL peak by reproducing the reasoning shown in [Nagler 2017, Brotons-Gisbert 2021]. In other words, we will apply the mean field approximation of the repulsive dipole-dipole interaction described in [Laikthman 2009] to the measurement shown in Fig(4.2).

We reverse the "plate capacitor" formula (cf Eq(1.25)) and obtain the expression of n_{IX} as a function of the interlayer PL peak blueshift :

$$n_{IX} = \frac{\Delta E \varepsilon_0 \varepsilon_r}{4\pi e^2 d} \qquad Eq(4.5)$$

Before we apply this formula to our measured shifts, we must make sure that both conditions of the mean field approximation are satisfied. The first condition, relative to the ratio between the dipole-dipole repulsion and the electron-hole attractive interaction is written:

$$n_{IX} d^2 \ll 1 \qquad Eq(4.6)$$

Given that the value of d is of the order of a few angstroms [Phillips 2021], this condition is satisfied even by the overestimated value of n_{IX} calculated from Eq(4.3).

The second condition to the mean field approximation is that the distance between excitons must be large in comparison to the exciton thermal wavelength $\lambda_{th} = \sqrt{\frac{2\pi\hbar^2}{M k_B T}}$ This second condition on n_{IX} is written :

$$n_{IX} {\lambda_{th}}^2 \ll 1 \qquad Eq(4.7)$$

For a temperature of $T = 4{,}5$ K, the thermal wavelength of the interlayer exciton is of the order of $\lambda_{th} \approx 10$ nm, which means that our overestimated value of n_{IX} satisfies both conditions of this mean field approximation. We can thus use Eq(4.5) to get a more realistic estimation the of the interlayer exciton density in our heterostructures. Fig(4.3) shows the values of n_{IX} calculated from Eq(4.5) with ΔE taken from the experimental values shown in Fig(4.2.c and 4.2.d), we have considered $\varepsilon_r \approx 7{,}3$ as the average of the out of plane permittivity of $MoSe_2$ and WSe_2 (values taken from [Laturia 2018]). The calculated values of n_{IX} range between $10^{10}\mathrm{cm}^{-2}$ and $10^{8}\mathrm{cm}^{-2}$ depending on the excitation power which is indeed a couple of orders of magnitude lower than the previous values obtained from Eq(4.3). However it is important to note that Eq(4.5) predicts a linear relation between n_{IX} and ΔE. This should also result in a linear relation between ΔE and the excitation power P which contradicts directly the observation shown in Fig(4.2.c) and Fig(4.2.d).

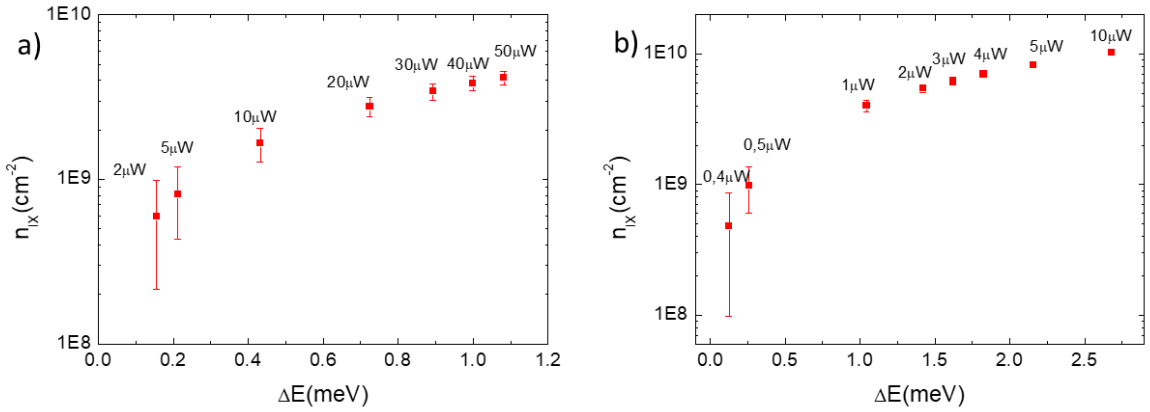

Fig4.3 Interlayer exciton density in **a)** Sample 1 and **b)** Sample 2 as a function of the blueshift shown in Fig(4.2). Each point is indexed by the corresponding excitation power. Error bars are related to the spectrometer energy resolution.

4.2.4 Lineshape changes of the interlayer PL spectrum with the excitation power.

As we have mentioned earlier, the sharp features appearing in the interlayer PL spectra at low excitation power have been presented as single photon emissions [Baek 2020] arising from individual excitons trapped in the moiré potential. Nevertheless, the same considerations apply: the sharp emissions can be seen as arising from individual interlayer excitons isolated in the reconstructed domains. The different emission energy would thus come from the differences of interlayer gap between domains.

Fig(4.4.a) shows a schematic representation of the heterobilayer's surface : considering that the optical power is homogenously distributed in a 1 μm radius spot, the excitation power is distributed among tens of thousands of $+K$ on $-K$ aligned domains each containing thousands of individual recombination sites. After the domain reconstruction, the energy of the interlayer optical gap fluctuates from domain to domain. This means that there are local minima of the optical gap, which are favored sites for exciton recombination. Indeed, pump-probe diffusion experiments presented in [Yuan 2020] show that the characteristic travel distance of interlayer excitons in TMD heterobilayers is of the order of hundreds of nanometers for times close to a nanosecond despite the strained borders of the reconstructed domains, which should act as potential barriers. The lifetime of interlayer excitons being of the order of few nanoseconds in non-encapsulated heterostructures [(Rivera 2017] and a few tens of nanoseconds in encapsulated HBL [Holler 2020] with long lifetime components of hundreds of ns [Miller 2019, Jauregui 2018]. An exciton created in the heterostructure potential can thus move to a local minimum site where its recombination is favorable from an energetic point of view. This is evidenced by the time decay measurement of interlayer excitons in a $MoSe_2/WSe_2$ presented in [Nagler 2017'] which shows that the lower energy components of the interlayer PL peak have a higher lifetime. We propose that the single emissions emerging at low excitation power originates preferentially from these local minima of the interlayer optical gap.

At high excitation power (Fig(4.4.b)), interlayer excitons are formed homogeneously over the surface covered by the excitation spot. The exciton recombinations are spatially homogeneous and the shape of the photoluminescence spectrum resulting from this collective emission reflects the statistical distribution of the value of the interlayer optical gap over the whole

surface of the excitation spot. Interlayer excitons do recombine at local minima of the interlayer optical gap, but the statistical occurrence of these sites is small compared to the overall distribution and the higher lifetime exhibited by these recombination result in a negligible contribution in the intensity of the measured PL spectrum.

At low excitation density (typically below$P = 1\mu W$), interlayer excitons are still created homogeneously over the excitation spot area, they move across the reconstructed domains to recombine at the site with the narrowest optical gaps (Fig(4.4.c)). This enhanced recombination at the local minima of the interlayer gap is the dominant contribution to the photoluminescence spectrum and results in the emergence of sharp individual emissions.

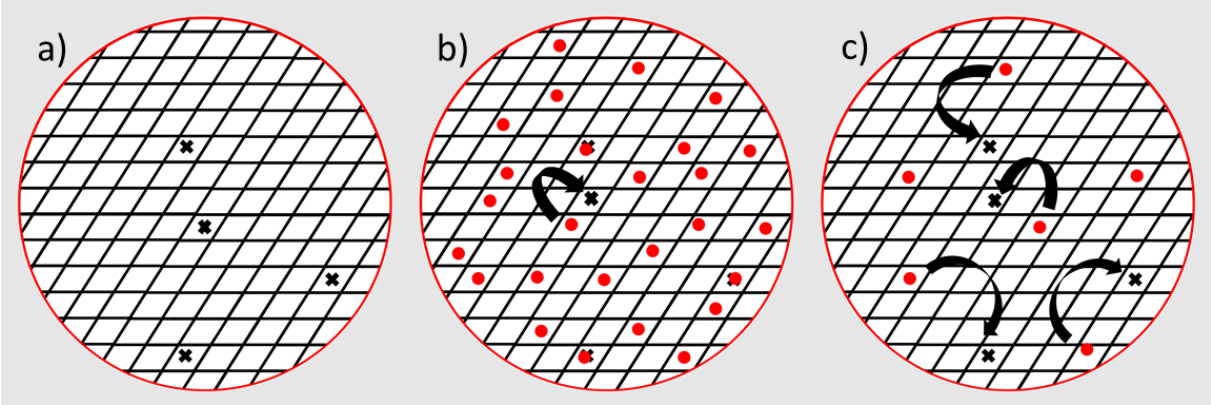

Fig4.4 Schematic of the HBL surface in the area of the excitation spot (red circle) under **a)** no excitation **b)** high excitation power **c)** low excitation power. The black lines picture the borders of the reconstructed domains, the black crosses picture the local interlayer gap minima and the red dots picture the interlayer excitons.

It is unclear if the ability of interlayer excitons to travel across reconstructed domains affects their recombination inside the area of the excitation spot at high excitation power. On one side, favorable recombination sites can be seen as recombination centers around which the local density of interlayer excitons is higher than the average n_{IX}, which would result in the breaking of the mean field approximation and in a higher energy shift of the interlayer excitonic peak than what is predicted in Eq(4.5) due to the exciton-exciton interactions. This is consistent with the non linear dependence of the blueshift with the excitation power shown in Fig(4.2). On the other hand, the repulsive dipole-dipole interaction clearly weights in favor of a spatially homogenous recombination of the interlayer excitons, especially at high n_{IX}. In the absence of results supporting either hypothesis, these are only speculations.

4.3/ Photoluminescence excitation experiment

4.3.1/ General discussion

As discussed in Chapter 1, the formation of interlayer excitons in TMD heterobilayers is a two-step process. First, intralayer excitons are created in the constituent monolayers, then one particle bound in the intralayer exciton transfers from its original layer to the second monolayer. Since, enhancing the formation of intralayer excitons in the constituent monolayers of the heterostructure also enhances the formation of interlayer excitons, we have carried out a

photoluminescence excitation experiment in which we sweep the energy of the excitation source between $E = 1{,}908$ eV ($\lambda = 650$ nm) and $E = 1{,}425$ eV ($\lambda = 870$ nm). We thus tune the excitation energy in resonance with intralayer transitions from the monolayers. In this experiment, the interlayer exciton density is not controlled by the excitation power, which is maintained constant at $P = 50$ µW, but by the absorption of the whole structure. The sample's temperature is maintained constant at $T \sim 4{,}5$ K.

4.3.2/ PLE results

Fig(4.5.a) shows the results of this photoluminescence excitation experiment and displays the interlayer photoluminescence spectrum as a function of the excitation energy. As evidenced by Fig(3.5), the photoluminescence spectrum of the interlayer exciton measured in Sample 2 is composed of two features : a main peak centered on $E = 1{,}395$ eV and a broader emission between $E = 1{,}33$ eV and $E = 1{,}36$ eV attributed to excitons trapped in the strain field of the heterostructure [Kremser 2020]. Fig(4.5.b) and Fig(4.5.c) shows the integrated intensity of these two features as a function of the excitation energy.

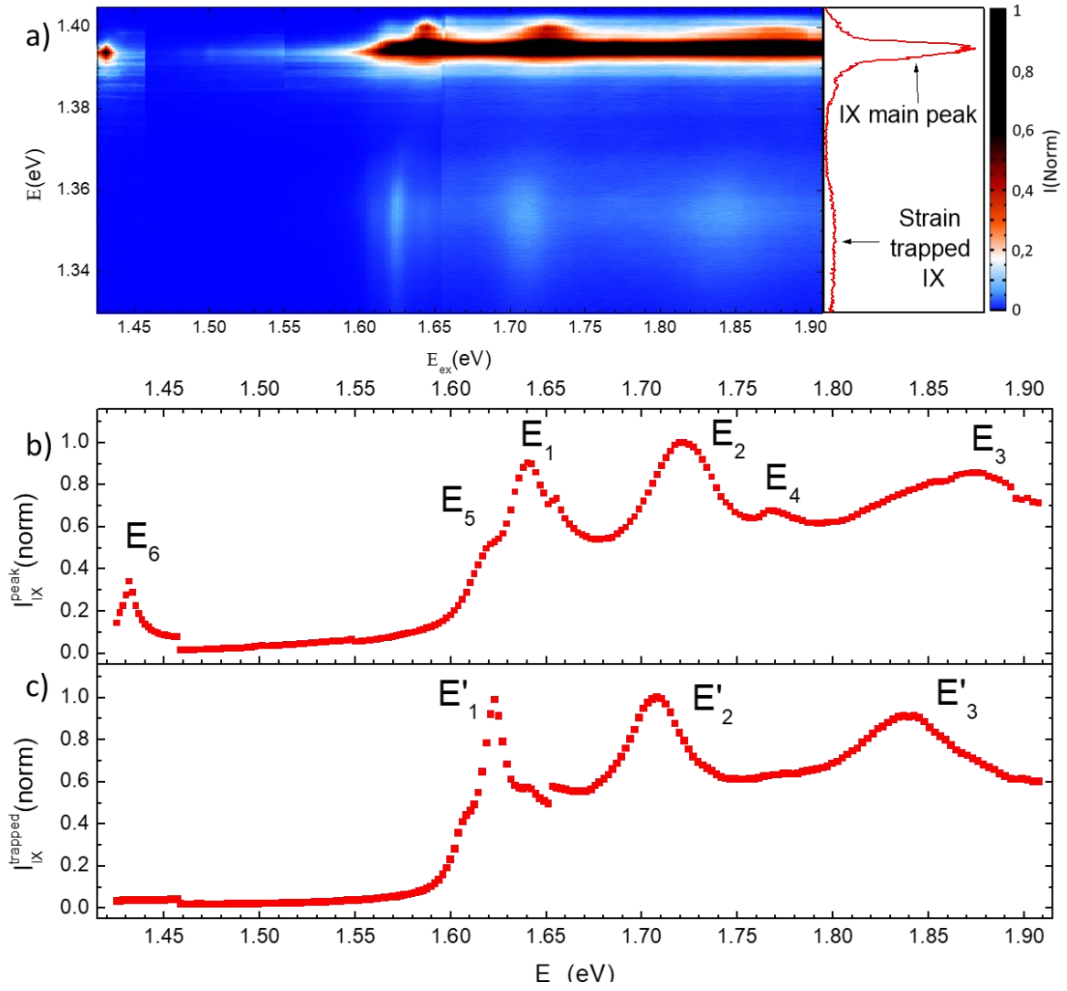

Fig4.5 a) False color map of the intensity of the interlayer exciton PL spectrum as a function of the excitation energy. A Pl spectrum has been added for a better readability. The color scale has been saturated for a better visualization of the low energy behavior. **b)** Integrated intensity of the main interlayer PL peak as a function of the excitation energy. **c)** Integrated intensity of the strain trapped IX as a function of the excitation energy. The resonant features are discussed in the main text.

Fig(4.5.a)) shows the integrated intensity of the main interlayer peak as a function of the excitation energy. The most prominent features on the plot are two peaks at $E_1 = 1{,}642$ eV and $E_2 = 1{,}723$ eV which are characteristic of the energy of "bright" excitonic transitions measured in monolayer $MoSe_2$ [Robert 2020] and WSe_2 [Barbone 2018], both excitations result in an increase of the interlayer exciton intensity by approximately 80% (compared to the intensity of an out of resonance excitation energy $E = 1{,}680$ eV) . Fig(4.7.a) shows the band structure of a $MoSe_2/WSe_2$ heterobilayer aligned with $\theta = 60°$, the transitions corresponding to E_1 and E_2 are represented by black arrows. In the case of the resonance with $MoSe_2$ "bright" exciton, the holes transfer from the $MoSe_2$ valence band to the WSe_2 valence band (grey arrows on Fig(4.7.a)) while in the case of the resonance with WSe_2 "bright" exciton, it is the electrons that transfer from the conduction band of WSe_2 to that of $MoSe_2$ (grey arrows on Fig(4.7.b)).

The curve shown in Fig(4.5.b) also exhibits an increase of the interlayer intensity by 50% for a broad range of excitation energy (between $E = 1{,}833$ eV and $E = 1{,}908$ eV) in which the highest intensity of the interlayer exciton is observed at $E_3 = 1{,}874$ eV (with an out of resonance reference intensity taken at $E = 1{,}680$ eV). It is to be noted that this energy sits between the energies of the "bright" B excitons measured in monolayer $MoSe_2$ $E^B_{MoSe_2} = 1{,}80$ eV in and monolayer WSe_2 $E^B_{WSe_2} = 2{,}1$ eV [Zimmermann 2020]. Finally, the intensity of the interlayer exciton is increased by 10% when the excitation energy is tuned around $E_4 = 1{,}774$ eV, this energy does not correspond to any intralayer transition. The energy difference $E_2 - E_4 = 50 \pm 3$ meV which converts to 400 ± 20 cm^{-1}. This energy corresponds to Raman resonant modes appearing when the excitation energy is tuned in resonance with the energy of the "bright" exciton in WSe_2 ML, more specifically the 3LA*(M)*^{b} mode at 394 cm^{-1} and the A_1'*(M)*+LA*(M)* mode at 398 cm^{-1} [Zhang 2015]. It is to be noted that the resonant feature centered on E_4 spans between $E = 1{,}759 \pm 0{,}003$ eV and $E = 1{,}708 \pm 0{,}003$ eV which converts to an energy difference with E_4 ranging from 296 ± 20 cm^{-1} to 520 ± 20 cm^{-1}. At first sight, this seems excessively broad to correspond to a phonon resonant process (the FWHM of the mode is ~8 cm^{-1}) however, we find a very good overlap between the width of the resonant feature centered on E_4 and the resonance with the "bright" exciton of WSe_2 centered on E_2 (cf Fig(4.6)). We thus propose the following mechanism for the appearance of the resonant feature: when the excitation energy is tuned in the range of E_4, the formation of WSe_2 intralayer excitons is enhanced, as if the excitation energy was in resonance with E_2. This leads to an enhancement of the formation of interlayer excitons and thus to the appearance of the resonant feature on the PLE.

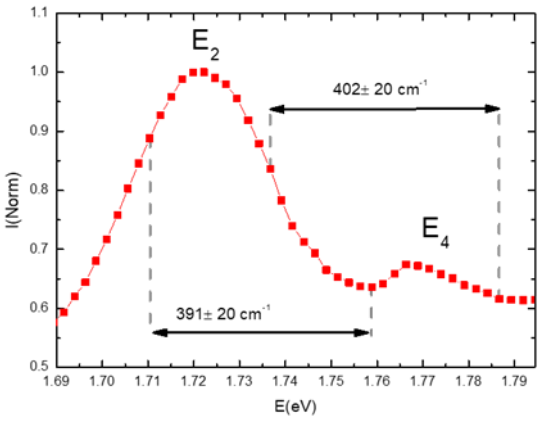

Fig4.6 A comparison between the FWHM of the E_2 resonance and the E_4 resonance reveals that the two features are distant by ~400 cm^{-1}in average.

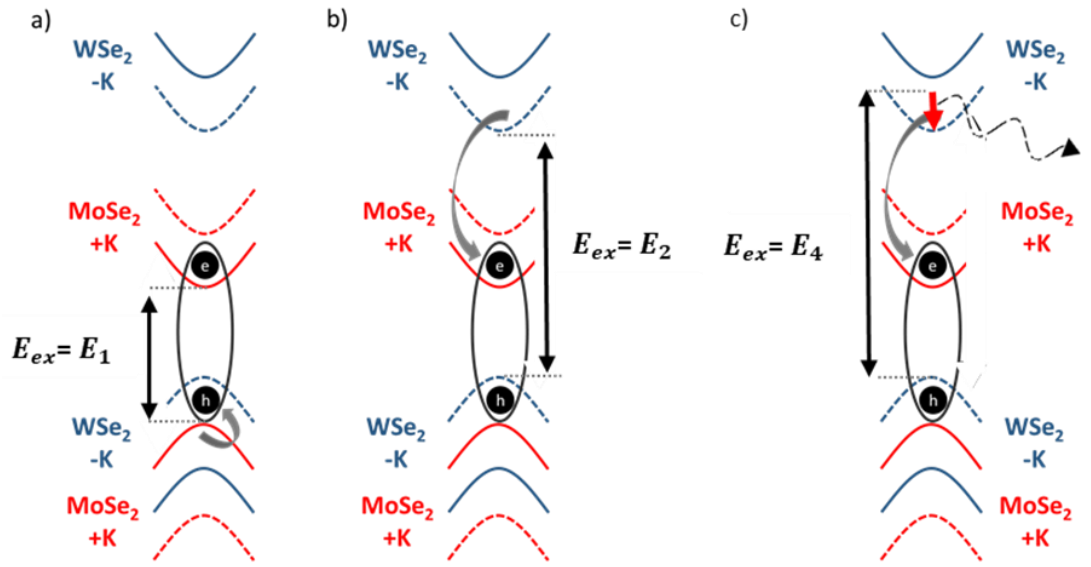

Fig4.7 Band ordering of a 60° aligned WSe2/MoSe2 HBL. The interlayer exciton formation process is enchanced when the excitation energy is tuned in resonance with **a)** the $MoSe_2$ "bright" exciton. The holes relaxes to the top of the valence band, which means it transfers to the WSe_2 layer in the real space. **b)** the WSe_2 "bright" exciton. The electron relaxes to the bottom of the conduction band, which means it transfers to the $MoSe_2$ layer in the real space. The black arrows picture the initial excitation while the grey arrows picture the non-radiative interlayer relaxation. **c)** The electron relaxes to the bottom of the conduction band of WSe2 (red arrow) as if the excitation energy was in resonance with E_2 by phonon emission (dashed arrow). The electron then transfers to the $MoSe_2$ monolayer and forms an interlayer exciton.

Since the interlayer excitons derive from the intralayer populations, we expect a sharp decrease of the interlayer intensity when tuning the excitation energy below the value of the "bright" exciton of monolayer $MoSe_2$, which is the constituent material with the narrowest optical gap. While the interlayer intensity does decrease by 80% between $E_1 = 1{,}642$ eV and $E_{ex} = 1{,}590$ eV, we can see that this diminution is not constant due to the presence of a narrow shoulder centered on $E_5 = 1{,}619$ eV. This energy corresponds to the intralayer trion in monolayer $MoSe_2$ [Robert 2020], there are evidences that optical transitions corresponding to trions can be excited directly albeit in an reduced way compared to the exciton [Chernikov 2014]. Finally, the last feature seen on Fig(4.5.b) is an increase of the interlayer intensity at low excitation energy $E_6 = 1{,}432$ eV, 37 meV above the energy of the probed interlayer emission. In this energy range, it is not possible to create intralayer excitons in the constituent monolayer, therefore the intensity increase of the interlayer exciton must come from the absorption of another interlayer state. [Brotons-Gisbert 2021] and [Wang 2019] show evidences of an interlayer state 30 meV above the interlayer excitonic peak.

Fig(4.5.c) shows the integrated intensity of interlayer broad emission as a function of the excitation energy. The two most prominent features on the plot are the peaks at $E_1' = 1{,}623$ eV and $E_2' = 1{,}708$ eV with an increase of the interlayer intensity for a broad range of excitation energy (between $E = 1{,}809$ eV and $E = 1{,}882$ eV) centered on $E_3' = 1{,}839$ eV. The low energy broad emission does not show any resonance near E_4 and E_6. The origin of these three resonant features is not fully understood : the energy delta $E_1 - E_1' = 19$ meV, $E_2 -$

$E_2' = 15$ meV and $E_3 - E_3' = 35$ meV are all different and do not correspond to the energy separation between the main interlayer exciton peak and the broader low energy emission $E_{peak} - E_{broad} \approx 50$ meV. Furthermore, they cannot be explained by phonon resonances since their energy position lies below resonant energies of the main interlayer peak. The explanation for this shift of the resonant energy is still debated.

4.3.3/ Excitation energy and exciton density

Fig(4.8) compares two interlayer exciton spectra measured with the same excitation power $P = 50\mu W$: the first one is measured with an excitation energy $E_{ex} = E_3 = 1{,}74$ eV in resonance with the intralayer WSe_2 exciton, the second one is measured while the excitation energy is tuned below both intralayer gaps at $E_{ex} = 1{,}45$ eV. Interestingly, the shape of this interlayer spectrum is reminiscent of the one measured at low excitation power as many sharp individual emissions can be resolved separately (cf Fig(4.1)) despite the fact that the excitation power is maintained constant at $P = 50$ µW. As we explained previously, this is because the interlayer exciton density is driven by the absorption of the heterobilayer. In other words : while the exciton density that can be created by the excitation beam is almost constant (it varies between $n_{IX} = 5{,}5 \times 10^{12}$ cm^{-2} for $\lambda_{ex} = 650$ nm and $n_{IX} = 7{,}5 \times 10^{12}$ cm^{-2} for $\lambda_{ex} = 870$ nm, values estimated from Eq(4.1)), the creation of interlayer excitons is limited by the capacity of the heterostructure to absorb the excitation photons and convert them into IXs. This is directly visible on Fig(4.9.a) showing the energy position of the main interlayer peak (fitted from the data shown in Fig(4.5.a)) as a function of the excitation energy. Note that the plots shown in Fig(4.9.a) and Fig(4.5.b) are remarkably similar, it is even possible to identify the resonant features at the same energy positions, including the feature centered on E_4 and E_5. We extract the energy shift of the main interlayer exciton peak from Fig(4.5.a) taking the lowest energy position as a baseline ($E_{peak} = 1{,}390$ eV for an excitation energy of $E_{ex} = 1{,}448$ eV) and we apply Eq(4.5) to obtain an estimation of n_{IX} as a function of the excitation energy. This dependency is presented in Fig(4.9.b) and shows that n_{IX} vary between 10^{10} cm^{-2} and 10^{8} cm^{-2} which is consistent with the values presented in Fig(4.3).

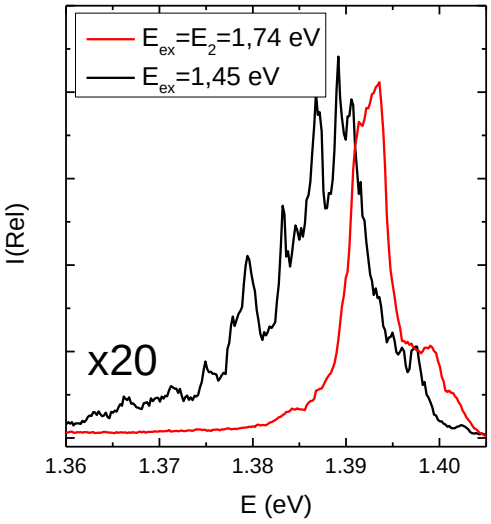

Fig4.8 Interlayer excitons PL spectra measured with an excitation energy in resonance with the "bright" exciton of WSe2 (red curve) and with an excitation out of resonance (black curve). The excitation power is $P = 50\,\mu W$ in both cases. The differences of lineshape and blueshift of the IX energy is reminiscent from the power dependency data shown in Fig(4.1). The intensity has been normalized by the acquisition time.

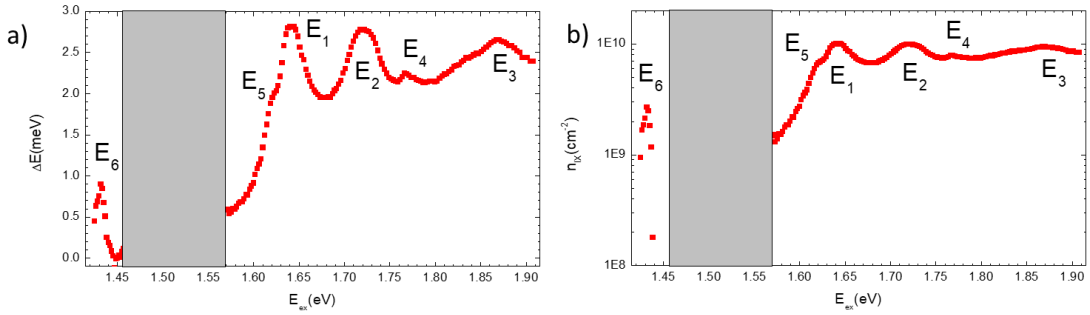

Fig4.9 a) Blueshift of the interlayer Pl peak as a function of the excitation energy. The positions of the peaks have been obtained by fitting the data of Fig(4.5). **b)** Interlayer exciton density obtained by applying Eq(4.5) to the values shown in a). In the greyed out areas, the PL intensity of the interlayer peak is too low to be fitted properly.

4.4/ Magneto-photoluminescence experiment

4.4.1/ General discussion

In the preceding chapter, we have characterized the magneto-optical properties of Sample 1 and of Sample 2 using our superconductive coil to apply a magnetic field up to $= 14$ T . We have observed that the σ+ and σ- polarized components of the interlayer exciton shift toward lower and higher energies, respectively, which results in a negative g-factor. While this behavior is similar to that observed in monolayer TMDs, the magnitude of the shift is much higher in the case of the interlayer exciton shifts at a rate of $0{,}472 \pm 0{,}004\ \mathrm{meV.T^{-1}}$ for Sample 1 and $0{,}463 \pm 0{,}004\ \mathrm{meV.T^{-1}}$ for Sample 2, which corresponds to g-factors of $g = -16{,}310 \pm 0{,}138$ and $g = -15{,}999 \pm 0{,}138$, respectively. In order to monitor the behavior of the interlayer exciton PL spectrum in extreme magnetic fields, we have performed magneto-photoluminescence experiments at high magnetic field using the LNCMI-Grenoble resistive magnet to apply magnetic field up to $B = 29$ T on both samples. The temperature of the samples is $T = 4{,}5$ K and we have used an excitation source with a power of $P = 40$ µW and an excitation wavelength of $\lambda = 514$ nm .

4.4.2/ Results description

Fig(4.10) shows the results of these measurements for Sample 1 and Samples 2 : as we have explained in Chapter 2, we use polarizing optics to collect the emission of a single valley and calculate the g factor from the energy positions of its emission for opposite values of the magnetic field. Thus, in the following figures, a positive magnetic field corresponds to the σ+ polarized component while a negative field corresponds to a σ- polarized component. We sweep the magnetic field between $B = -28$ T and $B = 28$ T, and fit the observed linear shift of the interlayer exciton energy. The magnitude of the shift is $0{,}466 \pm 0{,}004\ \mathrm{meV.T^{-1}}$ for Sample 1 and $0{,}457 \pm 0{,}004\ \mathrm{meV.T^{-1}}$ for Sample 2 which correspond to g-factors of $16{,}118 \pm 0{,}138$ and $15{,}781 \pm 0{,}138$.

While the evolution of the intensity position is linear up to highest values of the magnetic field, the intensity of the two circularly polarized emissions are non-monotonic and show an anomaly

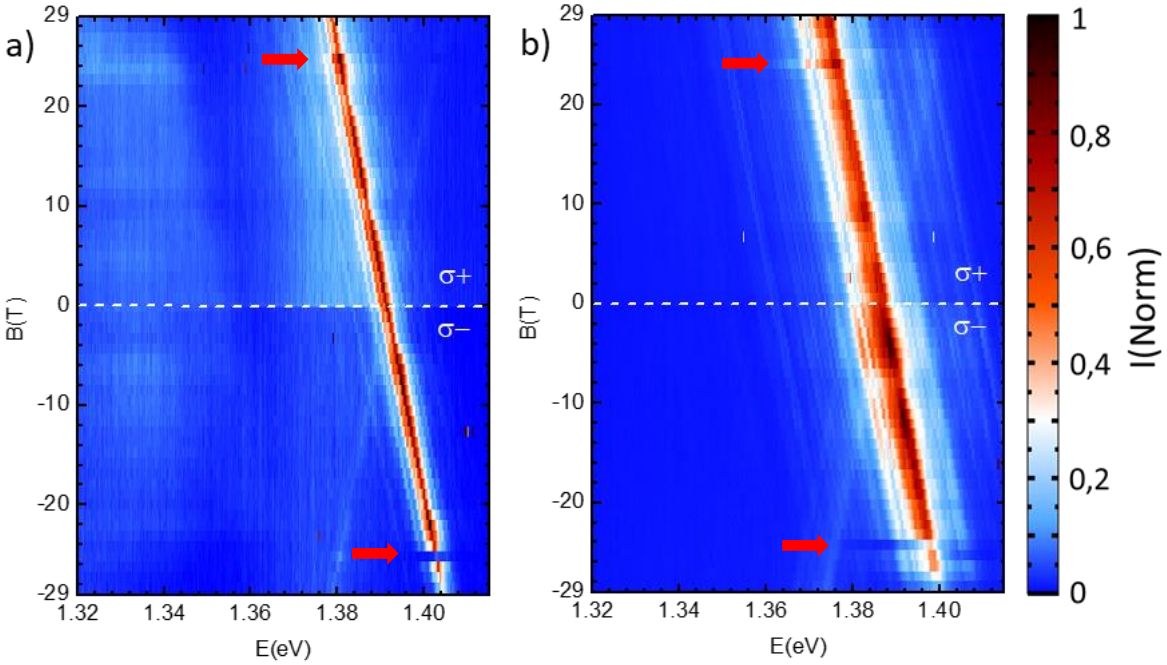

Fig4.10 Magneto-PL of the interlayer exciton measured in **a)** Sample1 **b)** Sample 2.The magnetic field is swept between $B = 29$ T B $= -29$ T with a step of 0,5 T. The temperature of the samples is $T = 4{,}5$ K and with use an excitation source with a power of $P = 40$ μW and an excitation energy of $= 514$ nm . The dashed line show which circular polarization is equivalent to the shift. The red arrows show the intensity anomalies discussed in the main text.

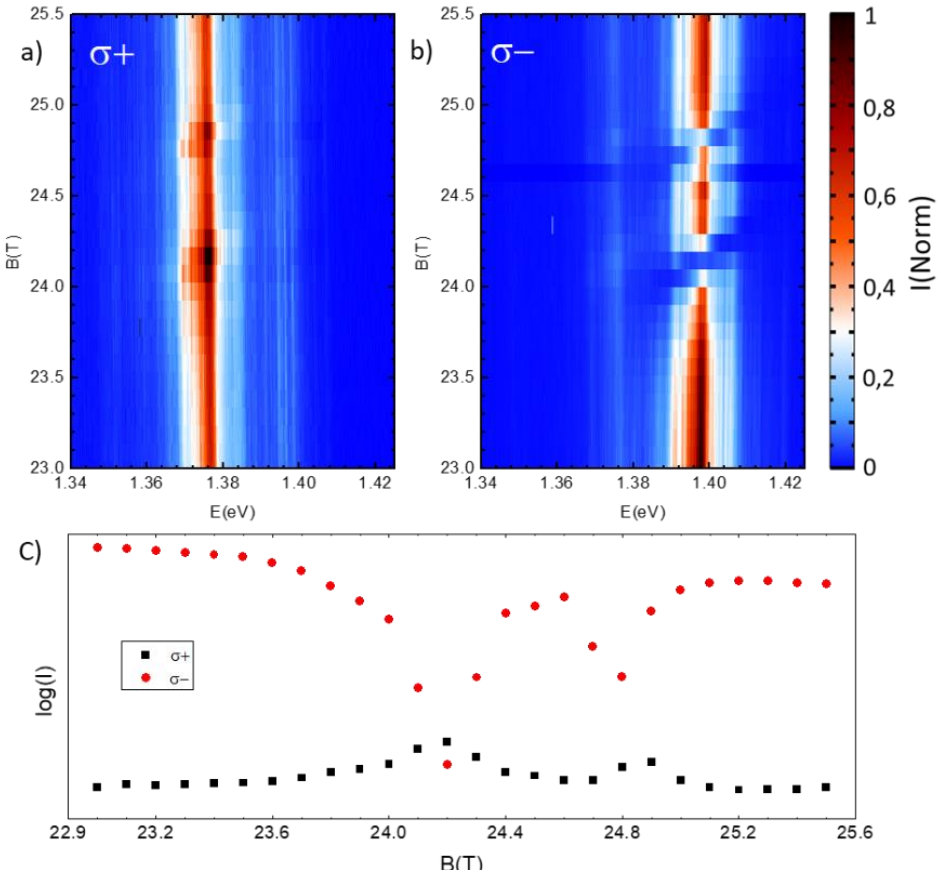

Fig4.11 **a)** False color map of the σ+ polarized interlayer component measured in Sample 2 **b)** False color map of the σ- polarized interlayer component measured in Sample 2. The magnetic field is swept from $|B| = 23$ T to $|B| = 25{,}5$ T with a resolution of 0,1 T. c) Integrated intensity of the σ+ and σ- polarized interlayer components highlighting the coincidental nature of the intensity anomalies. Intensities are extracted from a) and b)

for $B = -24$ T for which the IX peak of the σ- polarized component collapses to near zero while we observe a rise of the intensity of the σ+ polarized component for $B = +24$ T. This anomaly is consistently observed on Sample 1 and on Sample 2 across multiple sweeps of the magnetic field and is has been previously described in [Nagler 2017] as a level crossing of the conduction bands of $MoSe_2$. However, scanning the magnetic field in this area with a higher resolution (0.1 T) reveals the presence of a second magnetic field resonant phenomenon, at $B = 24{,}6$ T (cf Fig(4.11.a) and Fig(4.11.b)). These changes of intensity take place across a very small range of magnetic field: they span a few hundreds of mT after which the intensity of both components comes back to its original value. This is why the second resonance at $B = 24{,}6$ T is not visible in Fig(4.10) : our resolution is simply too low to resolve it. Fig(4.11.c) presents the integrated intensity of the two oppositely polarized interlayer components in this range of magnetic field and shows that the rise of the σ+ component and the intensity collapse of the σ- polarized component occur precisely at the same value of the magnetic field.

4.4.3/ Interlayer exciton resonance profile.

We increase further the magnetic field resolution to 0,01 T to obtain the precise profile of these resonances, Fig(4.12) shows the high resolution profiles for Sample 1 and Sample 2. Note that the x axis represents the absolute value of the magnetic field and that the colormaps are separated by a dashed line. In this figure, the spectra shown on the σ- side of the dashed line have been measured with $B < 0$ and the spectra on the σ+ side have been measured with $B > 0$, we have then joined both color maps for an easier visualization of the simultaneous changes of intensity.

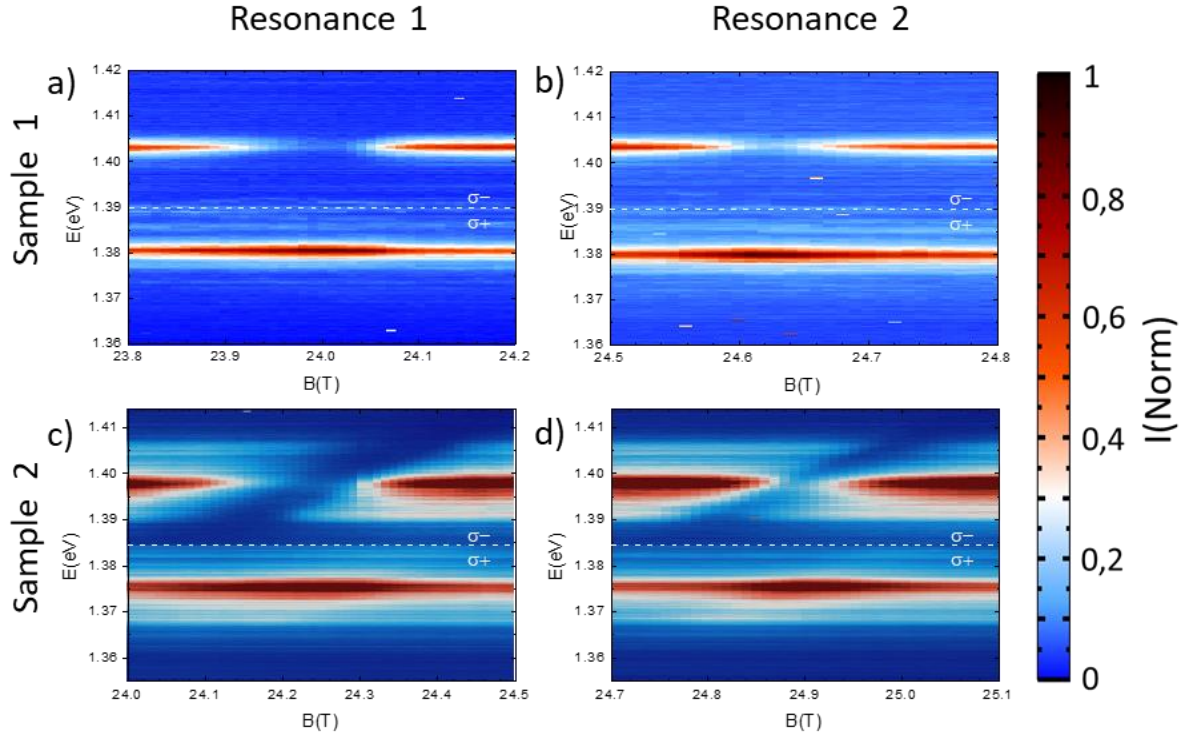

Fig4.12 a) False color map of the σ+ and σ- polarized interlayer components measured **a)** in Sample 1 in the range of magnetic field corresponding to the first resonance. **b)** in Sample 1 in the range of magnetic field corresponding to the second resonance. **c)** in Sample 2 in the range of magnetic field corresponding to the first resonance. **d)** in Sample 2 in the range of magnetic field corresponding to the second resonance. The field resolution is 0,01 T.The white dashed lines separates the σ+ polarized emission acquired at positive magnetic field from the σ- polarized emission acquired at negative magnetic field.

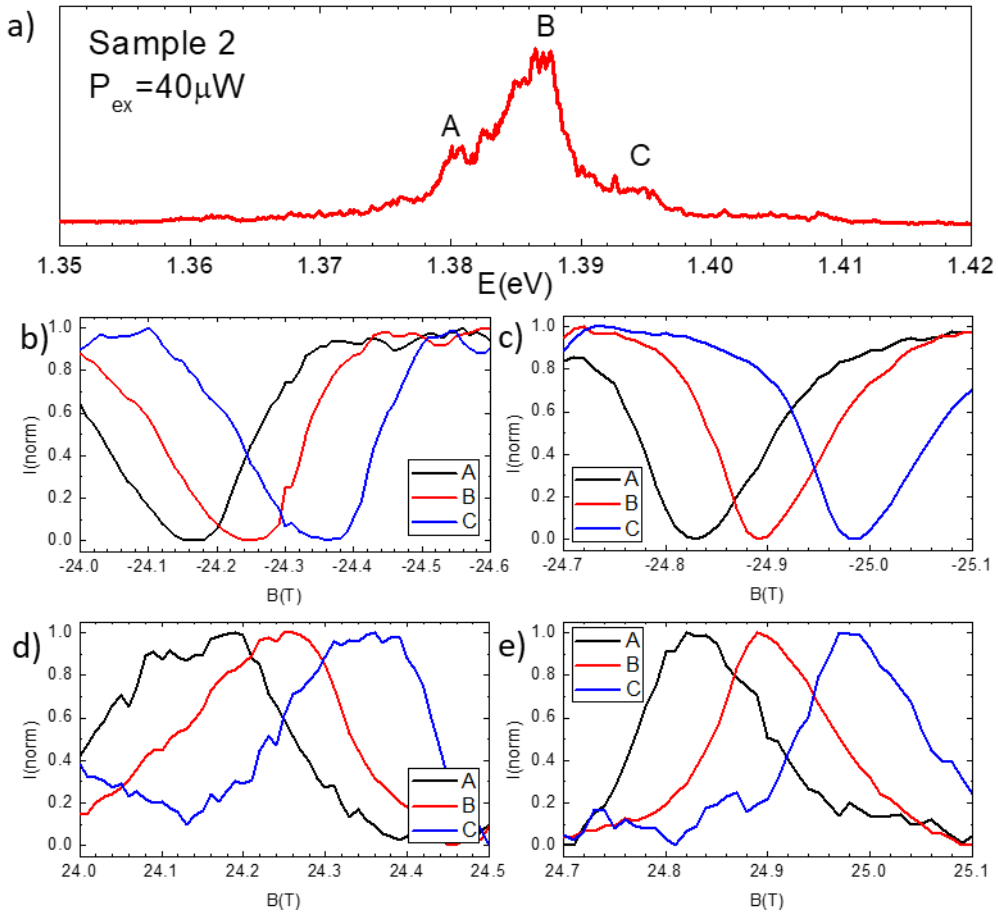

Fig4.13 a) Interlayer photoluminescence spectrum measured on Sample 2 with an excitation power of $P = 40$ µW. Three features contributing to the spectrum have been indexed Integrated intensity of the three features indexed in a) as a function of the magnetic field. Intensity extracted from the σ- polarized data shown in **b)** Fig(4.12.c) σ-. **c)** Fig(4.12.d) σ-. **d)** Fig(4.12.c) σ+. **e)** Fig(4.12.d) σ+.

In the case of Sample 2, the extinction of the σ- polarized component is not homogeneous across the interlayer exciton spectrum but presents a "diagonal" profile. As an illustration, Fig(4.13.a) shows the interlayer photoluminescence spectrum of Sample 2 at $B = 0$ T. The emission spans over 14 meV and can roughly be decomposed into three features A,B and C : the first feature is centered on $E_A = 1{,}380$ eV, the second is centered on $E_B = 1{,}387$ eV and the third one is centered on $E_C = 1{,}394$ eV.

Fig(4.13.b to 4.13.e) shows the integrated intensity of these three features extracted from the data presented in Fig(4.12.c and 4.12.d). For the σ- polarized emission, the minimum of intensity of the three features does not occurs for the same value of the magnetic field. The feature A, centered at the lowest energy, vanishes for a smaller value of the magnetic field than the feature B, which in turn resonates at a smaller magnetic field than the higher energy feature C. This behavior is also observed in the raise of the intensity of the σ+ polarized emission (cf Fig(4.13.d and 4.13.e)). In other words, the lower the energy of a feature is, the lower its resonant field. This example only considers three different energies, but the "diagonal" profiles presented in Fig(4.12.c and 4.12.d) show clearly that this behavior is continuous over the whole

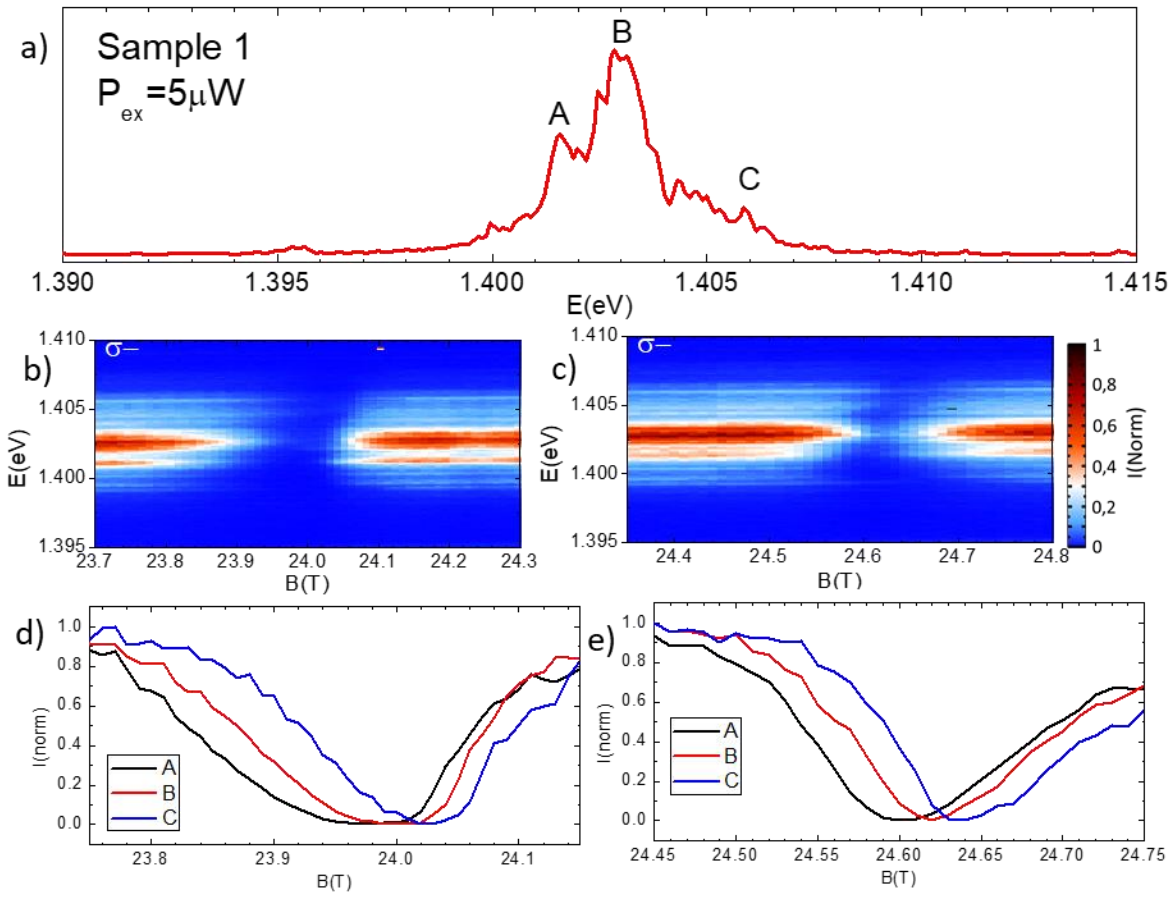

Fig4.14 a) Interlayer photoluminescence spectrum measured on Sample 1 with an excitation power of $P = 5\mu W$. Three features contributing to the spectrum have been indexed. False color map of the σ+ and σ- polarized interlayer component measured **b)** in Sample 1 in the range of magnetic field corresponding to the first resonance. **c)** in Sample 1 in the range of magnetic field corresponding to the second resonance. **d)** Integrated intensity of the three features as a function of the magnetic field. Values are extracted from the σ- polarized data shown in b). **e)** Integrated intensity of the three features as a function of the magnetic field. Values are extracted from the σ- polarized data shown in c).

width of the interlayer exciton, which means that it affects the individual emissions contributing collectively to the interlayer photoluminescence spectrum.

In the case of Sample 1, the width of the exciton is lower (~4 meV) and we lack the spectral resolution to see any "diagonal" profile. In order to broaden the interlayer exciton emission to potentially observe a behavior comparable to the one observed in Sample 2, we have decreased the excitonic power to $P = 5$ μW. We then apply the same method used in Fig(4.13) to extract the intensity profiles of three different features and observe the same correlation between the energy of the feature and the value of the resonant magnetic field, these data are presented in Fig(4.14). The origin of the resonant phenomena as well as the analysis of the "diagonal" shape of the intensity profiles are the main results of the work presented in this PhD and will be discussed in more details in the following chapter.

4.5/ Conclusion

In this chapter, we have presented the main results obtained on $MoSe_2/WSe_2$ heterobilayers samples aligned with $\theta = 60°$. We have shown the results of a power dependence measurement in which we have tuned the power of the excitation source over three orders of magnitude, from $P = 50$ µW to $P = 10$ nW. This allowed us to highlight the influence of the surface excitonic density over the shape the interlayer photoluminescence spectrum, to visualize the repulsive exciton-exciton interaction presented in [Nagler 2017, Brotons-Gisbert 2021] and to propose an explanation for the individual meV sharp emissions arising at low excitonic density that do not rely on the moiré supercell theory. We have then shown the results of a photoluminescence excitation experiment carried on Sample 1 in which the excitation energy has been tuned between $\lambda = 650$ nm and $= 870$ nm . We have measured an increase of the intensity of the main excitonic peak when the excitation energy is tuned in resonance with the "bright" A excitons of the constituent monolayers as well as possible resonances with the "bright" B excitons. We have observed what seems to be a resonance with the trion complex of the $MoSe_2$ as well as a resonant enhancement of the interlayer process via phonon emission in the WSe_2 monolayer. We have also visualized evidences of a second interlayer state lying 30 meV above the energy of the interlayer exciton. These results show that the intensity of the low energy broad emission that we have attributed to excitons trapped in the strain field of the heterostructure increase for excitation energies that are different detunes from the resonant energies of the main interlayer excitonic peak. At this time, the origin of this detuning is still unknown. Finally, this photoluminescence excitation experiment shows a strong correlation between the energy position of the interlayer peak and the intensity of the emission, which is directly dependent on the excitonic density. Lastly, we carried out a series of magneto-photoluminescence experiments to observe the behaviour of the interlayer excitons under a high magnetic field. We have measured magnetic field resonant anomalies in the intensity of the σ+ and σ- polarized interlayer emissions than can only be visualized a high magnetic field (around $B = 24$ T) swept at a very low resolution (0,01 T). These phenomena have been consistently reproduced across both samples and show a correlation between the energy of the individual emissions contributing collectively to the interlayer photoluminescence spectrum and the value of the resonant field.

Chapter 5: Optical selection rules and g-factors in TMD heterobilayers

5.1/ Introduction:

Before we start any discussion on the results presented in the previous chapter, it is capital that we identify the recombination path of the interlayer exciton measured in our samples. While previous works established that the electrons and holes forming the interlayer excitons were respectively hosted in the $MoSe_2$ and WSe_2 monolayers [Yu 2015], discussion about the sub-bands involved in the interlayer excitons recombination is recent [Brotons-Gisbert 2021]. This is because the prerequisite to the identification of the interlayer exciton recombination path is to know the value of the twist angle θ between the two constituent monolayers. The evidences of surface reconstruction presented in [Rosenberger 2020, Weston 2021, Phillips 2021] reinforce the determinant character on θ while [Parzifal 2021] have shown that the surface reconstruction is a necessary condition for interlayer exciton formation. Thus, we consider that our heterostructures are uniformly stacked in the configuration that is the most energy favorable, which directly depends of θ. The two notable values of θ are 0° and 60° corresponding respectively to +K/+K and +K/-K valley alignment, which reverses the spin ordering of the valence band. This means that in the case of heterostructures aligned with θ=0°, the lowest energy recombination path is the spin singlet state (i.e. recombination involves sub-bands with the same spin index) while in 60° aligned heterobilayers it is a spin triplet state (sub-bands with a different spin index).

As explained in Chapter 1, the Zeeman shift of the exciton, described by the g factor, results from the relative energy shift of the electronic band structure by a magnetic field B. In the 2019 paper [Seyler], the authors use Second Harmonic Generation to estimate the value of θ. They perform magneto-photoluminescence experiments using resonant excitation and observe different magnitudes between the Zeeman shifts of interlayer excitons emitted from heterobilayers aligned with θ=0° and θ=60° (respectively 0,18 and 0,50 $meVT^{-1}$) corresponding to g factors of $g_{\theta=0°} = +6{,}7$ and $g_{\theta=60°} = -16$. We have determined the alignment of our own samples by comparing the observed Zeeman effect to these two values and established that our heterobilayers were aligned with θ=60°. In this chapter, we want to make the point that together with the excitation energy, the g factor is the key to the identification of the interlayer exciton transition, and more generally to any excitonic recombination in TMDs. The sign and magnitude of the g factor are characteristic of the recombination path and they are the only information needed to identify the sub-bands involved in the interlayer exciton emission. We will present a simplified model allowing us to estimate the g factor of different transitions in heterobilayers based on experimental observations made in WSe_2 and $MoSe_2$ monolayers. This will allow us to identify the recombination path of the interlayer excitons observed in Sample 1 and Sample 2.

5.2/Estimation of the different contributions to the g factor

5.2.1/ General discussion

The action of the magnetic field on the energy of the bands involved in excitonic recombination is considered as the addition of two contributions: g_s the spin contribution and g_d the orbital contribution, which describes the magnetic moment of a particle in this sub-band. In theory, these parameters take different values for every sub-bands of the electronic band structure and depend of the considered material. We would like however to detail a simplified model with simple estimations of these two parameters based on experimental observations made in WSe_2 and $MoSe_2$ monolayers.

First, we consider that g_s and g_d take the same value in $MoSe_2$ and WSe_2 : both of these materials are formed of the same chalchogen Se and a metallic atoms from the sixth column of the periodic table and their "bright" exciton has the same g factor $g = -4$ [Kopersky 2018]. This consideration can also be extended to other TMDs: the "bright" exciton in monolayer WS_2 also shifts with the magnetic field with $= -4$. MoS_2 however cannot be considered from this perspective as it has been shown that the Zeeman shift of the "bright" exciton in monolayer MoS_2 is smaller (a value of $g = -2$ is reported in [Koperski2018] and can strongly depend on the carrier concentration even at low residual doping [Klein 2021] .

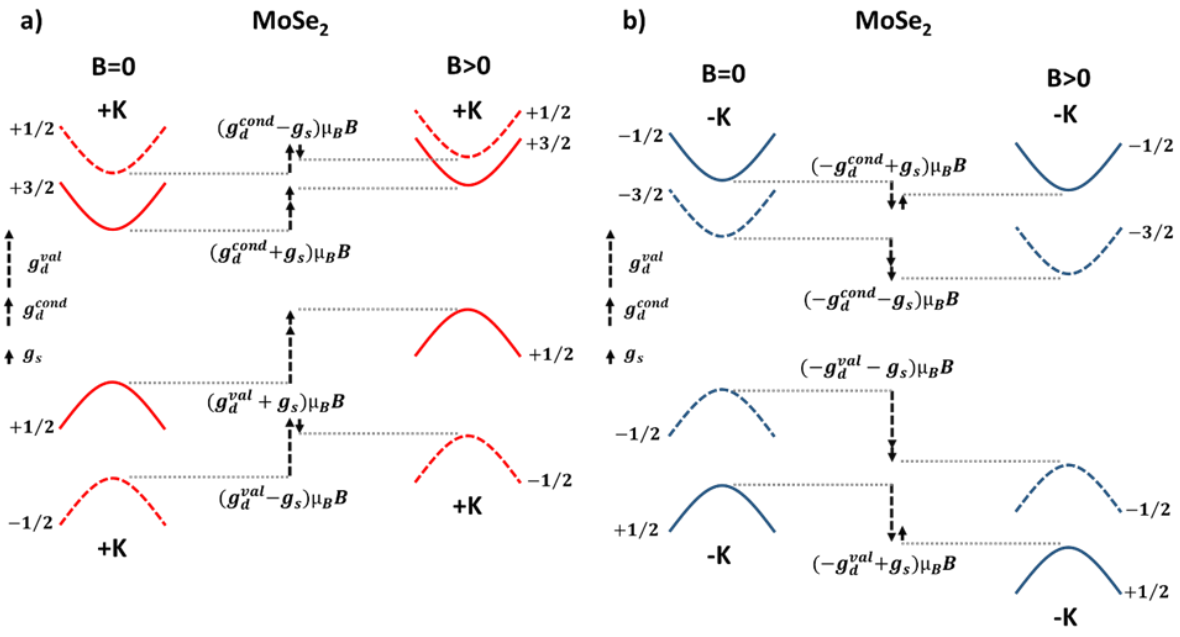

Fig5.1 Shift of the band structure of $MoSe_2$ with the magnetic field B **a)** in the valley +K **b)** in the valley -K Spin-down sub-bands in the +K valley are shown as red dashed lines (spin-up sub-bands as red plain lines). Spin-down sub-bands in the -K valley are shown as blue dashed lines (spin-up sub-bands as blue plain lines) Each sub-band is indexed by its angular momentum J_z. The contribution of g_d and g_s to the energy shift of the bands are represented by the black arrows (cf legend). The shift of each band is written in eV as a function of the magnetic field B(T). Shift of the band structure of $MoSe_2$ with the magnetic field B in the valley -K. Optical gaps and conduction/valence band splitting energies are not up to scale.

Secondly, we consider that the two contributions g_s and g_d are independent of each other. In other words: in a given valley (+K for example), g_s is only dependent of the spin index of the sub-band. This means that g_s can only take two different values: one in spin up bands g_s^{up} and one in spin down bands g_s^{down} while g_d, the orbital contribution, is independent of the spin. Thus, g_d also takes two different values: one in the conduction band g_c^{cond} and the other for the valence band g_c^{val}. As mentioned in Chapter 1, +K and –K valley transform into each other by time reversal symmetry. This symmetry flips the spin index of the sub-bands, which implies:

$$g_s^{up} = -g_s^{down} = g_s \qquad Eq(5.1)$$

In the presence of a magnetic field, the time reversal symmetry is broken and the energy of the bands at the two valleys +K and –K shifts, respectively towards the low and high energies. Fig(5.1) shows the shift of the band structure at the +K and –K valleys of monolayer $MoSe_2$. Each sub-band is indexed with the angular momentum quantity J_z and the value of the energy shift as a function of g_s and g_d. These values are independent of the spin orbit splitting which mean that they also apply for WSe_2, the only difference being the spin ordering of the conduction sub-bands at +K and –K. As mentioned previously, our estimates of g_s and g_d are based on experimental observations in WSe_2 and $MoSe_2$ monolayers. Indeed, cross-examining the g factor of the different recombination paths allows us to separate the contributions of g_s and g_d to the g factor and obtain approximated but robust estimations of the two parameters. It is to be noted that we will use the formalism introduced by Fig(5.1) all along this chapter : spin up/down sub-bands will be represented with plain/dashed lines and the band structure of a +K/-K valley will be pictures with red/blue line. We will index each sub-bands by their angular momentum J_z and by their shift in energy as a function of $\mu_B B$.

5.2.2/ Estimation of the orbital contribution g_d

Contrarily to the spin factor, which only contributes to the g-factor in the case of spin "dark" optical transitions, the orbital factor g_d always contributes to the g factor regardless of the recombination path since excitonic recombinations involve by definition a conduction and a valence sub-band. The two values of the orbital parameter g_d^{cond} and g_d^{val} are estimated by comparing the g factor of two different recombination paths in the monolayer: the spin singlet state ("bright exciton"), which has been measured many times in both $MoSe_2$ and WSe_2 monolayers [Koperski 2018], and the spin "bright" intervalley exciton, which recombines by interacting with phonon mode and has been measured in monolayer WSe_2 [He 2020]. These two recombination paths have already been presented in Chapter 1 but we will consider them in the context of this simplified model : the two g factors are equivalent to a set of two equations with g_d^{cond} and g_d^{val} as parameters .

First, let us consider the spin bright exciton recombination in $MoSe_2$ and WSe_2 monolayers. These two materials have been studied extensively and we will consider that $g_{bright}^{MoSe_2} = g_{bright}^{WSe_2} = g_{bright}^{ML} = -4$. A negative value of g_{bright}^{ML} means that $E_{bright}^{ML}(\sigma+)$, the σ+ polarized component emission from the TMD +K valley shifts from its original energy E_0 toward lower energy with the magnetic field. Conversely, $E_{bright}^{ML}(\sigma-)$ the σ- polarized

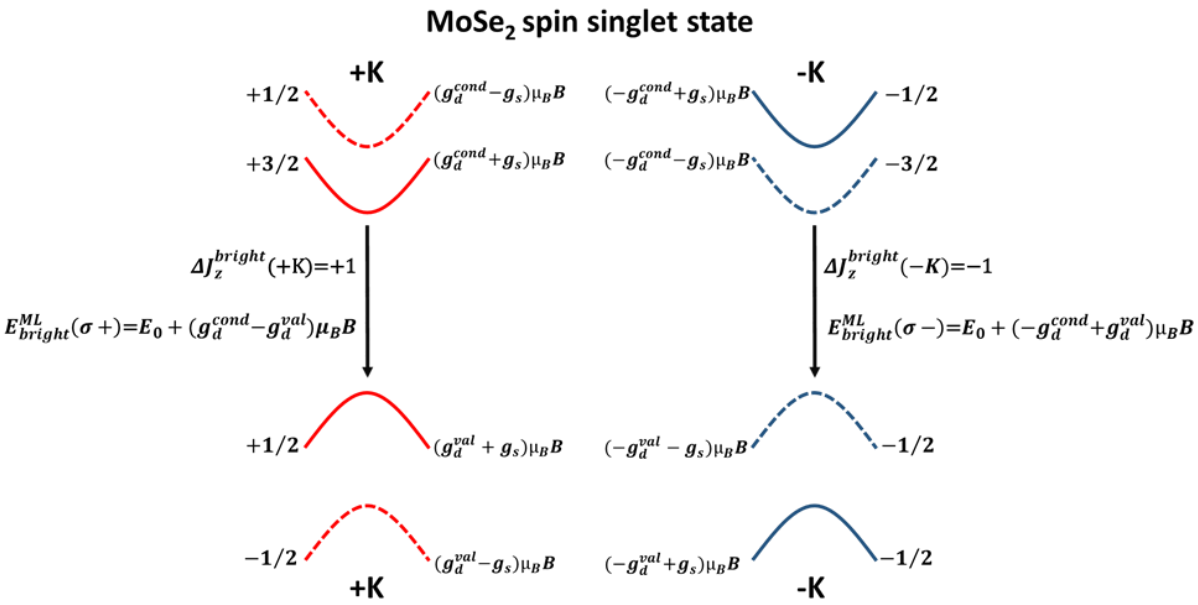

Fig5.2 Band structure of monolayer $MoSe_2$ at +K and –K valleys. Black arrows represent the recombination path of the spin singlet state. The recombination path at +K/-K point is indexed with the change of angular momentum $\Delta J_z^{bright}(\pm K)$ and the energy $E_{bright}^{ML}(\sigma\pm)$ of the photon emitted by the exciton recombination.

component emission from the TMD +K valley, shifts toward higher energy. According to Eq(1.19), the g factor is defined as:

$$E_{bright}^{ML}(\sigma+) - E_{bright}^{ML}(\sigma-) = g_{bright}^{ML}\mu_B B = -4\mu_B B \qquad Eq(5.2)$$

Fig(5.2) shows the zero field band ordering at K and –K points of $MoSe_2$, the relative movement of the bands with the magnetic field is written next to each sub-band as a multiple of $\mu_B B$. The sub-bands are indexed by their angular momentum J_z , defined modulo 3, and their energy shifts as a function of the magnetic field B(T). The "bright" exciton recombination path at $\pm K$ point is marked as a black arrow and indexed with the change of angular momentum $\Delta J_z^{bright}(\pm K)$ and the energy $E_{bright}^{ML}(\sigma\pm)$ of the photon emitted during the exciton recombination. Since the bright exciton recombination involves sub-bands of the same spin, only g_d contributes to the g factor, we can thus establish:

$$E_{bright}^{ML}(\sigma\pm) = E_0 \pm (g_d^{cond} - g_d^{val})\mu_B B \qquad Eq(5.3)$$

The expression of the g factor is written as:

$$g_{bright}^{ML} = \frac{E_{bright}^{ML}(\sigma+) - E_{bright}^{ML}(\sigma-)}{\mu_B B} = 2g_d^{cond} - 2g_d^{val} = -4 \qquad Eq(5.4)$$

We consider now the WSe_2 intervalley transition as presented in [He 2020]. Here, the electron switches valley by the emission of a phonon with a $PAM = \pm 1$. Fig(5.3) shows the band ordering of monolayer WSe_2 at the +K and –K valleys, the valley transfer are represented as dashed arrows, and the intervalley recombination path by black arrows. Otherwise, the

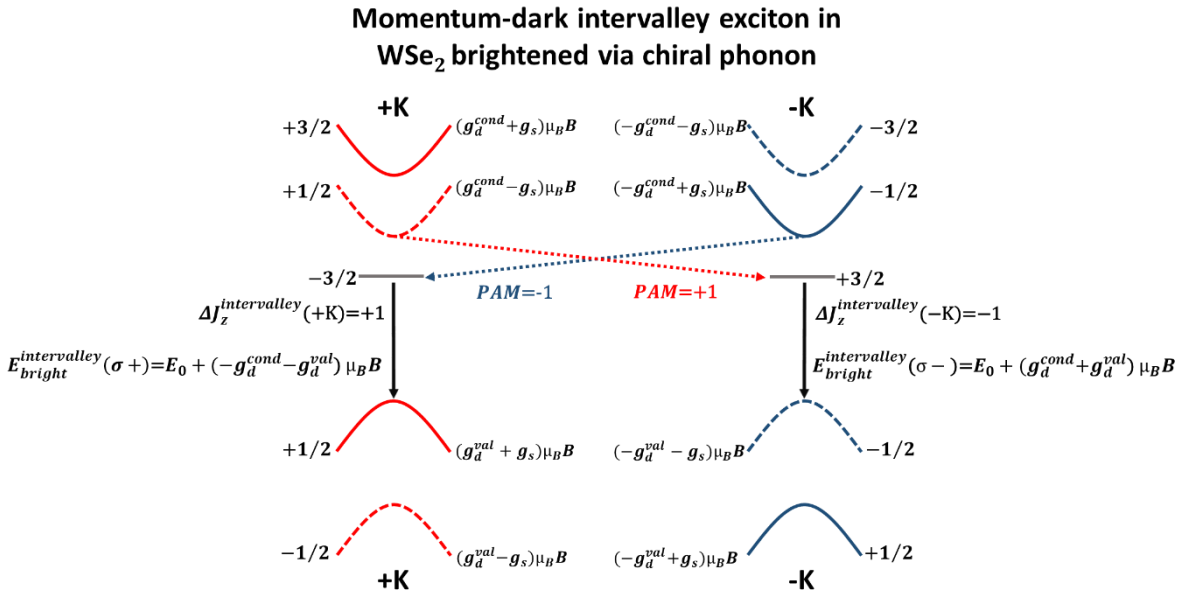

Fig5.3 Band structure of monolayer WSe_2 at +K and –K valleys. Black arrows represent the recombination path of the intervalley exciton. The red and blue dashed lines represent the intervalley transfer of the electron by phonon emission.

formalism is the same as in Fig(5.2). Magneto-photoluminescence experiments [He 2020] have shown that this intervalley exciton shifts with the magnetic with a g factor of $g_{bright}^{interlayer} = -12$.

There again the transition involves sub-bands with the same spin and only g_d contribute to the g-factor, thus :

$$E_{bright}^{intervalley}(\sigma \pm) = E_0 \pm (-g_d^{cond} - g_d^{val})\mu_B B \qquad Eq(5.5)$$

The g factor is written as:

$$g_{bright}^{interlayer} = -2g_d^{cond} - 2g_d^{val} = -12 \qquad Eq(5.6)$$

Which, combined with Eq(5.4) gives us the following system:

$$\begin{cases} g_d^{cond} - g_d^{val} = -2 \\ g_d^{cond} + g_d^{val} = +6 \end{cases} \qquad Eq(5.7)$$

Which give us the values for g_d^{cond} and g_d^{val} :

$$\begin{cases} g_d^{cond} = 2 \\ g_d^{val} = 4 \end{cases} \qquad Eq(5.8)$$

5.2.3/ Estimation of the spin contribution g_s

To approximate g_s, we consider the spin triplet exciton recombination measured in monolayer WSe_2 and monolayer $MoSe_2$. As explained in Chapter 1, "dark" exciton in WSe_2 have been studied extensively and magneto-photoluminescence experiments have estimated the absolute value of its g factor $g_{dark}^{WSe_2}$ to be equal to $|g| = 8$ in MoSe2 ML [Robert 2020] and $|g| = 8$ in

WSe_2 ML [Molas2017, Zhang 2017]. Fig(5.4) shows the zero field band structure at +K and –K points , the recombination path in represented by a black arrow. As explained previously, it is not possible to define the g factor in the same way as the spin singlet state because selection rules show that the "dark" excitons propagate within the plane of the TMD layer unless brightened by an external magnetic field applied in the parallel direction. However, as it is shown on Fig(5.4), it is clear that $E_{dark}^{ML}(K+)$, the energy of excitons emitted in the +K valley shift towards lower energies (and $E_{dark}^{ML}(K-)$ than the energy excitons emitted in the –K valley towards higher energies).

$$\begin{cases} E_{dark}^{ML}(K+) = E_0 + (g_d^{cond} - g_d^{val} - 2g_s)\mu_B B \\ E_{dark}^{ML}(K-) = E_0 - (g_d^{cond} - g_d^{val} + 2g_s)\mu_B B \end{cases} \qquad Eq(5.9)$$

We will thus keep the formalism introduced in Eq(5.2) and define g_{dark}^{ML} as :

$$g_{dark}^{ML} = \frac{E_{dark}^{ML}(K+) - E_{dark}^{ML}(K-)}{\mu_B B} \qquad Eq(5.10)$$

This pseudo g factor is negative and, combined with the experimental values presented above, we can write:

$$g_{dark}^{ML} = 2g_d^{cond} - 2g_d^{val} + 2g_s^{down} - 2g_s^{up} = -8 \qquad Eq(5.11)$$

Which, combined with Eq(5.4), gives the following approximation for $g_s = +1$.

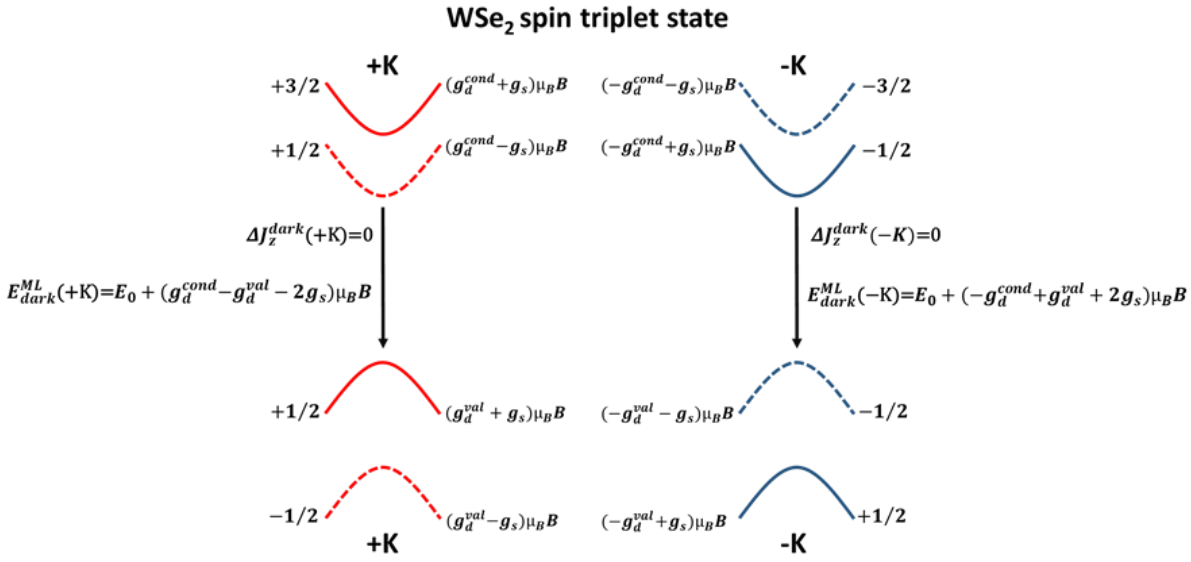

Fig5.4 Band structure of monolayer WSe_2 at +K and –K valleys. Black arrows represent the recombination path of the spin triplet state. The recombination path at +K/-K point is indexed with the change of angular momentum $\Delta J_z^{dark}(\pm K)$ and the energy $E_{dark}^{ML}(\sigma\pm)$ of the photon emitted by the exciton recombination.

5.3/Estimation of the g factor in TMD heterobilayers

5.3.1/ General discussion

As explained at the beginning of this chapter, twisting the two constituent monolayers defines the alignment between the K points of the first and second layer. In the case of Sample 1 and

Sample 2, we have observed a Zeeman shift of $0{,}5\ \mathrm{meV T^{-1}}$ for the interlayer exciton ,corresponding to a g factor with an absolute of $|g|$=16. Moreover, we have shown that the sign of the g-factor of the interlayer exciton is negative by comparing the Zeeman shift of the interlayer and intralayer excitons. Thus, we have established that our samples were aligned with θ=60° based on comparison with [Seyler 2017] which correspond to the R stacking configuration. We will now justify this choice by applying the model detailed earlier to TMD heterobilayers.

According to Fig(1.24), most heterobilayer built with a combination of TMDs with S, Se and Te as a chalcogen and W and Mo as a metal result in a type II heterostructure. We consider a TMD heterobilayer MX_2^1/MX_2^2 where MX_2^1 is the layer hosting the electrons and MX_2^2 the layer hosting the holes of the exciton. Since TMDs are commonly divided into two categories (bright and dark materials), there are four possibilities for $MX_2^{1/}\ MX_2^2$: bright/bright, dark/dark, bright/dark and dark/bright. However, the angular momentum and energy shift of the band structure with the magnetic field are independent of the spin-orbit coupling of the material. Thus, we only need to consider the two cases of spin singlet and spin triplet recombination in TMD heterostructures. In the following part, we will establish the selection rules and estimate the g-factors of these two recombination paths, presented in Fig(5.5), in the case of 0° and 60° aligned heterostructures.

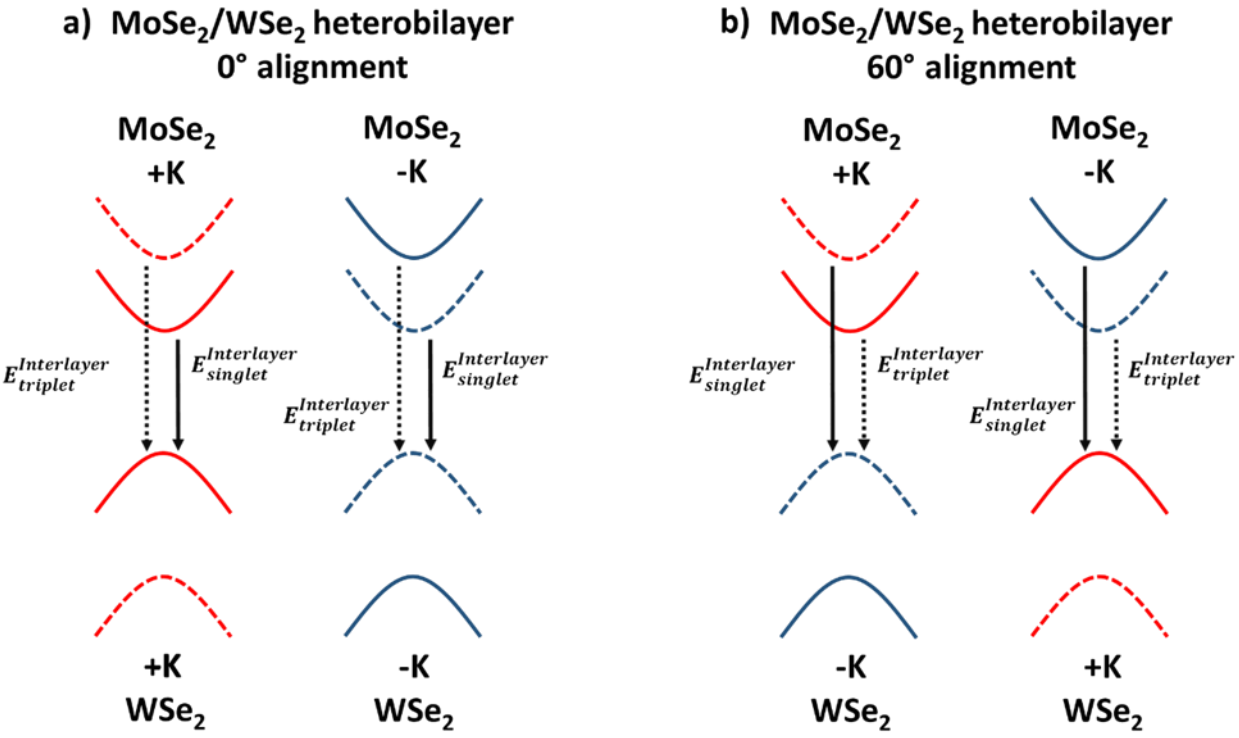

Fig5.5 Band structure of an $MoSe_2/WSe_2$ heterobilayer aligned **a)** with θ=0° (+K on +K). b) with θ=60° (+K on -K). The interlayer spin singlet recombination path is represented by a plain black arrow while the spin triplet state is represented by a dashed black arrow.

5.3.2/ Selection rules and estimation of the g factor in 0° aligned heterobilayers

Fig(5.6) shows the band structure of a $MoSe_2/WSe_2$ heterobilayer aligned with θ=0°, black arrows show the singlet spin recombination path. Each sub-band is indexed by its angular

momentum J_z, defined modulo 3, and by its energy shift with the magnetic field B. Just like in monolayer $MoSe_2$, the lowest energy state corresponds to the interlayer singlet spin state. The calculation of the angular momentum of this recombination path shows $\Delta J_z^{singlet} = +1$ in the +K valley and $\Delta J_z^{singlet} = -1$ in the –K valley. These are the same selection rules as for monolayer TMDs. Since the recombination involve sub-bands with the same spin and valley indices, the energy shift of the exciton emitted in the $\pm K$ valleys $E_{singlet}^{Interlayer}(\sigma \pm)$is written:

$$E_{singlet}^{Interlayer}(\sigma \pm) = E_0 \pm (g_d^{cond} - g_d^{val})\mu_B B \qquad Eq(5.12)$$

This expression is equivalent to the one shown in Eq(5.3) and thus the g factor $g_{singlet}^{Interlayer}$ is defined as in Eq(5.4) :

$$g_{singlet}^{Interlayer} = \frac{E_{singlet}^{Interlayer}(\sigma +) - E_{singlet}^{Interlayer}(\sigma -)}{\mu_B B} = 2g_d^{cond} - 2g_d^{val} = g_{bright}^{ML} = -4$$

$$Eq(5.13)$$

This means that recombination of the spin singlet state is allowed in heterobilayers aligned θ=0° with an expected g factor $g_{singlet}^{Interlayer} = -4$, which is exactly the same behavior as "bright" excitons in TMD monolayers.

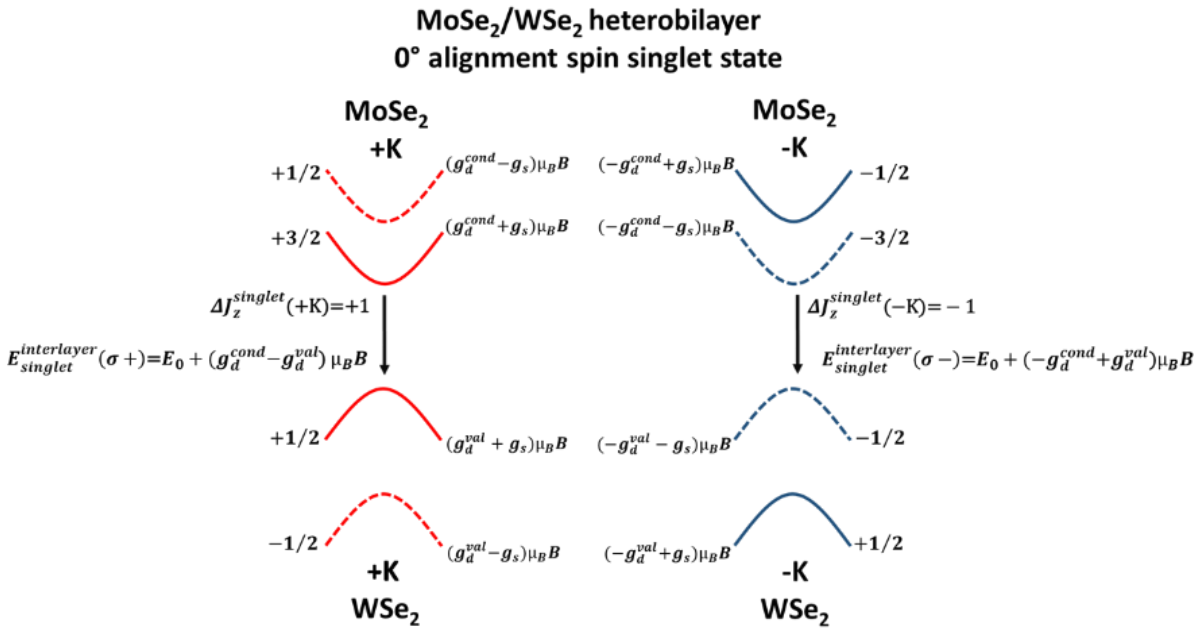

Fig5.6 Band structure of a $MoSe_2/WSe_2$ heterobilayer aligned with θ=0° (+K on +K). Black arrows represent the recombination path of the interlayer spin singlet state.

We consider now the spin triplet recombination path. Fig(5.7) shows the band structure of a $MoSe_2/WSe_2$ heterobilayer aligned with θ=0°, black arrows show the triplet spin recombination path. There again, just like in monolayers of TMDs, the recombination shows $\Delta J_z^{triplet} = 0$ at both +K and –K point, which means that in 0° heterobilayers , the spin triplet transition has no projection of angular momentum along the out of plane direction of the heterostructure.

The selection rules of the interlayer spin triplet state are the same as the "dark" exciton in monolayers, we apply formalism introduced if Eq(5.9) and Eq(5.10) to write the energy of the excitons emitted in the valley $\pm K$ $E_{triplet}^{interlayer}(K\pm)$:

$$E_{triplet}^{interlayer}(K\pm) = E_0 \pm (g_d^{cond} - g_d^{val} - 2g_s)\mu_B B \qquad Eq(5.14)$$

Which gives by definition a negative value of the g factor $g_{triplet}^{interlayer}$:

$$g_{triplet}^{interlayer} = \frac{E_{triplet}^{interlayer}(K+) - E_{triplet}^{interlayer}(K-)}{\mu_B B} \qquad Eq(5.15)$$

$$g_{triplet}^{interlayer} = 2g_d^{cond} - 2g_d^{val} + 2g_s^{down} - 2g_s^{up} = g_{dark}^{ML} = -8 \qquad Eq(5.16)$$

In the case of heterostructures aligned with θ=0°, this simplified model that the interlayer singlet and spin triplet states have the same selection rules as bright and dark excitons emitted in TMD monolayers. This weakness of the model results from our presupposition: we considered that the orbital contribution g_d and the spin contribution g_s were the same in $MoSe_2$ and WSe_2. Thus, a $MoSe_2/WSe_2$ heterostructure aligned with θ=0° has the same properties as a regular $MoSe_2$ monolayer, with a reduced energy of the optical gap due to the alignment with the WSe_2 monolayer. Thus, this model fails to describe the interlayer exciton g factor value $g_{\theta=0°}^{interlayer} = +6{,}7$ observed in [Seyler 2017, Holler 2021, Joe 2019]. We will see in the following paragraph that this is not the case with heterostructures aligned with θ=60°.

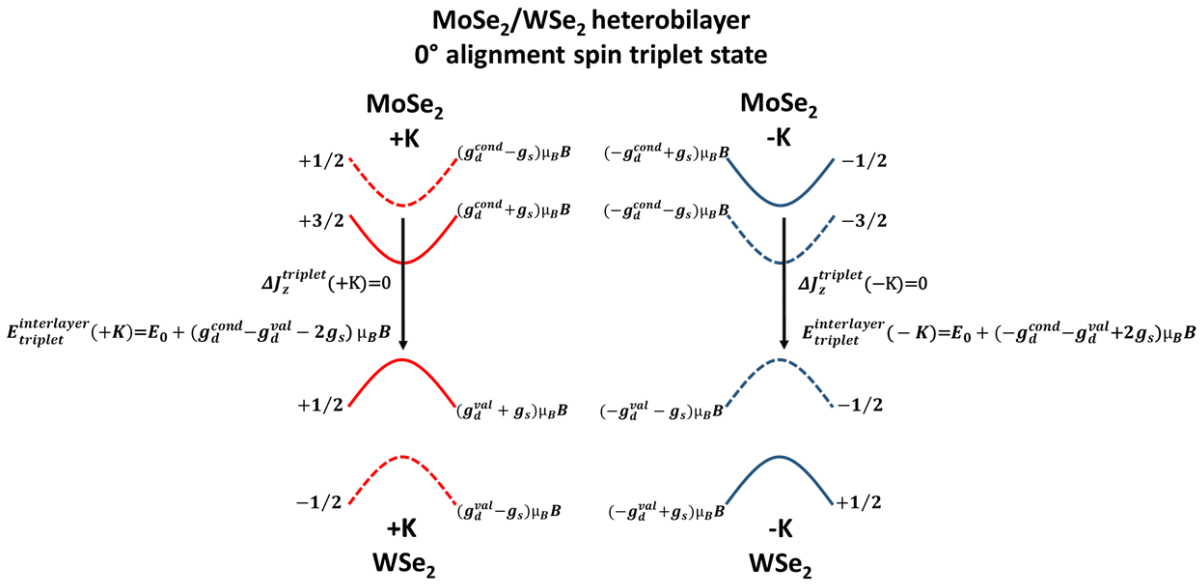

Fig5.7 Band structure of a $MoSe_2/WSe_2$ heterobilayer aligned with θ=0° (+K on +K). Black arrows represent the recombination path of the interlayer spin triplet state.

5.3.3/ Selection rules and estimation of the g factor in 60° aligned heterobilayers

In the case of heterostructures aligned with θ=60°, both valleys of the heterobilayer are the combination of +K and –K valleys of the monolayers. Fig(5.8) shows the band structure of a $MoSe_2/WSe_2$ heterobilayer aligned with θ=60°. Like the band structure of monolayer WSe_2, the lowest energy optical transition corresponds to a spin triplet state. Each sub-band is indexed

by its angular momentum J_z , defined modulo 3,and the value of its energy shift as a function of g_s and g_d. The combination of the -K valley of the $MoSe_2$ layer and the +K valley of the WSe_2 layer is defined as the interlayer valley $+K^i$ since the top of the valence band involve a spin-up sub-band. Conversely, the combination of the $MoSe_2$ +K valley and WSe_2 –K valley layer is defined as the interlayer valley $-K^i$ since the top of the valence band involve a spin-down sub-band.

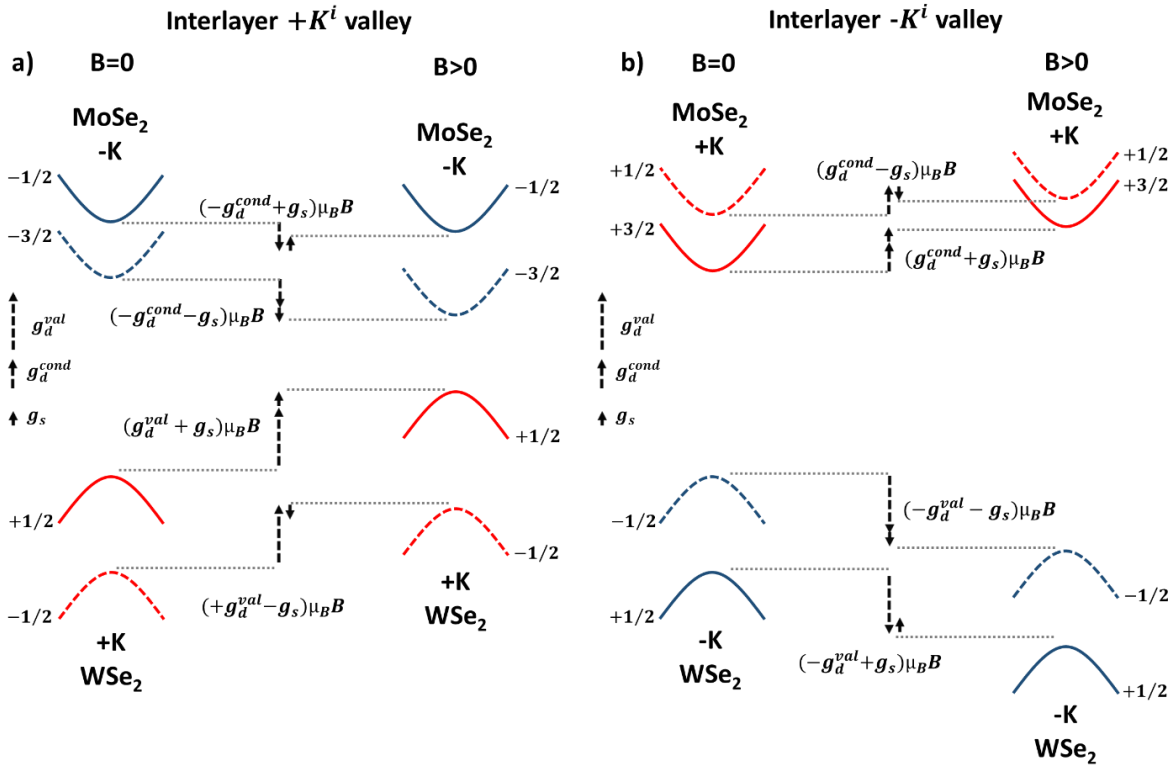

Fig5.8 Shift of the band structure of a $MoSe_2/WSe_2$ heterobilayer aligned with θ=60° with the magnetic field B **a)** at the interlayer valley $+K^i$. $+K^i$ is defined as the superposition of $MoSe_2$ conduction band in the –K valley (blue lines) and WSe_2 valence band in the +K valley (red lines). Spin-down sub-bands are shown as dashed lines (spin-up sub-bands as plain lines). **b)** at the interlayer valley $-K^i$. $-K^i$ is defined as the superposition of $MoSe_2$ conduction band in the +K valley (red lines) and WSe_2 valence band in the -K valley (blue lines).

Fig(5.9) shows the band structure of a $MoSe_2/WSe_2$ heterobilayer aligned with θ=60°. The spin singlet state recombination path is represented by a black arrow. The interlayer emission shows a change of angular momentum $\Delta J_z^{singlet} = -1$ in the $+K^i$ valley valley and $\Delta J_z^{singlet} = +1$ at the $+K^i$ valley. This is the opposite to what is observed in TMDs monolayers : the interlayer singlet state couple with σ- polarized light at the interlayer $+K^i$ valley and with σ+ polarized light at the interlayer $-K^i$ valley.

This apparent reversal of the selection rules is not the result of our definition of the interlayer valleys $+K^i/-K^i$: indeed, the g factor $g_{singlet}^{interlayer}$ does not depend of the definition of the valley , it only depends on the energy shift of the two oppositely polarized emission $E_{singlet}^{interlayer}(\sigma\pm)$.

$$E_{singlet}^{interlayer}(\sigma\pm) = E_0 \pm (g_d^{cond} + g_d^{val})\mu_B B \qquad Eq(5.17)$$

The expression of $g_{singlet}^{interlayer}$ is written as :

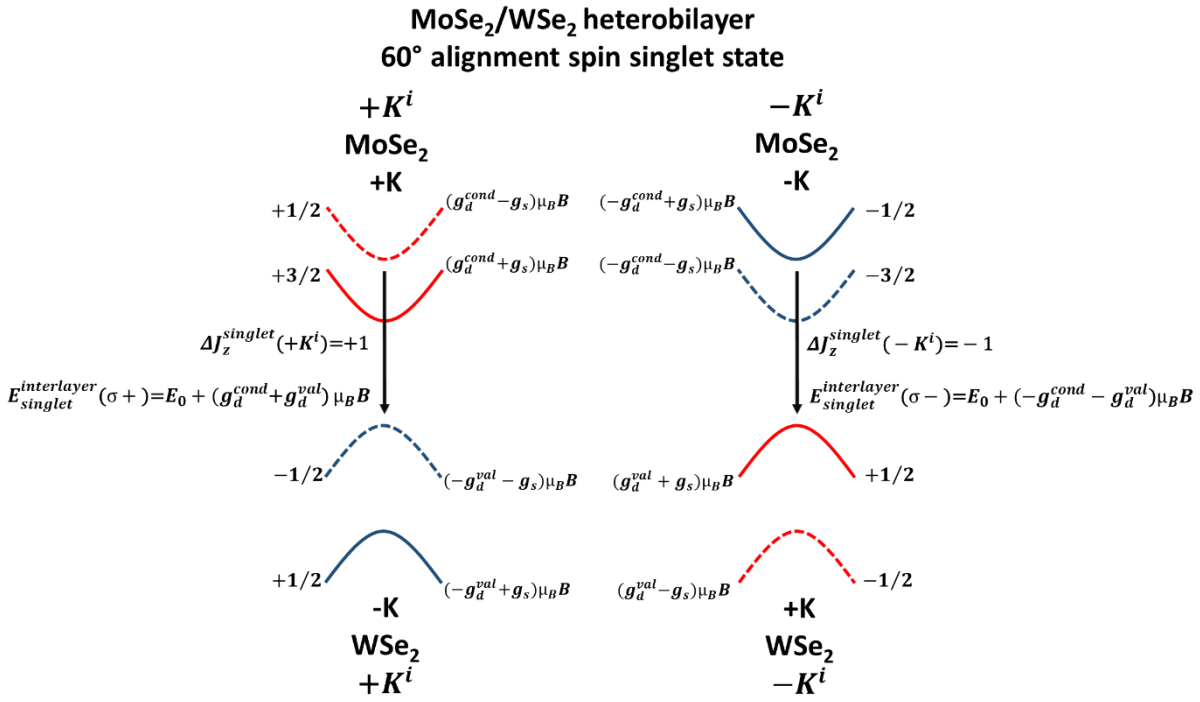

Fig5.9 Band structure of a $MoSe_2/WSe_2$ heterobilayer aligned with θ=60° (+K on -K). Black arrows represent the recombination path of the interlayer spin singlet state.

$$g_{singlet}^{interlayer} = E_{singlet}^{interlayer}(\sigma+) - E_{singlet}^{interlayer}(\sigma-) = 2g_d^{cond} + 2g_d^{val} \qquad Eq(5.18)$$

Which, considering our estimation for the g_d and g_s parameters results in a positive value of $g_{singlet}^{interlayer}$:

$$g_{singlet}^{interlayer} = 2 \times 4 + 2 \times 2 = +12 \qquad Eq(5.19)$$

As presented in Tab(1.8), there are experimental evidences of this positive value of the g factor $g = +12$. [Wang 2019] shows the results of a magneto-photoluminescence experiment on a $MoSe_2/WSe_2$ heterostructure aligned with θ=60°. The interlayer exciton photoluminescence spectrum shows two features that shift with the magnetic field at a different rate. Experimentalists do not seem to have characterized the polarization of the emitted interlayer excitons, they only discuss the absolute value of the two g factors $|g_1| = 15{,}3 \pm 0{,}2$ and $|g_2| = 10{,}7 \pm 0{,}2$. The magnitude of g_1 is close to 16, which would correspond to the g factor of -16 reported in other publications [Seyler 2017, Nagler 2017, Holler 2021, Baek 2020] while the magnitude of g_2 is also very close to the expected value of $g_{singlet}^{interlayer}$. This is confirmed by other results of magneto-photoluminescence experiments shown in [Brotons-Gisbert 2021] : the interlayer exciton photoluminescence spectrum also presents the two features and polarization analysis of the emited excitons indeed shows that the g factors of the two features are $g_1 = -15{,}71$ and $g_2 = +12{,}24$. Finally, magneto-PL data on a R stacked WSe_2/WS_2 HBL [Montblanch 2021] also reports two different magnitude of the g factors $|g_1| = 15{,}4$ and $|g_1| = 11{,}8$ but do not specify the sign.

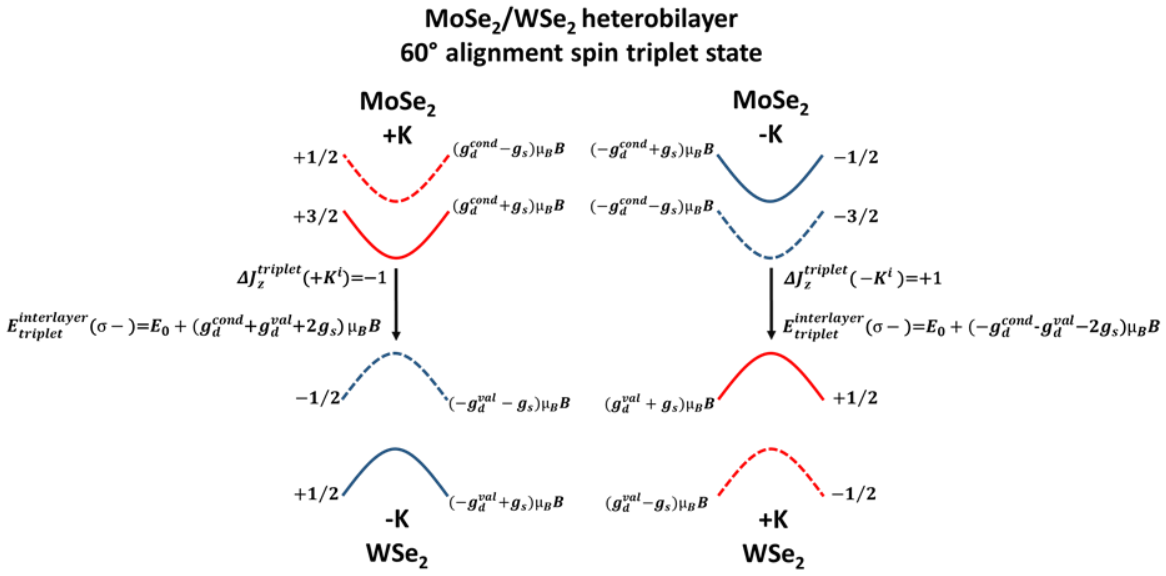

Fig5.10 Band structure of a $MoSe_2/WSe_2$ heterobilayer aligned with θ=60° (+K on -K). Black arrows represent the recombination path of the interlayer spin triplet state.

We have shown in Chapter 1 how the reported g factors of spin singlet excitons emitted in TMD monolayers take a negative value. The predicted value of $g_{singlet}^{interlayer} = +12$ and the experimentally measured value of $g_{singlet}^{intervalley} = -12$ have the same magnitude but different signs. This is because both of these recombination paths involve a conduction and valence bands with the same spin index as well as a different valley index and thus the magnitude of the g-factor is equal to $|g| = 2g_d^{cond} + 2g_d^{val}$. The difference is that in the case of the interlayer exciton, this set of sub-band is direct in momentum whereas the intervalley exciton is a momentum indirect transition that requires the emission of a phonon with a $PAM = \pm 1$ for satisfying the momentum conservation.

The last recombination path to consider is the interlayer spin triplet state. Fig(5.10) shows the band structure of a $MoSe_2/WSe_2$ heterobilayer aligned with θ=60°. The recombination path of the spin triplet state is represented by black arrows. The interlayer emission shows a change of angular momentum $\Delta J_z^{triplet} = +1$ in the $+K^i$ valley and $\Delta J_z^{triplet} = -1$ in the $-K^i$ valley. This is the capital difference compared to monolayer TMDs, in which the spin triplet recombination path is forbidden by the selection rules, and +K/-K aligned heterobilayers, in which both singlet and spin triplet state recombinations are allowed.

We write the energy $E_{triplet}^{interlayer}(\sigma \pm)$ of the $\sigma \pm$ polarized excitons emitted in the $\pm K^i$ interlayer valley:

$$E_{triplet}^{interlayer}(\sigma \pm) = E_0 \pm (-g_d^{cond} - g_d^{val} - 2g_s)\mu_B B \qquad Eq(5.20)$$

The recombination involve sub-bands with different spin indexes and different valley indexes. This means that the contribution to the g factor of g_d^{condl} , g_d^{val} and g_s add together. The g factor of the interlayer spin triplet state $g_{triplet}^{interlayer}$ is therefore maximized:

$$g_{triplet}^{interlayer} = \frac{E_{triplet}^{interlayer}(\sigma+) - E_{triplet}^{interlayer}(\sigma-)}{\mu_B B} = -2g_d^{cond} - 2g_d^{val} - 4g_s \qquad Eq(5.21)$$

Which, considering our estimations for the g_d and g_s parameters gives an estimated value for $g_{singlet}^{interlayer}$:

$$g_{triplet}^{interlayer} = -2 \times 4 - 2 \times 2 - 4 \times 1 = -16 \qquad Eq(5.22)$$

This magnitude of the g factor is the highest value of all the available recombination path in a $MoSe_2/WSe_2$ heterostructure aligned with θ=60°. We can thus assign the emission of interlayer exciton measured on Sample 1 and Sample 2 to the interlayer spin triplet state. This is consistent with the conduction band ordering of monolayer $MoSe_2$ in which the recombination path of lowest energy is the spin triplet state, the energy of the spin singlet state is superior because of the conduction band spin-orbit splitting.

In the magneto-photoluminescence experimental results presented in Fig(4.10) of Chap(4), the sample has been cooled to a temperature of T=4,5 K. As such, characteristic scale for thermal fluctuations in the MoSe2 conduction band is :

$$k_B T = 0{,}086 \times 4{,}5 = 0{,}387 \text{ meV} \qquad Eq(5.23)$$

This value is lower than the separation between the "bright" and "dark" excitons in monolayer $MoSe_2$ reported in [Robert 2020, Lu 2020] to be equal to $-1{,}4$ meV. At this temperature, only the low energy spin triplet state is populated while the spin singlet state is empty. In [Wang 2019], the photoluminescence spectrum showing both the singlet and spin triplet state has been measured with a sample temperature of T=77K, which imply $k_B T = 0{,}086 \times 77 = 6{,}622$ meV. At this temperature, both the singlet and spin triplet are populated and correspond to the two peaks shown in their magneto-photoluminescence results. [Brotons-Gisbert 2021] does not precise the temperature of the sample during the measurements.

5.4/ Conclusion

Before this discussion on the significance of the g factor, we had established that our samples were aligned with θ=60° (R stacked) based on comparison with results presented in [Seyler 2017]. In this chapter, we have justified this assignment by defining the selection rules of interlayer excitons for the singlet and spin triplet states in heterostructures aligned with θ=0° and θ=60°. We have presented a very simple model of TMD heterobilayers based on experimental observations in WSe_2 and $MoSe_2$ monolayers to estimate the value and the sign of the g factor for a given recombination path. We have applied this model to the case of a $MoSe_2/WSe_2$ heterobilayer and compared our predictions to the results found in [Seyler2017, Nagler 2017, Holler 2021, Baek 2020,Wang 2019, Brotons-Gisbert-2021]. While this model fails to describe the interaction of the band structure with the magnetic field in an heterobilayer aligned with θ=0°, it provides an estimation for the g factor of the singlet and spin triplet states in heterobilayers aligned with θ=60°. The g factor of -16 observed in the results the magneto-photoluminescence measurements on Sample 1 and Sample 2 thus corresponds to the spin triplet interlayer exciton.

Chapter 6: Interlayer exciton-phonon magneto-resonance

6.1/ Introduction:

We have assigned the interlayer exciton measured on our +K on –K aligned heterobilayers to the spin triplet state. This transition has the particularity to maximize the exciton g factor, as such, we have measured a value of $g = -16$ in both our samples, which is the highest value measured in TMDs. In this chapter, we will explain the resonant intensity anomalies presented in Chapter 4. We will show that the high value of the g-factor allows us to bring the Zeeman energy of the interlayer excitons to values unattainable using monolayer TMD systems. Notably, it is possible to tune E_Z in resonance with the chiral phonons modes of the constituent monolayers which opens a relaxation channel between the two oppositely polarized interlayer emissions. We will describe precisely the intensity anomaly observed in Sample 1 and Sample 2 and explain the arguments pointing toward this exciton-phonon interaction. We will then present the details of this relaxation process, the energy and angular momentum conservation conditions, as well as the limits of our reasoning. We will show our attempts to measure the Raman scattering signature the phonon modes involved in this interaction. Finally, we will focus on the "resonance profile" of the intensities anomalies. As presented in Chapter 4, the value of the magnetic field for which the intensity of the interlayer exciton is minimum is not the same across the energy range of the interlayer exciton PL spectrum. This profile is particularly visible in the case of Sample 2 (cf Fig(4.12.c and d)), since its interlayer emission peak is larger. Magneto-photoluminescence measurements at low excitation power also point toward the same behavior in Sample 1 (cf Fig(4.14)). We will show that these profiles are the consequence of the local fluctuations of the optical gap and that their "diagonal" shape is coherent with the expression of the orbital contribution to the g-factor. To conclude, we will extract the relationship between the g factor and the energy of the single interlayer excitons, which collectively give rise to the interlayer exciton photoluminescence spectrum. The results presented in this chapter have been published in [Delhomme 2020].

6.2/ Description of the observed resonances

6.2.1/ Zeeman energy:

Fig(6.1) shows the magneto-photoluminescence spectra of the interlayer excitons measured in Sample 1 and Sample 2 when the magnetic field is swept across the resonances . The integrated intensity of each interlayer emission is superimposed on its color-map . The sharp decrease of the intensity of the σ- polarized component and the rise of the intensity of the σ+ polarized components are synchronized. In the case of Sample 1, the first resonance R1 occurs for a magnetic field of $B_{S1}^{R1} = 24{,}00 \pm 0{,}01$ T, and the Zeeman energy of the interlayer exciton is $E_{Z_{S1}}^{R1}(B = 24\text{ T}) = 22{,}3 \pm 0{,}2$ meV. In the case of Sample 2, the extinction of the σ- polarized emission is not homogeneous over the whole PL spectrum. However, the resonance of the main interlayer peak which occurs for a magnetic field of $B_{S2}^{R1} = 24{,}25 \pm 0{,}01$ T, and the corresponding Zeeman energy is $E_{Z_{S2}}^{R1}(B = 24{,}25\text{ T}) = 22{,}4 \pm 0{,}2$ meV. The second resonance R2 is observed for higher magnetic field, at $B_{S1}^{R2} = 24{,}62 \pm 0{,}01$ T and $B_{S2}^{R2} = 24{,}89 \pm 0{,}01$ T in the case of Sample 1 and Sample 2, respectively. This correspond to a Zeeman energy of $E_{Z_{S1}}^{R2}(B = 24{,}62T) = 22{,}9 \pm 0{,}2$ meV and $E_{Z_{S2}}^{R2}(B = 24{,}89T) = 22{,}8 \pm 0{,}2$ meV.

It is quite clear from these observations that the resonances occur once the Zeeman energy reaches a well-defined value, $22{,}3 \pm 0{,}2$ meV and $22{,}9 \pm 0{,}2$ meV for the first and second resonance respectively. Since this energy is defined as $E_Z = g\mu_B B$, it is clear that the values of

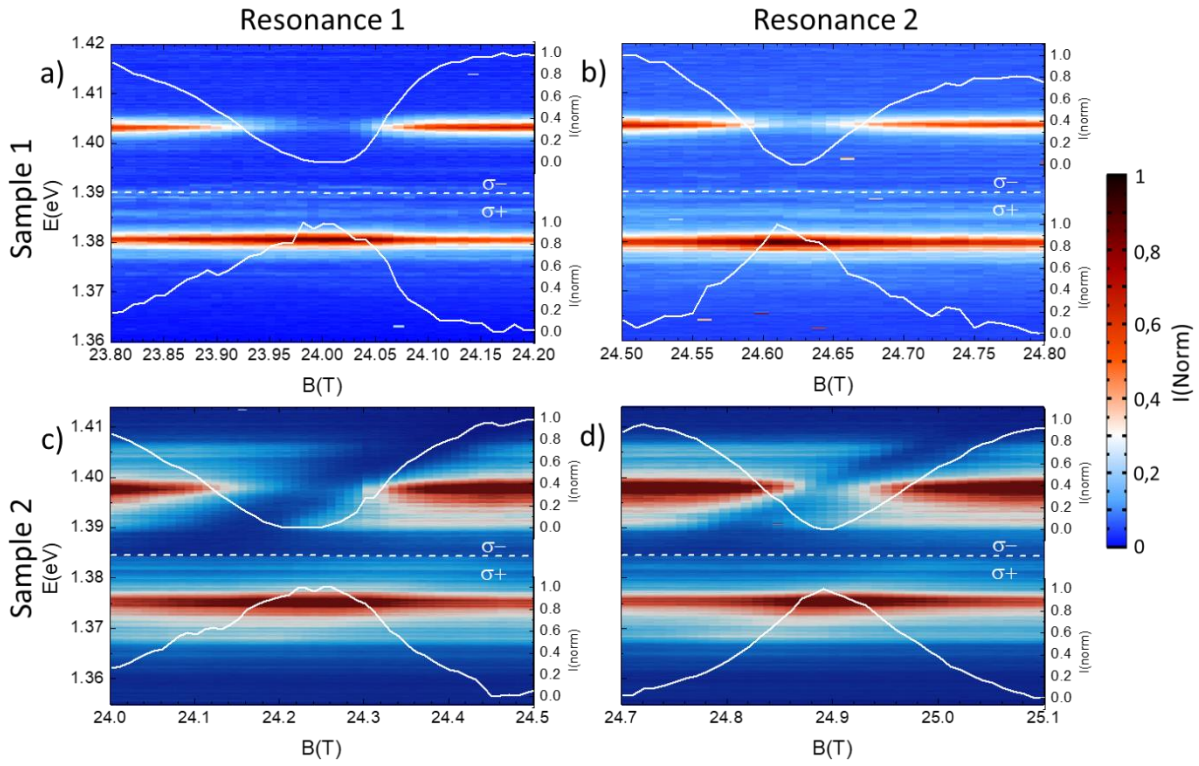

Fig6.1 Magneto-photoluminescence false color maps of the interlayer exciton measure in Sample 1 *a)* and *b)* and Sample 2 *c)* and *d)*. The magnetic field is swept across the range of Resonance 1 for *a)* and c) and Resonance 2 for *b)* and *d)*. The white curves represent the normalized intensity of the interlayer excitons.

E_{Zeeman} observed in Sample 1 and Sample 2 are only reachable through the combination of the high g-factor and a high magnetic field. This explains why such resonances have never been observed before in monolayer TMDs. The absolute value of the g-factor for "bright" excitons in monolayer TMDs is $\left|g_{Bright}^{ML}\right| = 4$, which is four times lower than the g-factor of spin triplet interlayer excitons $\left|g_{triplet}^{HBL}\right| = 16$. In order to tune the Zeeman energy of monolayer "bright" excitons to the values of $E_{Z_{S1/S2}}^{R1}$ and $E_{Z_{S1/S2}}^{R2}$, the applied magnetic field would have to be four times as strong, between 97 T and 98 T. Such values of B are well above the capacity of any continuous field facility in the world and near the limit of what is possible to reach with a pulsed field. For comparison, the mention of the highest pulsed magnetic field applied to monolayer TMDs is found in [Goryca 2019] which shows the absorption spectra of monolayer WS_2 and MoS_2 for fields up to $|B| = 65$ T.

6.2.2/ Width of the resonances

The second characteristic of these processes is the sharpness of the interaction which implies that E_Z is brought into resonance with very well defined modes. According to our magneto-photoluminescence results, FWHM of the first resonance is $\Delta B_{S1}^{R1} = 0{,}17 \pm 0{,}02$ T for Sample 1 and seems to be larger for Sample 2 with $\Delta B_{S2}^{R1} = 0{,}20 \pm 0{,}02$ T. The FWHM of the second resonance is lower in Sample 1 ($\Delta B_{S1}^{R2} = 0{,}15 \pm 0{,}02$ T) and in Sample 2 ($\Delta B_{S2}^{R2} = 0{,}15 \pm 0{,}02$ T). The fluctuation introduced on the value of E_Z by this variation of the magnetic field is also very small : considering a value of the g factor rounded to $\left|g_{triplet}^{HBL\,60°}\right| = 16$, $\Delta B = 0{,}2$ T and $\Delta B = 0{,}15$ T respectively correspond to a fluctuation of $\Delta E_Z = 0{,}19$ meV and $\Delta E_Z = 0{,}14$ meV which is of the order of our error bars in the measurement of E_Z.

ΔE_Z represents the energy scale on which the interaction is effective and is hence representative of the spectral width of the interacting mode. FWHM of 0,19 meV and 0,14 meV are one order of magnitude lower than the intrinsic linewidth of intralayer excitons in TMDs [Caditz 2017] which makes excitonic transitions unlikely candidates for the modes involved in the resonance process . These values of FWHM are more in line with the reported width of phonon modes in monolayer TMD. This points toward a resonant exciton-phonon interaction in which the interlayer exciton Zeeman energy would be tuned by the magnetic field to reach the value of defined phonon modes of the constituent $MoSe_2$ and WSe_2 monolayers (two layers corresponding two modes and thus two resonances). It is important to stress that the resonances are not a threshold effect: the intensity of both the σ+ and σ- polarized emissions come back to their original values when E_Z becomes higher than $E_{Z_{S1/S2}}^{R1}$ and $E_{Z_{S1/S2}}^{R2}$.

6.3/ Magnetic field resonant exciton phonon interaction

6.3.1/ Excitonic angular momentum flip

Fig(6.2) shows the band structure at the $\pm K^i$ valleys of a $MoSe_2/WSe_2$ heterobilayer aligned with θ=60°, the triplet state recombination paths in both valleys are pictured by black arrows. When E_{Zeeman} is brought to the value of $E_{Z_{S1/S2}}^{R1}$ and $E_{Z_{S1/S2}}^{R2}$, a relaxation channel opens between the high energy σ- polarized emission in the $-K^i$ interlayer valley and the lower energy σ+ polarized emission in the $-K^i$ interlayer valley. This relaxation requires switching the spin

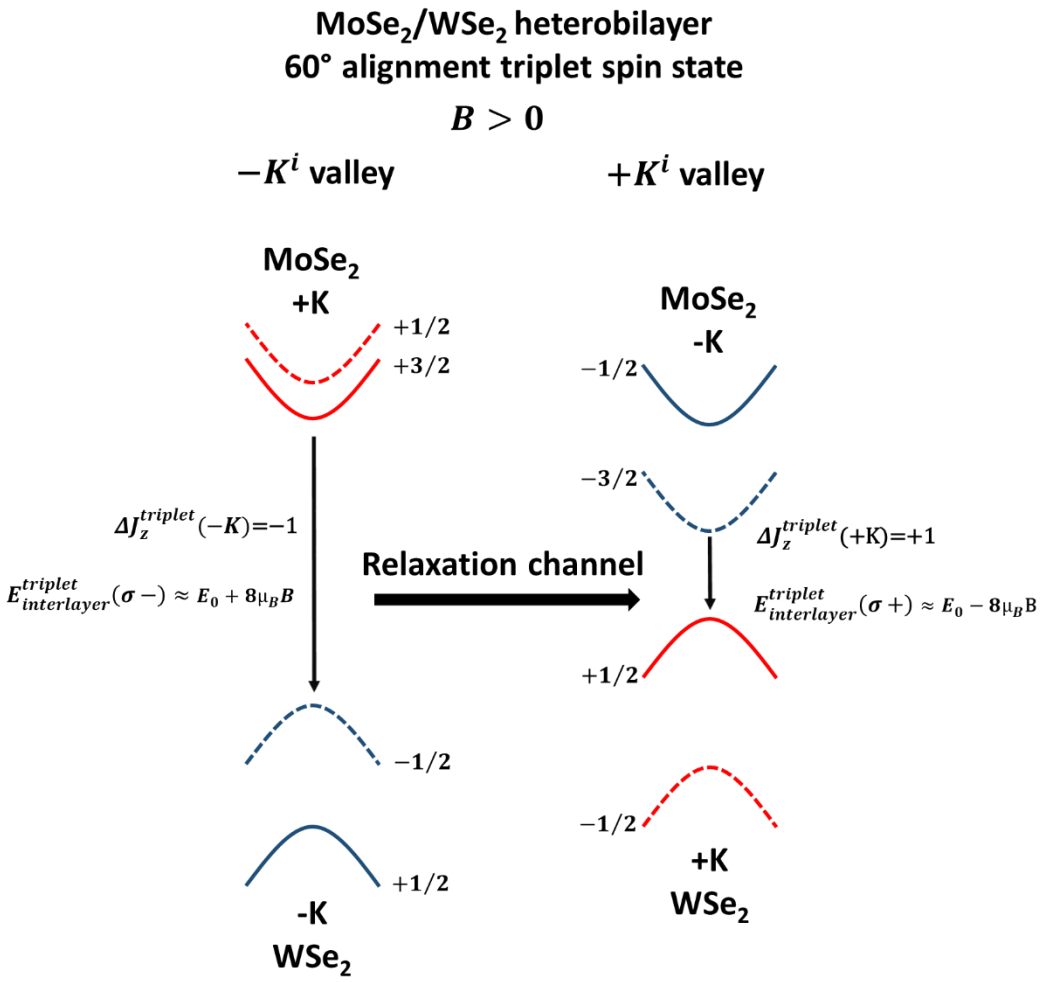

Fig6.2 Band structure of a $MoSe_2/WSe_2$ heterobilayer aligned with θ=60° (+K on –K). The black arrows represent the recombination path of the interlayer spin triplet state. The changes of intensity observed at Resonance 1 and 2 are seen as the relaxation of the $\sigma-$ polarized emission onto the mower energy $\sigma+$ polarized emission (bold black arrow).

component of both the electron and the hole constituting the σ- polarized interlayer emission, or as flipping the angular momentum of the σ- polarized interlayer emission from $\Delta J_{z\,triplet}^{\;interlayer}(-K^i) = -1$ to $\Delta J_{z\,triplet}^{\;interlayer}(+K^i) = +1$.

The latter is very similar to the case of an exciton-phonon interaction recently measured in TMD monolayers [He 2020, Zinkiewicz 2021]: the brightening of the momentum dark intervalley exciton/trion by emission of a chiral phonon mode (cf Chapter 1 and Chapter 5), . In this case, the $PAM = \pm 1$ carried by the phonon is necessary for the recombination to take place and the phonon-electron interaction is nonresonant. However, according to our comparision between the angular momentum quantity of the original bands and virtual recombination paths (cf Fig(5.3)), $\Delta J_z^{E''}$ effectively does switch the angular momentum of the optical transition from $\Delta J_z^{Intervalley} = -1$ to $\Delta J_z^{Intervalley} = +1$ during the transfer of the electron from the +K valley to the –K valley. As such, these E'' in plane chiral phonon modes emerge as the prime candidates for the resonant exciton-phonon interactions observed in Sample 1 and Sample 2.

It is complicated to get a relevant reported value of the energy of E'' since these modes are not Raman active in TMD monolayers. [Soubelet 2021] shows the Raman spectrum of a $MoSe_2$ bilayer : the E'' peak is centered on $E''_{MoSe2} = 170\ \text{cm}^{-1}$ corresponding to an energy of 21,1 meV. In the case of monolayer WSe_2, [Luo 2013] proposes a calculated value of $E''_{WSe2} = 175{,}96\ \text{cm}^{-1}$at the Γ point of the WSe_2 Brillouin zone, which correspond to an energy of 21,8 meV , while [Kim 2017] shows an experimental values of $175\ \text{cm}^{-1}$ for the equivalent E_{1g} mode in a few layers WSe_2 sample. These two energies are close to the values of the Zeeman splitting at $E_{Z_{S1/S2}}^{R1}$ and $E_{Z_{S1/S2}}^{R2}$, and the small differences between our measured values of E''_{MoSe2} and E''_{WSe2} and the one found in the literature can be attributed to the influence of the dielectric environment. [Soubelet 2021] considers a non encapsulated homo-bilayer of $MoSe_2$ while our system consist of a monolayer of $MoSe_2$ coupled to a monolayer of WSe_2 and encapsulated in h-BN. Likewise, our system is quite different from the one considered in [Luo 2013]which proposed a calculated value of E''_{WSe2} for an isolated WSe_2 monolayer. Note however that the energy difference given in the literature between E''_{MoSe2} and E''_{WSe2} is very close to the difference between our experimental values of $E_{Z_{S1/S2}}^{R1}$ and $E_{Z_{S1/S2}}^{R2}$ ($\Delta E \approx 0{,}7$ meV).

6.3.2/ Description of the effect

We thus propose the following explanation for the field resonant relaxation processes observed in Sample 1 and Sample 2. Because of the high g factor of the interlayer spin triplet excitons characteristic of the θ=60° aligned heterobilayers, the Zeeman energy split of the two oppositely polarized components of the interlayer exciton can be tuned to the values of E''_{MoSe2} and E''_{WSe2} by a high magnetic field. Fig(6.3) shows a schematic of the relaxation process : when the applied field is equal to $B_{S1/S2}^{R1} \approx 24$ T , a relaxation channel opens between the σ- polarized state characterized by the angular momentum $\Delta J_z^{\sigma-} = -1$ to the σ+ polarized state lying 22,3 meV below and characterized by the angular momentum $\Delta J_z^{\sigma-} = +1$. This relaxation results in the emission of a $MoSe_2$ E'' chiral phonon mode with an energy of $E''_{MoSe2} = E_{Z_{S1/S2}}^{R1} = 22{,}3$ meV. The momentum conservation is assured by the pseudo angular momentum (PAM) carried by the phonon $\Delta J_{MoSe2}^{E''} = +1$. Since J_z is defined modulo 3 :

$$\Delta J_z = J_z^{\sigma-} - J_{MoSe2}^{E''} = -1 - (+1) = -2 \equiv +1 = J_z^{\sigma+} \qquad \text{Eq}(6.1)$$

When the magnetic field is raised to $B \approx 24{,}3$ T, the Zeeman energy E_Z is tuned out of resonance with E''_{MoSe2} and the relaxation channel closes. The same phenomenon appears when $B_{S1/S2}^{R2} \approx 24{,}7$ T : the Zeeman energy is tuned this time in resonance with the energy of the WSe_2 chiral phonon mode ($E''_{WSe2} = E_{Z_{S1/S2}}^{R2} = 22{,}9$ meV).

This explanation works well when considering the interlayer exciton as a bound state purely characterized by its angular momentum $\Delta J_z^{\sigma\pm}$ and energy E_Z. However, it no longer holds when considering individually the electron and the hole forming the exciton. As shown previously in Fig(6.2), these resonant relaxation processes require the transition of the electron from the $MoSe_2$ spin-up conduction sub band in the $-K^i$ interlayer valley to the $MoSe_2$ spin-down conduction sub band in the $+K^i$ interlayer valleys. The same process is required for the hole,

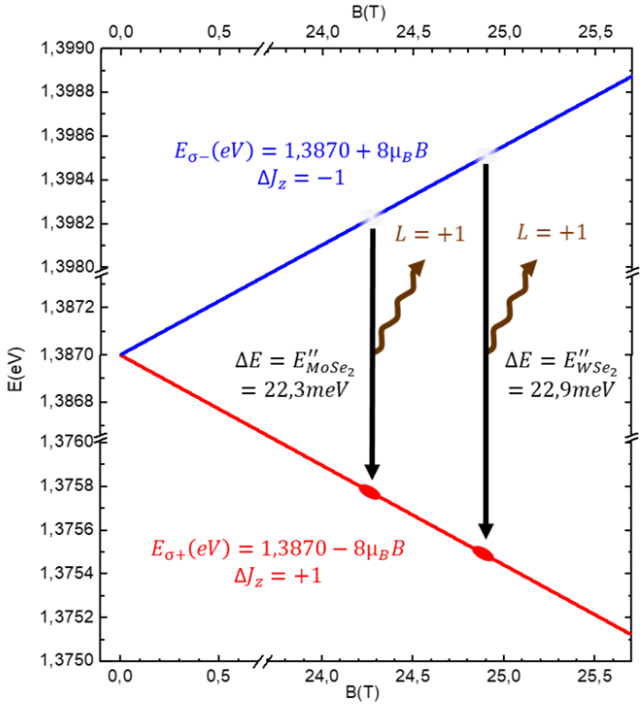

Fig6.3 Schematic of the magnetic field resonant relaxation processes observed in Fig(1), the energy difference between the $\sigma-$ polarized emission (blue line) and the $\sigma+$ polarized emission (red line) is tuned in resonance with the energy of the E'' chiral phonon mode of the $MoSe_2$ layer, the relaxation canal open (black arrow) with the emission of E''_{MoSe_2} (brown arrow). The same process occurs at higher field by an interaction with the E'' chiral phonon of the WSe_2 monolayer.

which transfers from the WSe_2 spin-down valence sub band in the $-K^i$ interlayer valley to the WSe_2 spin-up valence sub band in the $+K^i$ interlayer valley. This means that the angular momentum of the bands holding both particles is flipped during the relaxation, which is not possible in a single phonon process. A two phonon process (one for each particle of the exciton) is not coherent with our experimental observations since $E_{Z_{S1/S2}}^{R1}$ and $E_{Z_{S1/S2}}^{R2}$ are respectively equal to the energy of a single E''_{MoSe2} and E''_{WSe2} mode. This points toward a change of the exciton angular momentum as a whole and not as of its individual components.

6.4/ Measurement of the E'' chiral phonon modes

6.4.1/ Raman spectroscopy

The proposed mechanism implies a phonon emission that we have tried to detect in the Raman scattering response of the HBL in magnetic field. We have made two tentatives to image the E'' chiral phonon modes of $MoSe_2$ and WSe_2. Fig(6.4) shows Raman spectra taken at different locations of Sample 2. The first spectrum has been taken on the monolayer area of MoSe2 and shows the A'_1 Raman peak of $MoSe_2$, no traces of E''_{MoSe2} is seen around 170 cm^{-1}. The second spectrum is taken on the monolayer WSe_2 area and also show the A'_1 Raman peak of WSe_2 and no trace of E''_{WSe2} near 176 cm^{-1}. The third location is on the heterobilayer which show the attenuated A'_1 modes of both monolayers but no additional peaks corresponding to the chiral modes.

6.4.2/ Doubly resonant Raman spectroscopy

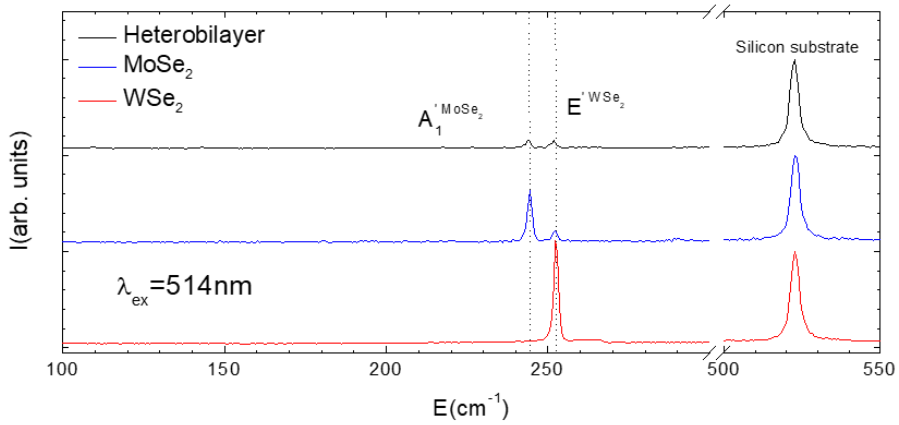

Fig6.4 Raman scattering spectrum measured at three different locations of Sample 1. The red and blue lines show spectra taken on the WSe_2 and $MoSe_2$ monolayers. The black line shows a spectrum taken on the heterobilayer.

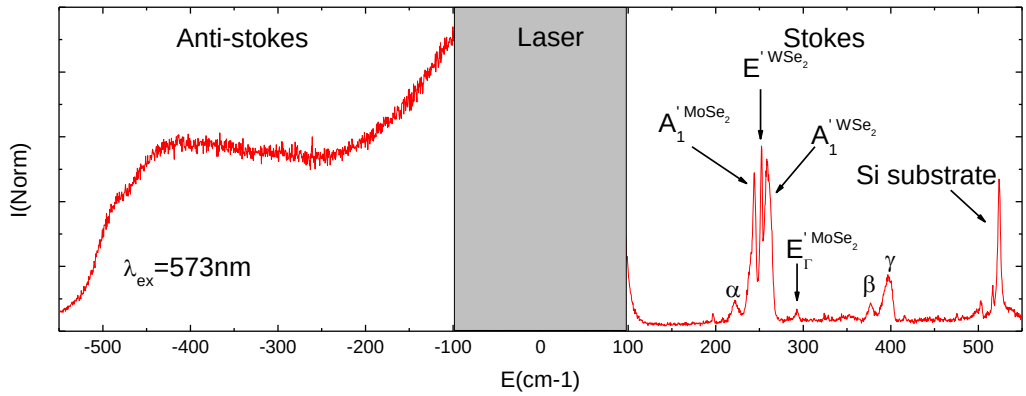

Fig6.5 Raman scattering Stokes (right) and anti-Stokes (left) spectra measured on the heterobilayer area of Sample1. The modes α,β and γ correspond to resonant Raman modes appearing in resonant excitation conditions (cf Ref(Zhang 2015)).

Our second attempt focuses on the measurement of the E'' phonon emitted during the resonant relaxation processes described above. Considering that the angular momentum flipping of the exciton requires the emission of a phonon carrying a PAM $\Delta J_z^{TMD} = +1$, we have carried out Raman spectroscopy measurements on Sample 1 while the magnetic field is tuned to the values of $B_{S1/S2}^{R1}$ and $B_{S1/S2}^{R2}$. The excitation energy is tuned in resonance with the WSe_2 B exciton similarly to the experimental conditions shown in [McDonnel 2021]. This resonant excitation is favorable for detailed Raman scattering spectroscopy as the efficiency of the Raman scattering processes is enhanced by the strong absorption leading to the observation of additional peaks in the Raman scattering spectrum. Fig(6.5) shows the Stokes and anti-Stokes spectra of the heterostructure area of Sample 1 under this resonant excitation. The Stokes spectrum shows the A'_1 modes of $MoSe_2$ and WSe_2 at 244 cm^{-1} and 259 cm^{-1} as well as the exalted E' mode of WSe_2 at 252 cm^{-1}. The three peaks α, β and γ located at 223 cm^{-1}, 376 cm^{-1} and 398 cm^{-1} corresponds to resonant Raman modes appearing in resonant excitation condition [Zhang 2015].Despite our efforts, we were unable to measure any anti-Stokes signal corresponding to a phonon mode.

Fig(6.6) shows the magneto-Raman spectrum of Sample 1 for magnetic field ranging from $B =$ 24,0 T to 24,7 T with steps of 0,05 T, this field range cover both resonances. The magnetic field has no effect on the energy position of the peaks already visible. Furthermore, we do not

observe the appearance of supplementary Raman peaks emerging at $E''_{MoSe2} = 170\ \mathrm{cm}^{-1}$ nor at $E''_{WSe2} = 175{,}96\ \mathrm{cm}^{-1}$. We have also measured the anti-Stokes spectrum of Sample 1 for the same range of the magnetic field: there are no signs of any new contribution to the Raman scattering spectra at the resonant conditions. We thus fail to measure Raman scattering signal that would illustrate the expected phonon emission.

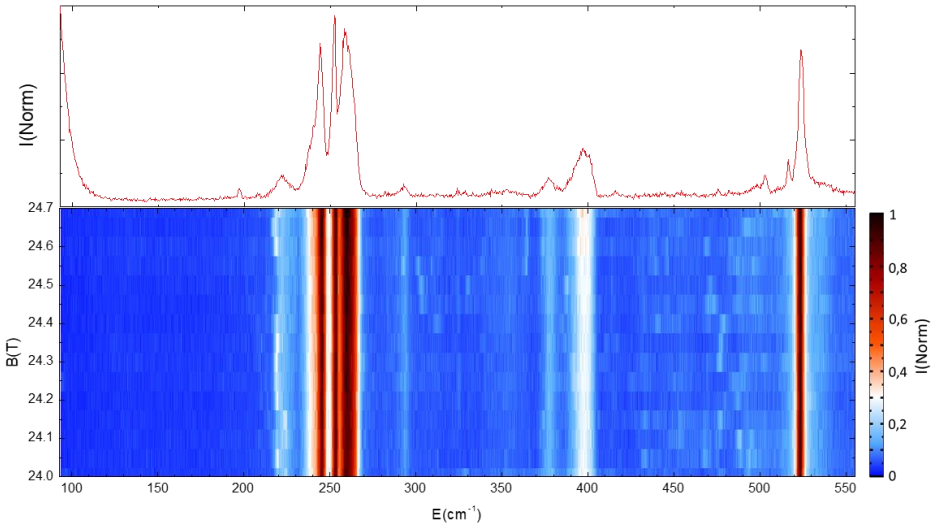

Fig6.6 Magneto-Raman Stokes spectrum measured on the heterobilayer area of Sample1. The magnetic field is swept from 24,0 T to 24,7 T with a step of 0,05 T across both resonances.

6.5/ Resonance intensity extinction profile

6.5.1/ General discussion

The diagonal profile of the resonance is the most unexpected consequence of the moiré reconstruction. As explained in Chapter 4: the excitation spot has a diameter of 1µm while the characteristic length of the homogeneous domains formed by the moiré surface reconstruction is of the order of 50 nm [Rosenberger 2020]. This means that our setup is collecting photons emitted from interlayer excitonic recombination stemming from a thousand of domain cells which collectively form the interlayer exciton photoluminescence spectrum. Considering that each of these emissions shows a g-factor close to $g = -16$ and thus originates from the same recombination path (the spin triplet interlayer exciton), one would expect that they all enter the resonance at the exact same value of the magnetic field or , in other words, that they have all have exactly the same g-factor. However it is clear from Fig(6.1.c and 6.1.d) that this is not the case. The extinction profile shows a "diagonal" shape where the low energy component of σ-polarized interlayer emission decreases in intensity at lower magnetic field. Similarly, the intensity of the high energy components decreases at a higher magnetic field. Since the energy of the interacting E'' phonon mode is independent of the local variation of the interlayer optical gap, we can only conclude that this extinction profile is shaped by fluctuations in the value of the g factor for the different components of the interlayer emission. This means that the observed "fluctuations" are not random, there seems to be a relation between the value of the g-factor and the emission energy.

This relation between the g-factor and the emission energy is coherent with the standard band theory expression for the orbital contribution g_d to the g-factor. In the paper [Roth 1959], the authors investigate oscillation in the infrared absorption spectra of semiconductors in the presence of a magnetic field. They develop the theory of magneto-absorption using the effective-mass approximation in the case of semiconductors with parabolic band structure. In the appendix, they generalize the effective mass approximation to include terms of higher order in k, and notably the orbital contribution of a single-electron band *i* due to virtual transitions to other bands j :

$$g_d = \sum_{j\neq i} \frac{|\langle i|\hat{p}_+|j\rangle|^2 - |\langle i|\hat{p}_-|j\rangle|^2}{m_0(\varepsilon_i - \varepsilon_j)} \qquad Eq(6.2)$$

Where $\hat{p}_\pm = \hat{p}_x \pm i\hat{p}_y$ are component of the momentum operator, ε_i and ε_j are the band energies and m_0 is the free electron mass. In the case of our heterobilayers, we are explaining the differences of the interlayer exciton components energy by the variations of the band energy across the surface of our collection spot. This means that in Eq(6.2), ε_i - ε_j does not refer to the interlayer exciton energy but to small fluctuations between close bands situated in a single layer (variation of the energy of the conduction or the valence band). Eq(6.2) gives a value of $\frac{\partial g_d}{\partial E}$ of the order of a few eV^{-1}. In the following text, we will get an experimental estimation of $\frac{\partial g_d}{\partial E}$ for Sample 1 and Sample 2 using two different approaches.

6.5.2/ Sample 2 first approach

In order to extract the relation between the g-factor g_i an individual emission at the energy E_i is to use the profile of Resonance 1 and Resonance 2 presented in Fig(6.1). We select different energies E_i along the broad interlayer excitonic peak and trace the intensity of the signal integrated at E_i as a function of the magnetic field (a schematic of this method can be found in Fig(6.7) . The magnetic field at which the intensity is the lowest is marked as the component resonance field $B_i^{R1/R2}$. We extract the value of B_i^{R1} and B_i^{R2} for each energy E_i.

At the first resonant field B_i^{R1}, the Zeeman energy of a component is considered equal to $E''_{MoSe2} = 22{,}3$ meV . We write :

$$g_i \mu_B B_i^{R1} = 22{,}3 \text{ meV} \qquad Eq(6.3)$$

Which give us the approximated value of g_i. The value of g_i as a function of E_i is represented on Fig(6.8.a) and shows a linear dependence, the error bars are calculated tacking into account the magnetic field resolution of 0,01 T in the measure of B_i^{R1} .A linear fit of $g_i(E_i)$ give the following relation for the first resonance :

$$\frac{\partial g_i}{\partial E_i} = -8{,}49 \pm 0{,}19 \text{ eV}^{-1} \qquad Eq(6.4)$$

This value is consistent with the order of magnitude estimated from Eq(6.2). We iterate the same process for the second resonance considering that when $B = B_i^{R2}$:

$$g_i \mu_B B_i^{R2} = 22{,}9 \text{ meV} \qquad Eq(6.5)$$

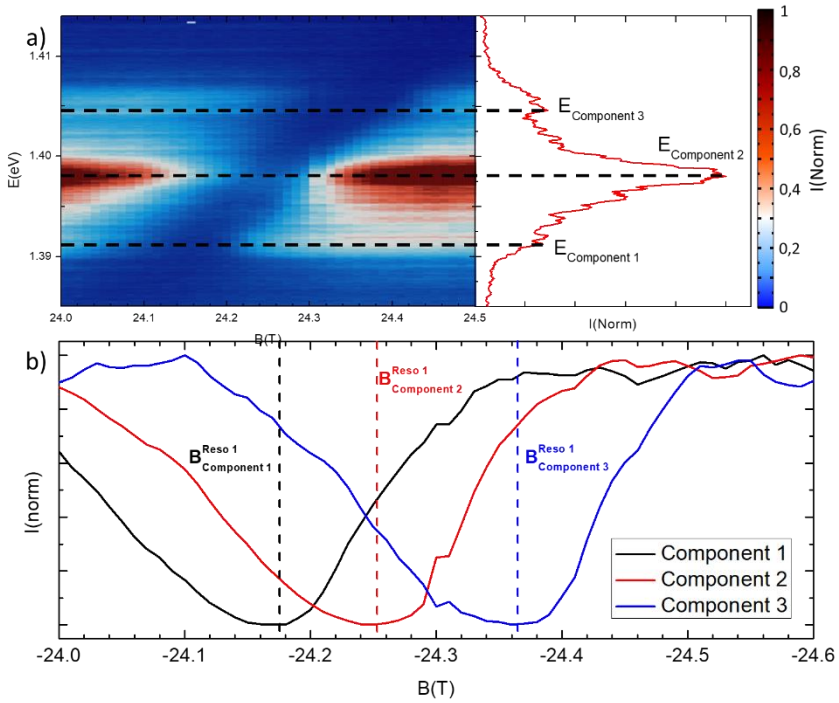

Fig6.7 g-factor extraction from the resonance profiles shown in Fig(6.1). **a)** Individual energies are selected along the exciton photoluminescence spectrum, the intensity of these energies as a function of the magnetic field are extracted. **b)** Intensity of the individual energies selected in a) as a function of the magnetic field, the value of $B_{component}^{Reso\ 1}$ is extracted from the minimum of intensity.

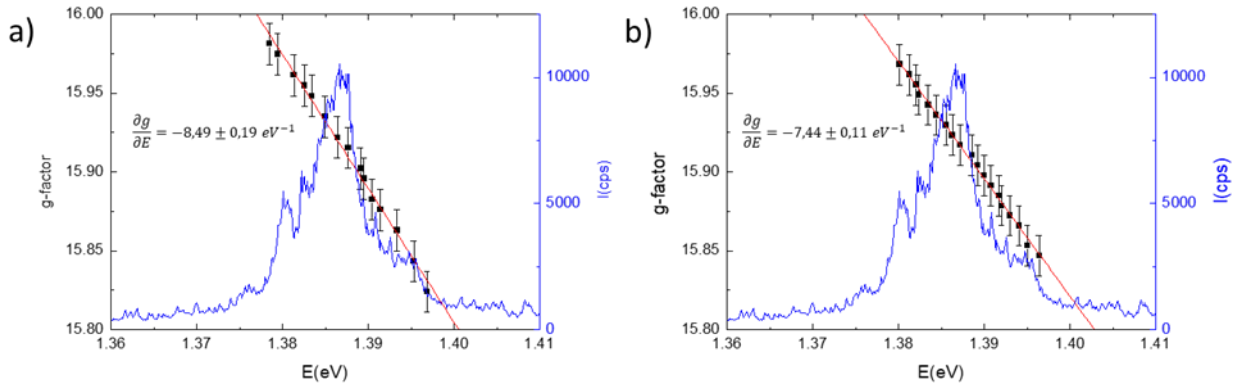

Fig6.8 Estimation of $\frac{\partial g}{\partial E}$ for Sample 2 using the method described in Fig(6.7) for **a)** Resonance 1 and **b)** Resonance 2

The value of g_i as a function of E_i is represented on Fig(6.8.b), a linear fit of $g_i(E_i)$ give the following relation for the second resonance :

$$\frac{\partial g_i}{\partial E_i} = -7{,}44 \pm 0{,}11\ \mathrm{eV}^{-1} \qquad Eq(6.6)$$

6.5.3/ Sample 2 second approach

To confirm our observation, we use a more direct approach : Fig(6.9) shows the result of a magneto-photoluminescence experiment on Sample 2 in the low excitation power regime. The

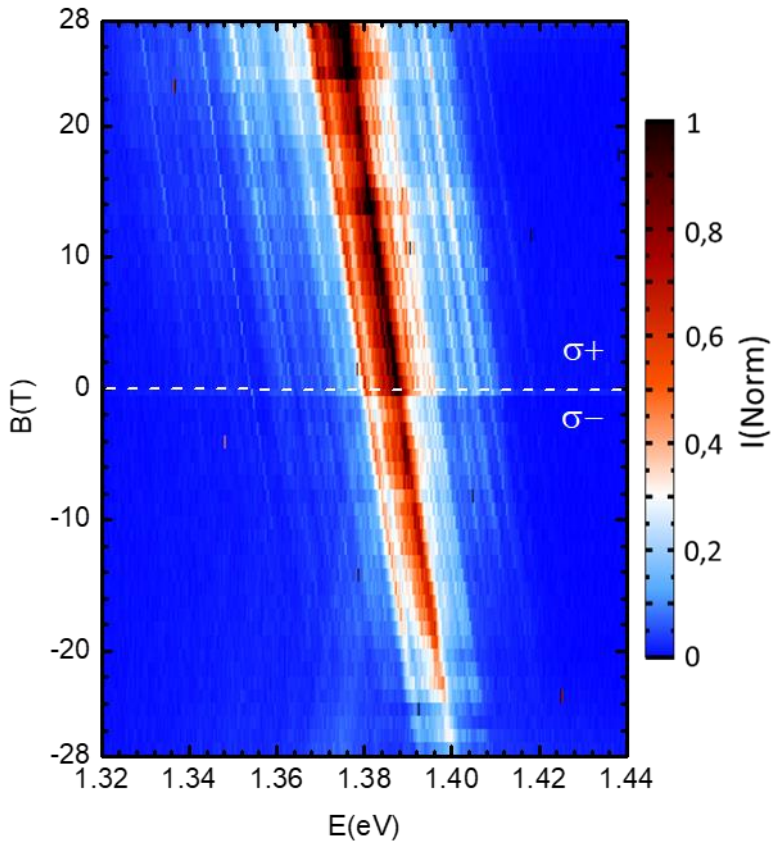

Fig6.9 Interlayer exciton magneto-photoluminescence spectrum measured on Sample 2. The temperature of the samples is $T = 4{,}5$ K with an excitation of 514 nm and with a power of 1 µW.

interlayer exciton photoluminescence spectrum is much more structured and the individual lines can be resolved separately and followed across most of the magnetic field range. Fig(6.10) shows the energy splitting of 14 different energies E_i distributed along the photoluminescence spectrum as well as the Zeeman energy for each line. We fit the linear dependency of the Zeeman energy for each line to get an estimation of g_i as a function of E_i. The resulting extracted g factors as a function of the component's energy can be seen on Fig(6.11). The linear fit of $g_i(E_i)$ give:

$$\frac{\partial g_i}{\partial E_i} = -4{,}43 \pm 1{,}09 \text{ eV}^{-1} \qquad Eq(6.7)$$

This approach cumulates the measurement errors of fourteen different linear fits, thus, our error bars are one order of magnitude higher. The value shown in Eq(6.7) is nevertheless of the same order of magnitude than the two previous values despite the differences of methodology.

6.5.4/ Sample 1

We estimate the g factor profile of Sample 1 in the same way. As explained previously, the interlayer exciton peak observed on Samples 1 is sharp compared to the one seen in Sample 2. We thus have measured the extinction profile of Sample 1 with an excitation of 5 µW.With this excitation condition, the structure of the interlayer exciton is broadened and several sharp individual lines can be resolved up close to the central peak. We proceed in the same way as

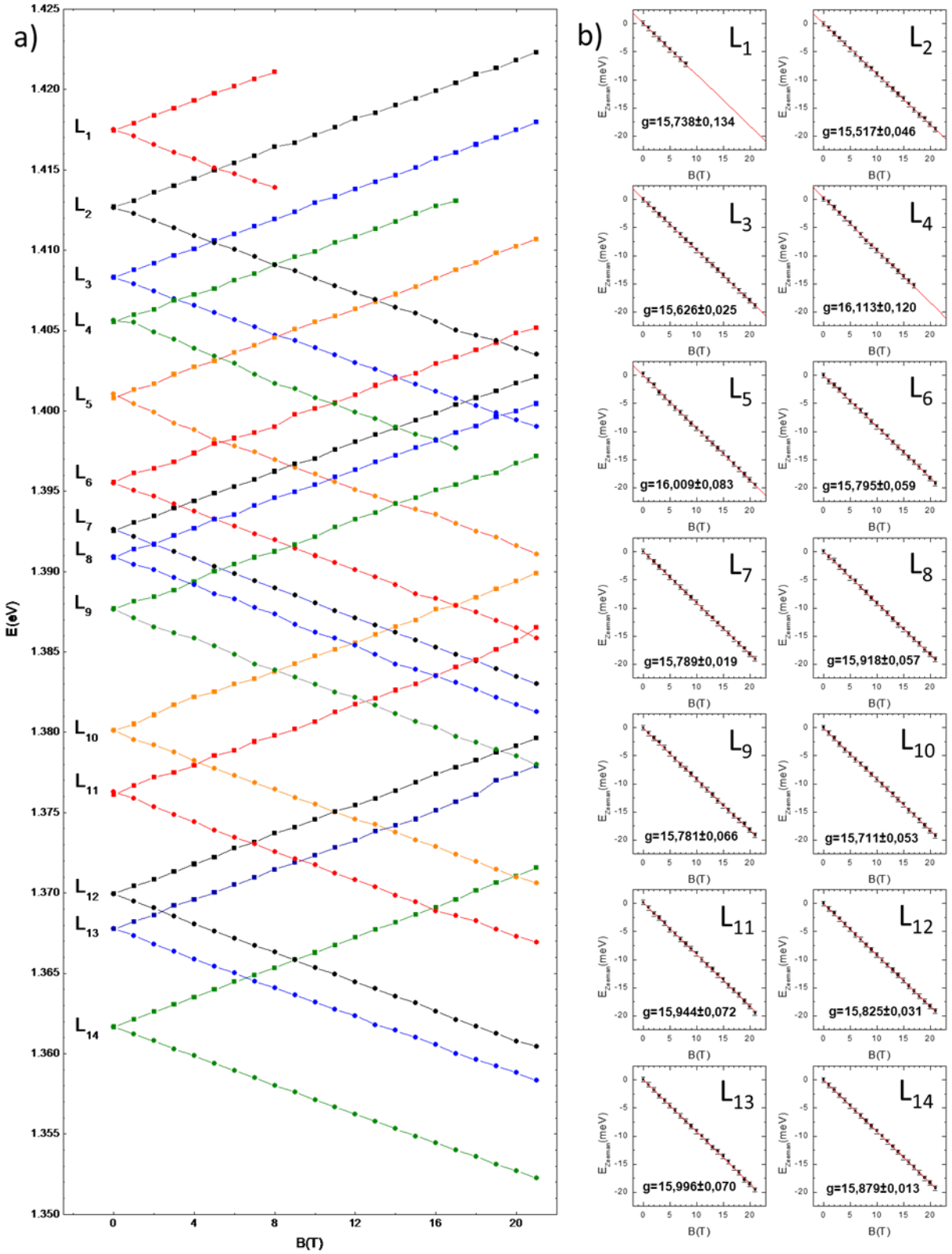

Fig6.10 a) Energy position of individual sharp lines as a function of the magnetic field. The position of the σ- (squares) and the σ+ (circles) emissions are plotted. **b)** Zeeman energy as function of the magnetic field for the 14 individual emissions shown in a), the g-factor of each individual line is extracted by a linear fit.

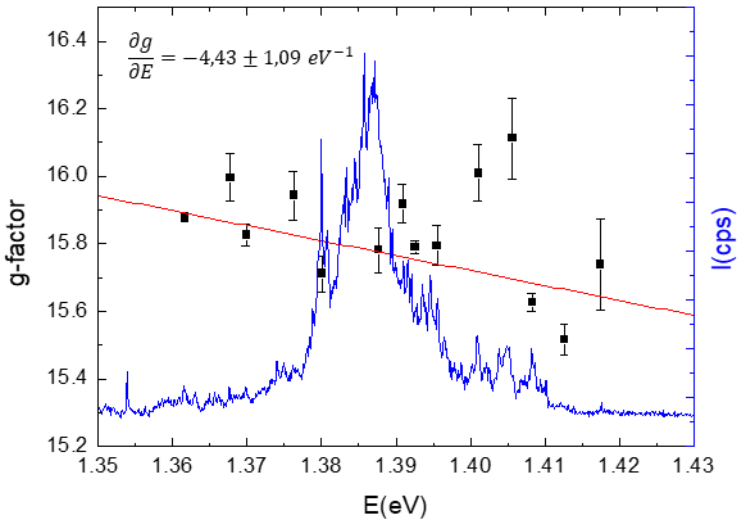

Fig6.11 Estimation of $\frac{\partial g}{\partial E}$ for Sample 2 using the method described in Fig(6.10).

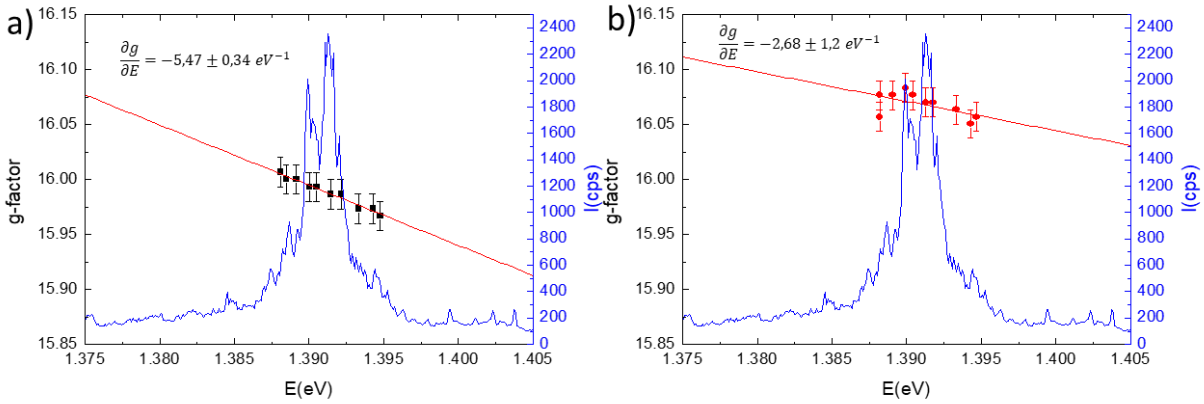

Fig6.12 : Estimation of $\frac{\partial g}{\partial E}$ for Sample 1 using the method described in Fig(6.7) for a) Resonance 1 a) and b) Resonance 2

with Sample 2. The first method (cf Fig(6.12)) give the following relation for the first and second resonances :

For Resonance 1 :

$$\frac{\partial g_i}{\partial E_i} = -5{,}47 \pm 0{,}34\ \mathrm{eV}^{-1} \qquad Eq(6.8)$$

For Resonance 2 :

$$\frac{\partial g_i}{\partial E_i} = -2.68 \pm 1{,}20\ \mathrm{eV}^{-1} \qquad Eq(6.9)$$

Note that while the two values of $\frac{\partial g_i}{\partial E_i}$ are consistent with each other, we find different values for $g_{component}$ in the case of Resonance 1 and Resonance 2. This is because the calculation of g_i is very sensitive to the presupposed value of the Zeeman energy at resonance. For reference, Fig(6.13) shows the values of g_i extracted from Resonance 2 with two different values of E''_{WSe_2} corresponding to our energy resolution (0,1 meV). However, $\frac{\partial g_i}{\partial E_i}$ is calculated with a fixed value of the Zeeman energy and is thus independent of our energy resolution. The estimated values are of the same order of magnitude than the values found in Samples 2.

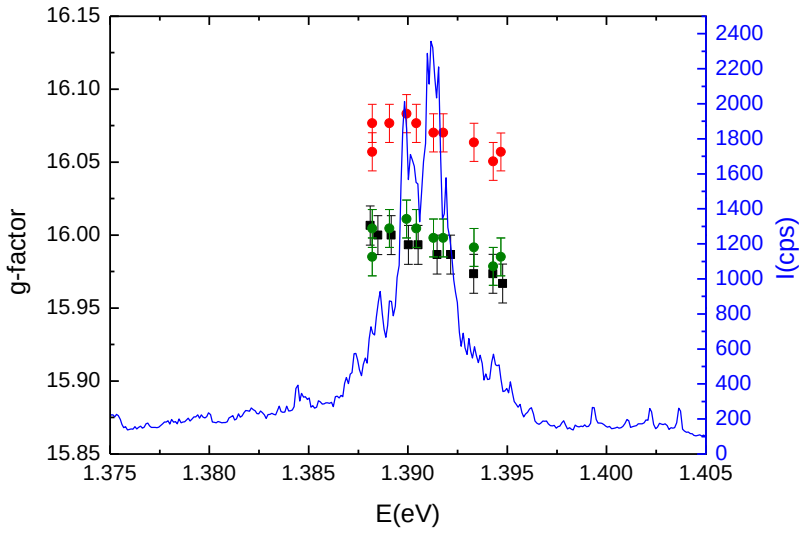

Fig6.13 : Estimation of $\frac{\partial g}{\partial E}$ for Sample 1 using the method described in Fig(6.7) for Resonance 1 (black plot), Resonance 2 with a value of $E''_{WSe_2} = 22{,}3$ meV (red plot) and Resonance 2 with a value of $E''_{WSe_2} = 22{,}2$ meV (green plot) .

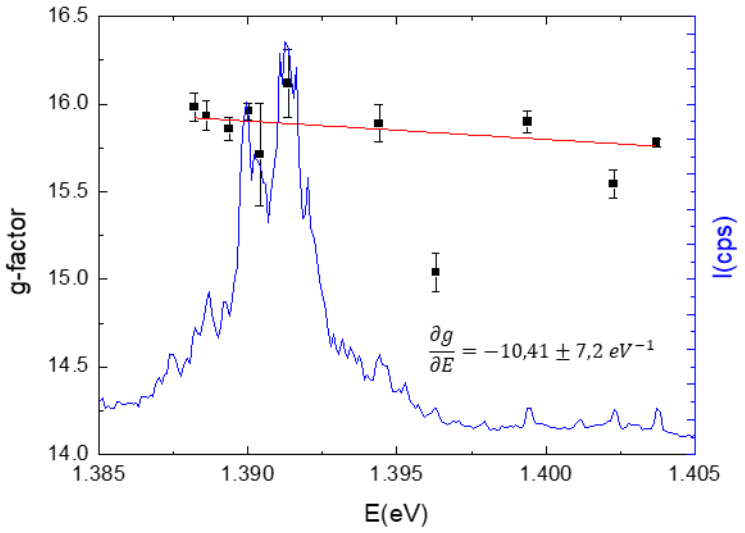

Fig6.14 : Estimation of $\frac{\partial g}{\partial E}$ for Sample 2 using the method described in Fig(6.10).

We also use the second approach described above, the resulting extracted g factors as a function of the component energy can be seen on Fig(6.14). The linear fit of $g_i(E_i)$ gives:

$$\frac{\partial g_i}{\partial E_i} = -10{,}41 \pm 7{,}20 \text{ eV}^{-1} \qquad Eq(6.10)$$

While being the highest value of $\frac{\partial g_d}{\partial E}$ estimated in both samples, it is still in line with the other values estimated above.

6.6/ Conclusion

In this chapter, we have presented an original interaction between the interlayer spin triplet state exciton and the chiral phonon modes E''_{MoSe2} and E''_{WSe2} arising from the constituent monolayers. Tacking advantage of the exceptionally high values of the excitonic g-factor measured in 60° aligned heterobilayers, we have tuned the excitonic Zeeman energy in the range of these optical phonons with an external high magnetic field. We have described a magnetic field resonant relaxation process in which the Γ point chiral phonons of the constituent monolayers transfer angular momentum to the σ- polarized interlayer emission, which, together with the C3 rotational symmetry, induces its relaxation onto the lower energy σ+ polarized state that can be revealed in polarization resolved photoluminescence experiments. The sharpness of this interaction allowed us to observe tiny variations of the g-factor stemming from local fluctuation of the band structure in the reconstructed surface of the heterobilayer. We have used two different methods to extract the dependency of the g-factor of these individual components and their emission energies.

Conclusion and outlook.

In this final section, we will summarize the main results presented in this PhD manuscript and discuss some ideas for future experiments that could be performed to further our understanding of interlayer excitons in TMD heterobilayers.

We have defined the selection rules for the recombination of interlayer excitons in the cases of H stacked (θ=0°) and R stacked (θ=60°) heterobilayers. We have established that, unlike TMD monolayers, both the spin singlet and the spin triplet states carry angular momentum along the z axis. We have presented a very simple model based on experimental observations in WSe_2 and $MoSe_2$ monolayers and used this model to estimate the value and the sign of interlayer exciton's g-factor for the interlayer spin singlet and spin triplet states in both the H stacked and R stacked configurations. We have observed that, while his model fails to describe the interaction of the band structure with the magnetic field in an H stacked heterobilayer , it provides an accurate estimation for the g-factor of the singlet and spin triplet states in R stacked heterobilayers. Further investigations are needed to explain the excitonic g-factors in H stacked heterobilayers, notably the positive value of $g = +6{,}7$.

Then, we have shown that the conservation of the total angular momentum in monolayers and heterobilayers of TMD not only defines the optical selection rules but also has some profound consequences on the electron-phonon interaction. We have highlighted an original relaxation process between the σ- and σ+ polarized components of the interlayer exciton in which the momentum conservation is satisfied by the emission of a chiral phonon. This process has been uncovered by the use of a magnetic field applied perpendicularly to the monolayer: tacking advantage of the high g-factor of the interlayer exciton spin triplet state, we have tuned the excitonic Zeeman energy in resonance with the energy of the E'' chiral phonon modes of the constituent monolayers. These phonons carry a pseudo angular momentum of ± 1 which, because of the C_3 symmetry, induce an excitonic spin flip that can be revealed in polarization resolved photoluminescence experiments. We have used this interaction to probe the influence of local fluctuations of the bandgap on the g-factors of interlayer excitons. While the high magnetic field required to activate this effect makes it an unlikely candidate for potential applications, this population switch, together with ability to control the twist angle of the heterobilayer, provides a tool to design heterostructures with tailored electronic properties. Thus, TMDs heterobilayers offer the possibility to control both the confinement of a quantum state and its relaxation. In the future, it would be interesting to reproduce the effect with singlet spin state interlayer exciton of a R stacked heterobilayer. Since this spin state shows a g-factor of $g = +12$, it is expected that this resonant relaxation effect would be observed for values of the magnetic field close to $B = 32T$. Furthemore, the positive sign of the g-factor implies a

relaxation of the high energy σ+ polarized interlayer component on the low energy σ- component.

To close this manuscript, I would like to present a list of publications to which i gave my contribution during this PhD. Some of these papers are related to the main topic of this manuscript and were cited in the bibliography.

1. Vaclavkova, D., Palit, M., Wyzula, J., Ghosh, S., Delhomme, A., Maity, S., ... & Potemski, M. (2021). Magnon polarons in the van der Waals antiferromagnet Fe PS 3. *Physical Review B*, *104*(13), 134437.
2. Neumann, T., Feldmann, S., Moser, P., Delhomme, A., Zerhoch, J., van de Goor, T., ... & Deschler, F. (2021). Manganese doping for enhanced magnetic brightening and circular polarization control of dark excitons in paramagnetic layered hybrid metal-halide perovskites. *Nature Communications*, *12*(1), 1-8.
3. Klein, J., Hötger, A., Florian, M., Steinhoff, A., Delhomme, A., Taniguchi, T., ... & Stier, A. V. (2021). Controlling exciton many-body states by the electric-field effect in monolayer MoS 2. *Physical Review Research*, *3*(2), L022009.
4. Kapuściński, P., Delhomme, A., Vaclavkova, D. *et al.* Rydberg series of dark excitons and the conduction band spin-orbit splitting in monolayer WSe_2. *Commun Phys* **4,** 186 (2021).
5. Delhomme, A., Vaclavkova, D., Slobodeniuk, A., Orlita, M., Potemski, M., Basko, D. M., & Faugeras, C. (2020). Flipping exciton angular momentum with chiral phonons in MoSe2/WSe2 heterobilayers. *2D Materials*, *7*(4), 041002.
6. Robert, C., Han, B., Kapuscinski, P., Delhomme, A., Faugeras, C., Amand, T., ... & Marie, X. (2020). Measurement of the spin-forbidden dark excitons in MoS 2 and MoSe 2 monolayers. *Nature communications*, *11*(1), 1-8.
7. Vaclavkova, D., Delhomme, A., Faugeras, C., Potemski, M., Bogucki, A., Suffczyński, J., ... & Saúl, A. (2020). Magnetoelastic interaction in the two-dimensional magnetic material MnPS3 studied by first principles calculations and Raman experiments. *2D Materials*, *7*(3), 035030.
8. Delhomme, A., Butseraen, G., Zheng, B., Marty, L., Bouchiat, V., Molas, M. R., ... & Faugeras, C. (2019). Magneto-spectroscopy of exciton Rydberg states in a CVD grown WSe2 monolayer. *Applied Physics Letters*, *114*(23), 232104.

Bibliography

[Baek 2020] Baek, H., Brotons-Gisbert, M., Koong, Z. X., Campbell, A., Rambach, M., Watanabe, K., ... & Gerardot, B. D. (2020). Highly energy-tunable quantum light from moiré-trapped excitons. Science advances, 6(37), eaba8526.

[Barbone 2018] Barbone, M., Montblanch, A. R. P., Kara, D. M., Palacios-Berraquero, C., Cadore, A. R., De Fazio, D., ... & Atatüre, M. (2018). Charge-tuneable biexciton complexes in monolayer WSe 2. Nature communications, 9(1), 3721.

[Bieniek 2020] Bieniek, M., Szulakowska, L., & Hawrylak, P. (2020). Band nesting and exciton spectrum in monolayer MoS 2. Physical Review B, 101(12), 125423.

[Boddison-Chouinard 2019] Boddison-Chouinard, J., Scarfe, S., Watanabe, K., Taniguchi, T., & Luican-Mayer, A. (2019). Flattening van der Waals heterostructure interfaces by local thermal treatment. Applied Physics Letters, 115(23), 231603.

[Brotons-Gisbert 2020] Brotons-Gisbert, M., Baek, H., Molina-Sánchez, A., Campbell, A., Scerri, E., White, D., ... & Gerardot, B. D. (2020). Spin–layer locking of interlayer excitons trapped in moiré potentials. Nature Materials, 19(6), 630-636.

[Brotons-Gisbert 2021] Brotons-Gisbert, M., Baek, H., Campbell, A., Watanabe, K., Taniguchi, T., & Gerardot, B. D. (2021). Moiré-trapped interlayer trions in a charge-tunable $WSe_2/MoSe_2$ heterobilayer. arXiv preprint arXiv:2101.07747.

[Cadiz 2017] Cadiz, F., Courtade, E., Robert, C., Wang, G., Shen, Y., Cai, H., ... & Urbaszek, B. (2017). Excitonic linewidth approaching the homogeneous limit in MoS 2-based van der Waals heterostructures. Physical Review X, 7(2), 021026.

[Cappelluti 2013] Cappelluti, E., Roldán, R., Silva-Guillén, J. A., Ordejón, P., & Guinea, F. (2013). Tight-binding model and direct-gap/indirect-gap transition in single-layer and multilayer MoS 2. Physical Review B, 88(7), 075409.

[Castellanos-Gomez 2014] Castellanos-Gomez, A., Buscema, M., Molenaar, R., Singh, V., Janssen, L., Van Der Zant, H. S., & Steele, G. A. (2014). Deterministic transfer of two-dimensional materials by all-dry viscoelastic stamping. 2D Materials, 1(1), 011002.

[Cebalos 2014] Ceballos, F., Bellus, M. Z., Chiu, H. Y., & Zhao, H. (2014). Ultrafast charge separation and indirect exciton formation in a MoS2–MoSe2 van der Waals heterostructure. ACS nano, 8(12), 12717-12724.

[Chen 2019] Chen, X., Lu, X., Dubey, S., Yao, Q., Liu, S., Wang, X., ... & Srivastava, A. (2019). Entanglement of single-photons and chiral phonons in atomically thin WSe 2. Nature Physics, 15(3), 221-227.

[Chernikov 2014] Chernikov, A., Berkelbach, T. C., Hill, H. M., Rigosi, A., Li, Y., Aslan, O. B., ... & Heinz, T. F. (2014). Exciton binding energy and nonhydrogenic Rydberg series in monolayer WS 2. Physical review letters, 113(7), 076802.

[Dean 2010] Dean, C. R., Young, A. F., Meric, I., Lee, C., Wang, L., Sorgenfrei, S., ... & Hone, J. (2010). Boron nitride substrates for high-quality graphene electronics. Nature nanotechnology, 5(10), 722-726.

[Delhomme 2019] Delhomme, A., Butseraen, G., Zheng, B., Marty, L., Bouchiat, V., Molas, M. R., ... & Faugeras, C. (2019). Magneto-spectroscopy of exciton Rydberg states in a CVD grown WSe2 monolayer. Applied Physics Letters, 114(23), 232104.

[Delhomme 2020] Delhomme, A., Vaclavkova, D., Slobodeniuk, A., Orlita, M., Potemski, M., Basko, D. M., & Faugeras, C. (2020). Flipping exciton angular momentum with chiral phonons in MoSe2/WSe2 heterobilayers. 2D Materials, 7(4), 041002.

[Ehrenreich 1960] Ehrenreich, H. (1960). Band structure and electron transport of GaAs. Physical Review, 120(6), 1951.

[Geim 2007] Geim, A. K., & Novoselov, K. S. (2010). The rise of graphene. In Nanoscience and technology: a collection of reviews from nature journals (pp. 11-19).

[Geim 2013] Geim, A. K., & Grigorieva, I. V. (2013). Van der Waals heterostructures. Nature, 499(7459), 419-425.

[Goryca 2019] Goryca, M., Li, J., Stier, A. V., Taniguchi, T., Watanabe, K., Courtade, E., ... & Crooker, S. A. (2019). Revealing exciton masses and dielectric properties of monolayer semiconductors with high magnetic fields. Nature communications, 10(1), 4172.

[Grzeszczyk 2020] Grzeszczyk, M., Molas, M. R., Nogajewski, K., Bartoš, M., Bogucki, A., Faugeras, C., ... & Potemski, M. (2020). The effect of metallic substrates on the optical properties of monolayer MoSe 2. Scientific reports, 10(1), 1-7.

[Grzeszczyk 2021] Grzeszczyk, M., Szpakowski, J., Slobodeniuk, A. O., Kazimierczuk, T., Bhatnagar, M., Taniguchi, T., ... & Molas, M. R. (2021). The optical response of artificially twisted MoS_2 bilayers. Scientific reports, 11(1), 17037.

[He 2014] He, K., Kumar, N., Zhao, L., Wang, Z., Mak, K. F., Zhao, H., & Shan, J. (2014). Tightly bound excitons in monolayer WSe 2. Physical review letters, 113(2), 026803.

[He 2020] He, M., Rivera, P., Van Tuan, D., Wilson, N. P., Yang, M., Taniguchi, T., ... & Xu, X. (2020). Valley phonons and exciton complexes in a monolayer semiconductor. Nature communications, 11(1), 618.

[Holler 2021] Holler, J., Selig, M., Kempf, M., Zipfel, J., Nagler, P., Katzer, M., ... & Korn, T. (2021). Interlayer exciton valley polarization dynamics in large magnetic fields. arXiv preprint arXiv:2111.03336.

[Hong 2014] Hong, X., Kim, J., Shi, S. F., Zhang, Y., Jin, C., Sun, Y., ... & Wang, F. (2014). Ultrafast charge transfer in atomically thin MoS 2/WS 2 heterostructures. Nature nanotechnology, 9(9), 682-686.

[Jauregui 2018] Jauregui, L. A., Joe, A. Y., Pistunova, K., Wild, D. S., High, A. A., Zhou, Y., ... & Kim, P. (2019). Electrical control of interlayer exciton dynamics in atomically thin heterostructures. *Science*, *366*(6467), 870-875.

[Jin 2019] Jin, C., Regan, E. C., Wang, D., Utama, M. I. B., Yang, C. S., Cain, J., ... & Wang, F. (2019). Identification of spin, valley and moiré quasi-angular momentum of interlayer excitons. Nature Physics, 15(11), 1140-1144.

[Joe 2019] Joe, A. Y., Jauregui, L. A., Pistunova, K., Lu, Z., Wild, D. S., Scuri, G., ... & Kim, P. (2019). Electrically controlled emission from triplet charged excitons in atomically thin heterostructures. *arXiv preprint arXiv:1912.07678*.

[Jones 2013] Jones, A. M., Yu, H., Ghimire, N. J., Wu, S., Aivazian, G., Ross, J. S., ... & Xu, X. (2013). Optical generation of excitonic valley coherence in monolayer WSe 2. Nature nanotechnology, 8(9), 634-638.

[Kang 2013] Kang, J., Tongay, S., Zhou, J., Li, J., & Wu, J. (2013). Band offsets and heterostructures of two-dimensional semiconductors. Applied Physics Letters, 102(1), 012111.

[Kapuscinski 2021] Kapuscinski, P., Delhomme, A., Vaclavkova, D., Slobodeniuk, A., Grzeszczyk, M., Bartos, M., ... & Potemski, M. (2021). Rydberg series of dark excitons and the conduction band spin-orbit splitting in monolayer WSe $ _2$. arXiv preprint arXiv:2102.12286.

[Kapuscinski 2020] Kapuściński, P., Vaclavkova, D., Grzeszczyk, M., Slobodeniuk, A. O., Nogajewski, K., Bartos, M., ... & Molas, M. R. (2020). Valley polarization of singlet and triplet trions in a WS 2 monolayer in magnetic fields. Physical Chemistry Chemical Physics, 22(34), 19155-19161.

[Karni 2021] Karni, O., Barré, E., Pareek, V., Georgaras, J. D., Man, M. K., Sahoo, C., ... & Dani, K. M. (2021). Moir\'e-localized interlayer exciton wavefunctions captured by imaging its electron and hole constituents. arXiv preprint arXiv:2108.01933.

[Keldish 1979] Keldysh, L. V. (1979). Coulomb interaction in thin semiconductor and semimetal films. Soviet Journal of Experimental and Theoretical Physics Letters, 29, 658.

[Klein 2021] Klein, J., Hötger, A., Florian, M., Steinhoff, A., Delhomme, A., Taniguchi, T., ... & Stier, A. V. (2021). Controlling exciton many-body states by the electric-field effect in monolayer MoS 2. Physical Review Research, 3(2), L022009.

[Kim 2017] Kim, S., Kim, K., Lee, J. U., & Cheong, H. (2017). Excitonic resonance effects and Davydov splitting in circularly polarized Raman spectra of few-layer WSe2. 2D Materials, 4(4), 045002.

[Koperski 2018] Koperski, M., Molas, M. R., Arora, A., Nogajewski, K., Bartos, M., Wyzula, J., ... & Potemski, M. (2018). Orbital, spin and valley contributions to Zeeman splitting of excitonic resonances in MoSe2, WSe2 and WS2 Monolayers. 2D Materials, 6(1), 015001.

[Kosmider 2013] Kośmider, K., González, J. W., & Fernández-Rossier, J. (2013). Large spin splitting in the conduction band of transition metal dichalcogenide monolayers. Physical Review B, 88(24), 245436.

[Kremser] Kremser, M., Brotons-Gisbert, M., Knörzer, J., Gückelhorn, J., Meyer, M., Barbone, M., ... & Finley, J. J. (2020). Discrete interactions between a few interlayer excitons trapped at a MoSe 2–WSe 2 heterointerface. npj 2D Materials and Applications, 4(1), 1-6.

[Laikhtman 2009] Laikhtman, B., & Rapaport, R. (2009). Exciton correlations in coupled quantum wells and their luminescence blue shift. Physical Review B, 80(19), 195313.

[Laturia 2018] Laturia, A., Van de Put, M. L., & Vandenberghe, W. G. (2018). Dielectric properties of hexagonal boron nitride and transition metal dichalcogenides: from monolayer to bulk. npj 2D Materials and Applications, 2(1), 6.

[Li 2015] Li, Y., Ludwig, J., Low, T., Chernikov, A., Cui, X., Arefe, G., ... & Heinz, T. F. (2014). Valley splitting and polarization by the Zeeman effect in monolayer MoSe 2. Physical review letters, 113(26), 266804.

[Li 2019] Li, Z., Wang, T., Jin, C., Lu, Z., Lian, Z., Meng, Y., ... & Shi, S. F. (2019). Emerging photoluminescence from the dark-exciton phonon replica in monolayer WSe 2. Nature communications, 10(1), 2469.

[Li 2020] Li, W., Lu, X., Dubey, S., Devenica, L., & Srivastava, A. (2020). Dipolar interactions between localized interlayer excitons in van der Waals heterostructures. Nature materials, 19(6), 624-629.

[Liu 2015] Liu, G. B., Xiao, D., Yao, Y., Xu, X., & Yao, W. (2015). Electronic structures and theoretical modelling of two-dimensional group-VIB transition metal dichalcogenides. *Chemical Society Reviews*, *44*(9), 2643-2663.

[Lu 2019] Lu, X., Li, X., & Yang, L. (2019). Modulated interlayer exciton properties in a two-dimensional moiré crystal. Physical Review B, 100(15), 155416.

[Lu 2020] Lu, Z., Rhodes, D., Li, Z., Van Tuan, D., Jiang, Y., Ludwig, J., ... & Smirnov, D. (2019). Magnetic field mixing and splitting of bright and dark excitons in monolayer MoSe2. 2D Materials, 7(1), 015017.

[Luo 2020] Luo, X., Zhao, Y., Zhang, J., Toh, M., Kloc, C., Xiong, Q., & Quek, S. Y. (2013). Effects of lower symmetry and dimensionality on Raman spectra in two-dimensional WSe 2. Physical Review B, 88(19), 195313.

[MacDonald 1986] MacDonald, A. H., & Ritchie, D. S. (1986). Hydrogenic energy levels in two dimensions at arbitrary magnetic fields. Physical Review B, 33(12), 8336.

[MacNeill 2015] MacNeill, D., Heikes, C., Mak, K. F., Anderson, Z., Kormányos, A., Zólyomi, V., ... & Ralph, D. C. (2015). Breaking of valley degeneracy by magnetic field in monolayer MoSe 2. Physical review letters, 114(3), 037401.

[Mak 2010] Mak, K. F., Lee, C., Hone, J., Shan, J., & Heinz, T. F. (2010). Atomically thin MoS 2: a new direct-gap semiconductor. Physical review letters, 105(13), 136805.

[Mak 2012] Mak, K. F., He, K., Shan, J., & Heinz, T. F. (2012). Control of valley polarization in monolayer MoS 2 by optical helicity. Nature nanotechnology, 7(8), 494-498.

[Mak 2016] Mak, K. F., & Shan, J. (2016). Photonics and optoelectronics of 2D semiconductor transition metal dichalcogenides. Nature Photonics, 10(4), 216-226.

[Manca 2017] Manca, M., Glazov, M. M., Robert, C., Cadiz, F., Taniguchi, T., Watanabe, K., ... & Urbaszek, B. (2017). Enabling valley selective exciton scattering in monolayer WSe2 through upconversion. Nature communications, 8(1), 14927.

[Marzin 1994] Marzin, J. Y., Gérard, J. M., Izraël, A., Barrier, D., & Bastard, G. (1994). Photoluminescence of single InAs quantum dots obtained by self-organized growth on GaAs. Physical review letters, 73(5), 716.

[McDonnel 2021] McDonnell, L. P., Viner, J. J., Ruiz-Tijerina, D. A., Rivera, P., Xu, X., Fal'ko, V. I., & Smith, D. C. (2021). Superposition of intra-and inter-layer excitons in twistronic MoSe2/WSe2 bilayers probed by resonant Raman scattering. 2D Materials, 8(3), 035009.

[Miller 2017] Miller, B., Steinhoff, A., Pano, B., Klein, J., Jahnke, F., Holleitner, A., & Wurstbauer, U. (2017). Long-lived direct and indirect interlayer excitons in van der Waals heterostructures. Nano letters, 17(9), 5229-5237.

[Molas 2017] Molas, M. R., Faugeras, C., Slobodeniuk, A. O., Nogajewski, K., Bartos, M., Basko, D. M., & Potemski, M. (2017). Brightening of dark excitons in monolayers of semiconducting transition metal dichalcogenides. 2D Materials, 4(2), 021003.

[Molas 2019] Molas, M. R., Slobodeniuk, A. O., Kazimierczuk, T., Nogajewski, K., Bartos, M., Kapuściński, P., ... & Potemski, M. (2019). Probing and manipulating valley coherence of dark excitons in monolayer WSe 2. Physical review letters, 123(9), 096803.

[Molas 2019'] Molas, M. R., Slobodeniuk, A. O., Nogajewski, K., Bartos, M., Babiński, A., Watanabe, K., ... & Potemski, M. (2019). Energy spectrum of two-dimensional excitons in a nonuniform dielectric medium. *Physical review letters*, *123*(13), 136801.

[Montblanch 2021] Montblanch, A. R. P., Kara, D. M., Paradisanos, I., Purser, C. M., Feuer, M. S., Alexeev, E. M., ... & Atatüre, M. (2021). Confinement of long-lived interlayer excitons in WS2/WSe2 heterostructures. Communications Physics, 4(1), 119.

[Nagler 2017] Nagler, P., Ballottin, M. V., Mitioglu, A. A., Mooshammer, F., Paradiso, N., Strunk, C., ... & Korn, T. (2017). Giant magnetic splitting inducing near-unity valley polarization in van der Waals heterostructures. Nature communications, 8(1), 1551.

[Nagler 2017'] Nagler, P., Plechinger, G., Ballottin, M. V., Mitioglu, A., Meier, S., Paradiso, N., ... & Korn, T. (2017). Interlayer exciton dynamics in a dichalcogenide monolayer heterostructure. 2D Materials, 4(2), 025112.

[Nayak 2017] Nayak, P. K., Horbatenko, Y., Ahn, S., Kim, G., Lee, J. U., Ma, K. Y., ... & Shin, H. S. (2017). Probing evolution of twist-angle-dependent interlayer excitons in MoSe2/WSe2 van der Waals heterostructures. ACS nano, 11(4), 4041-4050.

[Park 2021] Park, S., Han, B., Boule, C., Paget, D., Rowe, A., Sirotti, F., ... & Cadiz, F. (2021). Imaging Seebeck drift of excitons and trions in MoSe2 monolayers. arXiv preprint arXiv:2105.09617.

[Parzefall 2021] Parzefall, P., Holler, J., Scheuck, M., Beer, A., Lin, K. Q., Peng, B., ... & Schüller, C. (2021). Moiré phonons in twisted MoSe2–WSe2 heterobilayers and their correlation with interlayer excitons. 2D Materials, 8(3), 035030.

[Phillips 2021] Phillips, M., & Hellberg, C. S. (2019). Commensurate structures in twisted transition metal dichalcogenide heterobilayers. arXiv preprint arXiv:1909.02495.

[Ponomarev 2018] Ponomarev, E., Ubrig, N., Gutierrez-Lezama, I., Berger, H., & Morpurgo, A. F. (2018). Semiconducting van der Waals interfaces as artificial semiconductors. Nano letters, 18(8), 5146-5152.

[Psilodimitrakopoulos 2019] Psilodimitrakopoulos, S., Mouchliadis, L., Paradisanos, I., Kourmoulakis, G., Lemonis, A., Kioseoglou, G., & Stratakis, E. (2019). Twist angle mapping in layered ws 2 by polarization-resolved second harmonic generation. Scientific reports, 9(1), 14285.

[Pulkin 2016] Pulkin, A., & Yazyev, O. V. (2016). Spin-and valley-polarized transport across line defects in monolayer MoS 2. Physical Review B, 93(4), 041419.

[Raja 2017] Raja, A., Chaves, A., Yu, J., Arefe, G., Hill, H. M., Rigosi, A. F., ... & Chernikov, A. (2017). Coulomb engineering of the bandgap and excitons in two-dimensional materials. Nature communications, 8(1), 15251.

[Rhodes 2019] Rhodes, D., Chae, S. H., Ribeiro-Palau, R., & Hone, J. (2019). Disorder in van der Waals heterostructures of 2D materials. Nature materials, 18(6), 541-549.

[Rivera 2015] Rivera, P., Schaibley, J. R., Jones, A. M., Ross, J. S., Wu, S., Aivazian, G., ... & Xu, X. (2015). Observation of long-lived interlayer excitons in monolayer MoSe 2–WSe 2 heterostructures. Nature communications, 6(1), 6242.

[Robert 2017] Robert, C., Amand, T., Cadiz, F., Lagarde, D., Courtade, E., Manca, M., ... & Marie, X. (2017). Fine structure and lifetime of dark excitons in transition metal dichalcogenide monolayers. Physical review B, 96(15), 155423.

[Robert 2020] Robert, C., Han, B., Kapuscinski, P., Delhomme, A., Faugeras, C., Amand, T., ... & Marie, X. (2020). Measurement of the spin-forbidden dark excitons in MoS 2 and MoSe 2 monolayers. Nature communications, 11(1), 4037.

[Rodrigez 2021] Rodriguez, A., Kalbáč, M., & Frank, O. (2021). Strong localization effects in the photoluminescence of transition metal dichalcogenide heterobilayers. *2D Materials*, *8*(2), 025028.

[Rosenberger 2020] Rosenberger, M. R., Chuang, H. J., Phillips, M., Oleshko, V. P., McCreary, K. M., Sivaram, S. V., ... & Jonker, B. T. (2020). Twist angle-dependent atomic reconstruction and moiré patterns in transition metal dichalcogenide heterostructures. ACS nano, 14(4), 4550-4558.

[Ross 2013] Ross, J. S., Wu, S., Yu, H., Ghimire, N. J., Jones, A. M., Aivazian, G., ... & Xu, X. (2013). Electrical control of neutral and charged excitons in a monolayer semiconductor. Nature communications, 4(1), 1474.

[Roth 1959] Roth, L. M., Lax, B., & Zwerdling, S. (1959). Theory of optical magneto-absorption effects in semiconductors. Physical Review, 114(1), 90.

[Rytova 1967] Rytova, N. S. (2018). Screened potential of a point charge in a thin film. arXiv preprint arXiv:1806.00976.

[Santosh 2015] Santosh, K. C., Zhang, C., Hong, S., Wallace, R. M., & Cho, K. (2015). Phase stability of transition metal dichalcogenide by competing ligand field stabilization and charge density wave. 2D Materials, 2(3), 035019.

[Seyler 2017] Seyler, K. L., Rivera, P., Yu, H., Wilson, N. P., Ray, E. L., Mandrus, D. G., ... & Xu, X. (2019). Signatures of moiré-trapped valley excitons in $MoSe_2/WSe_2$ heterobilayers. *Nature*, *567*(7746), 66-70.

[Shan 1996] Shan, W., Little, B. D., Fischer, A. J., Song, J. J., Goldenberg, B., Perry, W. G., ... & Davis, R. F. (1996). Binding energy for the intrinsic excitons in wurtzite GaN. Physical Review B, 54(23), 16369.

[Shree 2021] Shree, S., Paradisanos, I., Marie, X., Robert, C., & Urbaszek, B. (2021). Guide to optical spectroscopy of layered semiconductors. Nature Reviews Physics, 3(1), 39-54.

[Soubelet 2021] Soubelet, P., Bruchhausen, A. E., Fainstein, A., Nogajewski, K., & Faugeras, C. (2016). Resonance effects in the Raman scattering of monolayer and few-layer MoSe 2. Physical Review B, 93(15), 155407.

[Splendiani 2010] Splendiani, A., Sun, L., Zhang, Y., Li, T., Kim, J., Chim, C. Y., ... & Wang, F. (2010). Emerging photoluminescence in monolayer MoS2. Nano letters, 10(4), 1271-1275.

[Srivastava 2015] Srivastava, A., Sidler, M., Allain, A. V., Lembke, D. S., Kis, A., & Imamoğlu, A. (2015). Valley Zeeman effect in elementary optical excitations of monolayer WSe 2. Nature Physics, 11(2), 141-147.

[Stier 2016] Stier, A. V., Wilson, N. P., Clark, G., Xu, X., & Crooker, S. A. (2016). Probing the influence of dielectric environment on excitons in monolayer WSe2: insight from high magnetic fields. Nano letters, 16(11), 7054-7060.

[Stolyarova 2009] Stolyarova, E., Stolyarov, D., Bolotin, K., Ryu, S., Liu, L., Rim, K. T., ... & Flynn, G. (2009). Observation of graphene bubbles and effective mass transport under graphene films. Nano letters, 9(1), 332-337.

Tran[2019] Tran, K., Moody, G., Wu, F., Lu, X., Choi, J., Kim, K., ... & Li, X. (2019). Evidence for moiré excitons in van der Waals heterostructures. Nature, 567(7746), 71-75.

[Vaclavkova 2018] Vaclavkova, D., Wyzula, J., Nogajewski, K., Bartos, M., Slobodeniuk, A. O., Faugeras, C., ... & Molas, M. R. (2018). Singlet and triplet trions in WS2 monolayer encapsulated in hexagonal boron nitride. Nanotechnology, 29(32), 325705.

[Van Tuan Dinh 2018] Van Tuan, D., Yang, M., & Dery, H. (2018). Coulomb interaction in monolayer transition-metal dichalcogenides. Physical Review B, 98(12), 125308.

[Walck 1998] Walck, S. N., & Reinecke, T. L. (1998). Exciton diamagnetic shift in semiconductor nanostructures. Physical Review B, 57(15), 9088.

[Wang 2015] Wang, G., Marie, X., Gerber, I., Amand, T., Lagarde, D., Bouet, L., ... & Urbaszek, B. (2015). Giant enhancement of the optical second-harmonic emission of WSe_2 monolayers by laser excitation at exciton resonances. Physical review letters, 114(9), 097403.

[Wang 2017] Wang, G., Robert, C., Glazov, M. M., Cadiz, F., Courtade, E., Amand, T., ... & Marie, X. (2017). In-plane propagation of light in transition metal dichalcogenide monolayers: optical selection rules. Physical review letters, 119(4), 047401.

[Wang 2018] Wang, G., Chernikov, A., Glazov, M. M., Heinz, T. F., Marie, X., Amand, T., & Urbaszek, B. (2018). Colloquium: Excitons in atomically thin transition metal dichalcogenides. Reviews of Modern Physics, 90(2), 021001.

[Wang 2019] Wang, T., Miao, S., Li, Z., Meng, Y., Lu, Z., Lian, Z., ... & Shi, S. F. (2019). Giant valley-Zeeman splitting from spin-singlet and spin-triplet interlayer excitons in WSe2/MoSe2 heterostructure. Nano letters, 20(1), 694-700.

[Weston 2021] Weston, A., Zou, Y., Enaldiev, V., Summerfield, A., Clark, N., Zólyomi, V., ... & Gorbachev, R. (2020). Atomic reconstruction in twisted bilayers of transition metal dichalcogenides. *Nature Nanotechnology*, *15*(7), 592-597.

[Yi 2015] Yi, M., & Shen, Z. (2015). A review on mechanical exfoliation for the scalable production of graphene. Journal of Materials Chemistry A, 3(22), 11700-11715.

[Yu 2017] Yu, H., Liu, G. B., Tang, J., Xu, X., & Yao, W. (2017). Moiré excitons: From programmable quantum emitter arrays to spin-orbit–coupled artificial lattices. Science advances, 3(11), e1701696.

[Yuan 2020] Yuan, L., Zheng, B., Kunstmann, J., Brumme, T., Kuc, A. B., Ma, C., ... & Huang, L. (2020). Twist-angle-dependent interlayer exciton diffusion in WS 2–WSe 2 heterobilayers. Nature materials, 19(6), 617-623.

[Zaslow 1967] Zaslow, B., & Zandler, M. E. (1967). Two-dimensional analog to the hydrogen atom. American Journal of Physics, 35(12), 1118-1119.

[Zhang 2015] Zhang, X., Qiao, X. F., Shi, W., Wu, J. B., Jiang, D. S., & Tan, P. H. (2015). Phonon and Raman scattering of two-dimensional transition metal dichalcogenides from monolayer, multilayer to bulk material. Chemical Society Reviews, 44(9), 2757-2785.

[Zhang 2015'] Zhang, L., & Niu, Q. (2015). Chiral phonons at high-symmetry points in monolayer hexagonal lattices. Physical review letters, 115(11), 115502.

[Zhang 2017] Zhang, X. X., Cao, T., Lu, Z., Lin, Y. C., Zhang, F., Wang, Y., ... & Heinz, T. F. (2017). Magnetic brightening and control of dark excitons in monolayer WSe 2. Nature nanotechnology, 12(9), 883-888.

[Zhang 2018] Zhang, N., Surrente, A., Baranowski, M., Maude, D. K., Gant, P., Castellanos-Gomez, A., & Plochocka, P. (2018). Moiré intralayer excitons in a MoSe2/MoS2 heterostructure. Nano letters, 18(12), 7651-7657.

[Zhou 2017] Zhou, Y., Scuri, G., Wild, D. S., High, A. A., Dibos, A., Jauregui, L. A., ... & Park, H. (2017). Probing dark excitons in atomically thin semiconductors via near-field coupling to surface plasmon polaritons. Nature nanotechnology, 12(9), 856-860.

[Zhu 2018] Zhu, H., Yi, J., Li, M. Y., Xiao, J., Zhang, L., Yang, C. W., ... & Zhang, X. (2018). Observation of chiral phonons. Science, 359(6375), 579-582.

[Zimmermann 2020] Zimmermann, J. E., Kim, Y. D., Hone, J. C., Höfer, U., & Mette, G. (2020). Directional ultrafast charge transfer in a WSe 2/MoSe 2 heterostructure selectively probed by time-resolved SHG imaging microscopy. Nanoscale Horizons, 5(12), 1603-1609.

[Zinkiewicz 2021] Zinkiewicz, M., Woźniak, T., Kazimierczuk, T., Kapuscinski, P., Oreszczuk, K., Grzeszczyk, M., ... & Molas, M. R. (2021). Excitonic complexes in n-doped WS2 monolayer. Nano letters, 21(6), 2519-2525.

[Zipfel 2018] Zipfel, J., Holler, J., Mitioglu, A. A., Ballottin, M. V., Nagler, P., Stier, A. V., ... & Chernikov, A. (2018). Spatial extent of the excited exciton states in WS 2 monolayers from diamagnetic shifts. Physical Review B, 98(7), 075438.

Résumé de la thèse en français

Les dichalcogénures de métaux de transition.

Les dichalcogénures de métaux de transition (TMD) sont une famille de matériaux de formule chimique MX2, où M est un atome de métal de transition (tel que Ti,V,Mo ou W) et X est l'un des trois chalcogènes Se,S ou Te. Plus de 60 TMD différents sont actuellement connus et ils peuvent présenter des propriétés très différentes selon la combinaison métal/atome de chalcogène [Pulkin 2016]. La plupart de ces matériaux sont dits stratifiés : l'état massif consiste en un empilement de plans monoatomiques maintenus ensemble par la force de van der Waals (vdW). Dans ce manuscrit, nous nous limiterons aux TMD semi-conducteurs et utiliserons ce terme général pour décrire uniquement les composés comportant un métal de transition de la sixième colonne du tableau périodique (c'est-à-dire Mo ou W) avec des atomes S ou Se comme chalcogène. Ces composés cristallisent dans les phases 2H.

Dans la cellule cristalline des TMD semi-conducteurs du groupe VI, chaque atome de métal est pris en tenaille entre deux plans de trois atomes de chalcogène. La répétition dans le plan de cette cellule façonne la monocouche en trois plans atomiques parallèles, un plan central d'atome de métaux de transition entre deux plans de chalcogènes. Il en résulte un réseau hexagonal presque 2D (0,6 nanomètre d'épaisseur) : un atome de métal occupe le site A, tandis que le site B est occupé par deux atomes de chalcogène et le site C est inoccupé. Dans le cas de la monocouche, cela brise la symétrie d'inversion dans la cellule et réduit son groupe de symétrie de C6 à C3. La zone de Brillouin de la monocouche est également hexagonale, mais du fait de

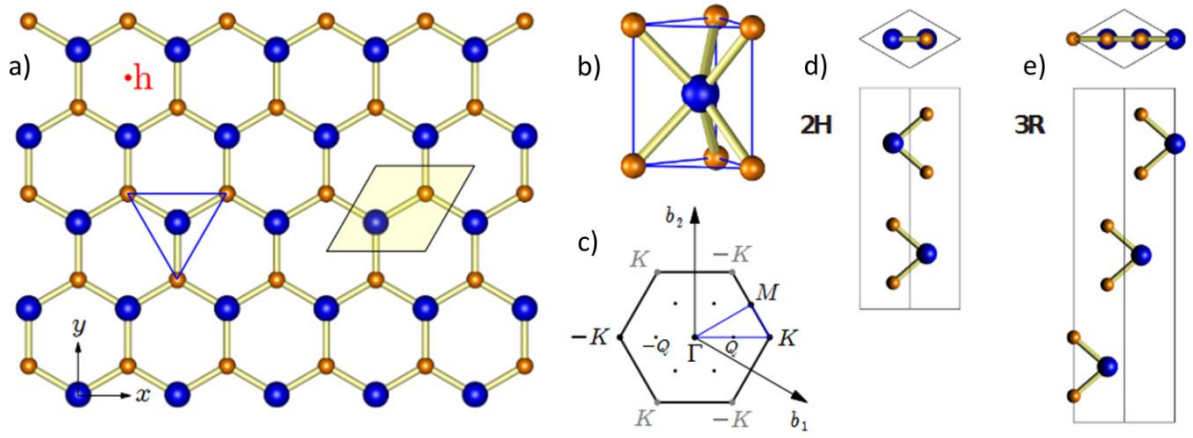

FigI a) Vue de dessus d'une monocouche de TMD. Les sphères bleues et orange représentent respectivement les atomes M et X. Le losange jaune clair est la maille unitaire 2D avec *a* le paramètre de maille. **b)** Cellule cristalline trigonale prismatique, correspondant au triangle bleu en vue de dessus. **c)** La première zone Brillouin. b1 et b2 sont les vecteurs de réseau réciproque. d) Configuration d'empilement 2H. **e)** Configuration d'empilement 3R. Figure adaptée de [Liu 2015].

cette brisure de symétrie, les points K voisins ne peuvent être considérés comme équivalents ; cela donne lieu à une alternance de vallées +K et -K aux angles de l'hexagone liées par la symétrie d'inversion du temps (cf Fig(I)). La transition de l'état massif à la monocouche modifie également la structure de bande électronique du matériau. Le gap du semi-conducteur, qui est indirect dans l'état massif ainsi que dans les multicouches, devient direct dans le cas de la monocouche [Cappelluti 2013].

Les excitons dans les TMD.

Du fait de la quasi-bi dimensionnalité des monocouches de TMD, l'interaction Coulombienne y est renforcée et l'électron et le trou existent en tant qu'état lié avec une énergie inférieure au gap électronique E_G du matériau : l'exciton, qui se recombine en un photon d'énergie E_{PL} inférieure à E_G. La différence entre $E_G$et E_{PL} définit l'énergie de liaison E_B qui est de l'ordre de $500meV$ dans les monocouches de TMD [Chenikov 2014, Wang 2015].

En analogie avec le modèle 2D de l'atome d'hydrogène (cf Fig(II)) [Zazlow 1967], l'exciton peut être décrit comme un état fondamental, l'état 1s, et une série d'états excités dénommés 2s,3s,etc... Cependant, il est impossible de décrire complètement la série de Rydberg excitonique à l'aide du modèle hydrogénoide 2D [MacDonald 1986]. Cela est attribué au fait que le potentiel de Coulomb ne prend pas en compte une propriété fondamentale des excitons des TMD : le champ électrique du dipôle excitonique traverse les limites de la monocouche et pénètre le milieu environnant. Cela signifie que l'écrantage diélectrique n'est pas seulement défini par la constante diélectrique du matériau, mais également par l'environnement de la monocouche.

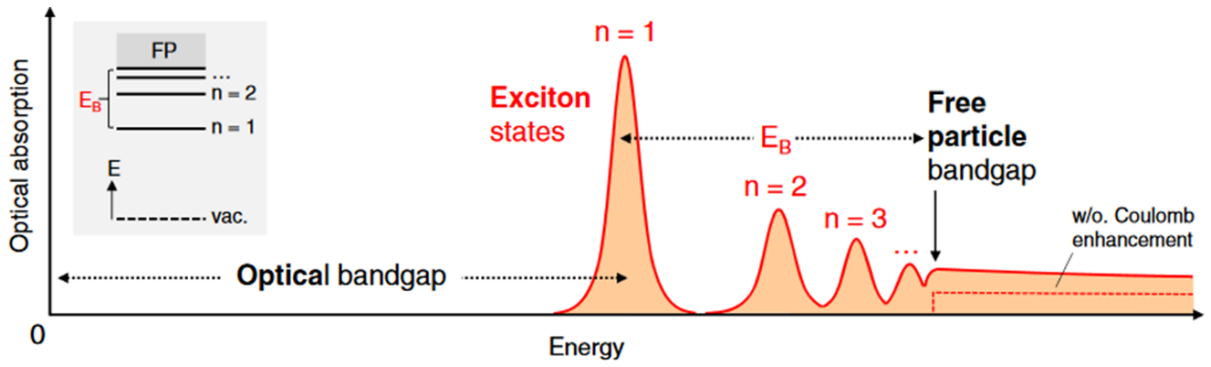

Fig.II Absorption optique d'un semi-conducteur 2D idéal incluant la série de Rydberg excitonique à l'intérieur du gap. L'encart montre le schéma des niveaux d'énergie de la série de Rydberg excitonique, les états excités sont désignés par leur nombre quantique principal n, l'énergie de liaison de l'état fondamental de l'exciton est notée E_B .Figure adaptée de [Wang 2017]

Ainsi, un potentiel d'écrantage tenant compte de l'environnement diélectrique voisin est nécessaire: le potentiel de Rytova-Keldysh [Rytova 1967, Keldish 1979], mieux adapté pour décrire l'interaction électrostatique de deux charges e_1 et e_2 au sein d'un diélectrique bidimensionnel entre deux couches de constante diélectrique ε_t et ε_b..

$$V_{RK}(r) = \frac{e_1 e_2}{r_0}\frac{\pi}{2}\left(H_0\left(\frac{(\varepsilon_t+\varepsilon_b)r}{2r_0}\right) - Y_0\left(\frac{(\varepsilon_t+\varepsilon_b)r}{2r_0}\right)\right) \qquad Eq(I)$$

Ou H_0et Y_0 sont les fonctions de Struve et de Bessel.

Couplage spin orbite et règles de sélection

Le couplage spin orbite (SOC) couple le moment angulaire L et le spin S avec $H_{SO} = L.S$ et peut être vu comme un champ magnétique clivant les bandes selon leurs composantes de spin et les séparant de leur position d'énergie dégénérée par une énergie E_{SOC} [Kosmider 2013]. La valeur du couplage spin orbite au point K divise donc les TMD en deux catégories, en fonction de l'indice de spin de la sous-bande de conduction la plus basse. Si le SOC est négatif, la sous-bande de conduction la plus basse et la sous-bande de valence la plus haute ont le même indice de spin, le matériau est classé comme « bright » si l'indice de spin est différent (SOC positif), il s'il est classé comme « dark » [Koperski 2018].

La Fig(III) montre la structure de bande de deux monocouche « bright » et « dark » les sous-bandes ont été indexées avec leur moment angulaire respectif J_z. En raison de la symétrie d'inversion temporelle, le moment angulaire dans +K et -K prend des valeurs opposées mais ont la même amplitude. Les règles de sélection excitonique sont ensuite appliquées à toute transition d'une sous-bande de conduction à une sous-bande de valence en calculant le changement de moment cinétique ΔJ_z. Dans le cas des transitions entre des sous-bandes avec le même indice de spin, telles que l'état fondamental des matériaux « bright »: $\Delta J_z = +1$ au point K et correspond au couplage avec un photon polarisé $\sigma +$ et $\Delta J_z = -1$ au point -K correspond à un couplage avec un photon polarisé $\sigma -$. Les excitons qui se recombinent à partir de cet état de spin singulet sont appelés excitons « bright». La transition de basse énergie dans les matériaux «dark» est un état de spin triplet. Pour cette transition, le changement de moment cinétique ΔJ_z est nul dans les deux vallées. Cela signifie que les excitons se recombinant à partir de ces transitions d'état de spin triplet ne portent pas de moment angulaire le long de l'axe z et sont donc dénommés excitons «dark ».

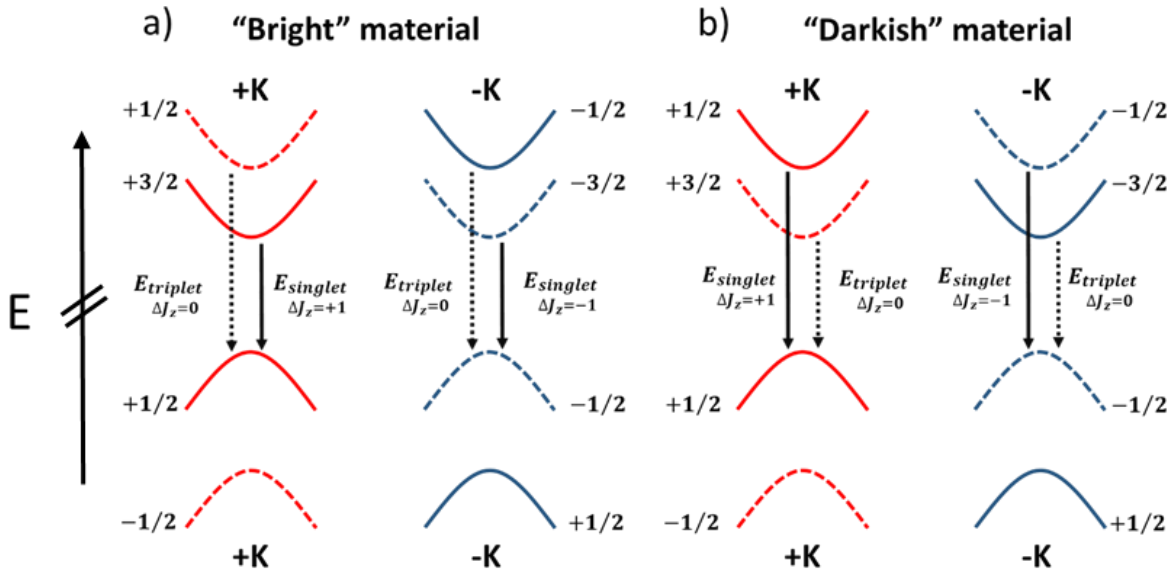

Fig.III a) Structure de bandes des vallées +K et –K d'une monocouche « bright » **b)** Structure de bandes des vallées +K et –K d'une monocouche « dark ». Les transitions optiques « bright » sont représentées par des flèches pleines (transitions « dark » par des flèches en pointillés). Chaque sous-bande est indexée par J_z.

Effet Zeeman dans les TMD

Un champ magnétique appliqué perpendiculairement au plan de la monocouche sépare les énergies des vallées +K et -K en agissant sur la structure de bande électronique en fonction des indices de spin et de vallées des sous bandes. Ainsi, l'énergie de l'émission polarisée $\sigma \pm$ résultant de la recombinaison excitonique dans la vallée +/-K se déplace linéairement vers des énergies plus basses/élevées. Il s'agit de l'effet Zeeman de vallée [Srivastava 2015, MacNeill 2015,Li 2015], qui reflète le décalage énergétique des sous-bandes impliquées dans le processus de recombinaison en fonction de leur moment magnétique (cf Fig(IV)). La correction apportée à l'énergie d'une transition optique est :

$$E(B) = E_0 - (\mu_{c\perp} - \mu_{v\perp})\mu_B B \qquad Eq(II)$$

Ou μ_B est le magnéton de Bohr $\mu_B = 5\,788\, eV.T^{-1}$ et $\mu_{c\perp}$le moment magnétique perpendiculaire de la sous-bande de conduction/valence impliquée dans le processus de recombinaison.

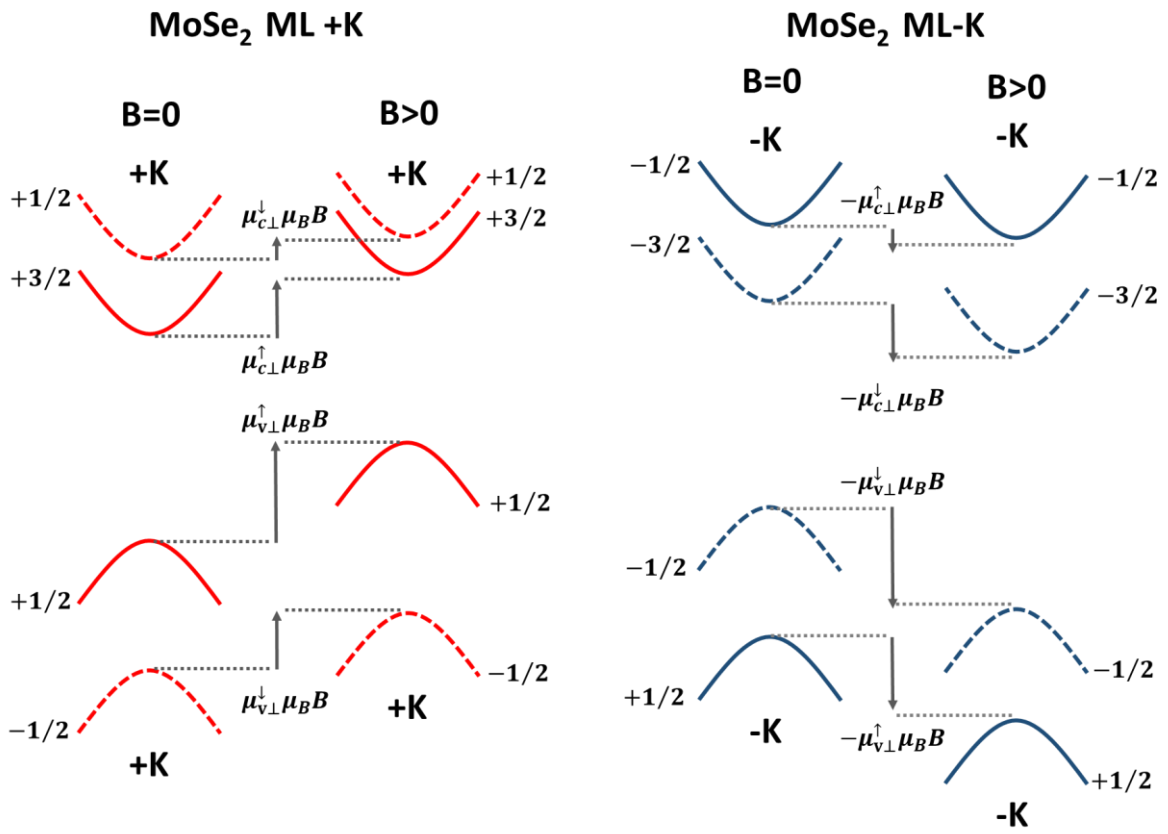

FigIV Effet d'un champ magnétique perpendiculaire sur la structure de bande des vallées +K et –K d'une monocouche de $MoSe_2$. Les sous-bandes de spin down/up sont représentées par des lignes pointillées /pleines. Chaque sous-bande est indexée par son moment angulaire Jz et son énergie Zeeman en fonction de $\boldsymbol{\mu_{c/v\perp}^{\downarrow/\uparrow}}$le moment magnétique perpendiculaire de la sous-bande .

Les hétérobicouches vdW et excitons intercouches

Les hétérobicouches TMD sont fabriquées en empilant deux monocouches de TMD différentes l'une sur l'autre. La plupart des hétérobicouches construites avec une combinaison de TMD du groupe IV sont des hétérostructures de type II (gap échelonné) [Kang 2013]. Cette configuration de la structure de bande donne lieu à l'émergence d'excitons intercouches, c'est-à-dire des excitons pour lesquels les deux particules liées sont localisées dans des monocouches différentes. On notera que cette recombinaison ne peut être envisagée de manière réaliste que si le gap est direct, c'est-à-dire si l'angle de rotation θ entre les deux monocouches est de 0° ou de 60° .

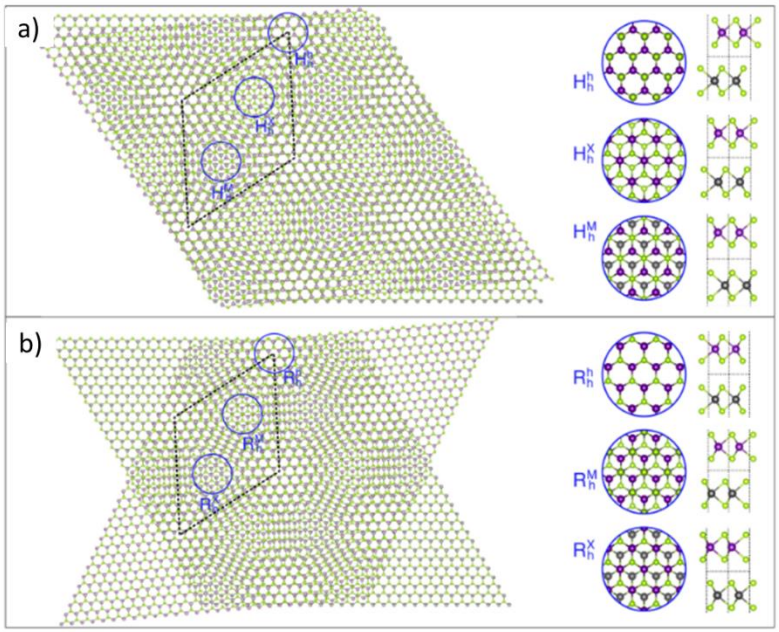

FigV Supercellule de moiré d'une hétérobicouche de $MoSe_2$ /WSe_2 dans le cas d'un alignement de type **a)** H (0°) **b)** R (60°). Figure adaptée de [Lu 2019].

La supercellule de moiré

Une petite déviation des angles θ=0° ou θ=60° entraine l'apparition d'un moiré atomique à l'interface de l'hétérobicouche. Ainsi, le réseau cristallin de l'hétérobicouche ne peut être décrit que par la périodicité d'une supercellule (cf Fig(V)). En réalité, même dans le cas d'un alignement parfait, la différence de paramètre de maille entre les deux monocouches se traduit par l'apparition d'un moiré. A l'intérieur de la supercellule, de nombreux alignements atomiques coexistent et l'on peut s'attendre à ce que les propriétés optiques du matériau soient complexes. Cependant, on considère que le voisinage direct des points de haute symétrie de la supercellule, définie dans [Yu 2017] comme les registres atomiques de la supercellule sont homogènes. De plus, les calculs de la modulation de la force d'oscillateur montrent que celui-ci est maximal aux alentours des registres atomiques correspondant au cas d'alignement atomique parfait de type H (0°) et R (60°). Cela indique qu'un registre atomique unique est à l'origine de la recombinaison des excitons intercouches dans l'hétérobicouche.

Reconstruction a l'interface de l'hétérobicouche

Cette théorie de la supercellule a été largement utilisée pour expliquer les propriétés des hétérobicouches TMD, mais elle a récemment été remise en question par des preuves de reconstruction atomique de l'interface entre les deux monocouches TMD [Rosenberger 2020, Weston 2021, Phillips 2021], Le calcul des énergies des différentes configurations d'empilement de la supercellule montre que la configuration d'empilement H (0°) présente deux minima dégénérés correspondant aux registres atomiques H_h^X et H_h^M tandis que la configuration R (60°) a un seul minimum correspondant au registre atomique R_h^h c'est-à-dire +K sur –K . Les résultats de mesures AFM montrent que, contrairement aux hypothèses des supercellules moirées, les deux monocouches TMD ne sont pas rigides et reconstruisent leur interface pour maximiser l'aire des domaines qui minimisent l'énergie d'empilement. L'hétérobicouche peut ainsi être considérée comme un ensemble de domaines homogènes. [Parzefall 2021] présente des éléments montrant que la reconstruction de l'interface est nécessaire à l'apparition d'excitons intercouches ce qui est une perspective tout à fait différente de la supercellule.

	$X_I(eV)$	θ	g
$MoSe_2/WSe_2$	$1.40^{[1]}$	60	-15
	$1.273-1.400^{[2]}$	60	–
	$1.35-1.400^{[3]}$	0 to 60	–
	$1.39^{[4]}1.33^{[4]}$	0	$+6.7$
		20	-15.9
		60	-15.9
	$1.36^{[5]}1.33^{[5]}$	–	$+6.06$
			-10.06
	$1.4^{[6]}$	60	10.7
			15.2
	$1.35^{[7]}$	–	–
	$1.39^{[8]}$	–	-15.8
	$1.42^{[9]}$	–	16.2
	$1.40^{[10]}$	56.4	$+12.2$
			-16.0
	$1.37^{[11]}$	0	$+5.2$
	$1.39^{[11]}$	60	-14.4
	$1.37^{[12]}$	–	–
MoS_2/WSe_2	$1.0^{[13]}$	2.2	–
$MoSe_2/MoS_2$	$1.35^{[14]}$	0 to 60	–
WSe_2/WS_2	$1.4^{[15]}$	50	15.4
			11.8
	$1.45-1.55^{[16]}$	0	–
	$1.4^{[17]}$	0	–

TabI Tableau résumant les valeurs d'énergie de l'exciton intercouche, d'angle d'alignement et de facteurs g rapportés dans la littérature. [**1**] [Nagler 2017] [**2**] [Rivera 2015] [**3**] [Nayak 2017] [**4**] [Seyler 2017] [**5**] [Joe 2019] [**6**] [Wang 2019] [**7**] [Jauregui 2018] [**8**] [Brotons-Gisbert 2020] [**9**] [Baek 2020] [**10**] [Brotons-Gisbert 2021] [**11**] [Holler 2021] [**12**] [Nagler 2017'] [**13**] [Karni 2021] [**14**] [Zhang 2018] [**15**] [Montblanch 2021] [**16**] [Jin 2019] [**17**] [Yuan 2020].Si il n'y a pas de signe devant le facteur g, la référence ne le renseigne pas

Magneto photoluminescence des excitons intercouches.

Les résultats d'expériences de magnéto-photoluminescence tirés de la littérature sont résumés dans Tab(I). La tendance générale est que quels que soient les matériaux, les hétérobicouches alignées avec θ=0° présentent un facteur g positif g=+6 (cf [Seyler 2017] et [Holler 2021]) qui est déjà supérieur à ce qui est observé dans les monocouches de TMD . Le signe positif est intriguant car la transition de plus basse énergie dans une monocouche alignée avec 0° correspond à un état de spin « bright » qui entraine toujours un facteur g négatif dans les monocouches. Cependant, dans le cas des hétérobicouches de type H (60°), les amplitudes du facteur g sont plus élevées que pour tout autre facteur g mesuré dans les matériaux 2D (g = -16) .De plus, [Brotons-Gisbert 2021] rapporte l'observation d'un exciton intercouche scindé en deux pics, l'un présentant un facteur g négatif g=-16 et l'autre présentant un facteur g positif g=+12

Résultats expérimentaux: Dépendance en puissance du spectre de photoluminescence des excitons intercouches.

L'influence de la puissance d'excitation sur le spectre de photoluminescence des excitons intercouches est double (cf Fig(IV)) et définit deux régimes d'excitation différents. À puissance d'excitation élevée, le spectre de PL est affecté par une interaction répulsive dipole-dipole [Laikhtman 2009]. Cet effet est observé par le décalage du pic de PL des excitons intercouches vers les hautes énergies, proportionnellement à la densité d'excitons intercouches, lorsque la puissance d'excitation augmente [Nagler 2017', Brotons-Gisbert 2020]. Le deuxième effet produit un changement de la forme de la ligne du spectre de PL qui se transforme d'un pic large (FWHM=15meV et 5meV) en une série de pics fins (FWHM=100µeV). Ce spectre à basse puissance d'excitation provient d'excitons piégés dans le potentiel de moiré.

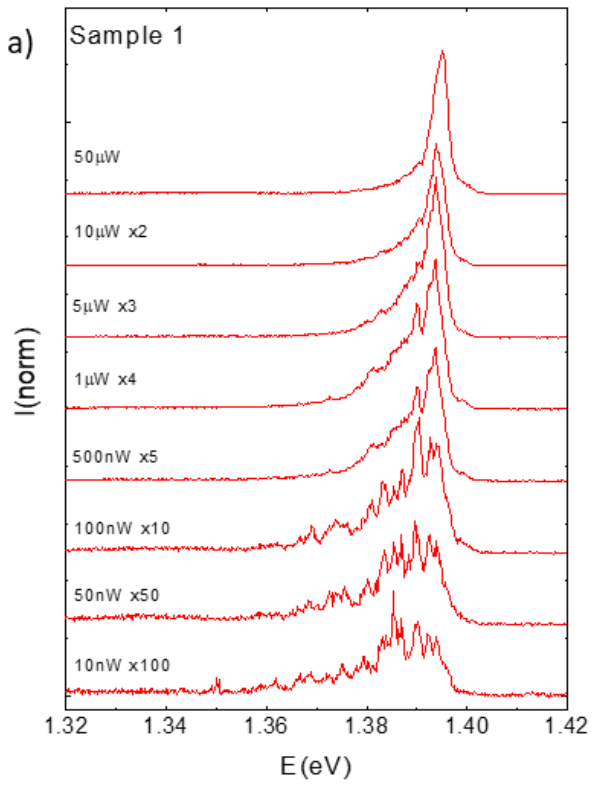

FigIV Dépendance en puissance du spectre PL des excitons intercouches. Les deux effets de la puissance d'excitation sont le décalage de la PL vers le hautes énergies a haute puissance d'excitation . Ainsi que le changement de la forme du spectre de PL à basse puissance d'excitation.

Résultats expérimentaux : Expérience d'excitation de photoluminescence

La Fig(VII) présente les résultats d'une expérience d'excitation de photoluminescence et montre le spectre de PL de l'exciton intercouche en fonction de l'énergie d'excitation. Le spectre de photoluminescence de l'exciton intercouche mesuré dans cet échantillon est composé de deux parties : un pic principal centré sur E=1,395eV et une émission plus large entre E=1,33eV et E=1,36eV attribuée aux excitons piégés dans le champ de contrainte de l'hétérostructure [Kremser]. Les Fig(VII.a) et Fig(VII.b) montrent l'intensité intégrée de ceux-ci en fonction de l'énergie d'excitation.

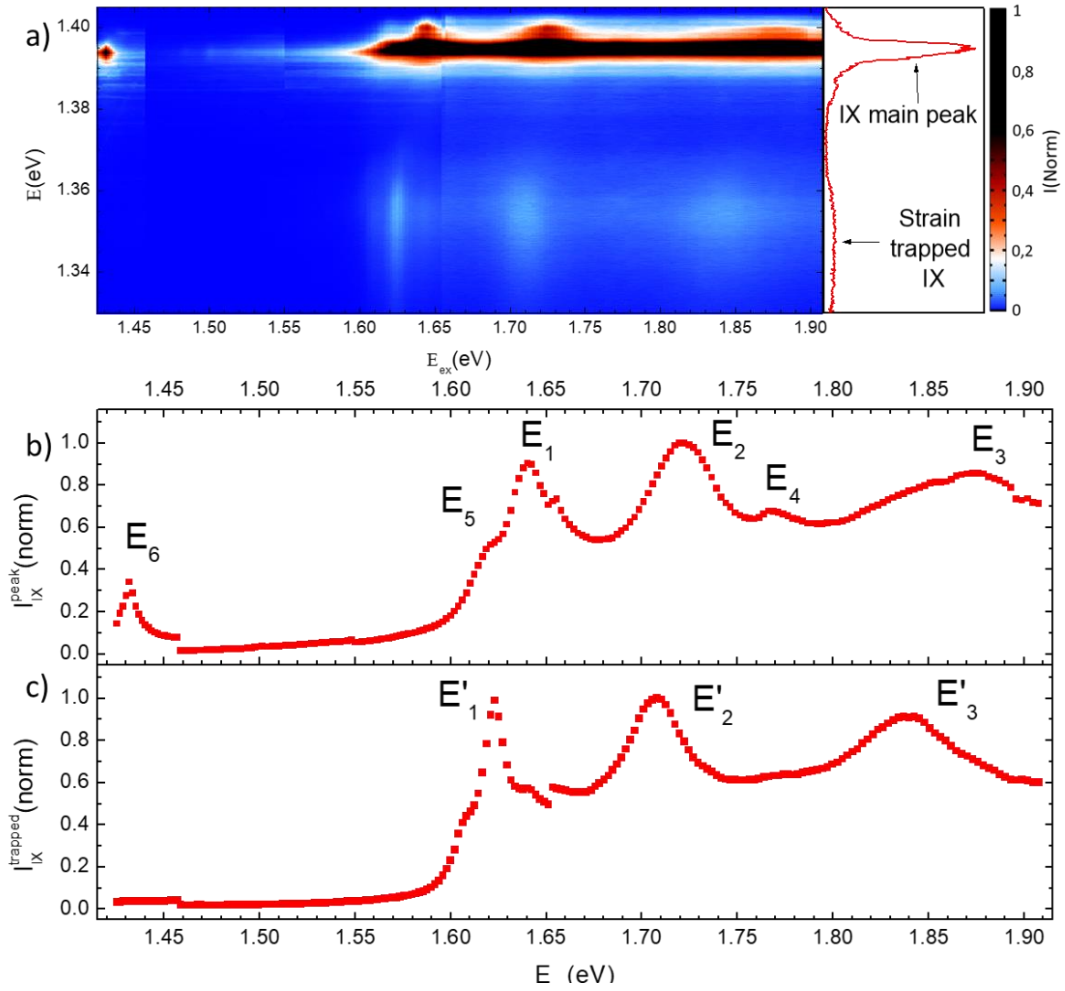

FigVII a) Carte de l'intensité du spectre PL de l'exciton intercouche en fonction de l'énergie d'excitation. Un spectre de PL a été ajouté sur la droite pour une meilleure lisibilité. L'échelle de couleurs a été saturée pour une meilleure visualisation du comportement à basse énergie. b) Intensité intégrée du pic PL principal de l'exciton intercouche PL en fonction de l'énergie d'excitation. c) Intensité intégrée des IX piègés dans le champ de contrainte en fonction de l'énergie d'excitation.

Dans le cas du pic principal, les énergies résonantes E_1 et E_2 correspondent aux énergies des excitons intracouches dans les monocouches de $MoSe_2$ et WSe_2. L'énergie E_3 se situe à mi-chemin entre l'énergie des excitons A des monocouches constituantes. L'énergie résonante E_4 est distante de E_2 d'une énergie correspondant à un phonon apparaissant dans le spectre Raman résonant de la monocouche de WSe_2. L'énergie E_5 correspond au trion de la monocouche de

$MoSe_2$. Dans le cas des excitons piégés dans le champ de contrainte, les énergies résonantes sont décalées par rapport au pic principal. L'origine de ce décalage est toujours débattue.

Prédiction du facteur g des excitons intercouches

Nous modélisons le facteur g par la somme des deux contributions indépendantes : la contribution orbitale g_d et la contribution de spin g_s qui dépendent des indices de vallées et de spin des sous bandes considérées et qui décrivent le moment magnétique d'une particule dans cette sous bande. La contribution orbitale peut prendre deux valeurs différentes : une pour les sous bandes de conduction g_d^{cond} et l'autre pour les sous bandes de valence g_d^{val}. Similairement, la contribution de spin prend deux valeurs, une pour les sous bandes spin-up et l'autre pour les sous bandes de spin-down (ces deux valeurs étant nécessairement opposées ; dû à la symétrie de renversement du temps). En considérant les valeurs de facteurs g de différentes transitions intra couches, nous obtenons les estimations suivantes pour les paramètres g_d et g_s :

$$\begin{cases} g_d^{cond} = 2 \\ g_d^{val} = 4 \\ g_s = 1 \end{cases} \qquad Eq(III)$$

A l'aide de ces paramètres, nous estimons les facteurs g des exciton « dark » et « bright » dans les hétérobicouches de $MoSe_2/WSe_2$ alignées avec un angle de 0° et 60°. Notablement, pour un angle de 60°, nos estimations prédisent un facteur g de $g = +12$ pour l'exciton « bright » et $g = -16$ pour l'exciton « dark ». Ces valeurs sont cohérentes avec les facteurs g rapportés dans la littérature pour de telles hétérostructures [Seyler 2017, Nagler 2017, Holler 2021, Baek 2020, Montblanch 2021].

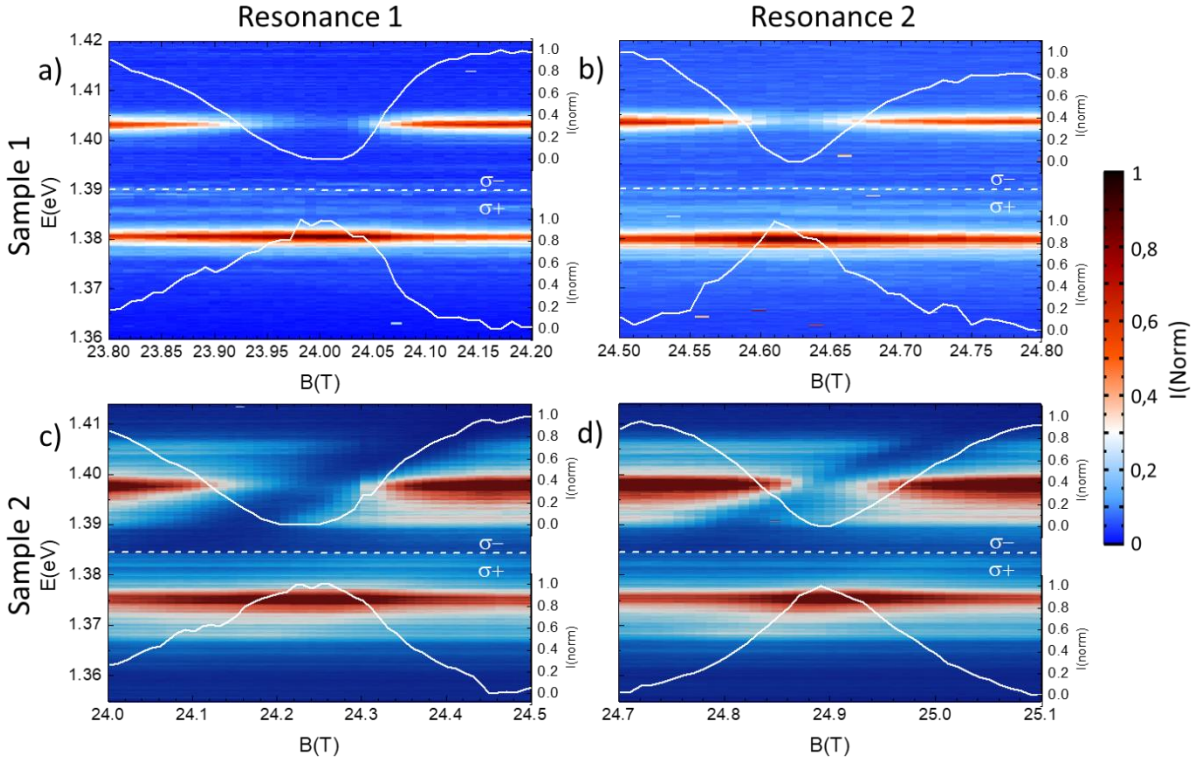

Fig VIII Cartes de la magnéto-photoluminescence des excitons intercouches dans l'échantillon 1 a) et b) et l'échantillon 2 c) et d). Le champ magnétique est balayé à travers la première résonance pour a) et c) et la deuxième résonance pour b) et d). Les courbes blanches représentent l'intensité normalisée des excitons intercouches.

Résultats expérimentaux : Expérience d'excitation de photoluminescence

Nous présentons les résultats d'expériences de magnéto-photoluminescence des excitons intercouches dans les hétérobicouches de $MoSe_2/WSe_2$ alignées avec un angle de 60°. Nous mesurons une valeur de g=-16 pour le facteur g de l'exciton intercouche ce qui correspond à un état de spin triplet [Brotons-Gisbert 2021]. Nous constatons que l'intensité de la composante polarisée σ- s'effondre pour une valeur de champ magnétique bien spécifique (B=-24T) de la même manière l'intensité de la composante polarisée σ+ augmente sensiblement. Cet effet est observé pour une deuxième valeur de champ magnétique plus élevé sur deux échantillons différents. La Fig(VIII) montre les cartes de magnéto-photoluminescence de l'exciton intercouche de ces deux échantillons pour les deux résonances. L'énergie Zeeman de l'exciton intercouche est de $E_z = 22{,}3 \pm 0{,}2\ meV$ pour la première résonance et de $E_z = 22{,}9 \pm 0{,}2\ meV$ pour la seconde. Ces énergies correspondent aux modes phonons chiraux E'' des monocouches de $MoSe_2$ et WSe_2 qui portent une quantité de moment pseudo angulaire (PAM) de ± 1.

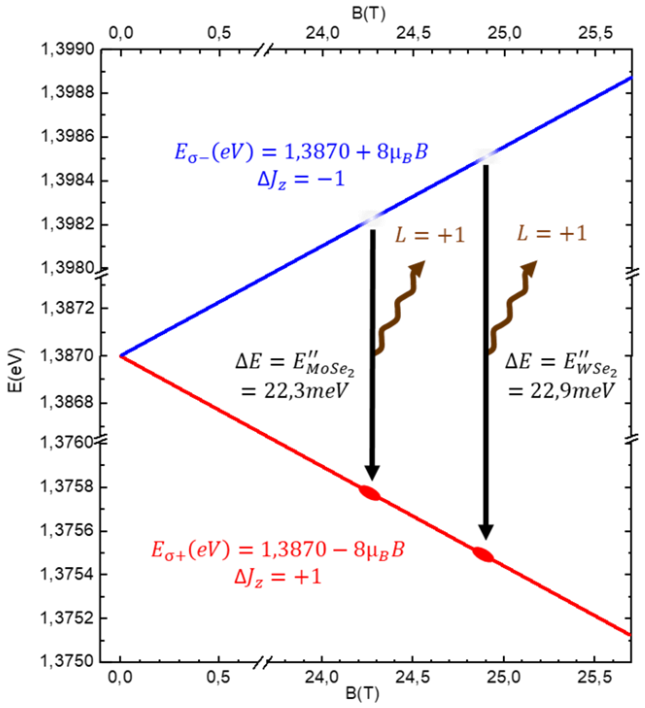

FigIX Processus de relaxation des excitons intercouches résonnant en champ magnétique. La différence d'énergie entre l'émission polarisée σ- (ligne bleue) et l'émission polarisée σ+ (ligne rouge) est en résonance avec les énergies du mode phonon chiral E" des monocouche de $MoSe_2$ et de WSe_2. Ainsi, un canal de relaxation (flèche noire) par l'émission de phonon E'' (flèche brune) s'ouvre entre les deux composantes.

Nous proposons donc l'explication suivante pour les processus de relaxation (cf Fig(IX)): en raison du facteur g élevé de l'état de spin triplet des excitons intercouches, l'énergie Zeeman atteint des valeurs bien plus grandes que pour des excitons dans les monocouches de TMD. Cette énergie peut être mise en résonance avec l'énergie des phonons E'' des monocouches constituant l'hétérobicouche par l'application d'un fort champ magnétique dans la direction perpendiculaire au plan de l'échantillon. A la valeur de champ magnétique résonant B=24T, l'énergie Zeeman de l'exciton intercouche est égale à l'énergie du mode chiral E'' de la monocouche de $MoSe_2$. Un canal de relaxation par émission d'un phonon E '' s'ouvre alors entre la composante de haute énergie polarisée σ- et la composante de basse énergie σ+. Il est important de noter que le moment pseudo-angulaire (PAM) porté par le phonon est essentiel

dans le phénomène de relaxation car il contribue à la conservation du moment angulaire total. Le canal de relaxation se ferme lorsque l'énergie Zeeman est hors résonance avec le mode E''. Dans le cas de la seconde résonance, le processus est le même mais implique un phonon E'' de la monocouche de WSe_2. Enfin, nous constatons que le profil de la résonance est diagonal : les excitons intercouches qui possèdent les énergies de recombinaison les plus basses entrent en résonance pour un champ magnétique plus faible que les excitons comportant les énergies de recombinaison les plus élevées. Il y a donc une relation de proportionnalité entre l'énergie de l'exciton intercouche et son facteur g. Nous attribuons cette dépendance à la variation de la contribution orbitale g_d entre les différents domaines reconstruits de l'hétérobicouche , selon la formule de [Roth 1959]. Nous extrayons donc ce facteur de proportionnalité et observons un coefficient d'un ordre de quelques eV^{-1}.

Conclusion et perspectives

Nous avons montré que la conservation du moment cinétique dans les monocouches et hétérobicouches de TMD définit non seulement les règles de sélection optique mais a également des conséquences profondes sur l'interaction électron-phonon. Nous avons mis en évidence un processus de relaxation entre les composantes polarisées σ- et σ+ de l'exciton intercouche dans lequel la conservation de la quantité de mouvement est satisfaite par l'émission d'un phonon chiral. Ce processus a été découvert par l'utilisation d'un champ magnétique : tirant parti du facteur-g élevé de l'état de triplet de spin de l'exciton intercouche, nous avons mis en résonance l'énergie Zeeman de l'exciton avec l'énergie des modes de phonons chiraux E" des monocouches de WSe_2 et $MoSe_2$. Ces phonons portent un moment pseudo angulaire ±1 qui, en raison de la symétrie C_3, induit un retournement de spin excitonique. Bien que le champ magnétique requis pour activer cet effet en fasse un candidat peu probable pour des applications potentielles, ces résultats montrent que les hétérobicouches TMD offrent la possibilité de contrôler à la fois le confinement d'un état quantique et sa relaxation.